AFCRL 336

Technical Report 73

PRECIPITATION CHARGING
AND CORONA-GENERATED INTERFERENCE
IN AIRCRAFT

Prepared for:

ELECTRONICS RESEARCH DIRECTORATE
AIR FORCE CAMBRIDGE R   CH LABORATORIES
OFFICE OF AEROSPACE RESEARCH
UNITED STATES AIR FORCE
BEDFORD, MASSACHUSETTS

CONTRACT AF 19(604)-3458

By: R. L. Tanner   J. E. Nanevicz

STANFORD RESEARCH INSTITUTE

MENLO PARK, CALIFORNIA

*SRI

ABSTRACT

Triboelectric charging, occurring when an aircraft is operated in precipitation, raises the aircraft potential until corona discharges occur from points of high dc field on the aircraft. These corona discharges generate noise which is coupled into receiving systems. The magnitude and spectral distribution of this radio interference, called *precipitation static*, depends upon three factors: (1) the strength and spectral characteristics of the source discharges, (2) the manner in which the disturbances produced by the discharges couple into the antennas, and (3) the magnitude of the discharge current and its distribution among the discharging extremities.

The coupling between the antenna and the noise source is discussed with the aid of a reciprocity relationship. Since the geometry of an aircraft is complicated, and a purely theoretical approach to the determination of coupling factors is not possible, a technique for measuring absolute values of coupling factor as a function of frequency and position on the aircraft was developed and is described in considerable detail.

A study was made of the spectral character of the corona-noise source. Included in this study was an investigation of the manner in which the source spectrum is affected by altitude. Since the noise-spectrum magnitude depends upon the total current discharged, methods for determining the discharge current were devised. Furthermore, given a total discharge current, the noise generated in an antenna depends upon the distribution of this current among the various extremities. The problem of determining this distribution was investigated

To test the validity of the theory and the results of the laboratory work, calculations were made to predict the noise currents induced in the two test antennas employed in a flight-test program conducted on the Boeing 367-80 aircraft (prototype of the KC-135 and 707). The results of these predictions are compared with the noise spectrum measured in flight.

Although most of the research was done with dipole-type receiving antennas in mind, a brief investigation was made of the characteristics of loop antennas. The results of this investigation indicate some interesting differences between dipoles and loops, regarding susceptibility to precipitation-static interference. In particular, the results indicate a reason for the frequently observed superiority of loops over dipoles from the standpoint of vulnerability to precipitation-static noise in the middle- and low-frequency ranges.

Considerable time was spent in devising, analyzing and testing techniques for reducing corona noise. The techniques considered include decoupled antennas, decoupled dischargers, biased decoupled dischargers, AN/ASA-3 wick dischargers, biased jet-engine exhausts, and interference blankers.

CONTENTS

▼

CONTENTS

ILLUSTRATIONS

ILLUSTRATIONS

viii

ILLUSTRATIONS

TABLES

PRECIPITATION CHARGING AND CORONA-GENERATED INTERFERENCE IN AIRCRAFT

I INTRODUCTION

A. HISTORY

When radio equipment came into use in aircraft, it was found that severe interference occurred in the receiving systems whenever the aircraft was operated in precipitation containing ice crystals. From this connection with flights through precipitation, this general class of interference was given the name *precipitation static*. Since the interference was often sufficiently severe to completely disable communications for hours at a time, it presented a serious flight safety hazard. Studies were undertaken, therefore, to determine the causes for the interference so that effective measures might be taken to eliminate it, or at least to reduce it to a tolerable level.

Early investigators found that one type of precipitation static was caused by corona discharges from the aircraft.[1,2,3] At first there was uncertainty as to how the aircraft became charged; some investigators felt that it was caused by charge transfer from charged particles in the cloud, but it was soon shown that "triboelectric" charging was the responsible mechanism.

Triboelectric charging occurs whenever two dissimilar materials are placed in contact and then separated. One material acquires a positive charge, and the other a negative charge, as in the case of a hard rubber comb rubbed with fur. In the case of an aircraft flying through precipitation containing ice crystals, the ice crystals generally acquire a positive charge, leaving the aircraft with a negative charge. Since the triboelectric charging mechanism is equivalent to a constant current source, the potential of an aircraft flying in precipitation will rise until corona threshold potential is exceeded, and finally the corona discharge current will equal the charging current.

1

A corona discharge consists of a series of extremely short pulses, and therefore generates noise containing frequency components well into the RF spectrum. This noise couples into the aircraft receiving antennas, generating interference in the communication and navigation systems.

One of the first approaches to the elimination of precipitation-static interference was directed at the elimination of aircraft charging.[3] It was known that all materials may be arranged in a triboelectric series such that, in general, materials higher in the series tend to charge positively when brought into contact with materials below them in the series. Since neighboring materials in the triboelectric series tend to charge one another less than do widely separated materials, it was felt that, through a suitable choice of paint, it might be possible to eliminate or at least minimize aircraft charging. Attempts along these lines were completely unsuccessful since triboelectric charging is a surface phenomenon, and a thin film of oil is sufficient to completely destroy any desirable properties that a coating might have. Furthermore, since position in the triboelectric series tends to be a function of dielectric constant, and since the dielectric constant of ice varies with temperature, it would be very difficult to find a coating suitable for all weather conditions.

Another approach to the problem was to devise methods for discharging the aircraft without generating noise in the receiving systems. One proposed system was the block and squirter in which a discharger is maintained at a high ac potential with respect to the aircraft.[4] The receiving circuits are blocked during the alternate half cycles during which discharges occur. Another system is the biased discharger in which a discharge is forced to occur between a point and a cylinder.[5] Discharging occurs when ions of the same polarity as the point are carried away by the airstream, while ions of the opposite charge are captured by the high fields of the point. Other proposed systems include flame dischargers, electron gun discharge tubes, and direct thermionic emitters.[6]

Still another approach was to operate on the noise signal after it had been coupled into the receiving antenna. A noise "blanker" inserted in the circuit between the antenna and receiver would short out the receiver terminals as soon as a noise impulse appeared at the input to the blanker. The receiver terminals would remain shorted for the duration of the noise impulse.

2

In an effort to study precipitation static quantitatively, the electromagnetic coupling between a noise-producing discharge and an antenna was analyzed.[7] One important result of this analysis is the coupling theorem by which the receiving-circuit response to an electrical discharge can be calculated. The theorem states that the coupling between a discharge and an antenna is proportional to the current density of the discharge and to the strength of the electric field which would exist along the path of the discharge if a voltage were applied to the antenna terminals.

Applying the results of the coupling theorem to the problem of corona noise it is evident that the coupled noise is least if the discharge occurs along the path of least reciprocal field. In the analysis mentioned above,[7] it was shown, furthermore, that corona discharges should be forced to occur from points of small radii since the discharge then consists of low-amplitude pulses having a high repetition frequency. A discharge of this type is inherently less noisy than one occurring from a point of large radius which consists of high-amplitude pulses having a low repetition frequency.

The analysis indicates the reasons for the partial success of certain procedures currently used to minimize corona noise. The use of dielectric-coated antenna wire prevents discharges in the high reciprocal field of the antenna itself. Wick dischargers located on the aircraft extremities force the discharges to occur from a number of points of small radii at the tip of each wick. Furthermore, since the distributed resistance of the wick does not alter the RF coupling fields, the discharge is removed from the region of high coupling field in the immediate vicinity of the aircraft extremity.

With the advent of high-performance aircraft and flush-mounted antennas, a second type of noise included in the general classification of *precipitation static* became important and was identified.[8] This second form of noise is associated with the charging of dielectric portions of the aircraft—such as canopies, radomes, and flush-mounted antennas. These sections of the aircraft also become charged by the triboelectric mechanism, but since they are insulators, the charge on them continues to rise until the potential is sufficiently high to induce a streamer, or spark discharge, across the dielectric surface to some adjacent metallic structure of the aircraft. It was found that these discharges involve a very rapid transfer of several thousand micromicrocoulombs of charge over

3

long distances and are thus energetic sources of noise, particularly if they occur on the dielectric covering of an antenna where the coupling is also high.

It was found in laboratory experiments and flight tests that a high-resistance conductive coating over the dielectric surface was effective in eliminating streamer noise.[8,9] The conductive coating drains away the charge as rapidly as it arrives, and prevents the voltage build-up which produces the streamer discharges. There were, however, reports of ADF malfunction when the receiving antennas were located under dielectric surfaces which had been coated with conductive paint, and it was suggested that perhaps some unexplained noise-generating mechanism which was not eliminated by the coating might be responsible for the interference.

It was subsequently shown that a third type of noise which may be included in the precipitation static category did indeed exist.[8] This noise was found to be produced by the individual impinging precipitation particles, and consists of overlapping step-fronted pulses produced by the individual precipitation particles as they acquire charge upon impact in a region of reciprocal antenna field. Since this mechanism requires a component of electric field tangent to the particle path at the time of impact, this noise is generated primarily on dielectric portions of the aircraft. Furthermore, since this type of noise is produced by acquisition of charge in a reciprocal field region, the noise mechanism is unaffected by the use of conductive coatings—unless the conductivity of the coatings is so high as to effectively short out the antenna--and this type of noise is found even under conductively coated dielectrics. The results both of flight tests and a detailed study of the noise generated on aircraft canopy surfaces indicated, however, that impact noise is much less serious than streamering, and that canopy-antenna noise should be reduced by as much as 54 db by eliminating streamering on the canopy surface.[8,9] Reports that ADF operation was not improved through the use of a conductive canopy coating, indicated, therefore, either that an un-identified noise mechanism existed, or that corona discharges from aircraft extremities were generating noise in the canopy antennas.

In an effort to dispel the existing uncertainty regarding the sources of precipitation-static interference observed in flight, techniques developed under Air Force Contract 19(604)-1296 were employed to determine the coupling between aircraft receiving antennas and points on the aircraft

from which corona discharges would occur in flight. The results of these measurements together with laboratory studies of corona-discharge characteristics were used to predict the corona-generated noise levels which should exist at the tail-cap and belly-antenna locations on the KC-135 aircraft. The predicted noise levels (sufficiently high to cause severe interference) were verified in subsequent flight tests, during which measurements were made of the noise levels in these two antennas.[10] During this same flight-test program, tests were made of the effectiveness of aircraft dischargers employing a noise-decoupling principle which follows from the work done on this contract.[10,11]

B. PURPOSES AND SCOPE OF INVESTIGATION

In general, the research carried out on this project consisted of theoretical investigations and laboratory work, but did not include flight testing. The purpose of the research was to develop an understanding of the problem of precipitation static noise generation and coupling which would eventually lead to the development of techniques for the elimination of this type of interference. Since the work on this contract paralleled in time that described in Refs. 10 and 11 [Contracts AF 33(616)-3914 and AF 33(616)-6561 which included provisions for flight testing], it was possible to flight test many of the schemes developed on the present project. Pertinent results of these flight tests will be included in this report. Although precipitation static can be generated by three different mechanisms—corona, surface streamering, and particle impact—it is felt that the mechanisms of streamering and particle impact were adequately treated in Refs. 8 and 9. For this reason, this report will confine itself primarily to the problems connected with corona-generated interference.

The magnitude and spectral characteristics of corona-generated interferences are principally dependent upon three factors: (1) the strength and spectral characteristics of the source discharges, (2) the manner in which the disturbances produced by the discharges couple into the antennas, and (3) the magnitude of the discharge current and its distribution among the various discharging extremities.

Perhaps the most poorly understood aspect of the corona noise problem was the coupling between the noise source and the antenna. This problem is discussed with the aid of the coupling theorem of Ref. 7. Since the

5

geometry of an aircraft is complicated, a purely theoretical approach to the determination of coupling factors is not possible. Therefore, a technique for measuring absolute values of coupling factor as a function of frequency and position on the aircraft was developed and is described in considerable detail.

A study was made of the spectral character of the corona noise source. Included in this study was an investigation of the manner in which the source spectrum is affected by altitude. Since the noise-spectrum magnitude depends upon the total current discharged, methods for determining the discharge current were devised. Furthermore, given a total discharge current, the noise generated in an antenna depends upon the distribution of this current among the various extremities. The problem of determining this distribution was investigated.

To test the validity of the theory and the results of the laboratory work, calculations were made to predict the noise currents induced in the two test antennas employed in the flight tests described in Refs. 10 and 11. The results of these predictions are compared with the noise spectra measured in flight.

Although most of the research was done with dipole-type receiving antennas in mind, a brief investigation was made of the characteristics of loop antennas. The results of this investigation indicate some interesting differences, regarding susceptibility to precipitation-static interference, between dipoles and loops. In particular, the results indicate a reason for the frequently observed superiority of loops over dipoles from the standpoint of vulnerability to precipitation-static noise in the middle- and low-frequency ranges.

Considerable time was spent in devising, analyzing, and testing techniques for reducing corona noise The techniques considered include decoupled antennas, decoupled dischargers, biased decoupled dischargers, AN/ASA-3 wick dischargers, biased jet engine exhausts, and interference blankers.

II COUPLING BETWEEN ANTENNA AND NOISE SOURCE

A. GENERAL

Perhaps the greatest impediment to progress in investigations of precipitation static has been a lack of understanding of the manner in which the noise generated by a discharge is coupled into the receiving systems. In particular, the lack of quantitative data regarding coupling makes the design of conclusive flight-test experiments extremely diffi-cult. Furthermore, intuitive judgment regarding coupling may often be completely erroneous. For example, it might appear reasonable to assume that coupling will decrease as the distance between the noise source and antenna is increased, whereas actually, as will be demonstrated later, it is often possible for the coupling to increase with increasing separation.

A reciprocity relationship which permits a study of the electromagnetic coupling between a noise-producing disturbance and an antenna was derived in conjunction with the study of corona-discharge noise in Ref. 7. For the sake of completeness, much of the discussion will be repeated here. A statement of the theorem is given below, and its derivation is reproduced in Appendix A.

B. STATEMENT OF COUPLING THEOREM

Before stating the theorem it is first necessary to define the terms which will be used. Referring to Fig. 1, consider a conducting body of arbitrary shape with two regions of particular interest. The first of these, T_1, represents a volume which has been removed from the body to form antenna terminals. The second region, T_2, is external to the body and is defined as the volume in which the noise-producing disturbance occurs.

It will be necessary to define two independent situations, as follows: Situation 1—A voltage $V_1(\omega)$ is applied to the antenna terminals at T_1, producing a field $\mathbf{E}_1(x,\omega)$ at all points external to the antenna, and in particular in region T_2.

7

REGION T_2 IN WHICH DISTURBANCE, CHARACTERIZED BY CURRENT DENSITY J_2, OCCURS
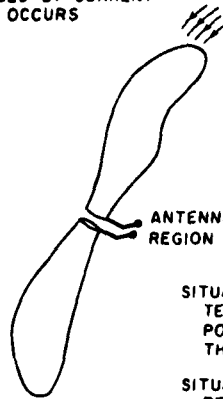
$$I_2 = \frac{1}{V_1} \int_{T_2} E_1 \cdot J_2 dv$$

ANTENNA TERMINALS
REGION T_1

SITUATION 1: VOLTAGE V_1 IS APPLIED TO TERMINALS T_1 PRODUCING FIELD E_1 AT ALL POINTS OF SPACE AND IN PARTICULAR IN THE REGION T_2

SITUATION 2: DISTURBANCE OCCURS IN THE REGION T_2. CURRENT DENSITY J_2 IS THEREFORE FINITE IN T_2. IN RESPONSE TO THE DISCHARGE A CURRENT I_2 FLOWS IN THE SHORT-CIRCUITED ANTENNA TERMINALS T_1

RA-2494-264

FIG. 1

ILLUSTRATION OF NOISE-COUPLING THEOREM

Situation 2—A disturbance occurs in region T_2 (either a discharge occurs or a moving charged particle exists) producing a current density $\mathbf{J}_2(x,\omega)$ in that region. In response to the disturbance a current $I_2(\omega)$ flows in the short-circuited antenna terminals at T_1.

For the conditions outlined in the situations described above, the coupling theorem states that

$$I_2(\omega) = \frac{1}{V_1(\omega)} \int_{T_2} \mathbf{E}_1 \cdot \mathbf{J}_2 dv \quad . \tag{1}$$

Equation (1) is derived using the Fourier-transformed form of Maxwell's equations, so that all quantities are functions of frequency. The field quantities $\mathbf{E}_1(x,\omega)$ and $\mathbf{J}_2(x,\omega)$ are also, as indicated, functions of the spatial coordinates. To obtain the response as a function of time it is necessary to perform the inverse Fourier transformation.

There are two useful interpretations of the coupling theorem of Eq. (1). If the field $\mathbf{E}_1$ existing in region T_2 when the voltage V_1 is applied at T_1 is known, together with the current density $\mathbf{J}_2$ occurring

during the disturbance, then Eq. (1) defines the short-circuit current induced in the antenna terminals. This information together with Norton's or Thevenin's theorems is sufficient to permit the calculation of the response of a radio receiver connected to the antenna terminals.

A converse interpretation of Eq. (1) is equally useful. If the field $\mathbf{E}_1$ produced by the voltage V_1 and the short-circuit terminal current I_2 are known, Eq. (1) may be regarded as an integral equation for the current density $\mathbf{J}_2$. Since several different distributions of $\mathbf{J}_2$ may produce the same terminal current I_2, the solutions to this integral equation are not unique. In many cases, however, supplementary information may be used with Eq. (1) to reduce the number of possible solutions for $\mathbf{J}_2$.

In applying the coupling equation to the study of corona-generated interference the most important fact to observe is that the signal coupled into the receiver from a discharge at any point on the aircraft structure is proportional to the electric field which would be produced at the point of the discharge by a voltage applied to the antenna terminals. From this fact several important conclusions can be drawn. For example, it is evident that the coupling is a function of frequency. Definite maxima and minima occur for the coupling from discharges at extremities of an aircraft, and are associated with the electromagnetic resonances of the structure. A further conclusion is that, quite perversely, the coupling tends to be very good from just those points where corona is most likely to occur. Thus, if we applied a radio-frequency voltage to the antenna terminals and examined the resulting field we would find that concentrations of field would occur at the extremities where most of the discharges occur. Furthermore, if we were to examine the field in detail over a relatively small volume near an extremity, we would find the configuration of the field to be indistinguishable from that of the dc field which induces the discharges. Sharp local concentrations, signifying good coupling, would occur at the protrusions where the dc field concentrates.

Although one could use Eq. (1) as it stands to determine the noise current coupled into an antenna, the practical problems involved would be far from trivial. It would be necessary, as was indicated above, to know both $\mathbf{E}_1$ and $\mathbf{J}_2$ throughout the region in which $\mathbf{J}_2$ is non-zero. Since the charge motion responsible for noise generation in a corona discharge is

confined to a region whose dimensions are of the order of the discharge-
point radius, it would be necessary to determine accurately the field
structure about an aircraft extremity, with particular attention to the
details of the structure about the burrs and imperfections from which the
corona discharges occur. It would, furthermore, be necessary to determine
the details of the structure of the current density J_2 in this same small
region. For these reasons it is much simpler to rewrite Eq. (1) slightly
to eliminate the necessity for determining these details of E_1 and J_2
which really are not of direct concern in the study of radio interference.
Let us define

$$\mathbf{E}_1(\mathbf{x}, \omega) \quad = \quad E_1(\xi, \omega) \frac{\mathbf{E}_1(\mathbf{x})}{E_1(\xi)} \tag{2}$$

where $E_1(\omega, \xi)$ is the magnitude of the electric field in a specified direc-
tion at a reference point near the point at which corona discharge is
assumed to occur as is indicated in Fig. 2. The reference point must be
sufficiently near the edge that its field varies with frequency and posi-
tion along the airfoil span in the same manner as does the field at the
discharge point. The term $\mathbf{E}_1(\mathbf{x})/E_1(\xi)$ describes the normalized field in
the vicinity of the discharge point, and, in particular, it includes the
detailed field variation in the region where J_2 is non-zero. Substituting
Eq. (2) into Eq. (1) we obtain

$$I_2(\omega) \quad = \quad \frac{E_1(\xi, \omega)}{V_1(\omega)} \frac{1}{E_1(\xi)} \int_{T_2} \mathbf{E}_1(\mathbf{x}) \cdot \mathbf{J}_2(\mathbf{x}, \omega) d\mathbf{x} \tag{3}$$

defining

$$\psi(\xi, \omega) \quad = \quad \frac{E_1(\xi, \omega)}{V_1(\omega)} \tag{4}$$

and

$$D(\omega) \quad = \quad \frac{1}{E_1(\xi)} \int_{T_2} \mathbf{E}_1(\mathbf{x}) \cdot \mathbf{J}_2(\mathbf{x}, \omega) d\mathbf{x} \quad . \tag{5}$$

10

AIRCRAFT EXTREMITY

TYPE–A REFERENCE POINT.
$E_1(\xi,\omega)$ IS THE MAGNITUDE OF THE
FIELD AT POINT ξ IN THE DIRECTION
NORMAL TO THE PLANE OF THE AIRFOIL

TYPE–B REFERENCE POINT.
$E_1(\xi,\omega)$ IS THE MAGNITUDE OF THE
FIELD AT POINT ξ IN THE PLANE OF THE
AIRFOIL AND NORMAL TO ITS EDGE.

A DISCHARGE OCCURS FROM IMPERFECTION
LOCATED HERE. $E_1(\kappa)$ EXPRESSES THE FIELD
BEHAVIOR AROUND THE AIRCRAFT EXTREMITY,
PARTICULARLY THE DETAILS IN THE IMMEDIATE
VICINITY OF THE IMPERFECTION.

RA-2494-288

FIG. 2

REFERENCE POINTS USED FOR COUPLING MEASUREMENTS

Equation (3) may be written

$$I_2(\omega) \;\; = \;\; \psi(\xi,\omega)D(\omega) \tag{6}$$

Here $D(\omega)$ describes the noise spectrum existing at the corona-discharge
noise source, taking into account the effects of imperfections in trailing
edge structure. The term $\psi(\xi,\omega)$—which will henceforth be termed the
"coupling function"—describes the manner in which the noise spectrum is
modified by the coupling between the source and the antenna.

Writing the coupling theorem in the form of Eq. (6) simplifies the
study of noise generation and coupling considerably since it is now pos-
sible to study the two aspects of the problem separately. For example,
model measurements may be made to determine the coupling between an antenna
and a reference point without the necessity for careful modeling of the

11

extremities and their imperfections. The source spectrum may be studied in the laboratory by measuring the noise generated by corona discharges from a full-scale section of aircraft extremity arranged in an electrode structure such that the fields about the section of extremity duplicate the field structure existing in flight. Since the source spectrum will be the same in flight as in the laboratory (for the same discharge current and the same air density), and since the coupling to the reference point in the laboratory set-up may be measured, the laboratory noise measurements may be used to determine the source spectrum $D(\omega)$.

C. DETERMINATION OF COUPLING

Although, in the case of a simple antenna geometry, it is possible to calculate the coupling function, ψ, it was apparent at the outset that aircraft shapes are sufficiently complex to render calculation impractical and that it would be necessary to devise a scheme for measuring the coupling. The method finally developed consists, in essence, of exploring the extremities on a model of the aircraft with a spark-discharge signal source and measuring the signal induced in the modeled receiving antenna.

As was indicated earlier, we are interested in the coupling between the antenna and a series of reference points near the extremities from which corona occurs. In general, each reference point is chosen to be sufficiently near the point at which corona occurs that the reference-point field varies with frequency ω and position ξ in the same manner as does the field at the corona-discharge point. Since coupling measurements are generally made using a model, however, the modeled distance of the reference point from the discharging extremity should be sufficiently great that the field at the reference point on the model is not influenced by the details of the extremity. In practice, reference points such as those shown in Fig. 2 were employed. Type A reference points were located on the surface of the airfoil and ten inches in from the edge on the full-scale aircraft. The field component measured at the reference point was the one normal to the airfoil surface. Type B reference points were located in the plane of the airfoil and ten inches out from its edge. The field component measured in this case was that in the plane of the airfoil and normal to its edge.

Let us now assume that we contrive to produce a spark discharge at the reference point ξ with the discharge axis directed along the component

12

of field $E_1(\xi,\omega)$ chosen to define coupling at this reference point (normal to the airfoil surface in the case of a Type A reference point). The signal induced in the receiving antenna by this spark discharge may be found by rewriting the coupling theorem of Eq. (1) as follows:

$$I_{2_s}(\omega) \quad = \quad \frac{E_1(\xi,\omega)}{V_1(\omega)} \int f(z)J_{2_s}(z,\omega)dz \qquad (7)$$

where $J_{2_s}(z,\omega)$ describes the current in the spark discharge and where $f(z)$ is the function relating the field existing within the spark gap to the reference field $E(\xi,\omega)$ as follows:

$$E_{gap}(z,\omega) \quad = \quad f(z)E_1(\xi,\omega) \qquad . \qquad (8)$$

Substituting Eq. (4) into Eq. (7) we obtain

$$I_{2_s}(\omega) \quad = \quad \psi(\xi,\omega) \int f(z)J_{2_s}(z,\omega)dz \qquad (9)$$

in which the integral describes the spectrum generated by the spark source. Since the same spark source is used for the measurements at all points on the aircraft, the integral term does not vary, and therefore variations occurring in $I_{2_s}(\omega)$ as the spark source is moved from point to point on the aircraft indicate changes in the coupling, $\psi(\xi,\omega)$. To make absolute measurements of coupling it is necessary first to calibrate the spark discharge by reading $I_{2_s}(\omega)$ in a standard geometry for which the coupling, ψ, is known.

D   INSTRUMENTATION FOR COUPLING MEASUREMENT

A block diagram of the instrumentation used in making the coupling measurements is shown in Fig. 3. The attenuator, receiver, and voltmeter were battery operated and were housed within the 1/10 scale mock-up of the KC-135 aircraft used in the coupling studies. A distributed resistance of high value was used to provide a dc ground return to the mock-up, which was mounted on a tower and isolated from ground at RF frequencies to re-produce as nearly as possible the RF field distributions existing in flight. Since a 1/10-scale mock-up was used, the measurement frequencies employed
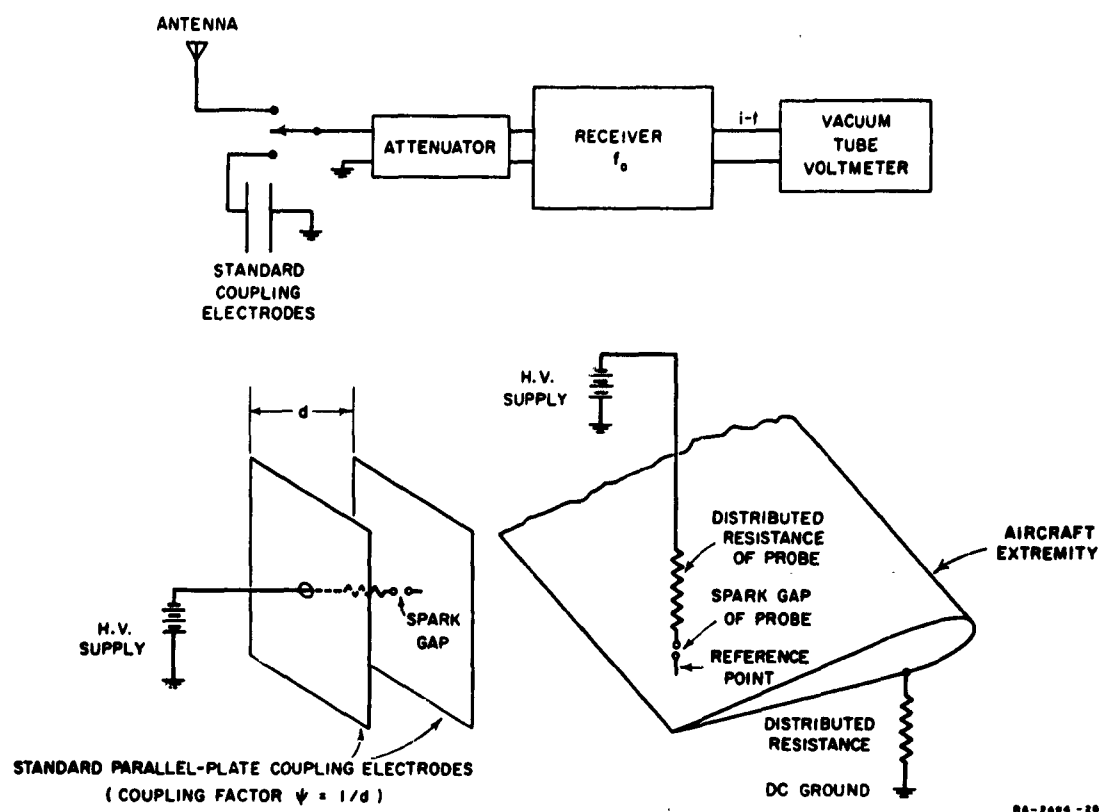
FIG. 3

BLOCK DIAGRAM OF COUPLING MEASUREMENT INSTRUMENTATION

were, of course, ten times the full-scale frequencies of interest, and the reference-point locations were scaled to lie along a line one inch away from the edge of an airfoil.

To make a measurement the spark-discharge signal source was held in place at the desired reference point on the mock-up as is indicated in Fig. 4. With the signal source probe in place at the reference point, the noise current at the antenna terminals was read by means of the receiver connected to the terminals and tuned to the proper scale value of the frequency being investigated. Following this measurement the receiver was connected to the standard parallel-plate coupling electrodes into which the probe was inserted. Attenuation was then inserted into the line connecting these electrodes to the receiver, until the reading was the same as that which was obtained with the receiver connected to the antenna.

14

In this way the receiver was used only as a frequency-determining and amplitude-comparison device; neither its absolute sensitivity nor its noise bandwidth was important. The coupling factor to reference point was thus defined in terms of the known coupling factor for the standard electrodes and the attenuation necessary to equalize the readings by the relationship:

$$\psi_{mod} = \psi_{std} \frac{A_{std}}{A_{mod}} \tag{10}$$

where

ψ_{mod} = coupling to scaled reference point on model

ψ_{std} = coupling factor of standard parallel-plate electrodes
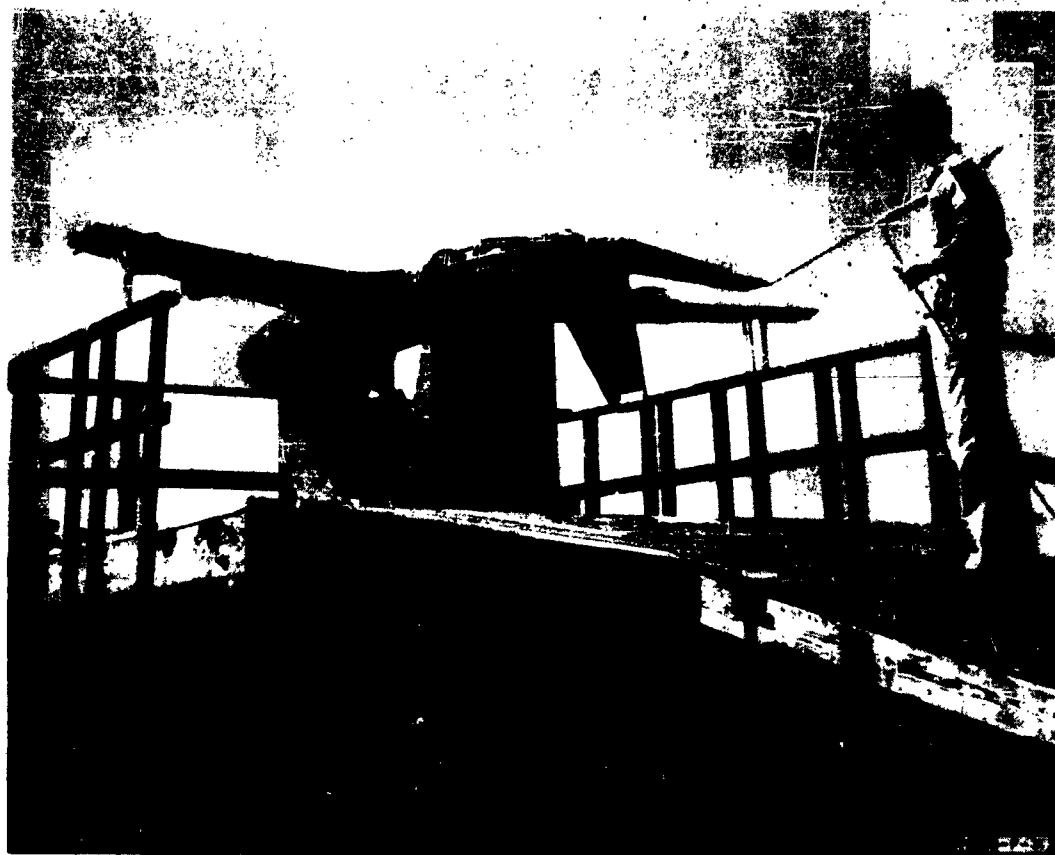
FIG. 4

MEASUREMENT OF COUPLING FACTOR FOR BOEING 707 AIRCRAFT

15

A_{mod} = gain of system including attenuator when model
antenna is connected

A_{std} = gain of system including attenuator when standard
coupling electrodes are connected.

Since the measurements were performed on a scaled-down model of the air-
craft, and since, for a given antenna voltage, the coupling fields vary
inversely as the dimensions of the aircraft, provided the antenna is also
scaled, the coupling to the reference point on the aircraft is given by

$$\psi = \frac{\psi_{mod}}{N} \tag{11}$$

where

N = modeling factor (for the KC-135 measurements, $N = 10$).

Details of the signal-source probe used in performing these measure-
ments are shown in Fig. 5. The signal is generated by a spark discharge
between the two platinum electrodes fed with high-voltage dc through the
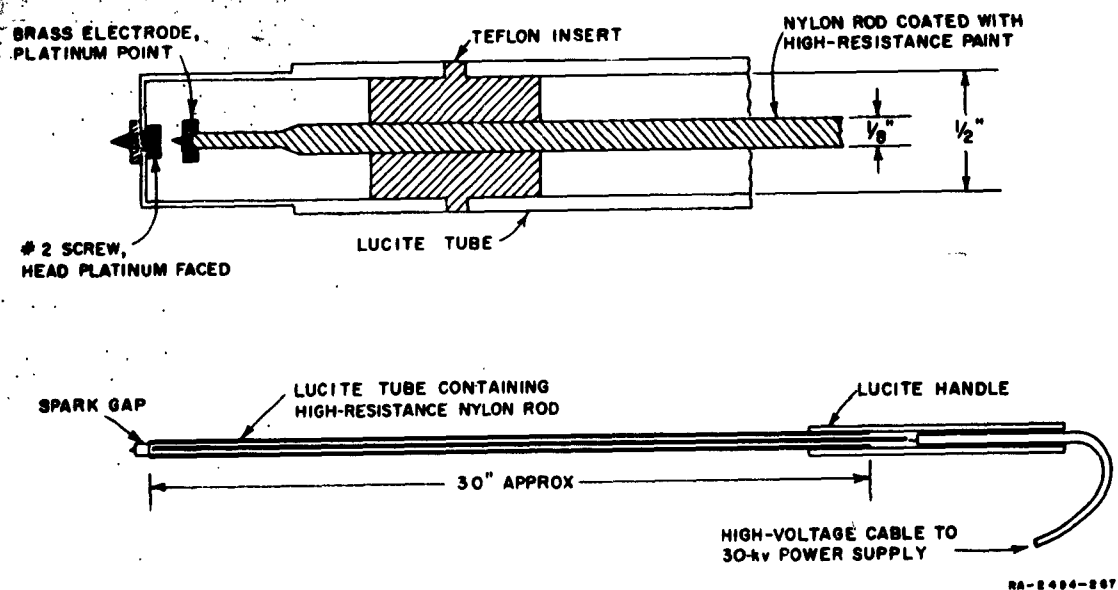
FIG. 5

DESIGN OF SPARK-SOURCE SIGNAL PROBE

16

long distributed resistance. Since the distributed resistance does not perturb the radio-frequency fields about the mock-up, the RF source is effectively confined to the very small volume containing the electrodes. The presence of the electrodes does, of course, perturb the field in the immediate vicinity of the reference point at which a measurement is made. However, since the reference points were chosen so that over the volume occupied by the electrodes the field is essentially uniform, and since the field in the space between the standard parallel-plate coupling electrodes is also uniform, the same field distortion will occur when taking the standard coupling reading. In this manner, the errors resulting from field distortions caused by the spark-gap electrodes are self-cancelling.

The spark discharge fed through the high resistance is a type of relaxation oscillator. Since the individual sparks composing the discharge are extremely sharp pulses it furnishes a white-noise type of signal of very broad band. (Frequencies as high as 160 Mc were used in making coupling measurements.) Since coupling measurements are made by using the same receiver to compare the magnitudes of the signals that the spark source induces in each of two coupling geometries, the precise shape of the noise spectrum generated by the probe is unimportant provided sufficient power to permit measurements is available at the frequencies of interest. It is, of course, essential that the characteristics of the spark noise source do not vary with time. If an oscilloscope were used to observe the individual pulses that the spark discharge generated in the receiver IF circuit, this would mean that the pulse shape and pulse amplitude could not vary. Since a voltmeter was used to measure the receiver IF output, however, it was necessary, in addition, that the pulse-repetition frequency be stable. It was found that the signal generated by the probe was stable in all respects. As a check on the stability of the spark source during the coupling measurements, periodic readings were made of the signal induced by the probe in the standard parallel-plate coupling electrodes.

It should be noted that in performing the actual coupling measurements the probe was not always held at a reference point. In regions of low coupling where the signal strength of the probe was marginal it was necessary to move the probe out to the region of higher field at the trailing edge to produce a useable signal in the receiver. Since the field distortions produced by the probe at the trailing edge were altogether different

17

from the distortions occurring in the standard electrodes, the trailing-edge readings could not be used in Eq. (10) directly. The ratio of the reference-point reading to the trailing-edge reading therefore was measured at a region of high coupling and used to correct the trailing-edge data before substitution into Eq. (10).

E.   RESULTS OF COUPLING MEASUREMENTS

Results of the coupling measurements performed on two antennas on the Boeing 367-80 aircraft (prototype of the KC-135 and 707) are shown in Fig. 6.   The antennas used in making these measurements were a small tail cap and a flush belly antenna located in the fairing at the root of the wing.   These were the antennas employed in making precipitation-static noise measurements during the flight test conducted on Contracts AF 33(616)-3914 and AF 33(616)-6561.   Although the coupling factors actually measured include
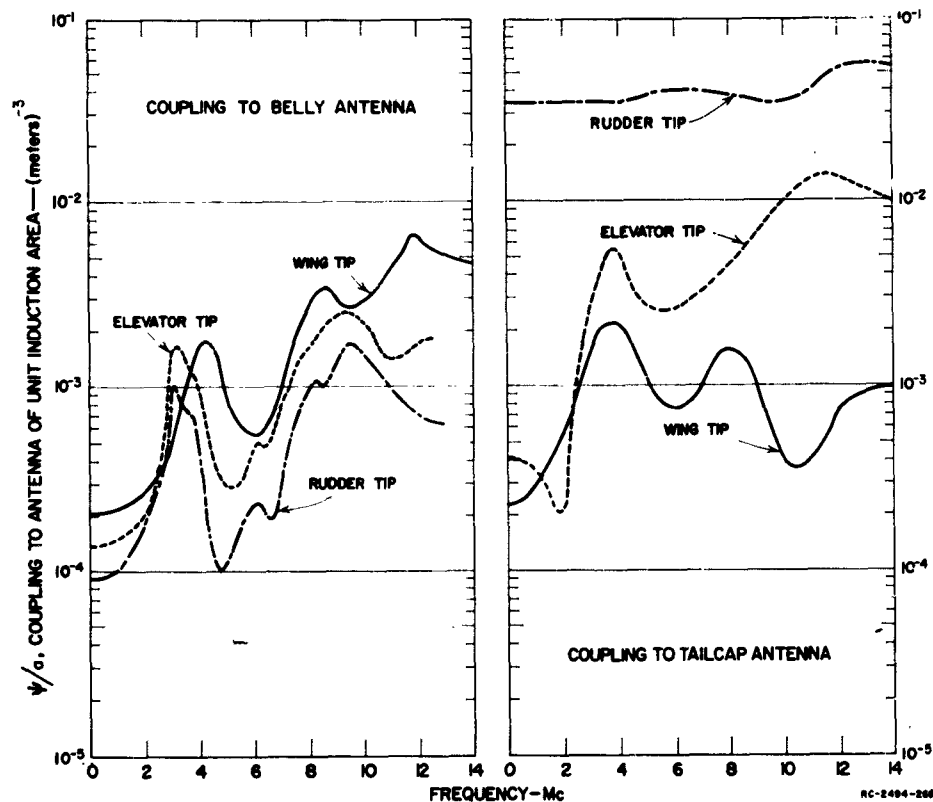
FIG. 6

MEASURED COUPLING FACTORS FOR ANTENNAS ON BOEING 367-80 AIRCRAFT

18

the characteristics of the particular antenna used in making the measurements, the form of the coupling as a function of frequency will not be affected by the details of the test antenna, provided the antenna dimensions are small compared to a wavelength at the frequencies of interest. In this case, only the magnitude of the coupling function will be affected by a change in the antenna. The data shown in Fig. 6 have therefore been adjusted to represent the coupling to an antenna having unity induction area, a, in response to a low-frequency, vertically-polarized, horizontally-propagating signal. (The induction areas of the test antennas mounted at the indicated locations were determined using the electrostatic-cage techniques developed by Bolljahn.)[12,13] Thus the curves shown in the figure may be considered to define the coupling between the various aircraft extremities and the general regions in which the test antennas were located. To apply the data to a particular antenna at one of these locations it is necessary to multiply the values of Fig. 6 by the induction area of the antenna in response to a horizontally-propagating, vertically-polarized signal. (For additional discussion of considerations involving coupling, see Sec. VI-C.)

The variation with frequency of the coupling to the various points is of considerable interest, since it shows the effect of the various electromagnetic resonances of the aircraft. For example, the peak in coupling between the belly antenna and the tips of the tail surfaces at approximately 3 Mc occurs at the frequency which makes the path distance from a point just aft of the wings to a tip of one of the tail surfaces one-quarter wavelength. As might be expected, the coupling factor, ψ, is related to the antenna impedance; the variations of which are also determined by electromagnetic resonances. In the case of simple structures for which the forms of z_{11}, the self impedance of the antenna, and z_{12}, the mutual impedance between the antenna and the noise source, are known, it is possible to calculate the form of ψ as a function of frequency.[7,14] The presence of the resonance peaks in the coupling function serves to emphasize the fact that the pulses arriving at the antenna terminals will differ from the pulses generated by the corona discharges at the extremities in that they will be stretched out in time by aircraft resonances.[14] As is indicated in Sec. VIII-G, this pulse-stretching is of interest in the design of interference "blankers" (devices designed to reduce interference by disabling the receiver for the duration of each noise pulse arriving at the antenna) since it sets a lower limit on the blanking period which may be used.

19

It is evident from Fig. 6 that each of the coupling curves shown has its own characteristic behavior as a function of frequency. Therefore, if a broad-band noise source such as a corona discharge is moved from one to the other of the aircraft extremities, the noise spectrum induced in the receiving antenna is determined by the location of the noise source. For example, the noise coupled into the tail cap from the rudder is particularly easy to identify since the antenna and rudder are sufficiently near one another that the coupling is relatively independent of frequency, whereas the coupling to the other extremities displays a marked frequency dependence. The ability to infer noise-source location from the antenna noise spectrum was useful in designing flight-test experiments and in analyzing flight-test data.

Also of interest is the variation of the coupling at a particular frequency, with position along an airfoil. This is illustrated in Fig. 7, which is a plot of the variation in coupling of the belly antenna to the trailing edge of the wing near the tip. The coupling is proportional to the charge density that would be excited by the antennas if a voltage were applied to them. At all frequencies the charge tends to concentrate at the extremities, as shown by the plot in Fig. 7. Thus the coupling tends to be maximum at the points where discharges are most likely to occur. The dip in coupling at 14 Mc occurs at a distance approximately one-quarter wavelength from the tip. This result also indicates the fallacy in assuming that the noise induced in an antenna on an aircraft will always decrease as the noise source is moved away from the antenna. From Fig. 7 it is apparent that on the trailing edge of the wing near the tip, moving a noise source away from the belly antenna increases the noise induced in the antenna.

FIG. 7

VARIATION NEAR TIP OF WING OF COUPLING TO
BELLY ANTENNA IN KC-135 AIRCRAFT

III   CORONA-DISCHARGE CHARACTERISTICS

A.   GENERAL

As was indicated earlier, an aircraft flying through precipitation generally becomes negatively charged as the result of triboelectric charging associated with precipitation particle impingement. Engine charging observed during the low-altitude operation of turbojet aircraft also charges the airplane negatively. In both cases, under the action of the charging, the aircraft potential will become progressively more negative until corona discharges occur from the regions of high dc field at the extremities. As a rule, the discharges occur from burrs and imperfections which exist on these extremities and which tend to produce further localized field concentrations. These negative-point corona discharges are responsible for the generation of RF interference; therefore their characteristics are of interest. Most significant in regard to noise generation is the fact that the discharges occur as a series of discrete impulses of short duration and rapid rise time and therefore produce noise over a broad spectrum. Explanations for many of the observed characteristics of the negative-point corona discharge follow from a qualitative description of the discharge process.

In order for a discharge to occur it is necessary that the field be sufficiently high that an electron, on the average, will acquire ionizing energy between collisions, thereby producing additional electrons. The action of this applied field upon a chance electron (produced perhaps by high-energy radiation) in the region near the point moves it away from the point and causes it to collide with air molecules which become ionized, producing additional electrons which in turn are accelerated by the field. This electron avalanche continues to propagate and grow until it reaches a region at a distance from the point where the field is too low to permit ionization by collision and where the electrons are slowed sufficiently that they attach to oxygen molecules to produce 0_2^- ions. Since the 0_2^- ions are much less mobile than the electrons, they may be considered to be stationary as far as the discharge processes are concerned. This relatively stationary cloud of 0_2^- ions tends to reduce the field between itself and the point, thereby reducing the distance to which the next avalanche can

propagate. The cloud of positive ions left behind by the electrons, on the other hand, tends to increase the field between itself and the point so that avalanches are initiated more readily in this region. Many of the free electrons necessary for avalanche formation are probably supplied by photoemission from the negative point. The discharge continues, therefore, as a series of successive avalanches. Each avalanche propagates a shorter distance than the last as the inner limit of the cloud of O_2^- ions approaches the discharge point. Meanwhile, the positive ions are being drawn into the point. Finally the negative space charge reduces the field near the point to such an extent that ionization by collision is no longer possible, and the discharge is choked off. At sea-level pressures this entire process is completed in roughly 0.2 microsecond.[7] Under the action of the wind and the applied electric field the ions are gradually swept away from the point, allowing the field to rise to a value sufficient to cause ionization by collision, and the whole process is repeated.

A thorough study was made in Ref. 7 of the characteristics of the pulses produced by negative-point corona discharges occurring from carefully prepared, thin, hemispherically capped cylinders. It was found that the rise times of the pulses were very short (less than 0.01 μsec at sea level) and that an exponential adequately described the pulse decay. It was found, furthermore, that both the rise and decay times varied inversely with the pressure. The results also indicated that the spatial extent of the discharge roughly equalled the point radius.

The observed pressure dependence may be explained qualitatively by considering the fundamental processes involved in a discharge. In order that a discharge may propagate it is necessary that between collisions an electron acquire ionizing energy from the electric field. If the air pressure is now halved, for example, the ionizing energy is not changed, but now the electron can travel twice as far in acquiring this energy, which indicates that the applied field required for the discharge to occur is only half as great. Thus the threshold potential is inversely proportional to pressure. (In these arguments it is assumed that over the extent of the discharge the field is relatively constant--a reasonable assumption in view of the observation that the spatial extent of the discharge is only one point radius. The argument obviously does not apply in the case of points with radii of the same order as the mean free path of the electrons.) Since at the halved pressure the ionizing energy is not changed, the final velocity of the electron is not changed, and its average

22

velocity is not changed. At the halved pressure, however, the distance
traveled between collisions is doubled, which means that the time between
collisions is doubled or that the time between collisions is inversely
proportional to pressure. If the elapsed time between the successive
ionizations constituting the discharge is inversely proportional to
pressure, the time structure of the entire discharge process should be
inversely proportional to pressure, as was indicated by the measurements.

The relationship between the spatial extent of the discharge and tip
radius follows from the fact that an avalanche will propagate until it
reaches a region where the field is too low to permit ionization. In order
that discharges may occur, the field at the surface of the discharge point
must reach a given value independent of the point dimensions. Furthermore,
the field a prescribed number of point radii from the surface will fall to
a given percentage of the surface field independent of the point dimensions.
Thus the avalanches should be expected to propagate a distance proportional
to the point radius—roughly one point radius according to the measurements.
From Eq. (1) it is evident that the amplitude of the induced current pulse
is proportional to the spatial extent of the current density J^{II}. Since
the spatial extent of the discharge is roughly equal to the point radius,
the amplitude of the current pulse measured in a given geometry should be
proportional to the radius of the discharge point. The measurements of
Ref. 7 indicated that the amplitude of the induced current pulse does
indeed increase with increasing discharge-point radius.

Although the results of Ref. 7 provide valuable insight into the
corona noise problem, it would be difficult to apply the results of the
measurements to the quantitative prediction of the noise generated in an
aircraft antenna. In particular, corona discharges on an aircraft
generally occur from imperfections on the outboard trailing edges of the
airfoils. Since the field near an edge decays more slowly than it does
near the end of a thin cylinder, the discharge from an edge may be expected
to have a structure different from that of a discharge from the end of a
cylinder. Furthermore, the discharges occur from various irregular imper-
fections along the trailing edge so that the character of the generated
noise can vary depending upon the particular imperfection from which the
discharge is occurring. In order to describe the RF fields which determine
the coupling it would be necessary to take into account the perturbations
caused by the imperfections from which the discharges occur. It would be
difficult, therefore, to determine the amplitudes of the generated noise

pulses. For these reasons laboratory measurements were made to study the characteristics of the noise generated by negative-point corona discharges occurring from the edge of a sheet.

B. INSTRUMENTATION FOR MEASUREMENT OF CORONA SPECTRAL CHARACTERISTICS

From the results of Ref. 7 it was evident that the structure of a corona discharge from the edge of a sheet should be very similar to that of a discharge from the end of a thin cylinder. Thus, the general form of the corona pulses occurring on an aircraft was known, and it would not be necessary to perform direct measurements of individual corona pulses using oscillographic techniques. For this reason, the characteristics of the corona discharge from an edge were studied more indirectly by confining the laboratory investigation primarily to the measurement of the source spectrum $D(\omega)$. Spectrum measurements performed on a full-scale mock-up of an airfoil automatically include the effects of burrs and imperfections in modifying discharge character and coupling. The results of these measurements therefore may be used to predict the noise spectra generated in aircraft receiving antennas. Furthermore, considerable information regarding the structure of an average corona pulse may be inferred from a knowledge of $D(\omega)$.

The source spectrum was studied by reproducing, in the laboratory, a full-scale section of airfoil trailing edge together with the dc and RF coupling fields which surround it. Near the trailing edge of the airfoil the field geometry is parabolic. In the laboratory, therefore, one of the equipotential surfaces was replaced, as is indicated in Figs. 8 and 9, by a sheet of aluminum bent to the shape of a cylinder of parabolic cross section. Voltage dividers and guard rings placed along appropriate equipotential surfaces were used to reduce field fringing, to permit the desired field structure to be obtained using electrodes of reasonable size. It will be noted that both capacitive and resistive dividers were used between the guard rings to be certain that both the RF and dc field structures were correct. The dimensions of the mock-up were chosen to be small compared to a wavelength at the highest frequency used in the measurements so that the coupling $\psi_L(\xi,\omega)$* to the reference point in the laboratory mock-up is independent of frequency, and any frequency variations

---

*The subscripts L on the quantities discussed here refer to quantities as measured on mock-ups in the laboratory.

24

NOTE: TO PERMIT
MEASUREMENT OF
DISCHARGE CURRENT,
ALL INSTRUMENTS
ARE OPERATED FROM
AN ISOLATION
TRANSFORMER AND
ALL INSTRUMENTS
ARE ABOVE GROUND
POTENTIAL

FIG. 8

DIAGRAM OF TRAILING-EDGE NOISE-MEASURING SET-UP

25
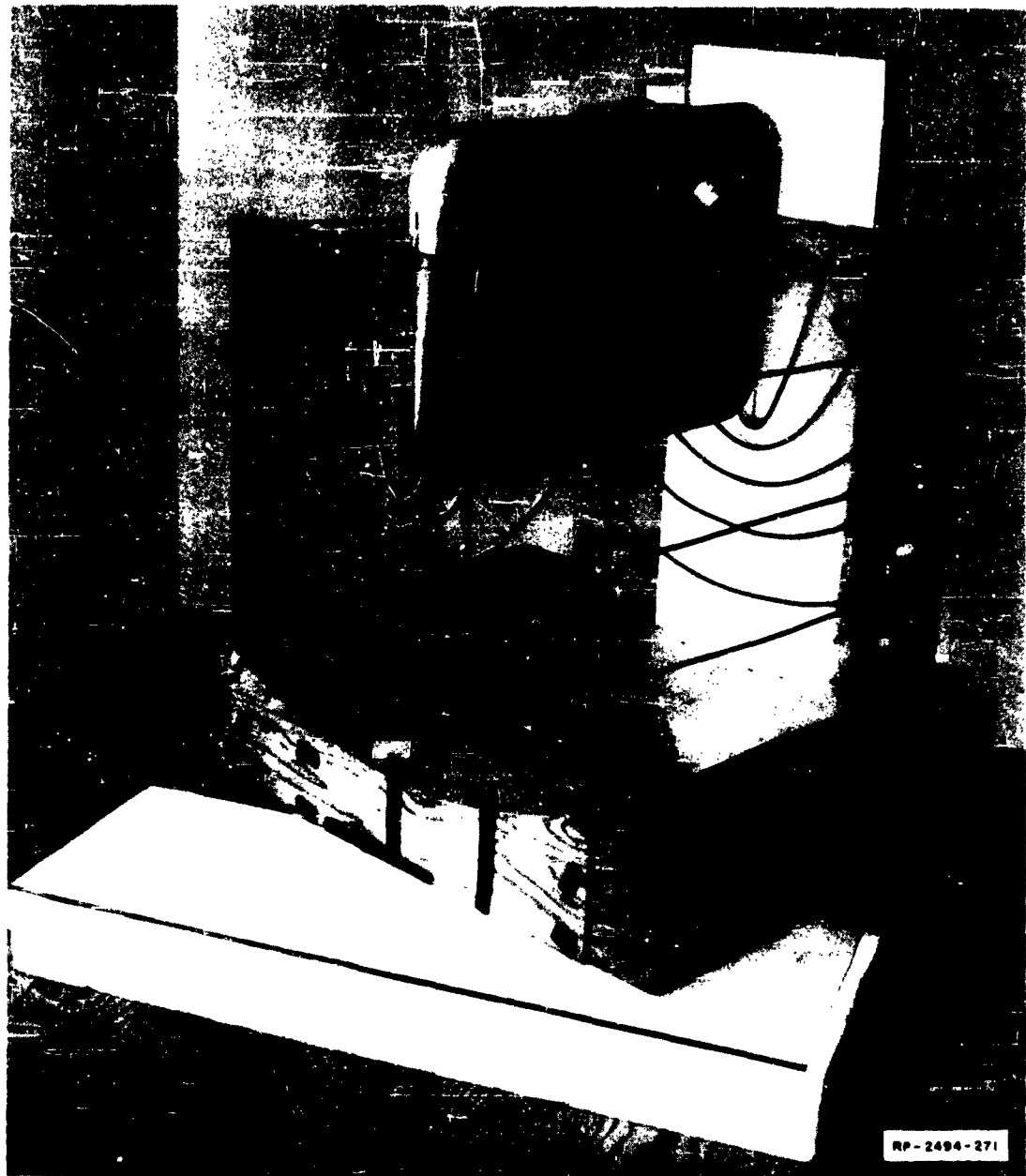
FIG. 9
CORONA NOISE MEASURING SET-UP

noted during the measurements may be attributed to the source spectrum. Furthermore, since the field geometry in the mock-up is known it is possible to calculate the magnitude of the coupling. It is. of course, possible to measure the coupling to the reference point in the mock-up using the techniques described in Sec. II-D. The measured and calculated values of $\psi_L(\xi,\omega)$ were in good agreement.

The measuring terminals of the mock-up were terminated with a 51-ohm resistor, the resistance of which is small compared to the reactance of the electrode structure. Thus, the RF current flowing through this resistor may be assumed to equal the short-circuit terminal current.

This same 51-ohm resistor formed part of the dc path to ground for the discharge current. The dc ground path was completed through the 100 $k\Omega$ resistor paralleled by the vacuum-tube voltmeter used to measure discharge current. In order that this circuit function properly, it was necessary that the 100 $k\Omega$ resistor provide the only path to ground. For this reason all of the measuring instruments were operated from an isolation transformer with all of their cases above dc ground potential. Although this particular current-measuring scheme complicates the problem of instrumentation somewhat, it was chosen since the meter measures directly the current leaving the airfoil section. A meter in the ground-return circuit of the power supply, for example, would also measure bleeder current and current lost in spurious corona discharges from the high-voltage wiring and the aluminum plate.

When the dc voltage applied to the mock-up is raised until corona occurs, noise will exist at the measuring terminals. The power spectral density $G_L(\omega)$ of this noise is defined by

$$P = \int_{\omega_1}^{\omega_2} G_L(\omega)\, d\omega \tag{12}$$

where P is the power dissipated in a one-ohm resistor in the band of frequencies from ω_1 to ω_2. The spectral density is related to the short-circuit current $I_{2L}(\omega)$ generated in the laboratory mock-up terminals by

$$G_L(\omega) = |I_{2L}(\omega)|^2 \quad . \tag{13}$$

27

Substituting this result into Eq. (6) gives

$$\sqrt{G_L(\omega)} = \psi_L(\xi) |D(\omega)|$$

or

$$|D(\omega)| = \frac{1}{\psi_L(\xi)} \sqrt{G_L(\omega)} \quad . \tag{14}$$

Since the mock-up duplicates the conditions existing in flight, the source spectrum measured in the laboratory is identical with that existing in flight. Thus we may write for the noise spectrum existing in an aircraft antenna

$$\sqrt{G(\omega)} = \psi(\xi,\omega) |D(\omega)| \tag{15}$$

where $|D(\omega)|$ is given by Eq. (14). and where $\psi(\xi,\omega)$ is the coupling to the reference point ξ on the airfoil of interest on the full-scale aircraft.

In making noise measurements in the laboratory the noise generated in the mock-up was fed through a calibrated attenuator to a receiver tuned to the frequency of interest. The attenuator was adjusted until the IF output of the receiver produced a convenient reading on the voltmeter. The receiver and attenuator were then connected to a diode noise generator and the attenuator was adjusted to produce the same voltmeter reading. The noise spectral density in the mock-up was found from the spectral density produced by the noise generator and the two attenuator settings. In this way the receiver was used only as a comparison device and the absolute values of its gain and bandwidth are unimportant provided they remain constant during the time required for a measurement.

To investigate the variation of noise spectrum with altitude a small mock-up of the airfoil and the surrounding fields was built and placed in a bell-jar. A photograph of this mock-up is shown in Fig. 10. Noise measurements were made at pressures ranging from sea level to 50,000 feet altitude. The instruments used for these measurements were identical with those shown in Fig. 8.

C. RESULTS OF CORONA-DISCHARGE MEASUREMENTS

The results of corona-noise measurements made using the airfoil trailing-edge mock-up are shown in Fig. 11. The measurements were made at sea level using a receiver frequency of 2 Mc.

28

FIG. 10

SET-UP USED TO STUDY EFFECTS OF ALTITUDE ON CORONA NOISE

29
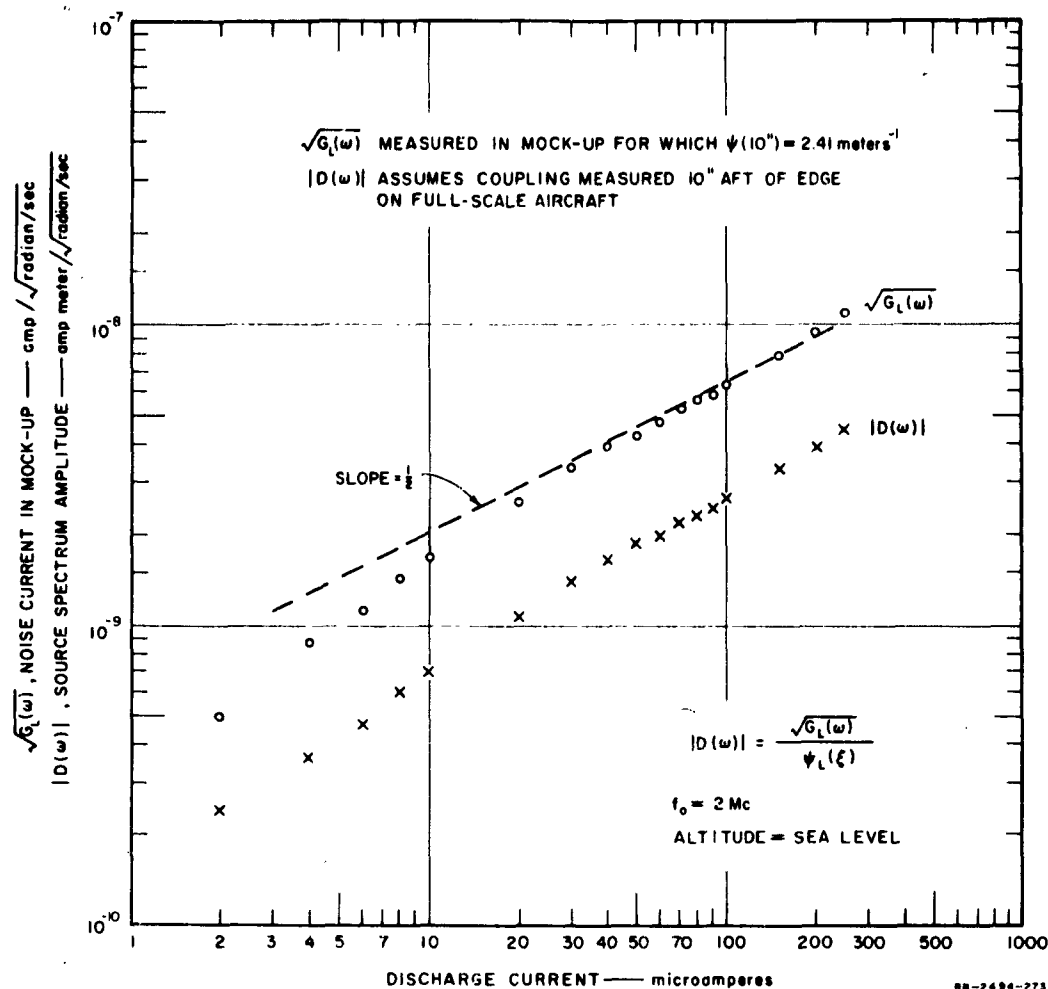
FIG. 11

NOISE AMPLITUDE FROM TRAILING EDGE

At high discharge-current values the noise-current spectral density varies as the square root of the discharge current. This result follows from the fact that the discharge is composed of a series of almost identical current pulses occurring at random times. If we assume that the individual corona discharges are identical, the number of discharges occurring per second will be proportional to the discharge current. Since the pulses are incoherent, each pulse will contribute an equal amount of noise energy to the system. Thus, the noise power will vary directly with discharge current, which means that the noise current varies as the square root of the discharge current.

30

At the lower discharge-current values, the noise current is seen to vary more rapidly with the discharge current. This result follows from two facts. First, at very low discharge currents, the discharge occurs from a very limited number of points, and the discharge from each of these consists of an almost periodic train of nearly identical pulses. Increasing the current from such a point increases the frequency of the discharge, but does not alter the pulse shape. The discharge thus tends to consist of a nearly coherent set of pulses, for which the noise power density tends to be proportional to the square of the discharge current. Second, in this current range the corona pulses occurring from the different points on the trailing edge differ considerably in amplitude. As the high voltage is applied, corona will occur first from the sharpest imperfections. Since it was found in Ref. 7 that the pulse magnitude increased with increasing discharge-point radius, these pulses should be of relatively low amplitude. As the voltage is raised, corona will occur from imperfections of slightly larger radius, generating pulses of larger amplitude. Thus the over-all effect of increasing the current is an increase in the average pulse amplitude, so that the noise current increases more rapidly than the square root of the discharge current. At the higher discharge currents the major local imperfections become used up, making local structure less important in determining the locations of individual discharges, so that pulse ampli-tude becomes almost independent of discharge current. Here the square root relationship between noise current and discharge current will apply almost exactly.

The manner in which noise-current spectral density varies with fre-quency and altitude is shown in Fig. 12. Since the noise-amplitude data of Fig. 11 were measured at sea level and at a frequency of 2 Mc, the data shown in Fig. 12 have been normalized to unity at 2 Mc at sea level. To obtain the source noise-current spectral density at any particular discharge current, altitude, and frequency, therefore, it is necessary only to multiply the absolute value obtained for the desired current from Fig. 11 by the relative spectral density for the desired altitude and frequency obtained from Fig. 12.

As has been indicated earlier, it was found in Ref. 7 that the rise time of a corona pulse is so short that for frequencies below 30 Mc no error results in representing the pulse by a decaying exponential with zero rise time. Thus it is possible to write for a typical corona noise pulse

31

$$f(t) \; = \; A_k e^{-\alpha_k t} \qquad \text{for} \; \; t > 0 \qquad\qquad (16)$$

where A_k and α_k are random variables describing the amplitude and decay time which vary from pulse to pulse, depending upon small local differences in trailing-edge geometry. Assuming that the variation in α_k is small, it is shown in Appendix B that the power spectrum produced by ν pulses per second is given by

$$G(\omega) \; = \; \frac{\nu}{\pi} \frac{A^2}{\omega^2 + \alpha^2} \qquad\qquad (17)$$

where

$$A^2 \; = \; \overline{A_k^2} \; = \; \text{mean square amplitude}$$

$$\alpha \; = \; \overline{\alpha}_k \; = \; \text{average decay constant}.$$
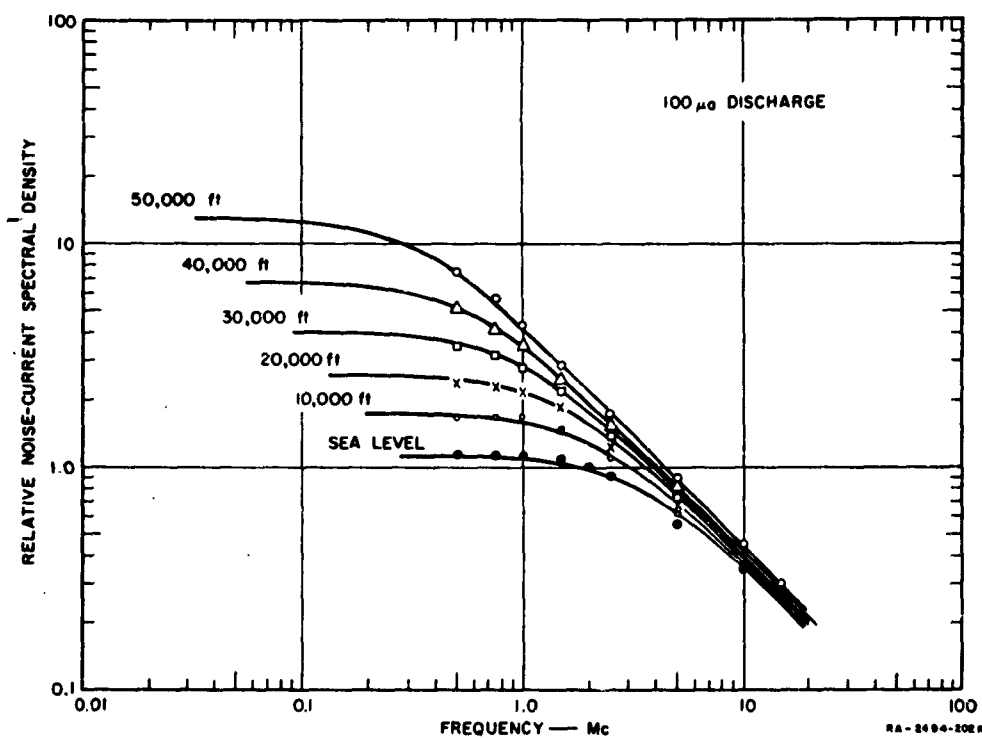
FIG. 12

NORMALIZED NOISE SPECTRUM FROM TRAILING EDGE

Thus the predicted current spectral density is given by

$$\sqrt{G(\omega)} = \sqrt{\frac{\nu}{\pi}} \frac{A}{\sqrt{\omega^2 + \alpha^2}} \quad . \tag{18}$$

Curves of this form were plotted on Fig. 12 to fit the experimental data points as well as possible. From these curves it is possible to obtain α and the value of the current spectral density at zero frequency

$$\sqrt{G(0)} = \sqrt{\frac{\nu}{\pi}} \frac{A}{\alpha} \quad . \tag{19}$$

The time constant $\tau = 1/\alpha$ and $\sqrt{G(0)}$ are plotted as a function of pressure in Fig. 13. The data indicate that the time constant varies inversely
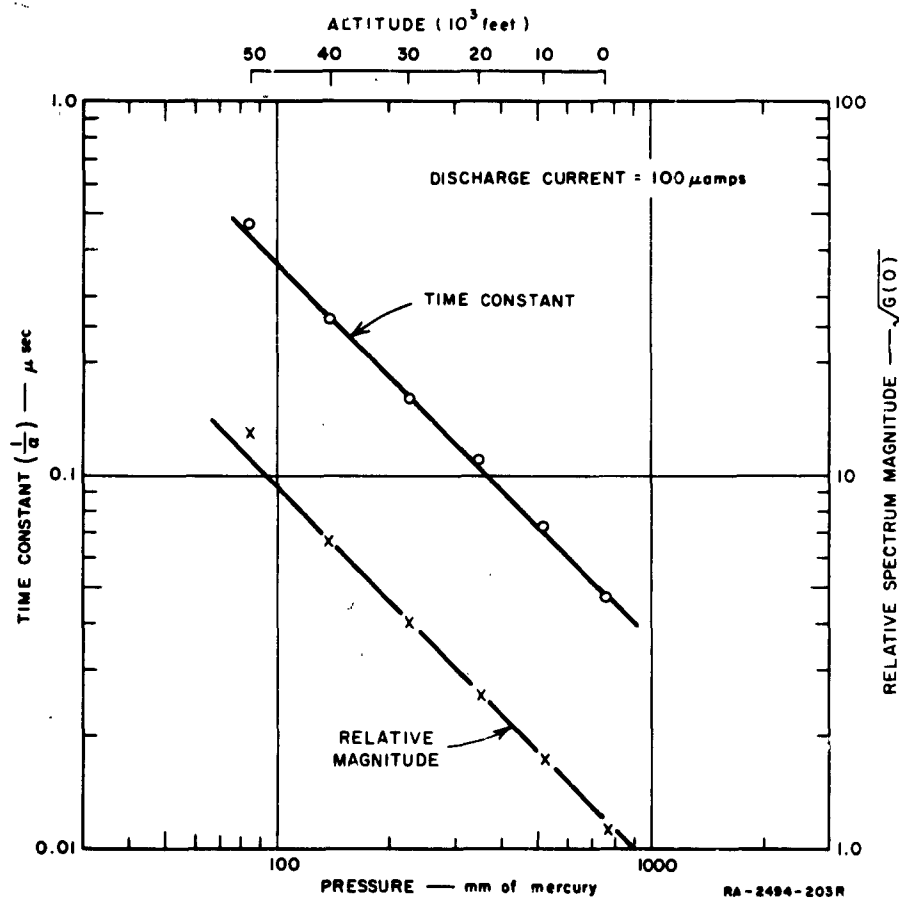
FIG. 13

CORONA SPECTRUM CHARACTERISTICS vs. PRESSURE

33
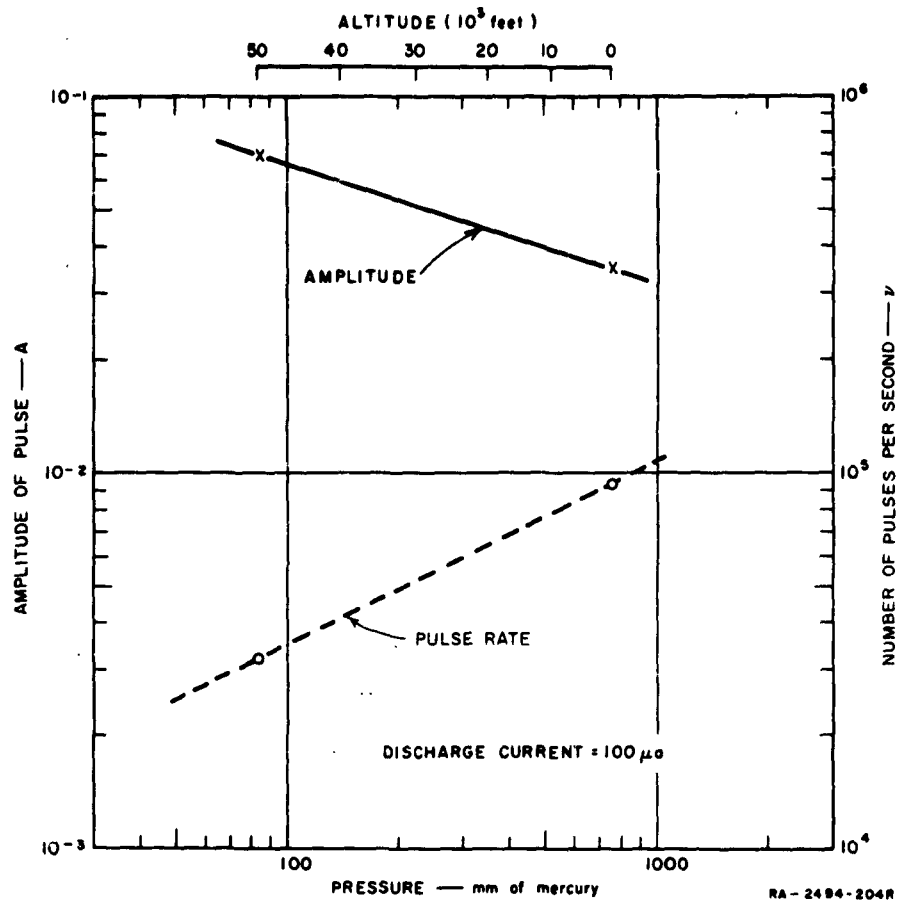
FIG. 14

CORONA PULSE AMPLITUDE vs. PRESSURE

with pressure. Furthermore, since the asymptote $\sqrt{G(0)}$ also varies inversely with pressure it is evident from Eq. (19) that the pulse rate ν and the pulse amplitude A must vary in such a manner that the product $A\sqrt{\nu}$ remains constant.

To determine the corona pulse rate the output from the bell-jar mock-up shown in Fig. 10 was fed to a Tektronix 121 amplifier which drove a Hewlett-Packard 523B electronic counter. Pulse rates were measured at sea level and at a pressure equivalent to 50,000 ft. altitude. The results of these measurements are plotted in Fig. 14. Also shown in this figure is the manner in which pulse amplitude must vary with pressure to meet the requirement that $A\sqrt{\nu}$ be independent of pressure. The fact that these results indicate that the amplitudes of the pulses from the edge of

34

a sheet decrease with increasing pressure was disconcerting, since the measurements of Ref. 7 using hemispherically-capped wires indicate that pulse amplitude increases with increasing pressure. In view of the relatively elaborate procedure employed in obtaining the amplitude data of Fig. 14 these data were suspect (the data of Ref. 7 were obtained by direct oscillographic measurement). For this reason a Tektronix 541 oscilloscope (30 Mc bandwidth) was connected to the output terminals of the trailing edge mock-up of Fig. 10 and employed to observe the corona pulses as the pressure was varied. Although there was a large spread in pulse amplitudes, the average amplitude did indeed decrease with increasing pressure in general agreement with the results shown in Fig. 14. As a further check on the validity of the measurements a 0.040-inch-diameter hemispherically-capped wire was mounted in the mock-up of Fig. 10 so that the wire protruded 0.5-inch beyond the edge and the character of the fields near the tip of the wire was not influenced by the edge of the sheet. In this case the pulse amplitude was found to increase with increasing pressure in agreement with Ref. 7. Thus the disagreement between the amplitude curve of Fig. 14 and the results of Ref. 7 stems from differences in the characteristics of the discharges studied in the two cases and not from errors in measurement.

The reasons for the differences in the character of the noise pulses produced by corona discharges occurring from points and edges are not well understood. Undoubtedly these differences stem from the differences in field structure in the two cases. For example, except in the immediate vicinity of burrs, the field about an edge is two-dimensional, so that it is possible for a discharge to spread laterally along the edge. In the case of a discharge from a point, however, the field drops off in all directions from the point permitting very little spreading of the discharge. Thus, a change in pressure might be expected to influence the spreading of a discharge from an edge more than it did the spreading from a point. Although a more detailed study of the properties of various corona discharges using the techniques developed here and in Ref. 7 would undoubtedly produce interesting results, it was thought that the main goals of this investigation could be achieved without such a detailed study; therefore, it was not undertaken.

Since much of the current at low charging rates leaves from the trailing edge tips of the airfoils, a brief investigation was made of the noise generated by these discharges. To make these measurements, a

full-scale wooden mock-up of an airfoil tip (coated with silver paint and employing a 0.020-inch-thick aluminum insert to simulate the trailing edge) was placed in the electrode structure shown in Fig. 9. Although the fields at a distance from the mock-up did not reproduce those existing about an actual aircraft, the fields near the tip where the discharges occur were adequately reproduced since they are determined primarily by the shape of the airfoil tip itself, provided all surrounding structure is sufficiently far removed. The results of these measurements are shown in Fig. 15 which indicates that the noise current $\sqrt{G_L(\omega)}$ generated in the mock-up is roughly 2.5 times that generated by discharges from a trailing edge (see Fig. 11).
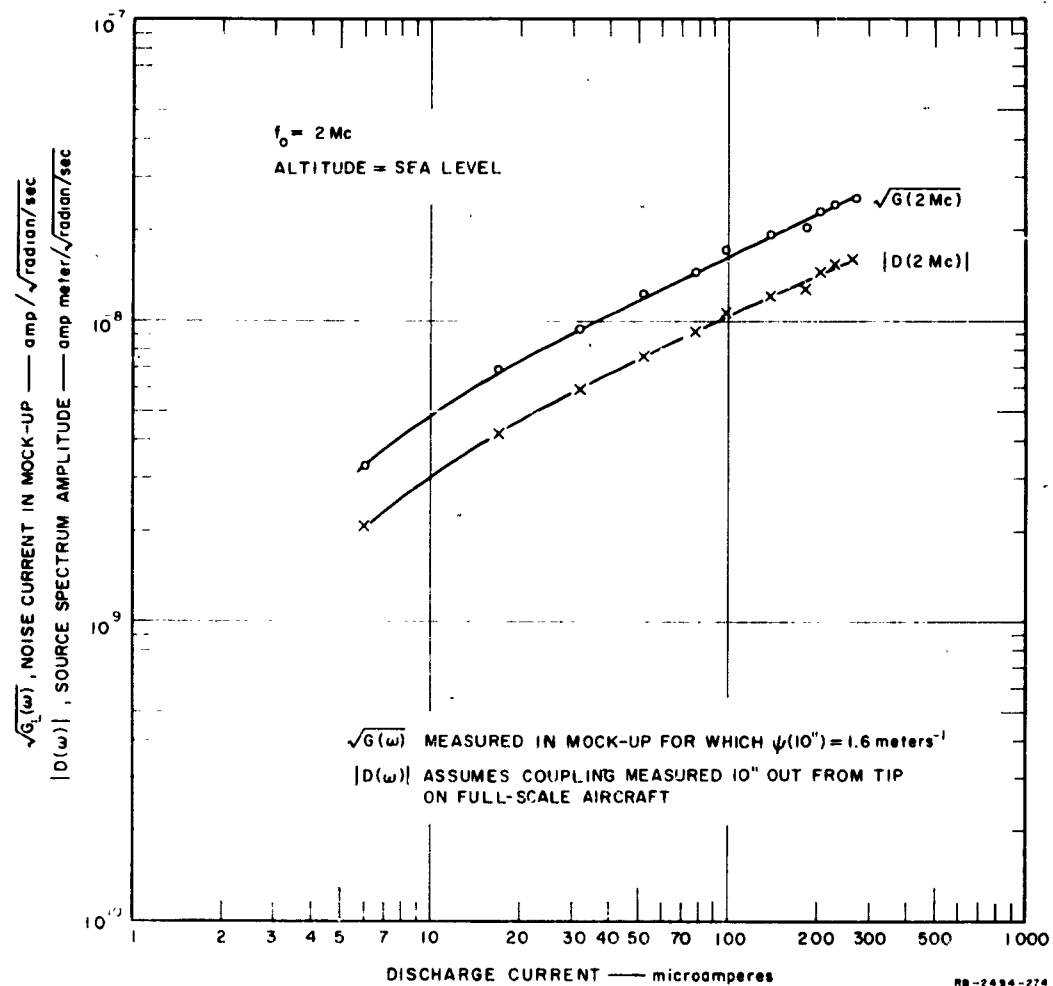
FIG. 15

NOISE AMPLITUDE FROM AIRFOIL TIPS

36

IV   TOTAL AIRCRAFT-CHARGING CURRENTS

A.   FACTORS AFFECTING PRECIPITATION-CHARGING RATE

Aircraft charging occurs as the result of charge separation when precipitation particles strike the aircraft. The charging therefore is proportional to the product of the average particle charge and the number of particles striking the aircraft per unit time. The number of particles striking the aircraft is proportional to the particle concentration in the cloud, the intercepting area of the aircraft, and the aircraft speed.

Particle concentration varies considerably from cloud to cloud, and even in the same cloud there is appreciable variation in particle concentration. Typical maximum concentrations are[8] for cirrus-type clouds 2×10^4 particles/meter^3 and for a thunderhead 6×10^4 particles/meter^3. The variation of particle concentration within the same cloud is illustrated in Fig. 16, which shows the results of particle concentration measurements made during a flight through a cirrus cloud at 19,000 ft altitude.
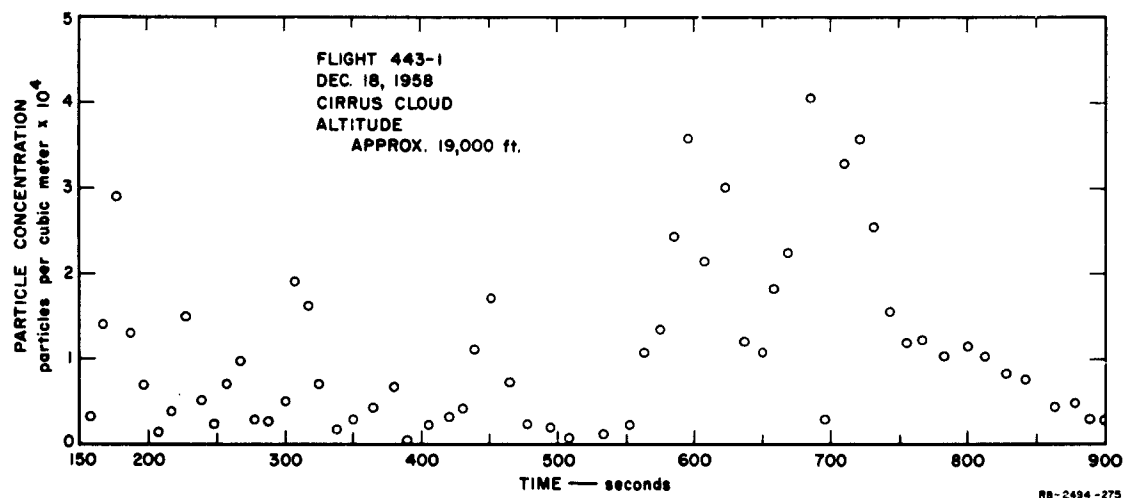
FIG. 16

PARTICLE CONCENTRATION DURING SPEED RUN

The charge deposited on the aircraft by an individual precipitation particle varies considerably from cloud to cloud and even from particle to particle within the same cloud. Typical average values are 10 to 12 $\mu\mu$coulombs in high-altitude cirrus clouds and as high as 50 to 60 $\mu\mu$coulombs or more in lower-altitude clouds containing snow crystals.[10] Although the magnitude of the average particle charge is of interest, the manner in which the average charge varies with speed is of more importance since there were indications that charging might vary as rapidly as the sixth power of the speed. If the sixth-power speed dependence did indeed exist, and if this dependence continued at supersonic speeds, the problem of designing a discharger capable of handling the required current would be extremely difficult.

Figure 17 shows the particle-charge data obtained in a flight during which the aircraft speed was varied over an almost 2-to-1 range.[10] These data were obtained by using two probes located in close proximity and so designed and placed that they intercepted 100% of the particles in the columns of air swept out by them. One probe was used to measure charging current per unit frontal area, while the other probe was used to count the number of particles impinging per second on a unit area. The
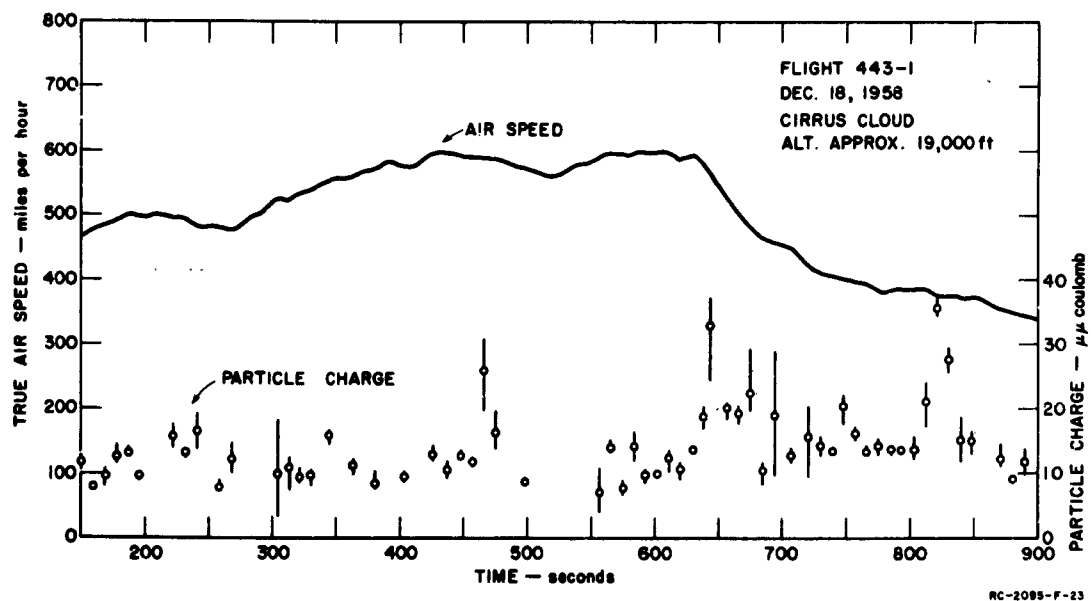
FIG. 17

PARTICLE CHARGE AND SPEED DURING SPEED RUN

particle-charge data shown in Fig. 17 were obtained by dividing the charging rate by the impingement rate. The uncertainty regarding the magnitudes of some of the data points in the figure stems from a peculiarity of the particle-counting circuit. The counter-triggering circuit was such that the counter operated for one second at some random time during a two-second interval. Since, at the time these data were obtained, the instrumentation did not include any provision for determining when during the two-second interval counting occurred, and since the charging rate often varied considerably during one second,[*] the data are presented as follows: The points in the figure indicate the particle charge obtained by averaging the charging rate over the entire two-second interval within which counting occurred. The upper and lower bounds on the data points represent the extremes which the particle charge could assume, and were obtained from the maximum and minimum average currents for a one-second interval in the period during which counting occurred.

It is evident from the figure that, although there was considerable variation in particle charge during the run, there appears to be no correlation between speed and particle charge. As a further test of the relationship between particle charge and speed, the particle-charge data points of Fig 17 were plotted as a function of speed in Fig. 18. Again, the particle charge appears to be independent of speed. From these data therefore, it is possible to conclude that any observed variation of charging with speed is not the result of variation in particle charge.

The one additional factor affecting charging and charging-rate measurements is the effective particle interception area of the aircraft or the measuring probe. Although at first glance it might appear that the area effective in intercepting particles should be a constant equal to the projected frontal area of the aircraft or measuring probe, the results of theoretical studies conducted by the NACA indicate that the aerodynamic forces resulting from the airflow about the aircraft divert many particles away from the aircraft so that the effective intercepting area is less than the projected frontal area.

The NACA studies were concerned with the impingement of spherical water droplets on various aerodynamic shapes.[15,16,17] Since ice crystals generally are flat plates or hexagonal prisms having a much higher

---

[*] See Figs. 24 and 26.

39
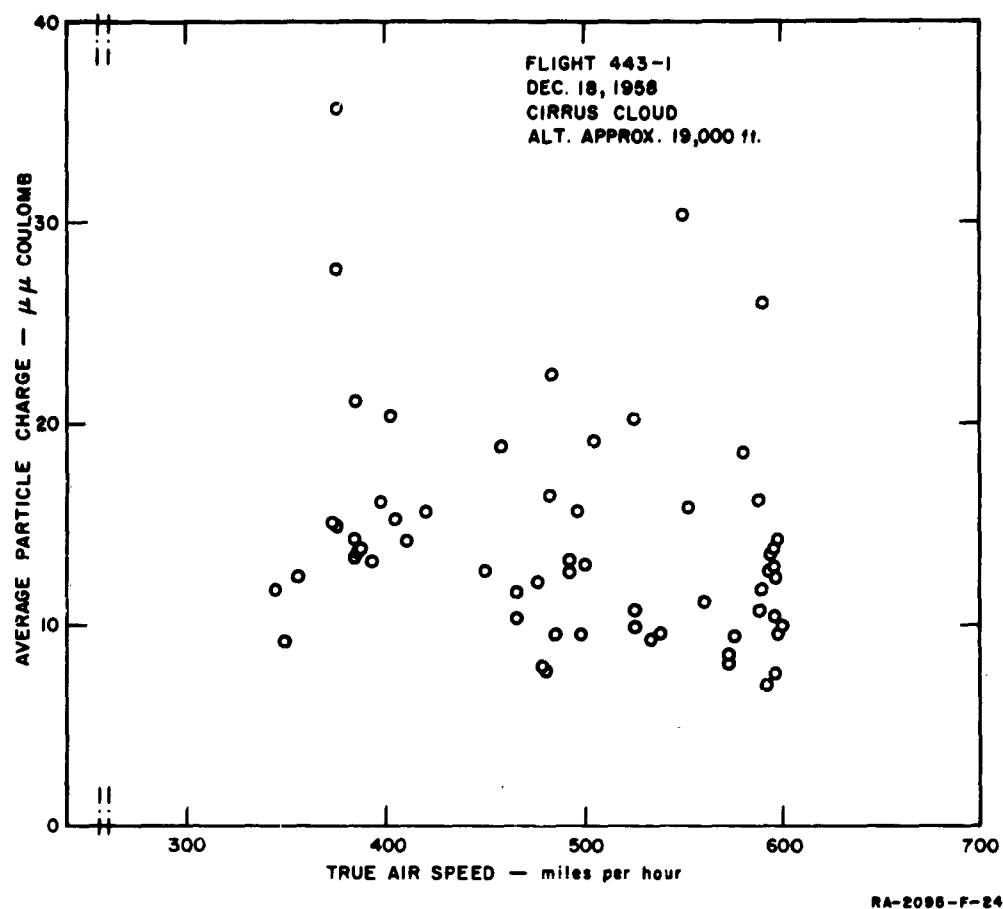
FIG. 18

PARTICLE CHARGE AS A FUNCTION OF SPEED

coefficient of drag than the spherical droplets, the NACA data may not be used directly. Assuming, however, that an ice crystal is roughly equivalent to a spherical droplet of smaller diameter, similar relationships should be valid for crystals and droplets. For this reason, typical results obtained in the study of impingement upon a prolate spheroid of fineness ratio 5 are reproduced in Figs. 19 and 20.

Shown in Fig. 19 is the manner in which the effective intercepting area varies with speed, droplet diameter, and spheroid length. It is significant to note that the fraction of the body effective in intercepting particles decreases as the size of the body increases. This result follows

40
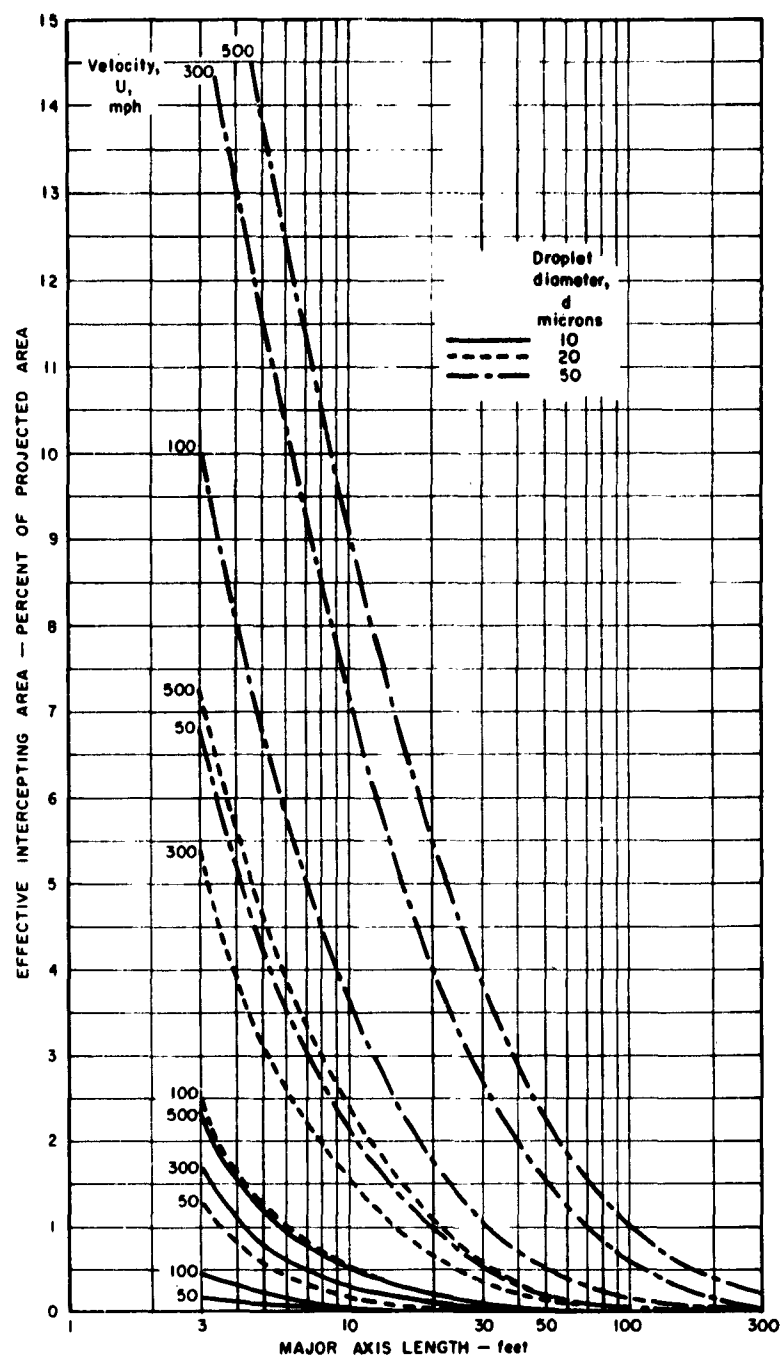
FIG. 19

EFFECTIVE INTERCEPTING AREA OF PROLATE SPHEROID
OF FINENESS RATIO 5

41
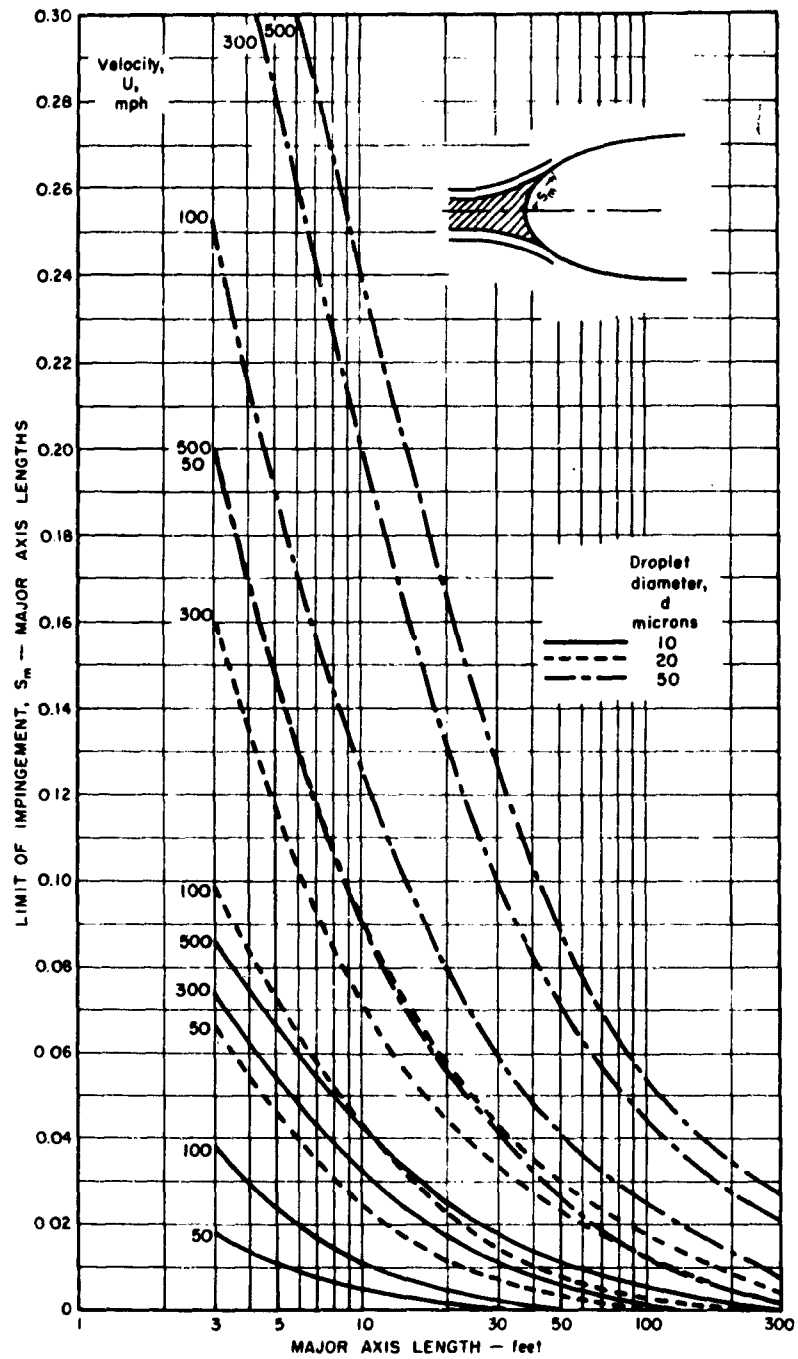
FIG. 20

LIMIT OF PARTICLE IMPINGEMENT ON PROLATE SPHEROID

42

from the fact that the body perturbs the air-flow lines ahead of it by introducing a radial flow component which acts on the particles, tending to divert them away from the body. The distance to which this perturbation extends is proportional to the dimensions of the body. Thus, in the case of a large body, the radial flow has a long time to act upon the particles, and can deflect them considerably before they reach the spheroid.

It should be noted also that the effective intercepting area decreases with particle size. This result follows from the fact that the smaller particles, having lower mass, tend to follow the air-stream lines more closely and miss the body altogether.

It is also apparent from the graphs that the effective area increases with increasing speed. This result may be explained by arguing that as the speed is increased the radial flow component has less time to act upon the particles, so that they are deflected less when they reach the body of the aircraft.

Thus, as was indicated earlier, the results of the NACA studies demonstrate that in computing total aircraft charging it is improper to assume that the area effective in intercepting particles equals the frontal area of the aircraft. It is apparent, furthermore, that the fraction of the frontal area intercepting particles will depend upon the size of the aircraft, its speed, and the characteristics of the precipitation through which it is flying.

In addition to indicating the manner in which aerodynamic effects influence aircraft charging, the results of these studies are useful in designing and locating particle-study probes. From Fig. 19, for example, it is apparent that if a probe is to intercept all of the particles in the column of air it sweeps out, the dimensions of the probe must be small. To obtain a true sample of the particles in the cloud, the probe must be mounted sufficiently far from the fuselage that it is located in relatively unperturbed air.

Further interesting results of these NACA studies are reproduced in Fig. 20. These data indicate the manner in which the limit of particle impingement, S_m, on a prolate spheroid varies as a function of spheroid size, speed, and particle size. It is evident from the figure that, for a given particle size, there is a point on the aircraft aft of which no

43

particle impingement occurs. This result should always be considered in designing probes to measure aircraft charging rate.

If, for example, charging rate were measured by means of a relatively small patch located off the roll axis of the aircraft as is indicated in Fig. 21, the patch current could be extremely sensitive to changes in speed. The aircraft nose was approximated by a spheroid with a ten-foot major axis and a fineness ratio 5, and the NACA data were used to determine the impingement limits shown in the figure. It is evident that for droplets smaller than 10 microns in diameter the effective area of the patch will
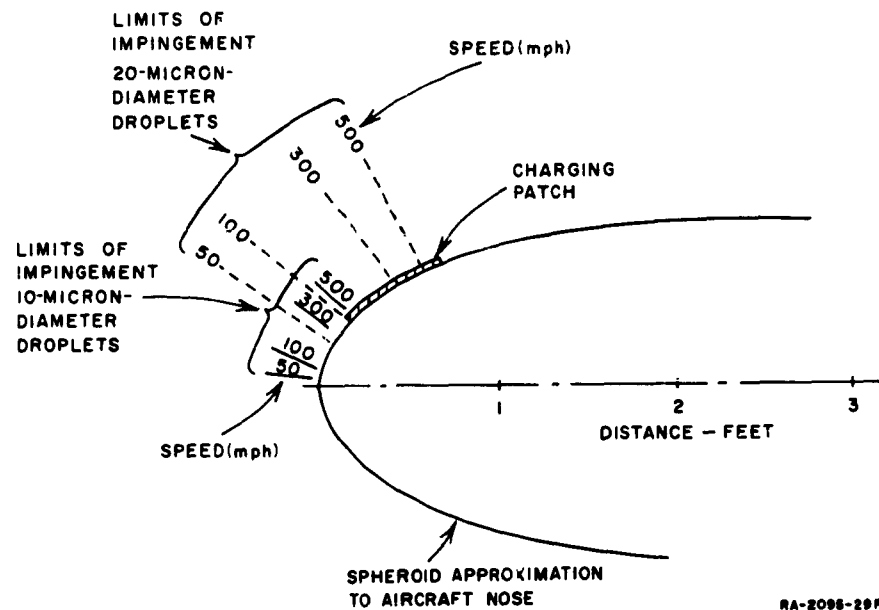
FIG. 21

EFFECT OF IMPROPER CHARGING-PATCH POSITION

be zero for speeds less than 500 mph, while for larger droplets the effective area will be extremely sensitive to speed. It is possible, therefore, that investigators reporting that the intrinsic charging rate varies as a high power of the speed were actually measuring the manner in which the intercepting area of their probe varied with speed.

The precautions taken in designing and positioning the particle study probes for the flight tests conducted on Contracts AF 33(616)-3914 and AF 33(616)-6561 are illustrated in Fig. 22. To achieve 100-percent particle
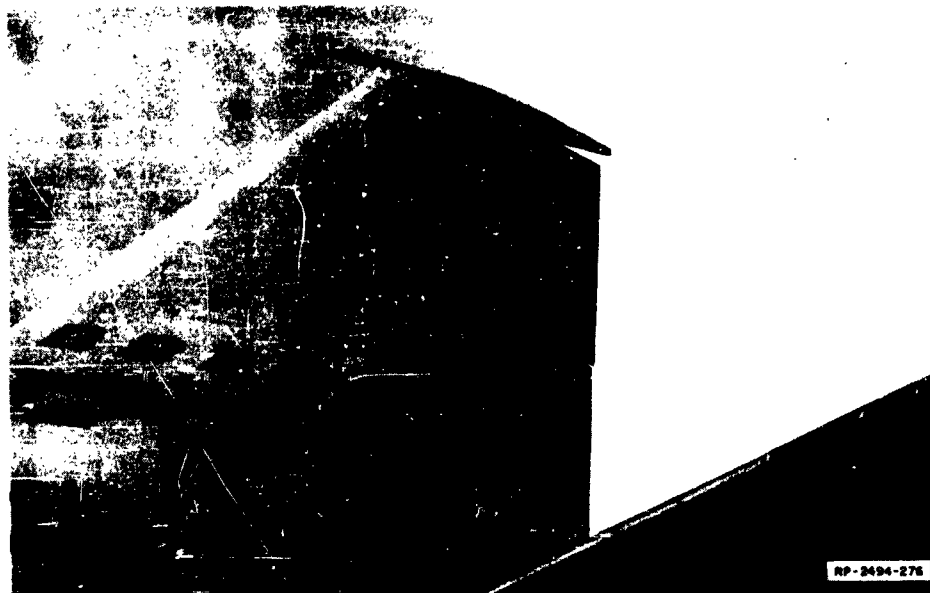
PROBES MOUNTED ON VERTICAL FIN CAP
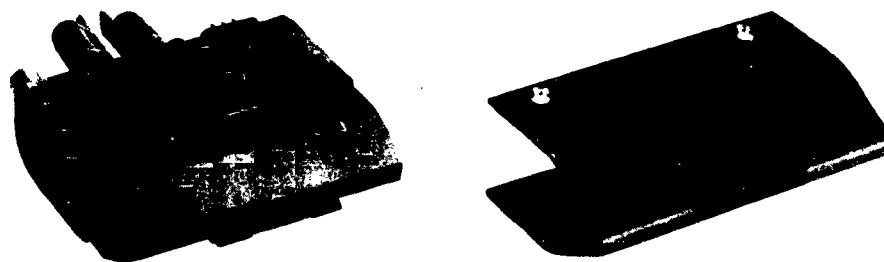
PROBE ASSEMBLY
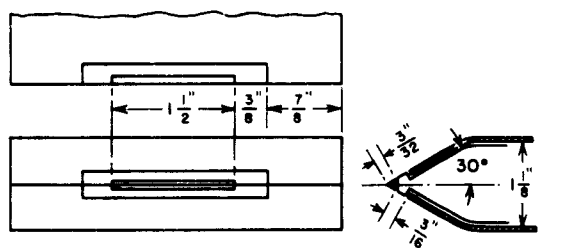
DIMENSIONS OF TYPICAL PROBE

FIG. 22

PRECIPITATION PARTICLE STUDY PROBES

45

interception the probe dimensions were made small, and the probes were mounted in an airfoil section whose thickness was only $1^1/_8$ inch. In order to locate the probes in a region of undisturbed air, they were mounted far from the fuselage on a boom projecting forward from the fin cap.

B. DETERMINATION OF CHARGING PARAMETERS

Although the results of the NACA studies indicate qualitatively how precipitation-particle impingement should vary with the various aero-dynamic parameters, the lack of information regarding drag coefficients of ice crystals made it impossible to use these data for quantitative calculations of effective intercepting area or total aircraft charging rate. Upon considering the problem of determining total aircraft charging, it appeared that a fruitful approach would be one designed to take advantage of the transient information contained in the flight-test data. As was indicated earlier, precipitation density changes considerably from point to point within a cloud formation so that intrinsic charging rate, aircraft potential, and discharge current all vary with time. The variations of these quantities must satisfy a differential equation containing a set of system parameters including the effective area of the aircraft. A least-square-error technique, presented in Appendix D, was devised to obtain these parameters using flight test data and certain subsidiary laboratory measurements.

By Kirchoff's law,[*] the charge arriving on the aircraft must either be stored or discharged. Hence we may write

$$I_{ch} = I_d(V) + C_a \frac{dV}{dt} \qquad (20)$$

where

I_{ch} = total charging current
I_d = total discharge current
V = aircraft potential
C_a = capacitance of aircraft.

---

[*] Illustrated in Fig. D-1.

Aircraft potential may be determined from flight-test data since normal flight-test instrumentation for precipitation-static tests includes provisions for recording, as a function of time, the electric field at some convenient point on the surface of the aircraft. If there are no externally applied fields, and if the field at one point on the aircraft is specified, the aircraft potential and the fields on the remainder of the surface are uniquely determined by aircraft geometry. The relationship between the airplane potential and the electric field at the field-meter location may be determined by charging a scale model of the aircraft to a known potential and using the electrostatic techniques illustrated in Fig. 23 to measure the field at the desired point. (Details of the techniques developed to perform measurements of this sort are presented in Appendix C.) Using the results of the model measurements and the flight-test recordings of electric field, therefore, aircraft potential, V, was expressed as a function of time.

The value of the aircraft capacitance, C_a, was found by measuring the capacitance of a scale model of the aircraft suspended in the laboratory using a Q-meter and subsequently increasing the measured value by multiplying by the model-scaling factor.

To find the total charging current, I_{ch}, it was assumed that the relationship between I_{ch} and the measured charging current per unit frontal area of the probe, i_p, is given by

$$I_{ch} = A_a i_p \qquad (21)$$

where the parameter A_a was assumed to be constant over each period of interest (twenty seconds at most). If the charging probe is designed as were the probes illustrated in Fig. 22, so that its intercepting area remains constant and equals its projected frontal area, the term A_a is then the effective intercepting area of the aircraft. Implicit in the use of Eq. (21) is the assumption that the charging conditions sampled by the probe are representative of the average conditions existing on all the aircraft surfaces. This assumption is reasonable, provided precipitation conditions do not change appreciably in distances of the order of a wing span, and provided the charging probe is sufficiently large that it averages out very localized statistical variations in precipitation

47
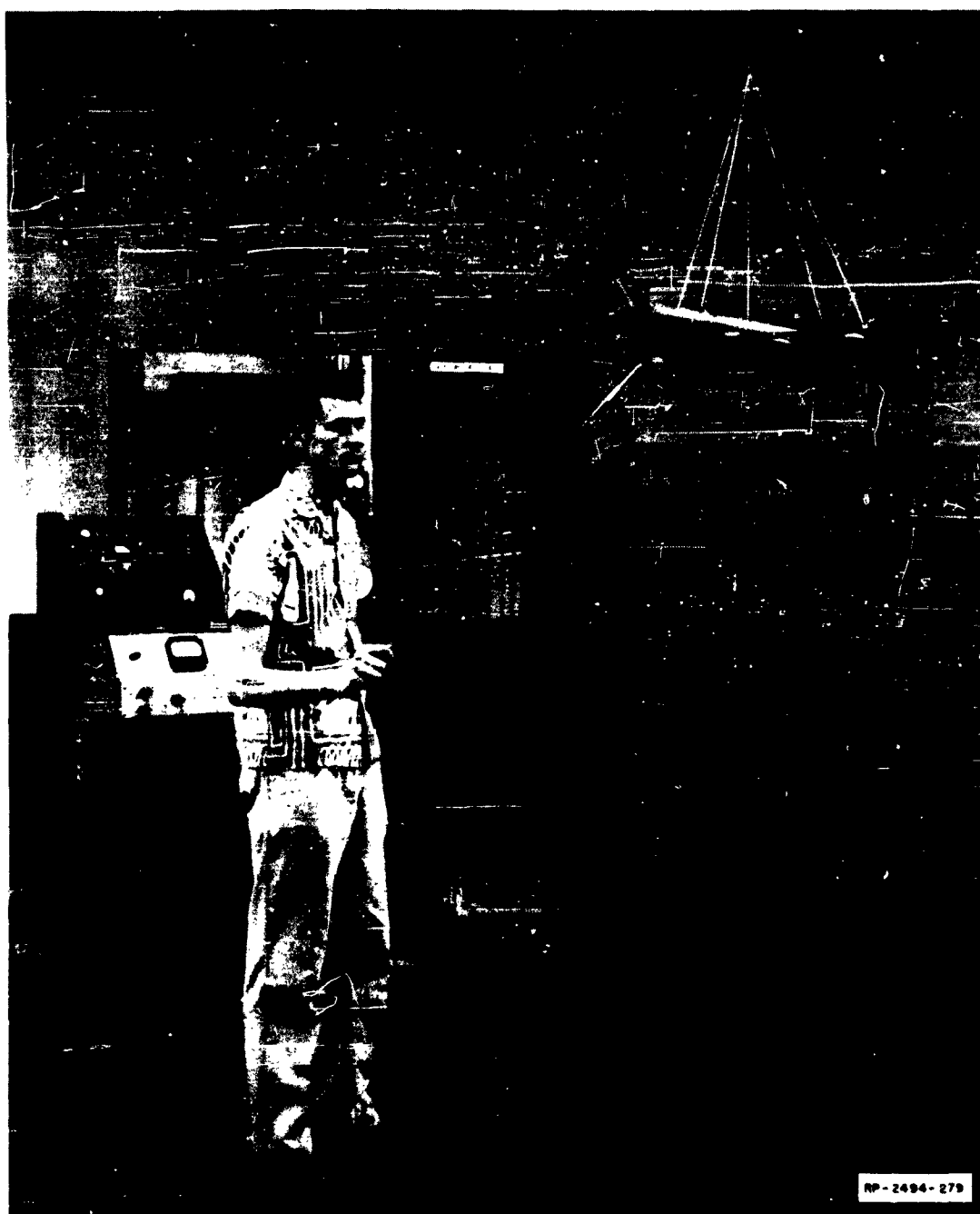
FIG. 23
LABORATORY SET-UP USED FOR FIELD MEASUREMENT

conditions. (As will be indicated later,[*] it appears that the probe used for the flight tests on the Boeing 367-80 aircraft would have been more satisfactory had its frontal area been somewhat larger.)

Although the discharge characteristics of the aircraft were unknown, it was felt that $I_d(V)$ could be represented with the required accuracy by retaining the first three terms of the Taylor's series expansion about the average aircraft potential, V_0, over the interval of interest. Thus, also substituting Eq. (21) into Eq. (20), we may write

$$A_a i_p = I_0 + a_1(V - V_0) + a_2(V - V_0)^2 + C_a \frac{dV}{dt} \qquad (22)$$

where A_a, I_0, a_1, and a_2 are as yet undetermined. By dividing through by A_a, Eq. (22) may be re-written in the normalized form

$$i_p = \lambda_1 + \lambda_2(V - V_0) + \lambda_3(V - V_0)^2 + \lambda_4 C_a \frac{dV}{dt} \qquad (23)$$

and used to compute the probe-charging rate from the aircraft potential (the current computed in this manner will be labeled i_p^*). The values of the parameters λ_i describing the aircraft charging characteristic, and in particular $\lambda_4 = 1/A_a$ defining the intercepting area, were determined by requiring that the mean square difference

$$R = \sum_{i=1}^{N} (i_{p\,i} - i_{p\,i}^*)^2$$

between the measured instantaneous probe current, $i_{p\,i}$, and the computed probe current, $i_{p\,i}^*$, be minimum. (Additional details of the mathematical process involved in the solution of this problem are presented in Sec. 1 of Appendix D.)

Using the data obtained during the flight test discussed in Refs. 10 and 11, readings of V_i and $I_{p\,i}$ were taken from the oscillograph record at 0.1- or 0.2-second intervals and read into a high-speed digital computer which computed the parameters λ_i. Using these parameters in Eq. (23) the

---

[*] In the discussion of Fig. 26.

computer calculated $i^*_{p_i}$ from the potential data, V_i. Typical results of
calculations of this sort are shown in Figs. 24(a) and 24(b) where the
agreement between the measured and calculated values of charging current
is evident. To provide a quantitative check on the method, however, the
computer was required to calculate the correlation between the computed
and measured charging currents. The result of this calculation is shown
in each of the figures.

The good correlation obtained between measured and calculated charging
currents indicates that the method of calculation is valid and that the
values obtained for the parameters λ_i (in particular the value of the
intercepting area, A_a) should be accurate. For this reason, this method
was used to study the manner in which the effective area varies. Unfor-
tunately the process of determining A_a is very time-consuming, since for
each calculation it is necessary to read at least 100 points from the
flight-test record; therefore, detailed study of the effective intercepting
area has been restricted primarily to the data obtained in a cirrus cloud
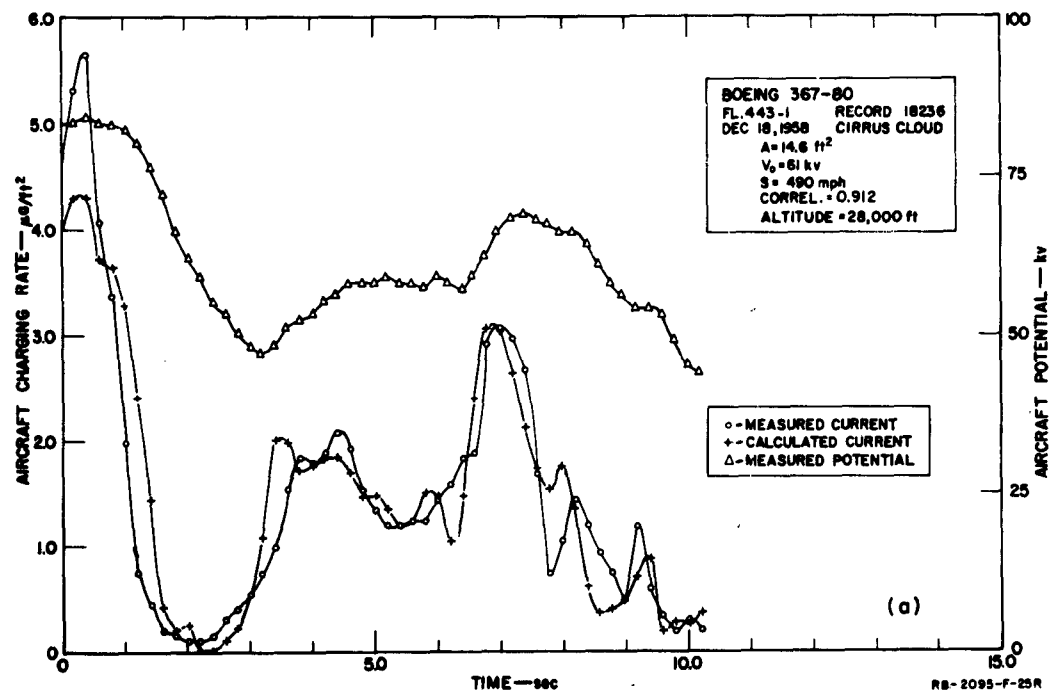
FIG. 24(a)

RESULTS OF CHARGING-RATE CALCULATION, FLIGHT 443-1
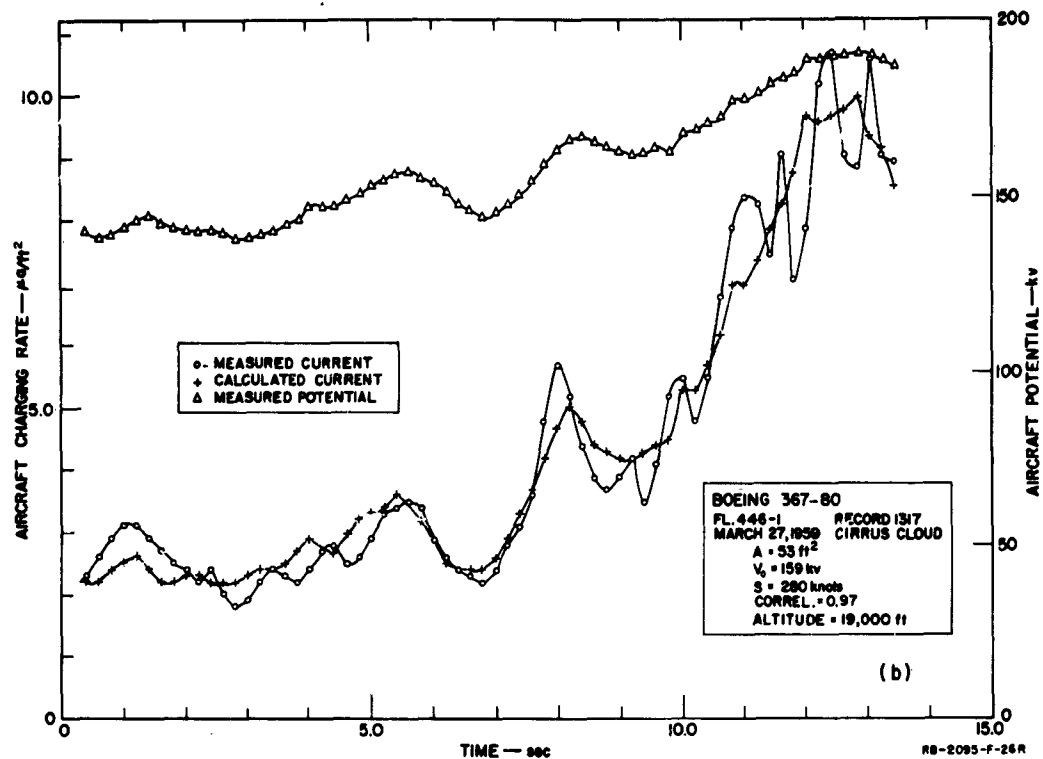
FIG. 24(b)

RESULTS OF CHARGING-RATE CALCULATION, FLIGHT 446-1

during the speed run of flight 443-1 on 18 December 1958. The effective
areas calculated for this speed run are plotted as a function of speed
in Fig. 25, from which it is evident that the intercepting area increased
with speed. Furthermore, since the projected area of the aircraft was
roughly 400 square feet, it is evident that the frontal area during this
run was always less than ten percent of the projected area of the aircraft.
The order of magnitude of the area and the manner in which the area varies
with speed are both in agreement with the results of the NACA impingement
studies shown in Fig. 19.

As a further test of the validity of the results of the effective
area calculations, an independent method for determining the area was
used. This second method described in Sec. 2 of Appendix D, consists es-
sentially of using the measured discharge current and measured aircraft
potential to compute the intrinsic charging rate which is then compared

51
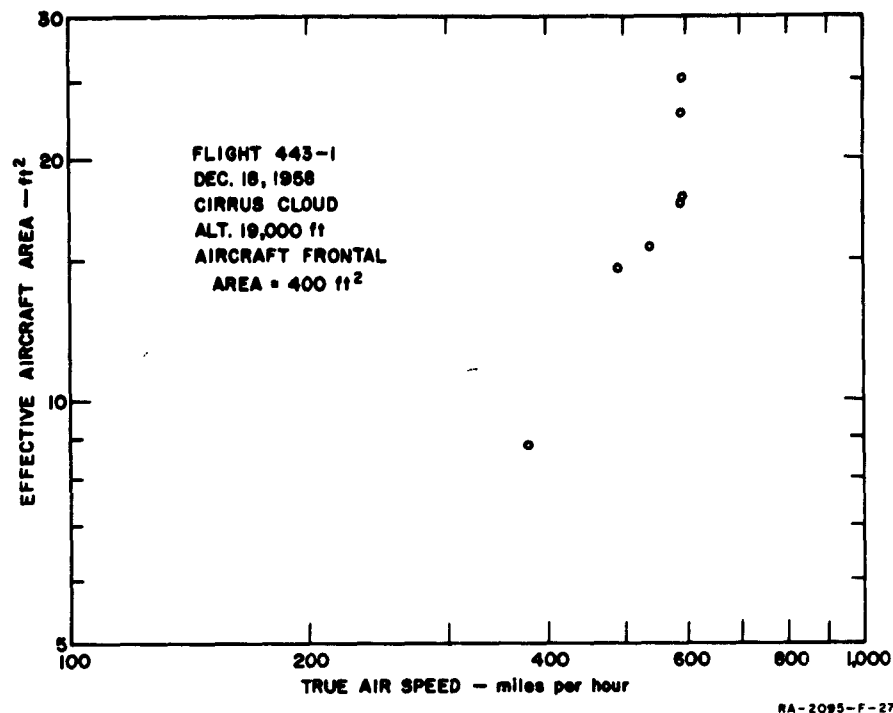
FIG. 25

EFFECTIVE INTERCEPTING AREA OF AIRCRAFT AS A FUNCTION OF SPEED

to the measured charging rate. This method may be used, therefore, only if some means for estimating total discharge current is available. Prior to December 1959 no measured discharge-current data were available. On the flights described in Ref. 11, however, the currents leaving certain of the dischargers on a wing (including the outboard trailing-edge discharger) were monitored and recorded. On subsequent flight tests current was also monitored from the fin cap. [13,18] The results of these current measurements were combined with the results of the laboratory work described in Sec. V-C and Sec. V-D to obtain an empirical equation relating total discharge current to the current discharged from the outboard discharger mounted on the trailing edge of the wing.

Using data obtained during the flights discussed in Ref. 11, charging-rate calculations were carried out using Methods 1 and 2 of Appendix D. The results of these calculations together with the measured charging rate

are shown in Figs. 26(a) and 26(b). In both figures the calculated points lie along the measured curve, and in both cases the correlation with the measured curve is high. A high degree of correlation between the three sets of data was normally observed, indicating that the calculated data may be accepted with confidence. In Fig. 26(b), however, the correlation between the two sets of calculated data is better than the correlation between the measured data and either of the calculations. When this result was obtained, the flight-test record was re-examined, and it was found that the charging-rate record in this region was noisy. Thus, in Fig. 26(b) the calculated charging-rate data are probably a more accurate representation of the actual charging than are the measured data.

Also listed on the figures are the intercepting areas calculated using the two methods. In general, the areas calculated using the two methods were never in perfect agreement. There was, however, no systematic difference between the calculated areas, and neither method consistently gave the larger area. The important result of these calculations
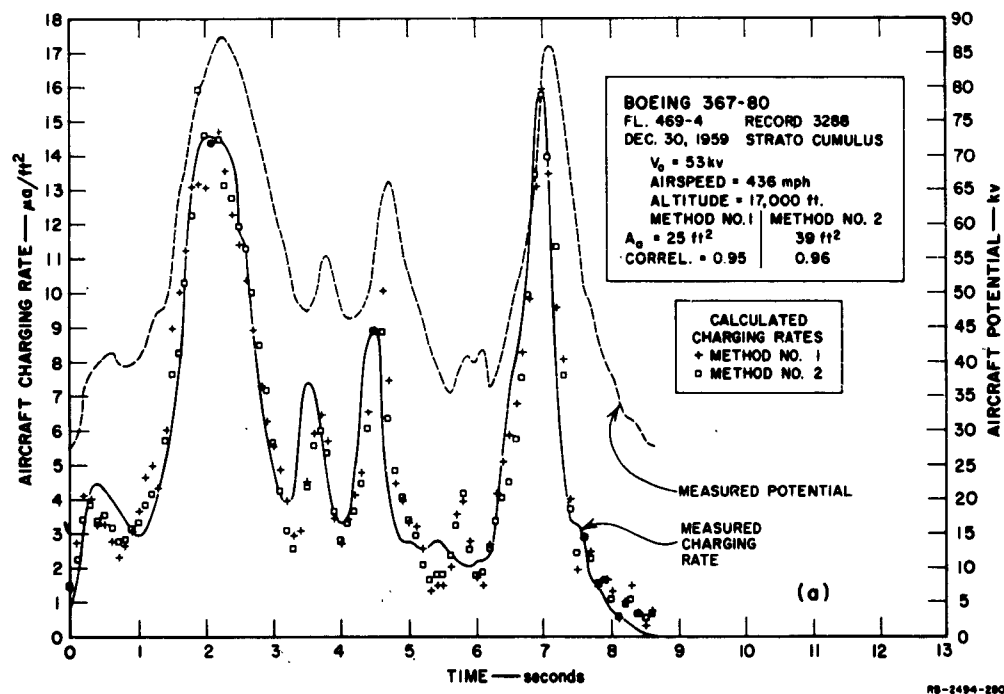
FIG. 26(a)

COMPARISON OF CHARGING DATA
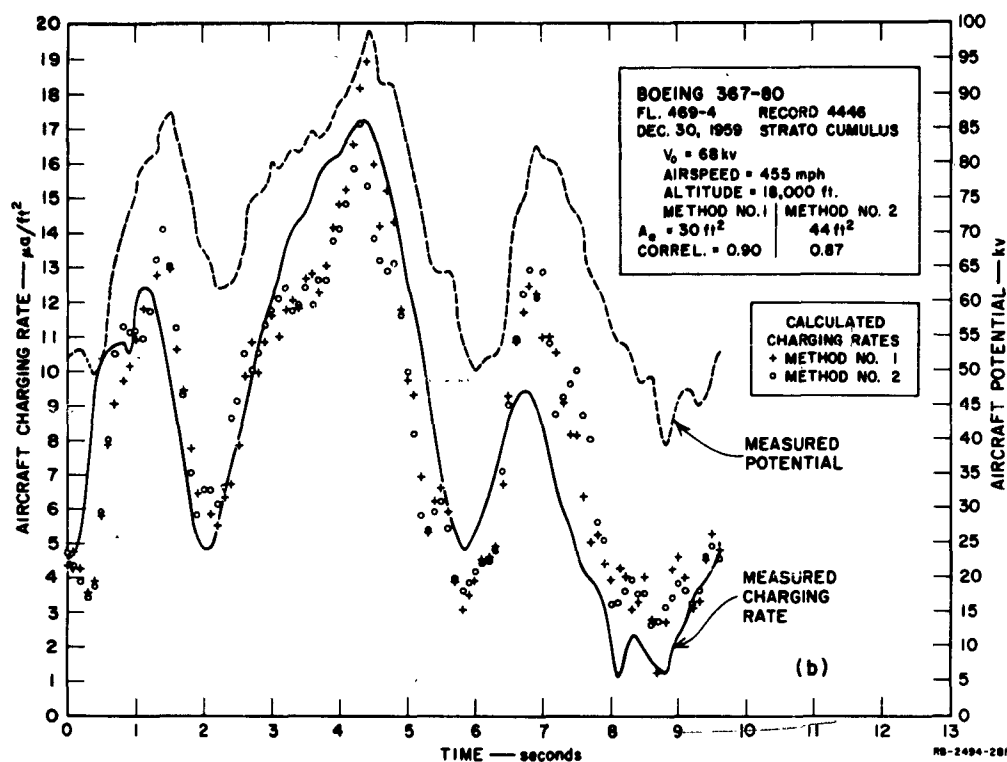
FIG. 26(b)

COMPARISON OF CHARGING DATA

is that both methods agree in indicating that the effective intercepting area of the aircraft used in the tests (Boeing 367-80, prototype of the 707 and KC-135) was always only a small fraction of its projected frontal area of roughly 400 sq ft. (The largest intercepting area calculated was 160 sq ft during a climb-out through frontal snow.)

C. PRECIPITATION-CHARGING CURRENTS

It will be worthwhile at this time to recapitulate the results of the aircraft charging studies presented in the two preceding sections and to consider some of their practical implications.

The intrinsic precipitation charging rate is given by

$$\rho = q_p cv \tag{24}$$

54

where

ρ = current per unit intercepting area
q_p = charge per particle
c = particle concentration in the cloud
v = aircraft velocity.

As was indicated in Sec. IV-A, q_p and c vary considerably, depending upon cloud conditions, but, since they are both independent of speed, they are both constant in a homogeneous cloud. Thus, the intrinsic charging rate ρ varies linearly with aircraft speed.

Typical peak charging rates encountered during the flight tests conducted using the KC-135 prototype aircraft are listed in Table I.[10,11,18,19] These rates should be typical for subsonic jet aircraft operating at normal cruising speeds.

TABLE I

PEAK CHARGING RATES ENCOUNTERED
WITH KC-135 PROTOTYPE

CLOUD TYPE	PEAK CHARGING RATE ρ (μamp/sq ft)
Cirrus	5 to 10
Strato Cumulus	10 to 20
Frontal Snow	30

Total aircraft charging current is given by

$$i = \rho A_a \tag{25}$$

where, as was indicated earlier, at normal KC-135 speeds, the effective intercepting area A_a is not constant, but increases with increasing airplane speed. Thus at these speeds the impression for total charging current may be written

$$i = q_p c v A_a(v) \quad , \tag{26}$$

and it is apparent that i varies more rapidly than the first power of v.

As the speed is increased, however, A_a approaches as a limit the projected frontal area of the aircraft, A_{proj}. Above this speed, therefore, the expression for the total charging current becomes

$$i = q_p c v A_{proj} \tag{27}$$

which, since A_{proj} is a constant, indicates that the total current varies linearly with speed. Thus, although the charging currents of supersonic

55

aircraft may be high, the fact that the current varies only as the first power of the speed indicates that the problem of providing adequate discharging capacity should not be prohibitively difficult.

Although the flights conducted using the KC-135 prototype were not typical of normal aircraft operation in that an effort was made to spend as much time as possible in clouds, some of the observations regarding charging rates during these flights nevertheless are of interest. The peak charging rate much of the time was of the order of 10 μ/ft^2, while the intercepting area was roughly 50 ft^2. Thus, the charging current to the aircraft was generally of the order of 500 μa. During climb-outs through snow the charging rate reached values as high as 30 $\mu\text{a}/\text{ft}^2$, while the maximum calculated area reached 150 ft^2. Assuming that the aircraft intercepting area can become as high as 200 ft^2, and that at the same time the charging rate is 30 $\mu\text{a}/\text{ft}^2$ the total charging rate can reach values as high as 6 ma. This latter value of charging current, however, is extreme and is not likely to be encountered.

In an effort to obtain statistical data regarding precipitation charging conditions, recordings were made (during 600 hours of normal operation) of the current leaving a wing-tip discharger on a Boeing 707 aircraft operated by QANTAS Empire Airways.[18,19]

From these recorded data it was possible to calculate the total charging current. These data were used to prepare Fig. 27, which shows the probability of encountering charging exceeding a given magnitude. In using these data it should be recalled that they were obtained on long-hop flights which generally operate at high altitude above much of the precipitation. On shorter flights at lower altitudes the probabilities may be expected to be considerably higher.

In applying the above precipitation charging data to estimate charging currents on other aircraft types, it will be necessary to correct for differences in speed and size. As was indicated earlier, ρ may be taken to vary linearly with speed. NACA water droplet impingement data such as that shown in Fig. 19 may be used to estimate the amount of variation of intercepting area with speed. Similarly, data of the type shown in Fig. 19 may be used to estimate the effect upon intercepting area of changing aircraft size. It is interesting to note that as aircraft size is reduced A_{proj} becomes smaller, but for a smaller aircraft, A_a is a greater fraction of
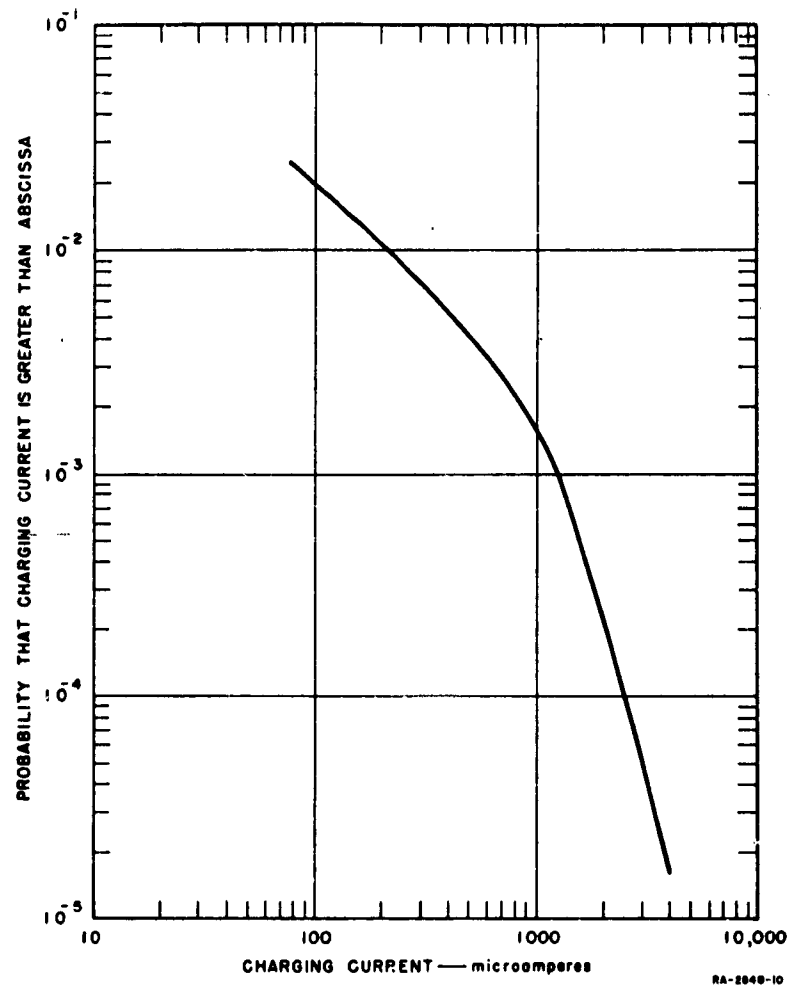
FIG. 27

PROBABILITY THAT AN AIRCRAFT WILL ENCOUNTER CHARGING
EXCEEDING A GIVEN MAGNITUDE

A_{proj}. Thus the charging currents to smaller aircraft will be greater
than might be expected on the basis of their frontal areas.

If the aircraft in question operates at higher altitudes than a
KC-135 or 707, the probabilities of encountering charging given in Fig. 27
should be reduced. Conversely, if the aircraft in question is piston
driven and operates at lower altitudes, these probabilities should be
increased.

57

D. ENGINE-CHARGING CURRENTS

In jet aircraft it is often found that radio interference exists at low altitudes even in clear air. The intensity of this interference is a function of the engine power settings, increasing with increasing power. Similar effects have been reported for turbo-prop aircraft, but are not well documented. Since the noise is often particularly severe following a change in power setting, it can be extremely objectionable during the maneuvering associated with landing, when good communication is important. Although this noise should not strictly be classified as precipitation static, the mechanism by which it is generated and coupled, and the means by which it can be eliminated, are identical with those for corona-generated precipitation static. For this reason, it is convenient to consider it in the same classification.

In considering the problem of the noise connected with jet engines, it was apparent that there are no processes occurring in the flame or exhaust which could constitute a source of the interference that was observed. It was postulated therefore (later confirmed) that the engines merely charge the aircraft and that the noise is generated by corona discharges occurring at the extremities. Hence this type of interference may be eliminated in two ways: by preventing the charging or by discharging the current noiselessly. Since some means for noiselessly discharging the aircraft was needed in any event to handle the current generated by precipitation, the same discharging scheme would serve to discharge the current generated by the engines. For this reason, no particular effort was made to study engine charging in detail to determine if the charging could be prevented. Instead, a plausible charging mechanism was postulated, and measurements were conducted to measure engine-charging current magnitudes to make certain that they were lower than the currents resulting from precipitation charging.

It was hypothesized that engine charging occurs because the electrons produced in the combustion chamber are much more mobile than the positive ions. Thus the electrons tend to diffuse to the chamber walls with the result that the exhaust stream is positively charged. As the charge is carried away in the exhaust, the aircraft potential will continue to rise until equilibrium is established by one of the following mechanisms:

(1)　The aircraft potential rises until it exceeds the corona threshold and, finally, the corona discharge current equals the engine charging current.

(2)　The aircraft potential rises until the field intensity in the vicinity of the jet exhaust is sufficiently high to overcome the wind and cause the excess positive ions in the exhaust stream to return to the aircraft.

(3)　Some of the excess positive ions return to the aircraft, and the rest of the current is discharged by negative-point corona discharges.

Which equilibrium situation is established depends upon the fields existing in the tail-pipe region. For example, by attaching rods to the tail pipe in such a manner that they protrude into the exhaust stream it is often possible to create a sufficiently large region of high field in the exhaust that all of the excess positive ions are extracted at potentials below corona threshold. Since the electric field produced around a rod by the charge on the aircraft is sufficient to extract enough positive ions from the exhaust to overcome engine charging, it was felt that it might be possible, by biasing the rod negatively with respect to the aircraft, to extract even more positive ions, and perhaps use the biased rod as a noiseless discharger under precipitation charging conditions. Even more attractive was the possibility of using a positively-biased rod in the exhaust stream to artificially charge the aircraft to permit precipitation static experiments to be conducted even in clear air. If the negative particles in the exhaust existed as free electrons, which are much more mobile than ions, they could be extracted relatively easily, and it might be possible to obtain substantial charging currents in this manner.

Tests were conducted using a jet engine mounted in a ground test stand at Boeing Airplane Company in Seattle.[19] In these tests a 24-inch-long steel rod connected to a variable high-voltage supply was placed along the engine axis immediately aft of the engine exhaust cone. It was found that with maximum throttle setting on the engine and with 10 kv applied to the rod, the current was roughly seven microamperes, regardless of the polarity of the applied voltage. Because of the very small conductance observed, and also because the current magnitudes were found to be independent of polarity, it was concluded that there are not appreciable numbers of negative ions in the exhaust having mobilities greatly higher than the positive ions. From this it was concluded that very few, if any, free electrons are present in the exhaust at the time of exit.

59

To further demonstrate that the current was being limited by the difficulty of removing the heavy ions from the exhaust stream, and not by the lack of ions, the length of the steel probe was increased to 48 inches, approximately doubling the surface area of the probe. With the double-length probe and an applied voltage of 10 kv, the current increased to 13 microamperes. These results indicated clearly that the conductivity of the exhaust gases is too low to permit their use either to charge the aircraft for experimental purposes or to discharge it in the presence of precipitation charging. To accomplish either function would require either prohibitively high voltage or a very large total electrode area immersed in the exhaust. For this reason, no further effort was made to test this method of aircraft charging.

Flight-test measurements of engine charging were made on several different aircraft types using several different current-measuring techniques.[11,18,19] These included:

(1) Measuring the biased discharger current necessary to maintain aircraft at zero potential

(2) Artificially charging the aircraft to a positive potential, turning off the charger, and determining the engine-charging current from the aircraft capacitance and the rate of change of potential when the potential goes through zero under the action of the engines

(3) Measuring the current from a discharger mounted at some standard location such as a wing tip.

Good agreement was obtained between the current values measured using the various techniques on the Boeing 367-80 aircraft, which was equipped to permit all three types of engine-charging current measurements to be made. The maximum values of engine-charging current obtained on the various aircraft investigated are listed in Table II.

It is evident from the table that the engine-charging currents are all lower than the currents generated by precipitation charging. Therefore, a discharging scheme which is satisfactory for precipitation charging will certainly be capable of handling engine-charging currents.

TABLE 1I

MAXIMUM MEASURED ENGINE-CHARGING CURRENTS

AIRCRAFT	ENGINE TYPE	CONDITION OF OPERATION	MEASUREMENT TECHNIQUE	MAXIMUM ENGINE- CHARGING (Microamperes)
Boeing 367-80 KC-135 Proto- type	Pratt & Whitney JT3C-1	Dry	1, 2, 3	50
Boeing 707-138	Pratt & Whitney JT3C-4	Water injection	3	800
Boeing 707-138	Pratt & Whitney JT3C-4	Dry	3	175
Convair 880	General Electric CJ-805-3	Dry	3	75
Douglas DC-8	Pratt & Whitney JT3C-6	Water injection	3	300-400
Douglas DC-8	Pratt & Whitney JT3C-6	Dry	3	100

V DISTRIBUTION OF DISCHARGES

A. GENERAL

A knowledge of the manner in which corona discharges distribute themselves on an aircraft is of interest in the study of corona-noise character and in the design of dischargers. It is evident from Fig. 6 that the coupling between a discharge and a particular antenna depends upon the location of the discharge. Both the spectral character and the magnitude of the noise induced in the antenna, therefore, will be determined by the corona source locations. Since dischargers should be located where corona normally tends to occur, many of the requirements on the design and location of dischargers are dictated by discharge distribution.

In attempting to eliminate corona noise on an aircraft it is important to have a technique for finding on the aircraft, regions with the lowest threshold potential and to be able to estimate the magnitude of this potential. This is necessary since the discharger system must be so designed that except for rare conditions of extremely high charging, corona cannot occur from these parts of the aircraft.

The problem of predicting discharge currents is complicated by the space charge left behind by the discharges. This space charge modifies the dc fields near each discharge point and influences the amount of current it can discharge. On flights through precipitation the problem is further complicated by the column of charged precipitation left behind by the aircraft.

B. ESTIMATING THRESHOLDS

1. POSSIBLE METHODS

A problem which often arises in the study of precipitation static is that of estimating the corona threshold potentials of various parts of an aircraft. The desired data may, of course, be obtained by properly instrumenting the aircraft in question and measuring the desired thresholds in flight through precipitation. This procedure, however, is time-consuming and costly. Another method which has been used is to isolate the full-scale aircraft from ground, connect it to a high-voltage supply, and

measure the potential at which corona occurs from various interesting parts. Since a full-scale aircraft is used, practical problems prevent its being removed appreciably from the ground. The dc fields about the aircraft, therefore, will be altered by the proximity of the ground, and will not duplicate those existing about the aircraft during flight. Since the measurements are made in still air, the threshold data do not include the effects of localized pressure reductions associated with vortex formation on such places as wing tips and propeller tips in producing localized threshold reductions in those regions. This method too is expensive since the aircraft must be removed from normal use, since a heavy installation is required to isolate the aircraft, and since the aircraft and its fuel system must be purged and "pickled" to prevent the possibility of explosion.

By making extensive use of models and mock-ups, and employing the field-measuring techniques described in Appendix C, it is possible to estimate corona thresholds with reasonable accuracy using only inexpensive laboratory equipment. Since the model used for the measurements may be suspended many model distances from the ground, the dc fields approximate very closely those existing about an aircraft in flight. Because all measurements are made in still air, the threshold data obtained using this method do not include the effects of localized pressure reductions that may occur in flight.

2. THRESHOLDS OF AIRFOIL TRAILING EDGES

Let us consider the problem of determining the threshold potential of the trailing edge of the wing near the outboard tip. Using the full-scale wing mock-up and electrode geometry of Figs. 8 and 9, the applied voltage was increased until at potentials ranging from 60 to 75 kv, corona occurred. Since the field structure about the mock-up is known, it is possible to calculate, from the measured electrode voltage, the field intensities existing at various points on the surface of the full-scale wing model when corona occurs from the trailing edge. The expression for the surface field E_s is

$$E_s = \frac{V_{electrode}}{2} \frac{1}{\sqrt{dx}} \tag{28}$$

64

where

> d = distance between trailing edge and aluminum
> sheet (d = 13.5 inch in Fig. 8)

> x = perpendicular distance to trailing edge from
> reference point on surface of wing.

(This expression for the field was verified for the geometry of Figs. 8 and 9 using the field-measuring technique described in Appendix C.) Let us assume that we are interested in the field existing at a reference point 43.75 inches in from the trailing edge on the full-scale wing. Substituting this distance, and the corona threshold potentials measured with the mock-up, into Eq. (28) the field existing at the reference point is found to be 48.6×10^3 to 60.7×10^3 volts/meter.

Using the field-measuring technique described in Appendix C, the field existing at the reference point on the wing may be related to the aircraft potential. This was done for the KC-135 by suspending a $\frac{1}{50}$ scale model of the aircraft in the laboratory as is shown in Fig. 23. The aircraft was charged to a known potential, and the field intensity at the scaled reference point ($\frac{7}{8}$ inch in from the trailing edge on the model) was measured. It was found that on the model a field intensity of 1 volt per meter was produced at the reference point when the model potential was 0.082 volts. Thus, on the full-scale aircraft, the potential necessary to produce a field intensity of 1 volt per meter at the reference point is $50(0.082)$ = 4.12 volts. Threshold potential for corona from the trailing edge at sea level, therefore, lies within the range $4.12 \ (48.6 \times 10^3)$ = 200×10^3 to $4.12 \ (60.7 \times 10^3)$ = 250×10^3 volts at sea-level altitude. Similar measurements conducted for the DC-8 which has thicker trailing edges indicate that the threshold should be roughly 1.6 times that of the KC-135, so that it should lie in the range from 320 to 400 kv.

During the KC-135 prototype flight tests reported in Refs. 10, 11, and 18, the corona threshold of the wings was estimated by noting the aircraft potential at which noise onset in the receiving systems occurred. The average of the values obtained in this manner for sea-level threshold was 212 kv, which is near the lower limit of the threshold estimates made in the laboratory. Actually one would expect the true corona threshold for the wing to be lower than that estimated in the laboratory since, on the aircraft, corona will first occur from the wing tip which has a lower threshold potential than the trailing edge. Since a reasonable amount of

65

current had to be discharged before noise could be detected, however, the noise threshold corresponds very nearly to the corona threshold of the trailing edge.

3. THRESHOLDS OF VHF ANTENNAS ON DC-8 AIRCRAFT

Another interesting application of laboratory techniques for corona-threshold determination is illustrated by a problem which arose in connection with the Douglas DC-8 aircraft. Soon after this aircraft was placed in service the operators found that interference was often observed in the VHF receiving systems when the aircraft was operated in precipitation. Since the corona-noise spectral density is very low at VHF frequencies, this noise should be observed only if corona discharges occur from some region of very high coupling such as the VHF antenna itself. Laboratory measurements illustrated in Fig. 28, therefore, were made to determine if one could reasonably expect corona discharges from the VHF antennas.

As is indicated in Fig. 28(a), a model of the aircraft was charged to a known potential, and measurements were made of the field intensity on the surface of the aircraft at the positions of the VHF blade antennas. Since the radius of the fuselage is large in comparison with the dimensions of the antenna, the fields in the region surrounding an antenna on the fuselage may be simulated with a high degree of accuracy by the uniform field existing between a pair of parallel plates, as shown in Fig. 28(b). In principle it would be possible to increase the potential applied to the parallel plates until corona occurred from the antenna mounted on one of the plates, thereby determining the field intensity which must exist at the aircraft skin in order that discharges occur from the antenna. This field intensity together with the results of the model measurements would specify the aircraft potential corresponding to the corona threshold of the VHF antenna. Actually, it was not possible to apply sufficient voltage to the parallel plates to produce corona, and the measurement had to be made in two steps.

A known field was established between the parallel plates, and the field intensity at a reference point on the metal leading edge of the blade antenna was measured. The antenna was then immersed in the structure of Fig. 28(c) (see also Fig. 9), which is sufficiently small that corona could be induced from the antenna with reasonable values of applied voltage. With a known voltage applied to the structure, a measurement

66

was made of the field at the reference point on the antenna. This measurement permits the applied voltage in the structure to be related to the full-scale aircraft potential necessary to produce the same field intensity at the reference point.

The results of these measurements indicate that, at an altitude of 20,000 feet, in the absence of externally applied fields, corona should occur at an aircraft potential of 750 kv from VHF antenna No. 2, and at a potential of 980 kv from antenna No. 3. In flight, localized pressure

(a) AIRCRAFT MODEL

$$E = \frac{V_p}{d}$$

(b) BLADE ANTENNA IN UNIFORM FIELD

(c) GEOMETRY FOR PRODUCING BREAKDOWN

RA-2494-282
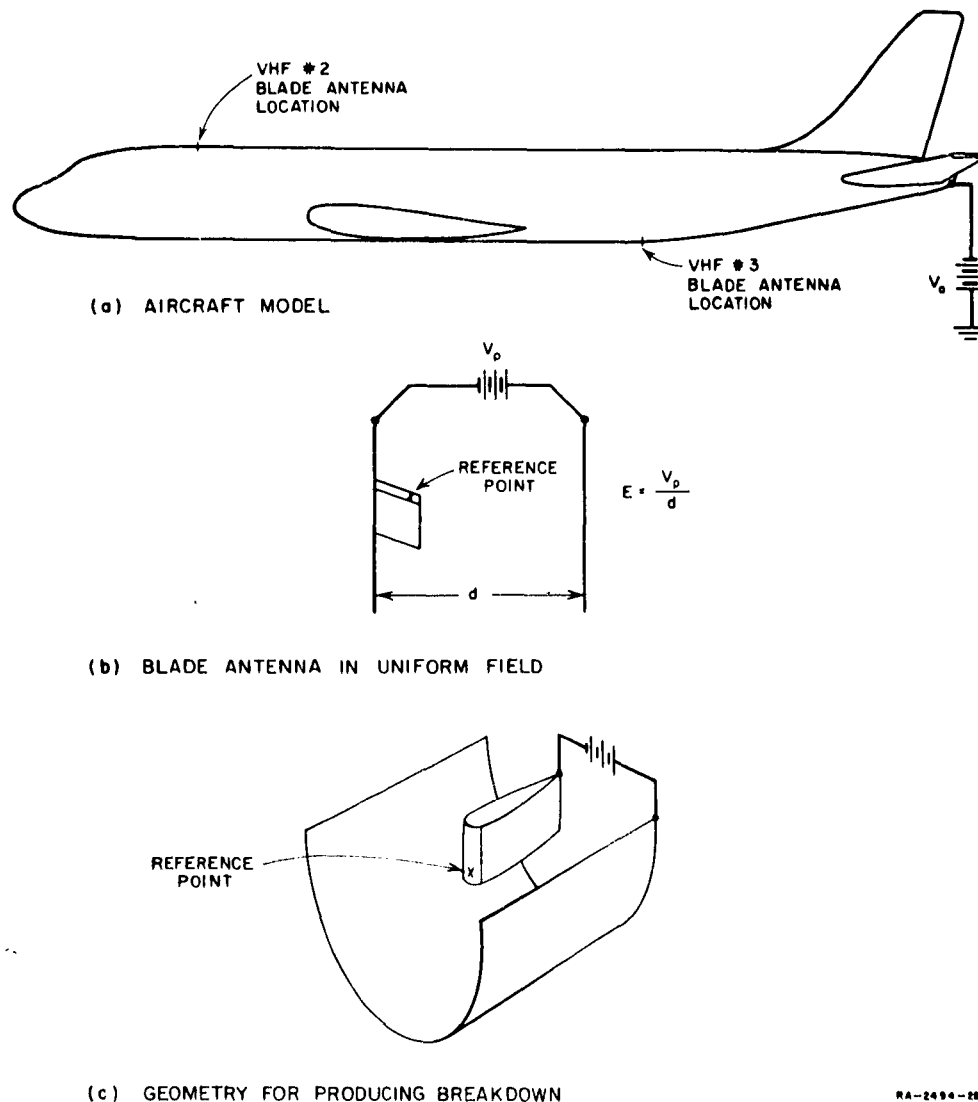
FIG. 28

ESTIMATING CORONA THRESHOLD OF VHF BLADE ANTENNA ON DC-8 AIRCRAFT

reductions aft of the metal strip on the leading edge of the antenna might reduce the thresholds below these values. From the results of the KC-135 prototype flight tests and laboratory measurements on a mock-up of a DC-8 wing it is estimated that the potential of the DC-8 at 20,000 ft altitude is roughly 310 kv when the charging rate is 1 ma. Thus, even if the antenna thresholds in flight are one-half the values estimated above, using still-air measurements in the laboratory, one should not expect discharges from the VHF blade antennas under low-charging conditions. It appears, however, that if the aircraft is in a region where the charging is high or if it is in a region of charging where an externally applied field exists and augments the fields produced by charge on the aircraft, discharges can be expected to occur from the blade antennas.

The conclusions drawn from the laboratory tests were verified in a flight test conducted by Delta Air Lines using their DC-8 No. 801. Provisions were made on the test aircraft to isolate the No. 3 VHF blade antenna from ground, permitting the corona current discharged from it to be read on a microammeter monitored by an observer in the cockpit area. During the cruise portion of a flight from Atlanta, Georgia, to Fort Worth, Texas, the aircraft was at 27,000 feet and flew through the tops of three thunderstorms. Each period in precipitation lasted roughly ten minutes. During each of these periods, intermittent discharge currents lasting from ten to thirty seconds and ranging from $5\mu a$ to $40\mu a$ were read on the instrumented antenna. Occasional surges to $250 \mu a$ were noted. There were periods when no current was discharged from the instrumented antenna but noise was observed in the No. 2 VHF receiver.

The fact that discharge current was not measured throughout each ten-minute interval indicates that discharges occurred from the instrumented antenna only during periods of high charging or when external fields were of sufficient magnitude to provide the necessary field augmentation. Noise observed in the No. 2 VHF receiver when there was no current leaving No. 3 VHF antenna tends to verify the laboratory results, indicating that the corona threshold potential of No. 3 VHF antenna is higher than that of No. 2 VHF antenna.

4. RADOME LIGHTNING-DIVERTER-STRIP THRESHOLDS

After commercial jet transports had been in service for roughly a year, the operators began to experience with increasing frequency a new noise which affected all receiving systems including VHF and VOR. The

68

noise occurred in conditions of low charging and even in clear air as the result of engine charging. The low corona threshold of the noise source indicated that the noise was not being generated by discharges from the VHF antennas. Since the noise was experienced on a QUANTAS 707 equipped with ortho-decoupled dischargers (these dischargers are discussed in Sec. VIII-B) it was not being generated by discharges from the airfoils. The source of the noise was finally pinpointed during a United Air Lines DC-8 flight in which it was observed that the intensity of the noise was a function of the position of the weather radar dish. Upon landing it was found that the lightning diverter strips (thin strips of aluminum foil extending out from the fuselage on the surf.ce of the radome) on the nose radome had become detached from the radome surface, that many of the conductors were broken into several segments separated by gaps, and that sharp edges of the metal foil were protruding through the paint. The diverter strips were removed from the radome, and upon resuming flight, it was found that the noise had been eliminated.

An explanation for this noise can be offered by noting that if the diverter strip is broken into segments or if it is isolated from the fuselage at the base of the radome, current flowing into the strip will be returned to the airframe by sparking from segment to segment. Sparks are extremely energetic noise sources, and, unlike corona discharges, may generate appreciable energy at VHF. For example, the spectrum of the signal generated by the spark probe illustrated in Figs. 4 and 5 was virtually flat to frequencies of 100 Mc. Furthermore, the coupling to a discharge occurring in a gap between the segments of conductor is high. The coupling should be particularly high at VHF since at these frequencies the strips are a large fraction of a wavelength long. Thus, particularly at VHF, a defective diverter system can degenerate into an efficient antenna system driven by a spark noise source.

It is of interest to consider methods by which discharges from the diverter strips can be produced. In precipitation charging it is inevitable that discharges occur from isolated diverter strips. In this case the strip and the surrounding region of radome will be charged negatively by the impinging precipitation. Since a potential difference can exist between the isolated strip and the aircraft, the charge on the strip will increase until it is relieved either by a spark discharge to the aircraft or by a corona discharge into space occurring at the forward end of the strip.

69

When reports were received that VHF noise was being experienced under engine-charging conditions it appeared that the lightning diverters were not only handling the radome-charging current, but that their corona threshold might be sufficiently low that they were acting as dischargers for the main body of the aircraft as well. For this reason laboratory measurements were made to estimate the corona threshold of a diverter strip the forward end of which has become detached from the radome and is protruding into the airstream. Two extreme possibilities were considered:

(1) The radome is a good insulator and does not influence the electric fields so that the fields about the diverter strip are the same as they would be if the radome did not exist--*i.e.*, if the strips were self-supporting pieces of conductor protruding forward from the aircraft fuselage.

(2) The radome in the vicinity of the forward end of the strip is a sufficiently good conductor so that the protruding end of the strip merely modifies locally the dc-field structure determined by the radome itself.

The laboratory techniques again consisted of field measurements on a $\frac{1}{50}$-scale model followed by field measurements on mock-ups of sections of the radome. From these measurements it was estimated that for an aircraft such as the KC-135 or DC-8 the threshold potential of a strip at sea level altitude is:

Possibility (1)--Threshold Potential = 20 kv

Possibility (2)--Threshold Potential = 800 kv.

In practice the threshold will lie somewhere between these two limits. If the radome is not coated with conductive paint, the threshold potential should be nearer that indicated by Possibility (1), and defective discharger strips will act as dischargers for the aircraft even under conditions of low charging. Noise should be heard in the VHF systems, therefore, even during periods when the engines are the sole charging source. If the radome is coated with conductive paint, the threshold should be near the value indicated by Possibility (2), and defective diverter strips will act as dischargers only at high charging rates. In this case, noise should occur in the VHF receiving systems only under conditions of high precipitation charging.

70

C.   SPACE-CHARGE-LIMITED DISCHARGES

1.   THEORETICAL RESULTS

As was indicated earlier, a problem which often arises in connection with precipitation static studies is that of estimating the current discharges from various parts of an aircraft. It is essential that the estimating procedure take into account the effect of the space charge in restricting discharge current and the effect of the wind in removing the space charge.

In Appendix E a solution is obtained for the current discharged from an infinite ion source placed along an edge of a charged conducting strip located in a windstream, as is indicated in Fig. 29(a). This model approximates very closely the conditions existing in the case of corona discharges occurring from the trailing edge of an airfoil in flight. It should be noted that placing an infinite ion source along the edge of the
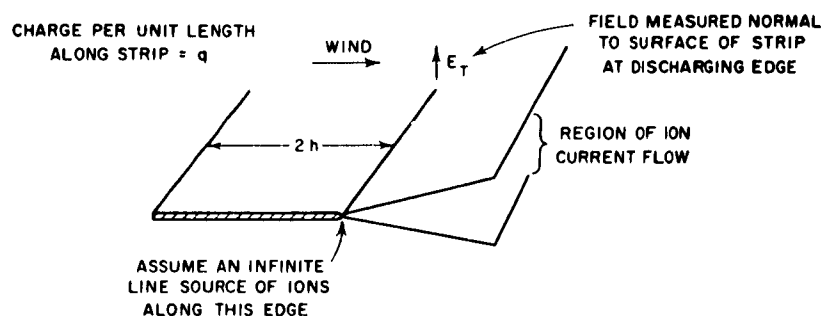
(a) MODEL USED FOR ANALYSIS
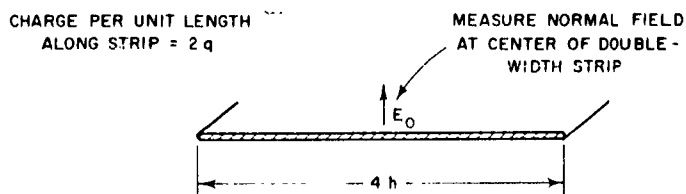
(b) TECHNIQUE FOR ESTIMATING FIELD AT AFT EDGE
OF DISCHARGE STRIP

RA- 2494-283

FIG. 29

ILLUSTRATION OF METHOD FOR DETERMINING CURRENT DISCHARGED
FROM EDGE OF STRIP IN WIND

71

strip used in the calculations is equivalent to assuming that the threshold potential of the trailing edge of an airfoil is zero. Since the threshold potential in fact is not zero, the numerical values obtained for the discharge current using the theoretical solution must be corrected to take into account the finite threshold potential.

The analysis indicates that the current discharged per unit length from the strip is given by

$$i \;=\; 2 \left(E^2 + \frac{W^2}{K^2} \right) \epsilon_0 K \; \tan^{-1} \frac{EK}{W} \tag{29}$$

where

W = wind velocity - meters/sec

ϵ_0 = dielectric constant - farads/meter

E = electric field intensity - volts/meter

K = ion mobility - meters/sec per volt/meter.

The electric field, E, as is illustrated in Fig. 29(a), is that existing at the edge of the strip in the direction normal to the plane of the strip when the discharge is in process. For the case where $W/K \gg E$,

$$\tan^{-1} \frac{EK}{W} \;=\; \frac{EK}{W}$$

and Eq. (29) may be reduced to

$$i \;=\; 2W\epsilon_0 E \tag{30}$$

which indicates that, at high speeds. the discharge current varies linearly with both wind speed and electric field. To calculate the current discharged from the strip, using either of the equations, it is necessary to devise a method for determining the value of E.

As is indicated in Appendix E, the field, E, existing at the edge of the discharging strip in Fig. 29(a) is the same as the normal field, E_0, existing at the center of a strip of twice the width and having twice as much charge per unit length [shown in Fig. 29(b)]. Using this result together with Eq. (29) it is possible to estimate discharge currents on the basis of laboratory measurements. For example, the width of an airfoil on a model may be doubled in the region where discharges occur, by attaching

72

a conducting tab at the aft edge as illustrated in Fig. 30. Then, using
the charge-separation techniques described in Appendix C, the field at the
junction may be measured and used to estimate the discharge current from
the airfoil.
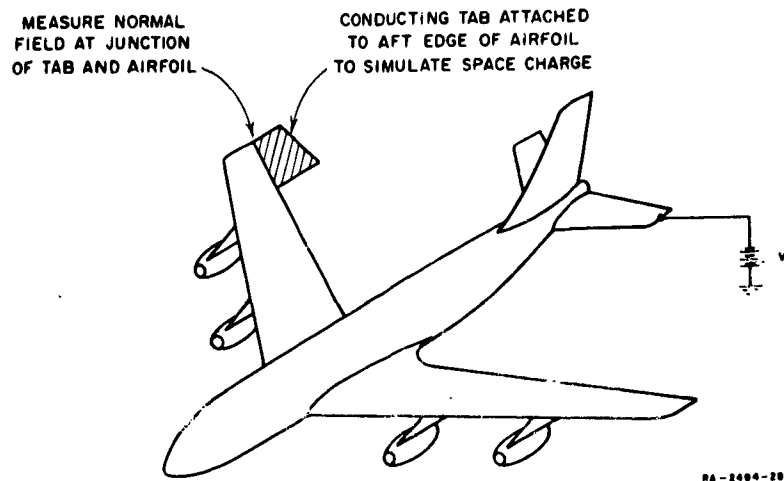
FIG. 30

CONDUCTING TAB USED TO SIMULATE EFFECT OF SPACE CHARGE

A similar analysis is carried through in Appendix E for the case
illustrated in Fig. 31(a) of space-charge-limited corona discharge from
the end of a cylinder. This problem is of interest since cylindrical
structures are commonly used as aircraft static dischargers. It is demon-
strated that the discharge current from the end of a cylinder is given by

$$i = WaE_a 2\pi\epsilon_0 \qquad (31)$$

where

$a =$ radius of cylinder

$E_a =$ field intensity

and where E_a is the normal field existing at the end of the rod when the
discharge is in progress, as indicated in the figure. In obtaining the
solution it was assumed that an infinite source of ions was placed at the
end of the cylinder. This is equivalent to assuming that the threshold
potential of the cylinder is zero. Since all practical dischargers have
a finite threshold potential, the values obtained using Eq. 31 must be

73

(a) MODEL USED FOR ANALYSIS

(b) TECHNIQUE FOR ESTIMATING FIELD
AT AFT END OF DISCHARGING CYLINDER

RA-2494-285
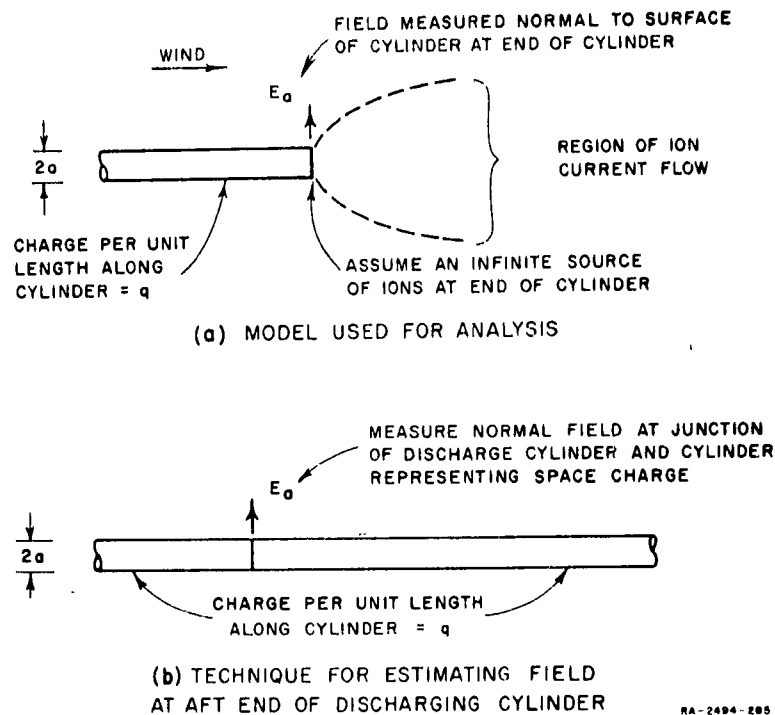
FIG. 31

ILLUSTRATION OF METHOD FOR DETERMINING CURRENT DISCHARGED
FROM END OF CYLINDER IN WIND

corrected. The required correction, however, is small when the discharge current is high and E_a is far above its corona threshold value.

To estimate the discharge current, therefore, it is necessary to devise a method for determining the value of the field, E_a. It is shown that, for discharge currents such that the fields about the rod are far above their threshold values, E_a may be determined by replacing the space charge by a conducting cylinder of radius, a, with a charge per unit length, q, and measuring the normal field at the junction of the discharger and the new conducting cylinder as is indicated in Fig. 31(b). These measurements may, of course, be made on an aircraft model provided the cylinders representing the dischargers and space charge are scaled.

2. WIND-TUNNEL VERIFICATION

In an effort to obtain experimental verification for the predicted behavior of space-charge-limited corona discharge in wind, two sets of wind tunnel tests were undertaken. In the first set of tests, discharges

74

from the trailing edge of an airfoil section were studied using the 7-by-10-foot wind tunnel at Ames Aeronautical Laboratory, Moffett Field, California. The second set of tests, to study discharges from cylinders, was conducted in the 4-inch-diameter dust tunnel at Stanford Research Institute.

A photograph of the test set-up used for the airfoil discharge tests is shown in Fig. 32. The airfoil section was insulated from ground and connected to a 0-to-100-kv power supply. Provisions were made to record the applied voltage and the current discharged from the airfoil.
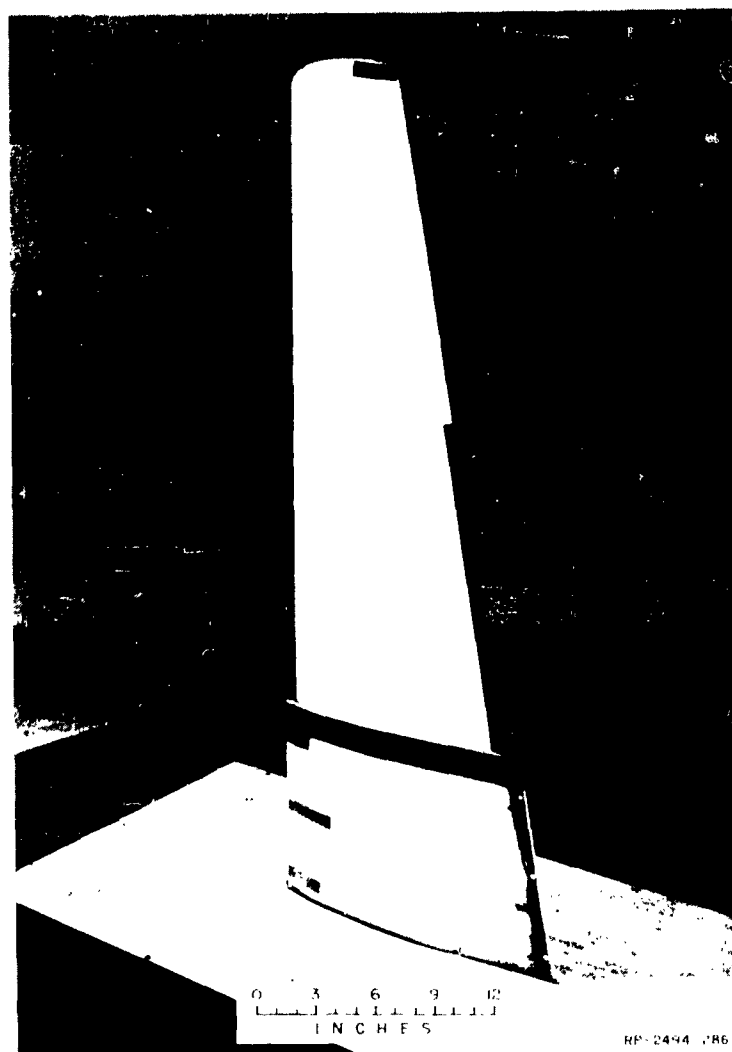
FIG. 32

SET-UP USED FOR WIND-TUNNEL TESTS OF DISCHARGE
FROM AIRFOIL

75

Before undertaking the wind-tunnel tests, however, a scaled mock-up
of the wind tunnel and airfoil was assembled in the laboratory and used
to make a set of electric-field measurements which were used together with
Eq. (29) to predict the currents which should be discharged from the
airfoil in the wind tunnel. With a known voltage applied between the
airfoil mock-up and the walls of the wind-tunnel model the electric-field
intensity was measured at the junction of the airfoil and a conducting tab
(simulating the presence of space charge) attached to the trailing edge
in the manner illustrated in Fig. 30. The results of this measurement,
properly scaled, indicate the relationship between the applied voltage in
the tunnel and the magnitude of the electric field at points along the
trailing edge of the discharging airfoil. A plot of the field intensity
(per volt applied to the airfoil in the wind tunnel) along the 18-inch
interval in which the discharge was permitted to occur is shown in Fig. 33.
It is apparent that there was considerable variation in field intensity
along the discharging region of the airfoil. For this reason this region
was divided into ten equal intervals for each of which the average field
was determined as is indicated in the figure. These values of field
intensity were substituted into Eq. (29) and the current discharged by each
1.8-inch-long interval was determined. The total current discharged from
the airfoil was found by summing the currents from the ten intervals. The
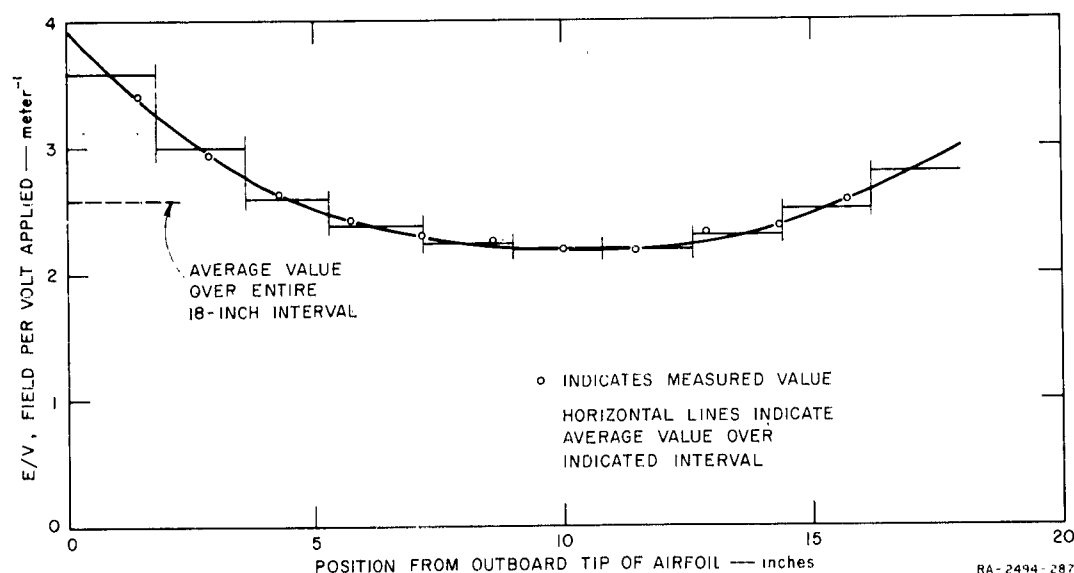
FIG. 33

MEASURED FIELDS ALONG DISCHARGING REGION OF AIRFOIL IN TUNNEL

76
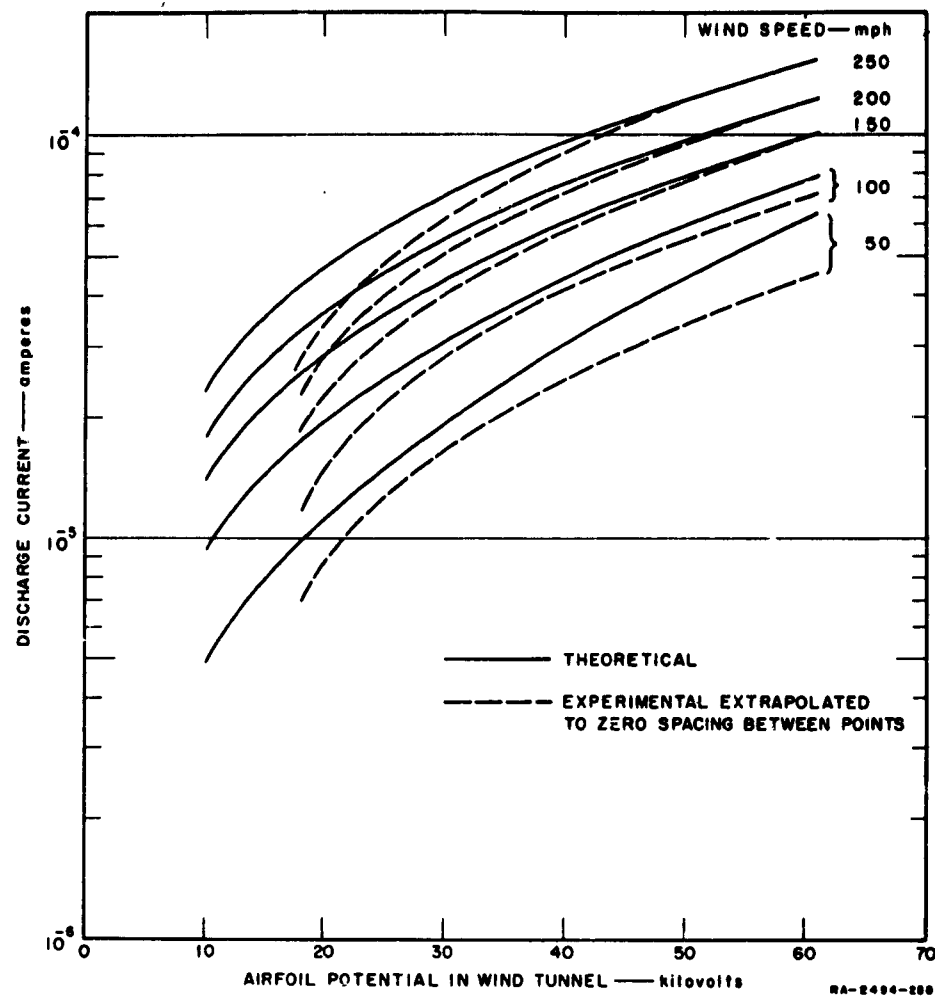
FIG. 34

DISCHARGE FROM 18-INCH SECTION OF AIRFOIL IN WIND TUNNEL

results of this calculation are shown by the solid curves in Fig. 34.
(The significance of the broken curves will be discussed later.)

Since the process of calculating the discharge currents from the ten
1.8-inch-long intervals along the trailing edge of the airfoil is tedious,
a simpler technique was tried. In this method, the average value of E/V
for the entire 18-inch interval along the airfoil was determined from
Fig. 33 and substituted into Eq. (29). The currents calculated in this
manner were imperceptibly different from those calculated using the longer
method. Under normal circumstances, therefore, much time will be saved
and little accuracy lost if one uses the average value of E/V over the
entire discharging interval in computing discharge current.

77

The wind-tunnel tests were planned to permit the investigation of several different aspects of the problem of corona discharge from the edge of a strip. In the first set of tests the objectives were to verify the theoretical predictions and to investigate the effect upon the discharge current of varying the number of points per unit length along the edge of the strip from which discharges could occur. (This latter information is of interest in the design of flush-mounted dischargers.) In these tests, 0.005-inch-diameter wires (not visible in Fig. 32) were attached at regular intervals along the outboard 18-inch section of the trailing edge of the airfoil in such a manner that a ¼-inch length of the wire protruded past the trailing edge. The discharge points made of fine wire were used to reduce the corona threshold of the airfoil to the lowest possible value in order that it approach as nearly as possible the condition of zero threshold potential assumed in deriving Eqs. (29) and (30). Tests were conducted with spacing of ½, 1, 2, and 4 inches between adjacent discharger wires. The results of the tests with the ½-inch and 1-inch spacings are shown in Fig. 35. It is evident that decreasing the spacing between discharger wire increased the discharge current. The increase, however, was small. Doubling the number of discharger points increased the current discharged by only ten percent.

To better illustrate the manner in which discharge current varies with spacing between discharger wires, the wind-tunnel data were replotted in the form illustrated in Fig. 36. Here, for a particular windspeed and various applied voltages, the discharge current is plotted as a function of wire spacing. From the figure it is evident that throughout the range of spacings used in the tests, very little is gained by doubling the number of discharging points. This result is very reasonable if one considers the fact that the current from a particular discharge point is limited by the region of space charge aft of the point. Thus if one doubles the number of discharge points, the number of corona discharges will be doubled. The space charge generated by the current leaving from the new points, however, will reduce the field intensity at the locations of the old points, thereby reducing the current leaving via the old points. The net result is only a slight increase in discharge current.

It will be observed that the curves of Fig. 36 are extrapolated to zero wire spacing. This was done for each windspeed, and the zero-spacing data used to plot the broken curves in Fig. 34. (It will be recalled that, in obtaining the theoretical discharge current data in Fig. 34, it was
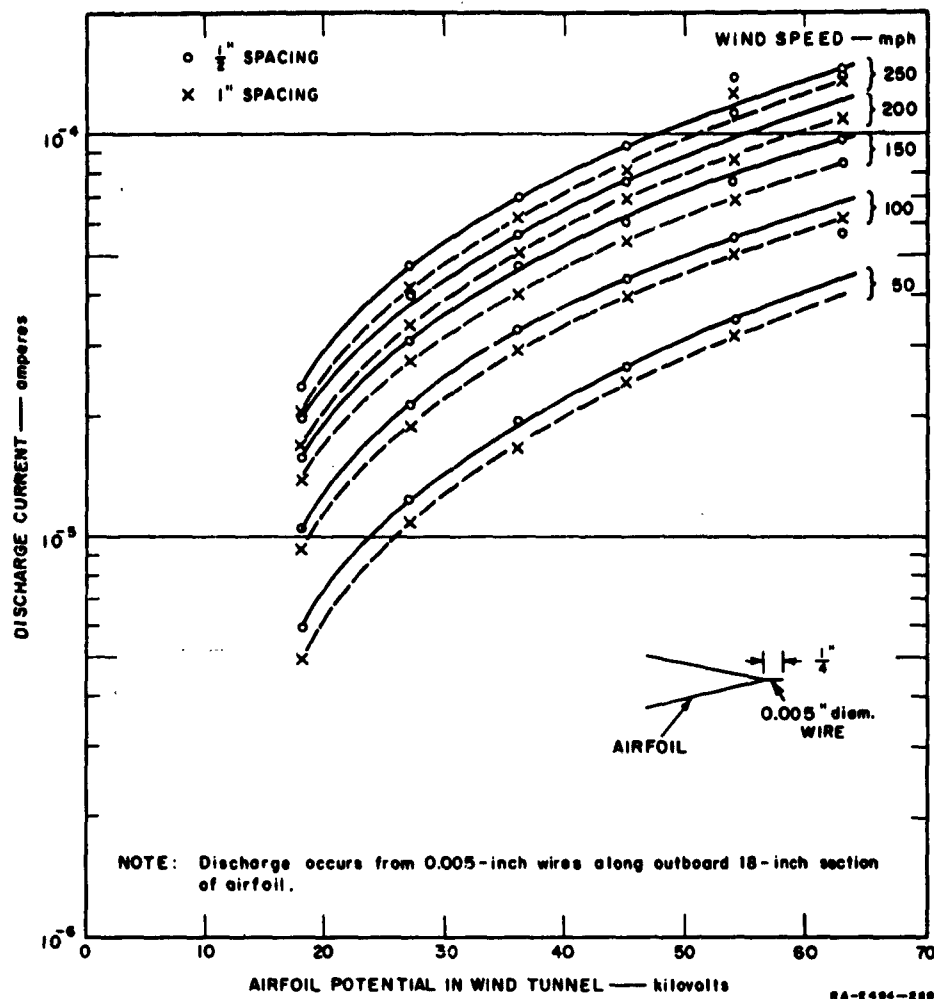
FIG. 35

DISCHARGE CURRENTS MEASURED IN WIND TUNNEL

assumed that the discharge was continuous along the trailing edge.) Upon comparing the two sets of curves in Fig. 34 it is evident that, in general, they agree very well at high airfoil potentials, but that the measured current is lower than the predicted current at the lower potentials. This disagreement stems from the fact that the theoretical expression for discharge current is based upon the assumption that the corona threshold is zero, whereas the threshold of the airfoil with the 0.005-inch-diameter wires actually is roughly 8 kv.

Another set of tests was conducted to investigate the effect upon the discharge current of changing the location of the discharge points. (This

information is of interest in the design of flush-mounted dischargers.)
In these tests the 0.005-inch-diameter wires used earlier were replaced
with sewing needles spaced two inches apart. For the first tests the
needles projected aft from the trailing edge of the airfoil as is shown
in the upper sketch of Fig. 37 (Configuration A). The solid curves in the
figure represent the data obtained with this configuration. Except for a
somewhat higher threshold potential, these data are the same as those
obtained with the 0.005-inch-diameter wires.

Next, the sewing needles were moved to a position ½-inch forward of
the trailing edge and positioned at right angles to the airfoil surface,
as indicated in the lower sketch of Fig. 37 (Configuration B). (This is
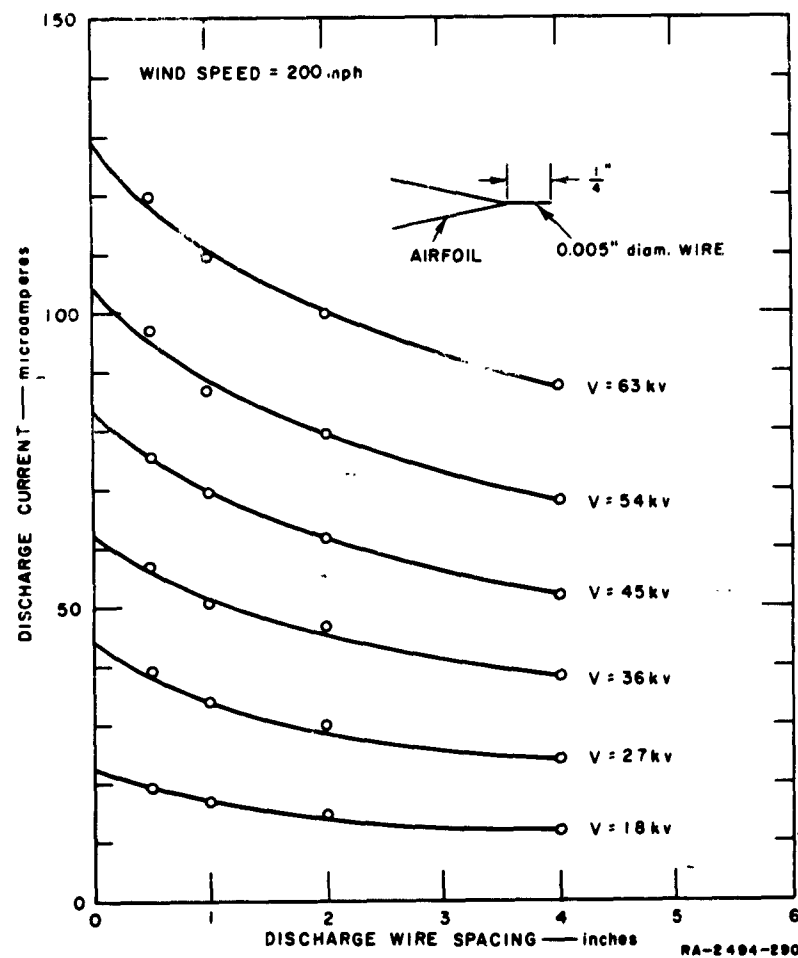
FIG. 36

VARIATION OF DISCHARGE CURRENT WITH DISCHARGER WIRE SPACING

80
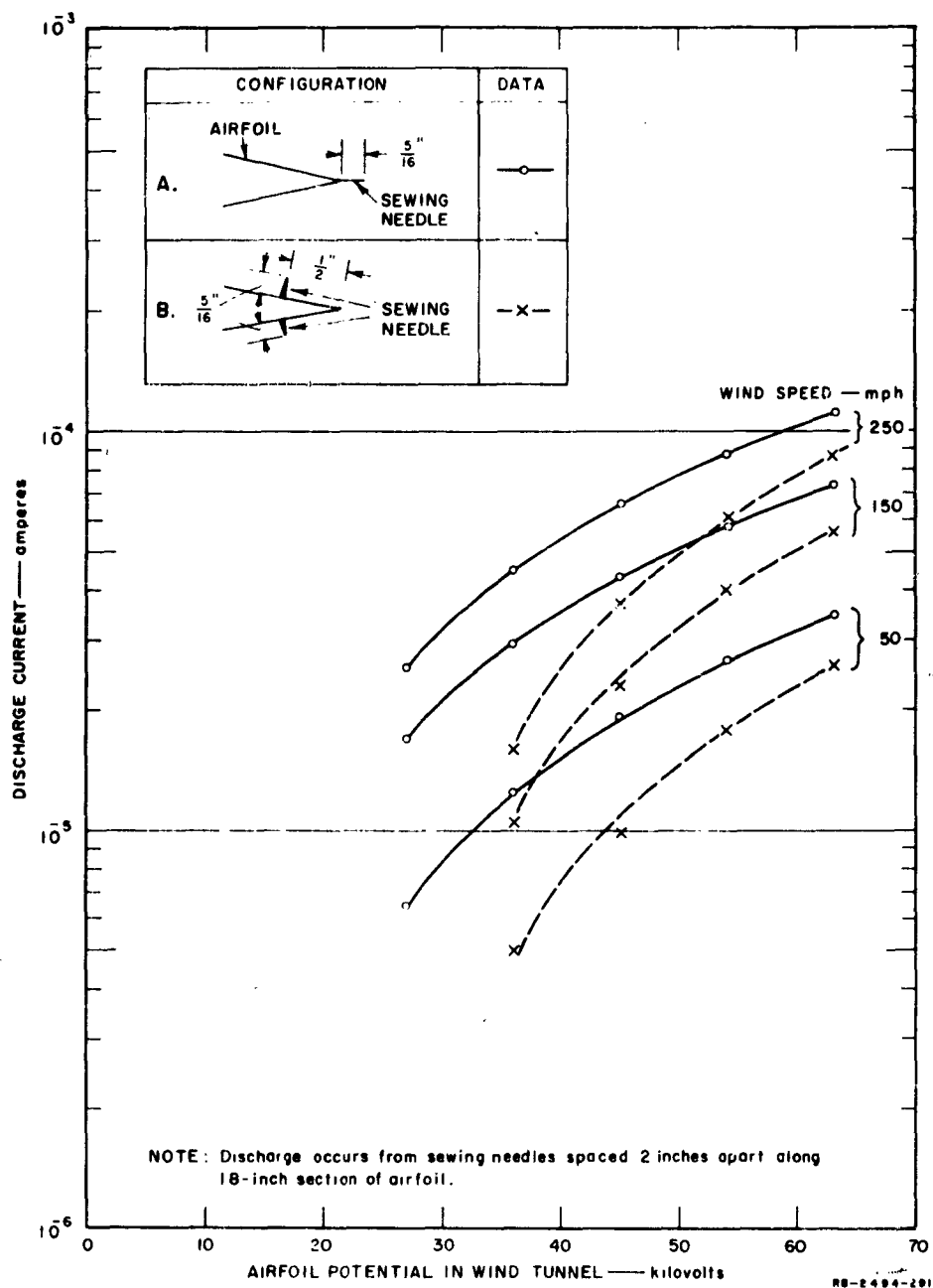
FIG. 37

EFFECT UPON DISCHARGE CURRENT OF POSITION OF DISCHARGE PIN

81

the general configuration of the discharge pins on the flush-mounted ortho-decoupled discharger discussed in Sec. VIII-B.) The data obtained with Configuration B are shown by the broken curves in Fig. 37. It is evident that moving the pins to the new location increased the corona threshold considerably. At the higher applied potentials, however, the discharger current is reduced by only roughly 30 percent. It was concluded, therefore, that Pin Configuration B would be satisfactory for use in a flush-mounted discharger.

As was indicated earlier, a set of wind tunnel tests was conducted to study discharges occurring from the end of a cylinder. Unfortunately, perhaps because of the small size of the wind tunnel used, the results of these tests were not satisfactory. For this reason, these tests will not be discussed. As will be indicated later, the theory regarding discharges from cylinders was verified during flight tests in which current leaving rod-shaped dischargers mounted on the airfoils was monitored.

D. DISCHARGE DISTRIBUTION FOR A TYPICAL AIRCRAFT

1. UNMODIFIED AIRCRAFT

The success with which the field measurements on the laboratory model, used together with Eq. (29), predicted the discharge currents from the airfoil in the wind tunnel indicated that it should be possible to use a similar technique to obtain reasonably accurate estimates of the manner in which the discharge current distributes itself among the various discharging extremities on an aircraft.

Before attempting to devise a scheme to determine the discharge-current distribution, it will be of interest to consider some of the relationships which must exist on an aircraft on which corona discharges are occurring. As the aircraft potential is raised from zero, corona will first occur at the airfoil extremities where the electric fields are highest. As the potential is raised further the fields at the outboard sections of the trailing edges of the airfoils will reach threshold value and discharges will occur from them. If the potential is raised still further, the discharge will move further inboard along the airfoil. Thus, we will find that at the inboard limit of the corona-discharge region on each airfoil, the field intensity equals the corona-threshold value. Since the structure of all airfoil trailing edges on a given aircraft is generally quite similar, the fields at the inner limits of discharge will be the

82

same on all airfoils, and the discharge current per unit length at this position will be the same for all airfoils. Furthermore, the discharge current per unit length on all airfoils will increase as the outboard tip is approached.

If one now assumes that the manner in which the discharge current varies with position within the discharge region is the same for all airfoils (position expressed in units of discharge extent on that airfoil), then the current discharged from an airfoil is directly proportional to the linear extent of the discharge along that airfoil. Although this assumption is not strictly valid, the error it introduces is smaller than that caused by other factors such as the presence of charged precipitation particles surrounding the aircraft, which cannot be properly taken into account in the laboratory. Thus, the discharge-current distribution may be estimated by using a charged model of the aircraft equipped with devices to simulate the space-charge clouds aft of the airfoils. The extent of the space-charge cloud along each airfoil should be adjusted until equal field intensities are measured at corresponding points along the trailing edge in the region of discharge on each airfoil. For example, the field might be measured at the center of the region of discharge on each airfoil. The fraction of the total current discharged by a particular airfoil is given by the transverse extent of space-charge cloud along that airfoil divided by the total extent of space-charge cloud used on the model.

Measurements of this sort were carried out in the laboratory to investigate discharge current division on the Boeing 367-80 aircraft used in the flight tests conducted on Contract AF 33(616)-3914.[10] A $\frac{1}{50}$-scale model of the aircraft was suspended in the laboratory and connected to a high-voltage power supply. Tabs of metal simulating the space charge were attached to the trailing edges of all airfoils in a manner similar to that illustrated for the wing in Fig. 30. The field at the center of each tab along the junction with the trailing edge was measured, and the width of the tabs was adjusted until equal field readings were obtained on all airfoils.

Actually, conducting tabs do not produce an accurate representation of the fields in the region of discharge along an ordinary airfoil. Reference to Fig. 33 indicates that, with a conducting tab, the field in the discharge region is maximum at the ends and minimum in the middle. This situation will exist if the discharging region is treated (as by the addition of the fine wire discharge points in the wind tunnel experiments)

to have a much lower threshold than the remainder of the airfoil edge. To represent the conditions about an ordinary airfoil in corona, however, the field should be minimum at the inboard limit of the discharge. The difference stems from the fact that Fig. 33 represents the field conditions which exist when the discharge is restricted to a given region along the airfoil as it was by the discharger wires in the wind tunnel experiments. (In this case the field intensity at the inboard limit of the discharge region can be far above the threshold field intensity in the treated discharging section, so that it is possible for E to decrease as one moves outboard and still not drop below threshold field in this region.) The effect of the tabs, however, is to reduce the field intensity along the trailing edges as would space charge. Furthermore, the same sort of error inherent in using tabs to represent space charge exists on all of the airfoils so that errors from this source tend to cancel one another. The discharge distribution determined using the tabs, therefore, should be representative of that existing in flight.

It was found from the laboratory measurements that equal field readings were obtained on all the airfoils on the $\frac{1}{60}$-scale model when tabs of the following widths were attached to the airfoils indicated:

> Each wing tab = 3 inch
>
> Each elevator tab = 1.5 inch
>
> Rudder tab = 1.5 inch.

These results indicate that the discharge current should divide among the airfoils as follows:

> Current from wings = 4/7 = 57.2% of Total
>
> Current from elevators = 2/7 = 28.5% of Total
>
> Current from rudder = 1/7 = 14.3% of Total.

It was not possible to measure the distribution of discharge current on the unmodified aircraft. During the flight-test evaluation of the flush-mounted decoupled discharger system, however, provisions were included to measure the current leaving the dischargers incorporated into the trailing edges of the wings, and the data obtained during these tests provided a rough check on the current distribution.[10] Since the dischargers were installed on all of the airfoils and since the corona threshold of a discharger-equipped airfoil was only slightly lower than the threshold of a normal airfoil, the discharge data obtained during these tests should

be representative of the conditions which would exist on the unmodified
aircraft. The dischargers, furthermore, occupied a considerable extent
of the outboard portion of each airfoil (12 feet on the wing, for example)
so that at normal charging rates it is certain that nearly all of the
current left via the dischargers.

Listed in Table III are typical measured discharge currents from the
wings and the total charging currents calculated using the methods of
Sec. IV-B. In view of the indirect procedure used to determine total
charging current, its value may not be accurate. It is not unreasonable,
therefore, that there should be considerable scatter in the experimental
values obtained for the fraction of the current leaving from the wings.
The values listed in the table, however, are of the same order of magnitude
as the percentage indicated by the results of the laboratory measurements.

TABLE III

COMPARISON OF CALCULATED TOTAL DISCHARGE CURRENT
WITH MEASURED DISCHARGE CURRENT FROM WINGS

FLIGHT DATE	RECORD NO.	ALTITUDE (feet)	A_a CALCULATED INTERCEPTION AREA (sq ft)	I_p MEASURED CHARGING RATE (μamp/ft^2)	$I_T = A_a I_p$ CALCULATED TOTAL CHARGING CURRENT (μamp)	I_W MEASURED DISCHARGE CURRENT FROM WINGS (μamp)	$I_W/I_T \times 100$ PERCENT OF CURRENT DISCHARGED FROM WINGS
3/27/59	1320	18,500	53.0	3.64	193	78.8	40.8
3/27/59	1322	18,500	53.0	4.85	257	111	43.3
3/27/59	1328	18,500	53.0	10.4	561	204	36.3
3/27/59	1330	18,500	53.0	9.92	526	204	38.3
3/27/59	1371	22,700	40.2	2.75	111	55.6	50
3/27/59	1373	22,700	40.2	3.08	124	55.6	44.7
3/27/59	1375	22,700	40.2	7.59	306	130	42.5
3/27/59	1377	22,700	40.2	6.65	268	125.4	46.8
4/ 1/59	18465	33,400	33.3	2.85	95.0	51.0	53.7
4/ 1/59	18469	33,100	33.3	2.50	83.2	41.8	50.2
4/ 1/59	18472	32,900	33.3	3.55	118.5	69.6	58.7
4/ 1/59	18475	32,700	33.3	2.50	83.2	41.8	50.2

A closer examination of the data in the table indicates that the
percentage of current discharged from the wings tended to decrease as the
total charging current increased. One explanation for this observed result
offers itself if one notes that the threshold potential of the wings is
lower than the thresholds of the empennage airfoils. Thus, if the charging
rate started at zero and were slowly increased, one would find that at
first the wings discharged all of the current. Then as the aircraft

85

potential exceeded the thresholds of the empennage airfoils, they would
begin to discharge an increasing fraction of the total current as the
charging rate and potential increased. At high charging rates, the dis-
charge distribution should approach that indicated by the laboratory
measurements.

Another factor which can influence discharge distribution at the
higher charging rates is the sheath of positively charged precipitation
generated by the aircraft. Most of the charged precipitation is generated
near the fuselage, while negative charge is discharged from the extremities.
Thus, although the net charge in the region aft of the aircraft is zero
(assuming steady conditions in which charging current must equal discharge),
and the various charged particles existing at distances of the order of
an airplane length aft of the aircraft will produce no influence on the
aircraft fields; in the immediate vicinity of the aircraft, the positive
charge in the precipitation sheath will influence fields on the aircraft
to a greater extent than will the negative charge which is further removed.
In particular, the sheath of positive precipitation will tend to enhance
the fields at the empennage of the aircraft and increase the proportion
of current discharged from the empennage airfoils. If the charge generated
in one airplane length of precipitation is only a small fraction of the
airplane charge, its effect upon the airplane fields will, of course, be
small. If, however, the charge in an airplane length of precipitation is
an appreciable fraction of the airplane charge, it will have a significant
effect upon the field structure about the airplane.

Let us consider, for example, a KC-135 aircraft flying at 250 meters
per second at 20,000 ft. altitude in light precipitation such that the
total charging rate is 100 μamp. At this charging rate the aircraft
potential will be roughly 125 kv, which is only slightly above threshold
potential. Since the aircraft capacitance is roughly 1000 $\mu\mu$f, the total
charge, Q, on the aircraft is

$$Q = C_a V$$

$$= 1.25 \times 10^{-4} \text{ coulomb} \quad .$$

At the given charging current and aircraft speed the line-charge density,
σ, in the precipitation column will be

$$\sigma = i/v$$

$$= 4 \times 10^{-7} \text{ coulomb/meter} \quad .$$

Since the airplane is roughly 36 meters long, the charge in one airplane length of precipitation is 1.44×10^{-5} coulomb, which is 12 percent of the charge on the airplane. At this charging rate, therefore, the discharge current distribution should not be seriously affected by the sheath of charged precipitation.

If the charging current is now raised to one milliampere the airplane potential will rise to roughly 250 kv, resulting in an airplane charge of 2.5×10^{-4} coulomb. The charge per airplane length of precipitation is now 1.44×10^{-4} coulomb, which is roughly 60 percent of the charge on the airplane. In this case the discharge distribution should be altered appreciably by the charged precipitation.

This sort of change in distribution was observed during flight tests conducted with rod-shaped retrofit dischargers installed on the airfoil trailing edges. The results of these tests will be discussed in the next section.

2. AIRCRAFT EQUIPPED WITH DISCHARGERS

A very common physical configuration used for aircraft static dischargers is a rod of conducting material attached to the trailing edge of an airfoil with the axis of the rod directed along the airstream. This is the general form of the AN/ASA-3 discharger and of the retrofit ortho-decoupled discharger discussed in Sec. VIII-C. An attractive feature of this design is that the conducting rod concentrates even further the high fields existing near the airfoil extremities so that the corona threshold potential of the dischargers can be made extremely low--an important consideration in a discharger installation. For this reason rod-shaped dischargers will certainly continue to be used on aircraft, and it was important that an investigation should be made into their discharging capabilities.

Illustrated in Fig. 31 is a method by means of which it is possible to predict the current that would be discharged from a rod of zero threshold potential. In this method the presence of space charge aft of the discharger is simulated by attaching to the end of the discharger a conducting cylinder

87

whose diameter equals that of the discharger. Actually, since the threshold of a practical discharger is not zero, it is apparent that, at low potentials particularly, the charge per unit length in the space-charge region will be lower than at the surface of the discharger. This effect is illustrated in Fig. 34, in which the measured discharge currents at low potentials fall below the values predicted on the basis of zero threshold potential. To adequately simulate this situation one would have to devise a structure such as a series of short isolated cylinders which could be given a charge of the proper magnitude and positioned aft of the discharger rod. The laboratory procedures involved in a simulation of this sort would of course be very tedious. To save time, therefore, it was noted that when the potential is far above threshold very little error will result from using "space charge cylinders" of the same diameter as the discharger rods. Since the problem of primary concern is generally the discharging capability of the system under conditions of high charging, no effort was made to develop a laboratory technique suitable for low-current conditions.

Details of the technique used to estimate currents leaving dischargers at various locations on an aircraft are illustrated in Fig. 38. In essence, brass rods simulating the dischargers and space charge were attached to the trailing edge of a $\frac{3}{8}$-scale model of an airfoil tip. The field measured at the point representing the junction of a discharger and its "space charge" was used in Eq. (31) to compute the current leaving via that discharger. To permit the computed discharger currents to be related to an aircraft potential, the field at a reference point on the airfoil tip model was measured. A field measurement was also made at the same reference point, appropriately scaled, on each of the airfoils on a $\frac{1}{50}$-scale model of the flight-test aircraft suspended in the laboratory and charged to a known potential.

Although they are not illustrated in Fig. 38, the airfoil tip model was surrounded with a set of guard rings and equipotential surfaces in order that the fields about the model duplicate as nearly as possible the fields existing about the airfoil on the aircraft. To check the accuracy with which the fields were duplicated, systematic measurements were made of the fields at various points on the wing-tip model. Field measurements were made at corresponding points on the $\frac{1}{50}$-scale airplane model. The two sets of field measurements were in good agreement, indicating that the fields on the wing-tip model accurately duplicated those existing on the aircraft.

REFERENCE POINT

REFERENCE POINT

$\frac{1}{50}$-SCALE MODEL SUSPENDED IN LABORATORY

V = 4 kv

ALUMINUM SHEET, $\frac{3}{8}$-SCALE MODEL OF AIRFOIL TIP

REFERENCE POINT

16.5"

24.6"

SIMULATES DISCHARGER ROD

MEASURE FIELD AT THIS POINT

SIMULATES SPACE CHARGE

#6

#5

#4

#3

2"

15"

#2

#1

$\frac{3}{32}$ diam. BRASS RODS

FULL-SCALE DISCHARGER diam. = $\frac{1}{4}$"

RA-2494-292
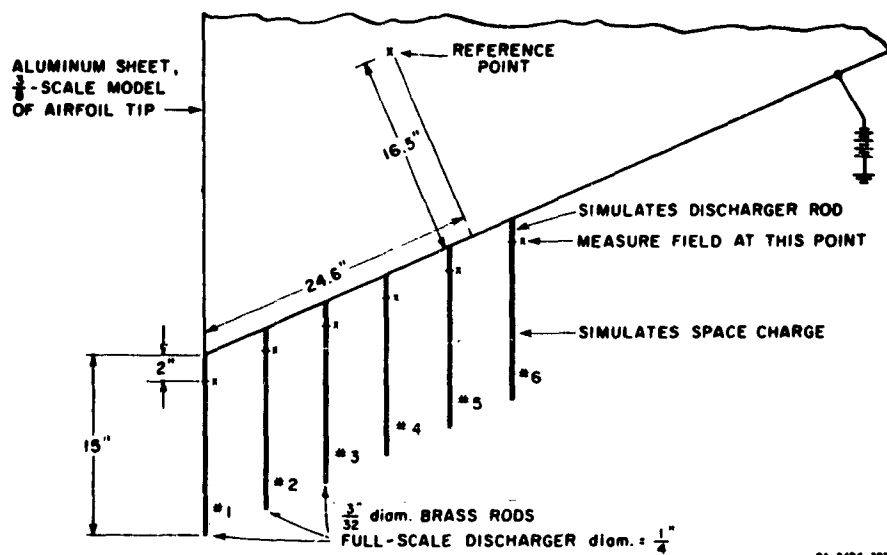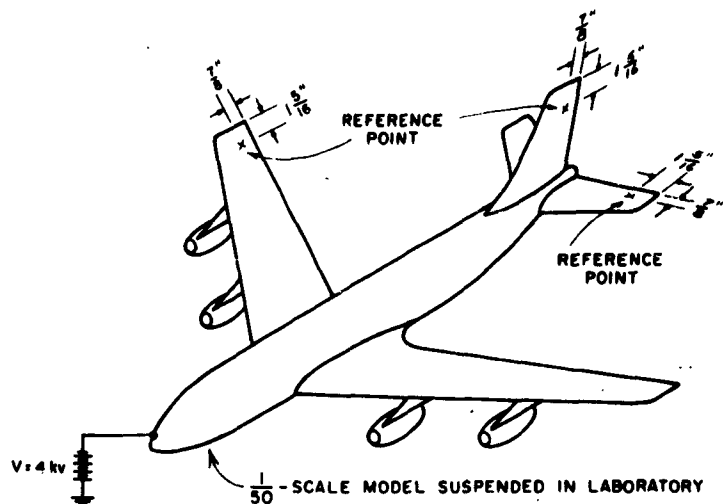
FIG. 38

ILLUSTRATION OF LABORATORY TECHNIQUE FOR ESTIMATING CURRENT LEAVING DISCHARGERS

89

An important question which arose in connection with the assembly of
the mock-up was how long the conducting cylinders should be made to ade-
quately represent the space charge. This problem was investigated by
measuring the radial fields near the ends of the modeled discharger rods
as the length of the cylinders representing the space charge was varied.
It was found that extending the cylinders beyond a length of 13 inches had
very little effect upon the measured fields. For this reason the space-
charge cylinders used in the laboratory discharge-current investigation
were 13 inches long.

To further clarify the method by which the discharge currents were
determined, a typical set of measurements will be described in detail.
First, a $\frac{1}{50}$-scale model of the flight-test aircraft was suspended in the
laboratory and charged to a potential of 4 kv as illustrated in Fig. 38.
Using the charge-separation techniques described in Appendix C, a measure-
ment was made of the normal field at each of the reference points located
on the wing, rudder, and elevator. In the case of the wing, it was found
that the field intensity at the reference point was 52.9 kv/meter. On
the full-scale aircraft charged to a potential of 1 kv, therefore, the
reference-point field intensity will be

$$E_{ref} = \frac{52.9}{4(50)} = 0.264 \text{ kv/meter} \quad .$$

The reference-point fields on the other airfoils were found in the same
manner. Thus, on the full-scale aircraft, the reference-point field
intensities are:

$$E_{wing} = 0.264V \quad \text{kv/meter}$$

$$E_{rudder} = 0.163V \quad \text{kv/meter}$$

$$E_{elevator} = 0.213V \quad \text{kv/meter}$$

where V is the airplane potential in kilovolts.

Next, the $\frac{3}{8}$-scale model of the airfoil tip was charged to a con-
venient potential, and measurements were made to determine the relationship
between the reference-point field intensity and the radial field near the
end of a discharger. (This same relationship will exist on the full-scale
aircraft.) With the particular potential used in the laboratory, it was

found that E_1, the field at the first discharger (farthest outboard), was 283 kv/meter when E_{ref}, the field at the reference point, was 6.78 kv/meter. Thus, for No. 1 discharger,

$$E_1/E_{ref} = \frac{283}{6.78}$$

$$= 41.2 \quad .$$

Now, using the results of the $\frac{1}{50}$-scale model reference-point field measurements we can say that on the full-scale aircraft the surface-field intensity near the end of No. 1 discharger on the wing will be

$$41.2(0.264)V = 10.9V \quad kv/meter$$

$$= 10,900V \quad volts/meter \quad .$$

Similar measurements were carried out for each of the other dischargers on the airfoil.

The values obtained above for the discharger surface fields were substituted into Eq. (31) to predict the current leaving via each of the dischargers on the wing. In evaluating the equation, the values of the parameters were chosen to correspond to the conditions existing on the aircraft during a period of charging encountered during the last flight test using the Boeing 367-80 aircraft. These were

$$W = 435 \text{ mph} = 194 \text{ meters/sec}$$

$$2a = \frac{1}{4} \text{ inch} = 6.35 \times 10^{-3} \text{ meter} \quad .$$

Thus, for No. one discharger on the wing, the predicted discharge current is

$$i = (194) \frac{6.35 \times 10^{-3}}{2} (10,900) \frac{2\pi}{36\pi \times 10^9} V$$

$$= 0.375V \quad microamperes$$

where V is the full-scale airplane potential in kilovolts. Calibration factors were computed also for the remaining dischargers on the airfoil and are listed in Table IV.

91

TABLE IV

COMPARISON OF PREDICTED DISCHARGE CURRENTS FROM
DISCHARGERS ON WING WITH MEASURED CURRENTS

DISCHARGER NUMBER	CURRENT CALIBRATION FOR V = 435 mph (μa)	V = Airplane Potential = 286 kv V = 435 mph, $2a$ = ¼-inch		
		Predicted Current (μa)	Measured Current (μa)	$\dfrac{i_{meas}}{i_{predict}}$
1 (Outboard)	i = 0.375V*	108.0	116.5	1.08
2	i = 0.215V	61.5	69.5	1.13
3	i = 0.184V	52.6	estimated (63)	(1.20)
4	i = 0.175V	50.1	67.2	1.34
5	i = 0.178V	51.0	estimated (79)	(1.58)
6 (Inboard)	i = 0.197V	56.4	98.8	1.75
Total Current from Above Dischargers		379.6	494.0	1.30

*V is the airplane voltage in kilovolts.

Listed in the same table are the discharger currents predicted on the
basis of these laboratory measurements for an airplane potential of 286 kv.
The validity of this laboratory technique is demonstrated when the pre-
dicted currents are compared to the measured discharger currents (also
listed in the table) obtained in flight at 286 kv potential on the
Boeing 367-80 aircraft. Excellent agreement between predicted and measured
currents was obtained for the dischargers near the outboard end of the
wing. The range of aircraft potential over which the laboratory predic-
tions were valid is illustrated in Fig. 39 in which measured data read
from three widely separated regions of the flight record obtained on the
last test using the Boeing 367-80 aircraft are compared to predicted
discharge currents for dischargers No. 1 and No. 2. The measured currents
from the inboard dischargers, however, were somewhat higher than the
laboratory investigation predicted. This result is not unexpected since,
although the laboratory mock-up included provisions for simulating the
effect of the negative space charge cloud to the rear of the dischargers,
no provisions were made to simulate the cloud of positively-charged pre-
cipitation particles to the rear of the wing. In flight through precipi-
tation, therefore, the positively-charged particles will tend to raise the
fields at the dischargers to values higher than those indicated by the
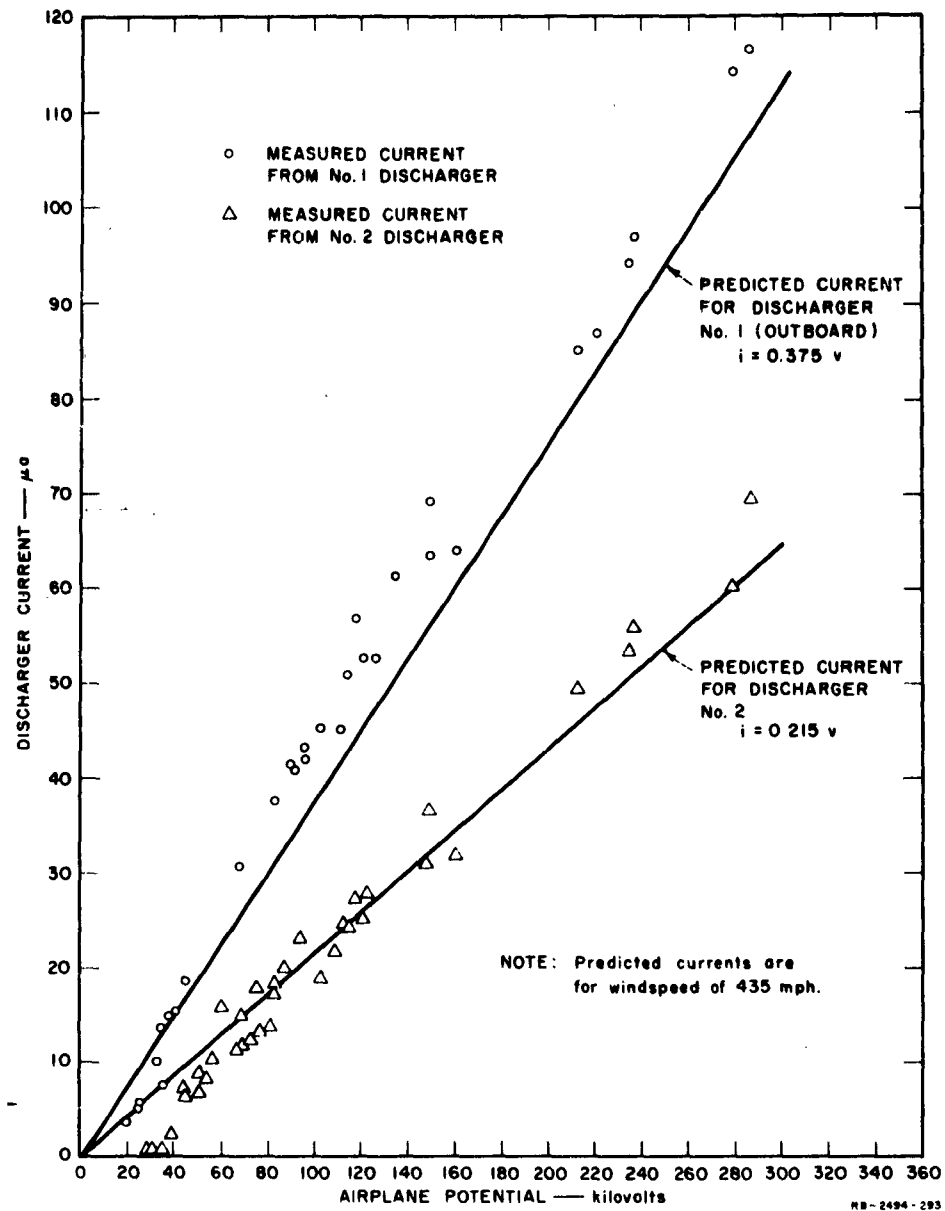
FIG. 39

COMPARISON OF PREDICTED AND MEASURED CURRENTS FROM WING
TRAILING-EDGE DISCHARGERS

93

laboratory measurements. Thus, the currents measured in flight should be
higher than the predicted currents. Since the outboard dischargers are
shielded from the positive particles by the negative ion cloud, however,
the current from them should be only slightly higher than that predicted
from the mock-up measurements. In spite of the above shortcomings of this
method it should be observed that it was possible, using nothing more
elaborate than a few brass rods, a sheet of aluminum and an inexpensive
$\frac{1}{50}$-scale model of the aircraft to predict with an error of only 30 percent
the absolute magnitude of total current leaving the dischargers on a
particular airfoil on an aircraft. The poorest estimates of the individual
discharger currents, furthermore, were only slightly less accurate.

Using the appropriate number of dischargers on the $\frac{3}{8}$-scale mock-up
together with the reference-point field intensities measured on the rudder
and elevator it was possible to predict the total current leaving from the
dischargers on these airfoils. For the configuration of dischargers used
on the trailing edge of the rudder during the flight tests on the
Boeing 367-80 and QANTAS 707,[14,18,19] for example, the laboratory measurements
indicated that the currents should be given by

$$i_1 \text{ (outboard)} = 0.266V \quad \mu a$$

$$i_2 = 0.152V \quad \mu a$$

$$i_3 \text{ (inboard)} = 0.167V \quad \mu a$$

where V is the airplane potential in kilovolts. Unfortunately, on all
of the flight tests in which provisions were included to record airplane
potential the current leaving the empennage dischargers was not monitored,
so that the expressions for rudder current in terms of airplane voltage
cannot be verified directly. However, for a given airplane potential--
in other words, for a given time in flight--the results of the laboratory
tests indicate that the current leaving No. 1 discharger on the wing
should be related to the current leaving No. 1 discharger on the rudder by

$$\frac{i_{1 \text{ wing}}}{i_{1 \text{ rudder}}} = \frac{0.375V}{0.266V}$$

$$= 1.41 \quad .$$

During the QANTAS tests the currents leaving these two dischargers were recorded. During periods of engine charging shortly after take-off, it was found that

$$\frac{i_{1\ wing}}{i_{1\ rudder}} = \frac{60\ \mu a}{44\ \mu a}$$

$$= 1.36$$

which is in good agreement with the predicted ratio of currents.

On flights through precipitation with the same current leaving the wing, it was found that the current leaving the tail increased until

$$\frac{i_{1\ wing}}{i_{1\ rudder}} = \frac{60\ \mu a}{72\ \mu a}$$

$$= 0.84 \quad .$$

This result indicates that in precipitation charging the field at the empennage of the aircraft is enhanced by the factor $^{72}/_{44} = 1.63$ as the result of the positive sheath formed near the fuselage of the aircraft. This sheath is composed of particles that have given up negative charge upon impact with the forward part of the aircraft.

The results of the rudder-discharger current measurements were combined with the detailed measurements of wing-discharger current to obtain an empirical expression for the total discharge current, I_d, expressed as a function of the No. 1 wing-discharger current:

$$I_d = 2I_{w_1} + 3.17 \times 10^{-5}\ I_{w_1}^2 \tag{32}$$

where I_{w_1} = current discharged from the outboard trailing-edge discharger on the wing. This expression, plotted in Fig. 40, was used in Part 2 of Appendix D in connection with the calculation of effective aircraft intercepting area and charging rate. Equation (32) and Fig. 40 also proved useful when dischargers were installed on aircraft which could not be elaborately instrumented. In this case, by monitoring the current from one discharger, it was possible to obtain an accurate estimate of total discharge current. This technique was used, for example, in obtaining the statistical data regarding aircraft charging shown in Fig. 27.

95

No effort was made to further refine the laboratory techniques to take into account the charged precipitation. It was felt that the results indicated in Table IV and Fig. 39 demonstrate the general validity of the method. Furthermore, it was felt that its utility lies not in predicting every detail of the discharge-current distribution during every conceivable charging situation, but rather in providing an inexpensive method for studying the effects upon discharge capability of changes in discharger location.

EMPIRICAL EQUATION
$$I_d = 2I_{w_1} + 3.17 \times 10^5 I_{w_1}^2$$
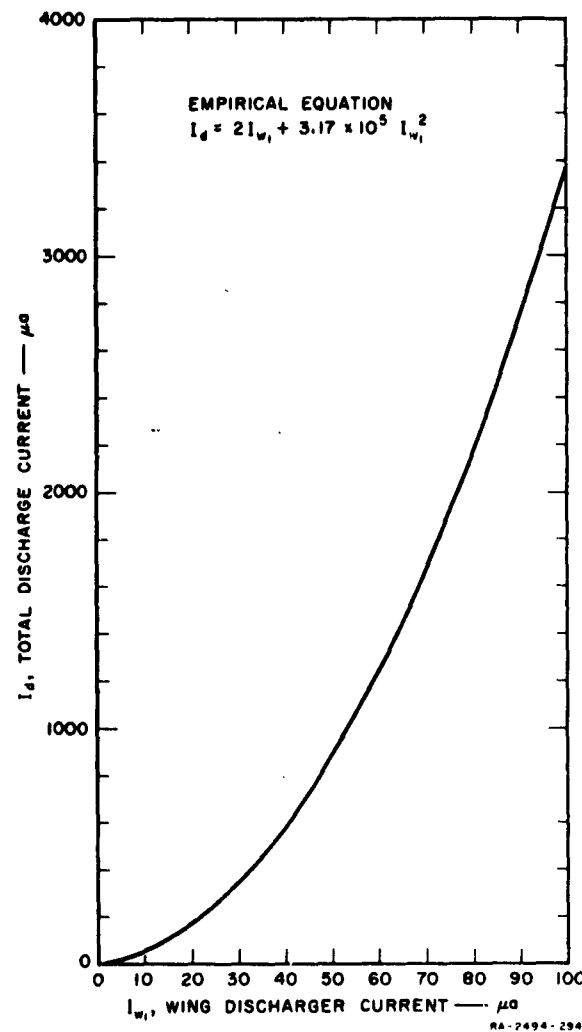
FIG. 40

TOTAL DISCHARGE CURRENT AS A FUNCTION OF CURRENT DISCHARGED FROM OUTBOARD DISCHARGER ON WING TRAILING EDGE IN PRECIPITATION CHARGING

It is important, for example, that the discharger arrangement on an aircraft be so chosen that it achieves as nearly as possible the maximum discharge current for that number of dischargers. If this condition is fulfilled, the airplane potential for a given charging current will be minimum, and discharges from the airframe itself will thereby be minimized. The amount of current that a discharger will discharge at a given aircraft potential and airspeed is determined primarily by two factors: the field strength about the airfoil at its loca- (in the absence of other dischargers) and the proximity of other dischargers. Thus a discharger located on the wingtip will discharge more current than one located inboard from the tip because the field about the tip is more intense. Also a discharger on an airfoil trailing edge will discharge more current when it is isolated than it will if a second

96

discharger is placed next to it, because the space charge from the second discharger will have a shielding effect on the first. Consequently one is led to seek an optimum distribution for a given number of dischargers such that the dischargers are far enough apart that discharging capability is not severely limited by mutual shielding effects, and yet not so far apart that the inboard dischargers must be placed in the low field regions.

To determine the optimum distribution of dischargers along the trailing edge of an airfoil, six model dischargers were uniformly spaced along the trailing edge of the wing of a KC-135 model and the total current discharged by these six dischargers was determined for several spacings. The results of this test are shown in Fig. 41, where the total current is plotted as a function of spacing between the dischargers. As seen in the figure, the maximum current for a uniform spacing is obtained when the dischargers are approximately 24 inches apart. However, because the curve
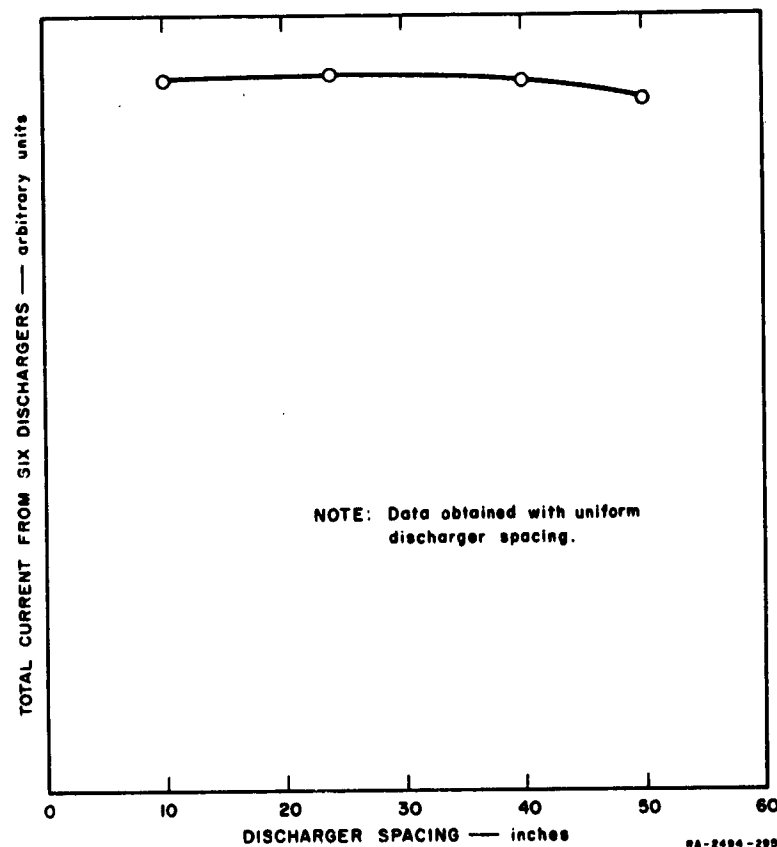
FIG. 41

EFFECT OF DISCHARGER SPACING ON TOTAL DISCHARGE CURRENT

97

is quite flat in this region, increasing or decreasing the spacing by a factor of two does not appreciably reduce the total current discharged.

To determine whether some other spacing might be better than the uniform spacing, several non-uniform spacings were investigated, in which the dischargers were placed close together in the high field regions near the outboard tip and further apart inboard from the tip. The total currents discharged by these arrays were compared to the current discharged by an equal number of dischargers uniformly spaced over the same portion of the trailing edge. In all cases examined, the non-uniform spacings appeared to offer no increase in the total current discharged, although currents discharged by individual dischargers in the array varied considerably.

The fact that the total current is relatively independent of spacing may be explained by observing that, within the range of spacings investigated, changes in mutual shielding almost exactly nullify changes in field intensity as spacing is varied. As was indicated earlier, with close spacing the dischargers are located in the high dc-field region near the airfoil tip, but the current is severely limited by mutual shielding. With wide spacing, on the other hand, there is less mutual shielding, but more of the dischargers are located in regions of reduced field farther inboard from the airfoil tip.

In the next laboratory test an investigation was made of the manner in which the discharge current varies with the number of dischargers installed on an airfoil. Measurements were made to determine the total current discharged when from 4 to 14 dischargers spaced 18 inches apart are installed on an airfoil. The results of these measurements, shown in Fig. 42, indicate that, after the first few dischargers are installed, each additional discharger provides an equal increment of discharging capacity. This result together with the results of the spacing tests indicate that simply by installing additional dischargers it is possible to increase the discharging capability of an installation to any reasonable value.

While a uniform discharger spacing is adequate to discharge maximum current for a given aircraft potential, one should not immediately conclude that this is the optimum distribution of dischargers. It is important also that one take advantage of the space-charge cloud produced aft of each discharger to maximize the threshold potential for discharges from the airframe itself (since these discharges, if permitted to occur, would
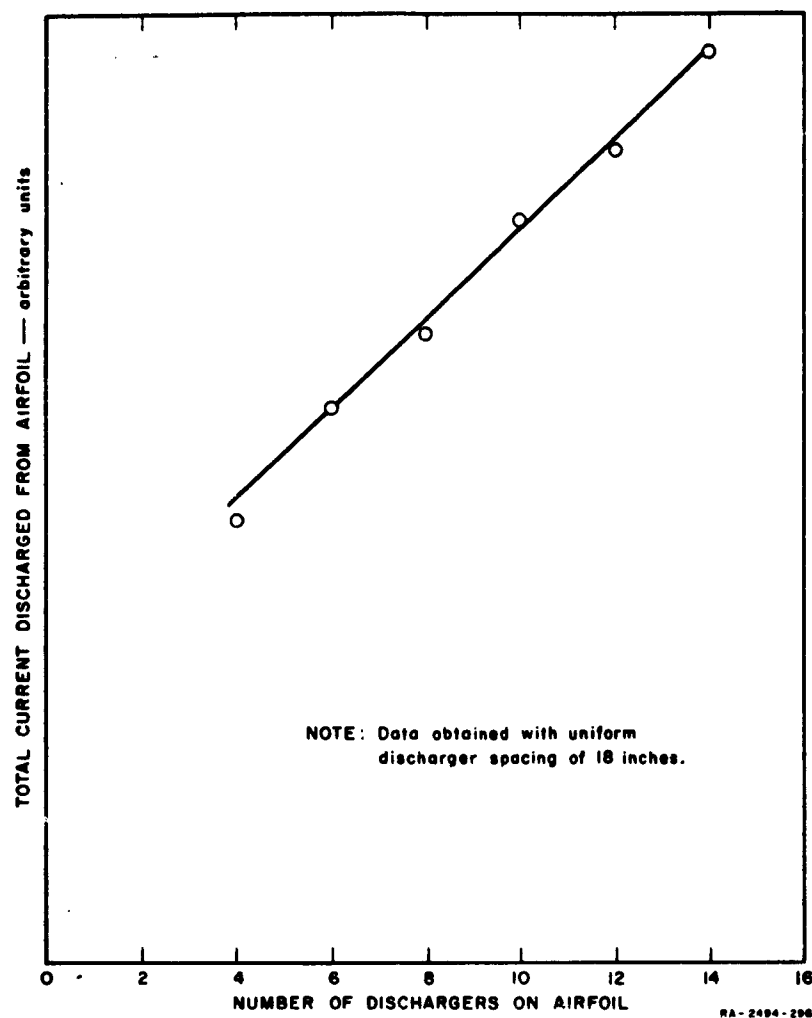
FIG. 42

**VARIATION OF DISCHARGE CURRENT WITH NUMBER
OF DISCHARGERS INSTALLED**

generate noise). For turbojet aircraft in particular this implies that the corona threshold potential of points along the trailing edge between the dischargers be maximized, subject to the condition that the discharger current also remain maximized.

The threshold potential of points along the trailing edge of an airfoil was determined in the laboratory using a technique similar to that described in Sec. V-B-2. Using the set-up shown in Figs. 8 and 9, a measurement was made to determine the field intensity, $E_t(d)$, existing at a distance d forward of the trailing edge at corona threshold. Next, a

99

charged $\frac{1}{50}$-scale model of the aircraft was suspended in the laboratory as in Fig. 23 and static-field measurements were made to determine the airplane potential necessary to produce the threshold value of field $E_t(d)$ at various distances in from the tip of the airfoil. In these measurements again, the presence of space charge aft of the dischargers was simulated by attaching conducting rods to the trailing edge at the discharger locations.

The lower curve in Fig. 43 describes the airplane potential necessary to produce corona from points along the trailing edge of the wing on a KC-135 assuming no discharges are occurring elsewhere on the wing. As one would expect, the threshold of the outermost portion is much lower than that of the rest of the wing. Since it has been demonstrated that total discharge current does not depend critically upon spacing, it appears that maximization of the trailing-edge corona threshold is most easily accomplished
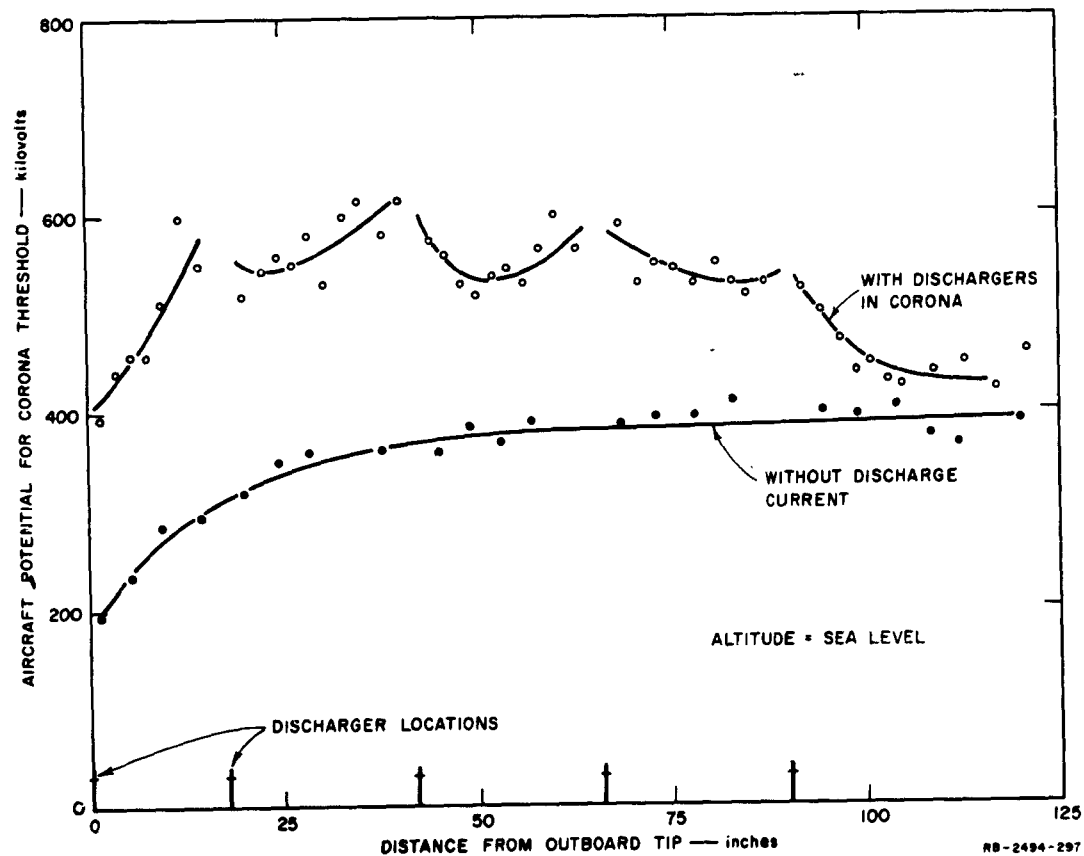
FIG. 43

THRESHOLD POTENTIALS OF POINTS ALONG TRAILING EDGE OF WING ON KC-135

100

by decreasing the spacing of the outboard dischargers. In this way space-charge density would be highest in this region and the trailing-edge fields here would be reduced most.

By attaching dischargers at the locations shown at the bottom of Fig. 43 the threshold potentials were raised to the values indicated by the upper curve. The threshold potential of the trailing edge between the two dischargers furthest outboard could be increased further by reducing their spacing even more. Decreasing the spacing below about 12 inches offers little advantage because at this spacing the threshold potential of the trailing edge in the discharger region is as high as, or perhaps higher than, some other points on the aircraft such as points inboard of the dischargers on the wing. Thus, a distribution such that the two furthest outboard dischargers are 12 to 18 inches apart and the remainder are 24 inches apart is very nearly optimum. With the discharger arrangement corresponding to Fig. 43, and making use of the data of Figs. 39 and 40, we conclude that at an altitude of 15,000 feet, high-field points on the wing just inboard of the innermost discharger would reach corona threshold with a total aircraft charging current of approximately 3.5 ma. We see therefore that the discharger complement used in the flight tests is adequate to discharge without noise the highest charging currents encountered in the tests, but would not handle appreciably greater currents than these.

VI PREDICTION OF PRECIPITATION-STATIC NOISE FIELDS

A. PREDICTED NOISE IN 707 AIRCRAFT ANTENNAS

By employing the information regarding charging magnitude, discharge distribution, corona characteristics, and noise coupling presented in the preceding sections, it is possible to predict the characteristics of the precipitation-static noise generated in an aircraft antenna. Calculations of this sort were carried out for the antennas employed in the flight tests conducted on the Boeing 367-80. To illustrate the noise-prediction technique, the noise current generated in the tail-cap antenna on the unmodified flight-test aircraft will now be evaluated.

Let us say that we are interested in the noise current generated in a one-kc bandwidth at a frequency of 500 kc. Let us assume, furthermore, that the aircraft is at an altitude of 20,000 feet in precipitation such that the charging rate is 5 microampere/sq ft and the effective intercepting area is 50 sq ft so that the total charging current is 250 microamperes. These conditions were chosen since they are typical of those often existing during the precipitation-static flight tests.

The results of the laboratory tests described in Sec. V-D-1 indicate that on the unmodified flight-test aircraft the total discharge current, I_d, should be distributed among the various airfoils as follows:

$$I_{rudder} = \frac{1}{7} I_d = 0.143 I_d$$

$$I_{elevators} = \frac{2}{7} I_d = 0.285 I_d$$

$$I_{wings} = \frac{4}{7} I_d = 0.572 I_d \quad .$$

The QANTAS tests described in Sec. V-D-2 indicated that the laboratory results should be valid for engine-charging conditions, but that in

precipitation charging, the empennage currents are increased relative to the wing currents by a factor of approximately 1.6 as a result of the positively charged precipitation sheath formed about the aircraft. For this calculation, therefore, it will be assumed that the discharge current is distributed as follows:

$$I_{rudder} = 0.182 \ I_d$$

$$I_{elevators} = 0.364 \ I_d$$

$$I_{wings} = 0.454 \ I_d \quad .$$

For a total charging current of 250 microamperes this means that

$$I_{rudder} = 45.5 \text{ microamperes}$$

$$I_{elevators} = 91 \text{ microamperes}$$

$$I_{wings} = 103.5 \text{ microamperes}$$

Before proceeding further it is well to note from Fig. 15 that the noise-spectrum amplitudes generated by the three sources differ at most by only 50%. From Fig. 6, on the other hand, it is evident that for frequencies below 10 Mc the coupling between the tail-cap antenna and the rudder tip is almost always an order of magnitude greater than the coupling to the other extremities. Thus, on the unmodified aircraft, the noise existing in the tail-cap antenna will be almost entirely that generated by discharges from the rudder. To simplify the calculations, therefore, we will consider only the noise coupled from the rudder tip

From Fig. 15 for a discharge current of 45.5 microamperes we obtain

$$|D(2 \text{ Mc})|_{sea \ level} = 7.0 \times 10^{-9} \text{ amp meter}/\sqrt{\text{radian/sec}} \quad .$$

From Fig. 12 we find that the relative spectral density at 20,000 feet altitude for a frequency of 500 kc is 2.4. Thus

$$|D(500 \text{ kc})|_{20,000 \ ft} = 2.4 \ (7.0 \times 10^{-9})$$

$$= 1.68 \times 10^{-8} \text{ amp meter}/\sqrt{\text{radian/sec}} \quad .$$

At a frequency of 500 kc, the normalized coupling between the tail cap and the rudder is found from Fig. 6 to be

$$\frac{\psi(\xi, \ 500 \ kc)}{a} \ = \ 3.5 \times 10^{-2} \ meters^{-3} \quad .$$

The induction area, a, of the tail cap antenna used in the flight tests was

$$a \ = \ 8.6 \ m^2 \quad .$$

Therefore the coupling between the tail-cap antenna and the rudder tip is

$$\psi(\xi, \ 500 \ kc) \ = \ 3.5 \times 10^{-2} \ (8.6)$$

$$= \ 0.301 \ meter^{-1} \quad .$$

The noise-current spectral density may be found by substituting these results into Eq. (15):

$$\sqrt{G(500 \ kc)} \ = \ \psi(\xi, \ 500 \ kc) \ \left| D(500 \ kc) \right|_{20,000 \ ft}$$

$$= \ 0.301 \ (1.68 \times 10^{-8})$$

$$= \ 5.06 \times 10^{-9} \ amp/\sqrt{radian/sec} \quad .$$

From the definition of noise-current spectral density, $G(\omega)$, the short-circuit noise current in the antenna is given by

$$I_{sc} \ = \ \sqrt{G(\omega)} \ \sqrt{BW} \tag{33}$$

where BW is the bandwidth in radians. (For a one-kc bandwidth $\sqrt{BW} = 79.2$.) Thus for a total discharge current of 250 microamperes at an altitude of 20,000 feet we find that the short-circuit noise current in a one-kc bandwidth generated in the tail-cap antenna at a frequency of 500 kc should be

$$I_{sc} \ = \ 79.2 \ (5.06 \times 10^{-9})$$

$$= \ 4.02 \times 10^{-7} \ ampere \quad .$$
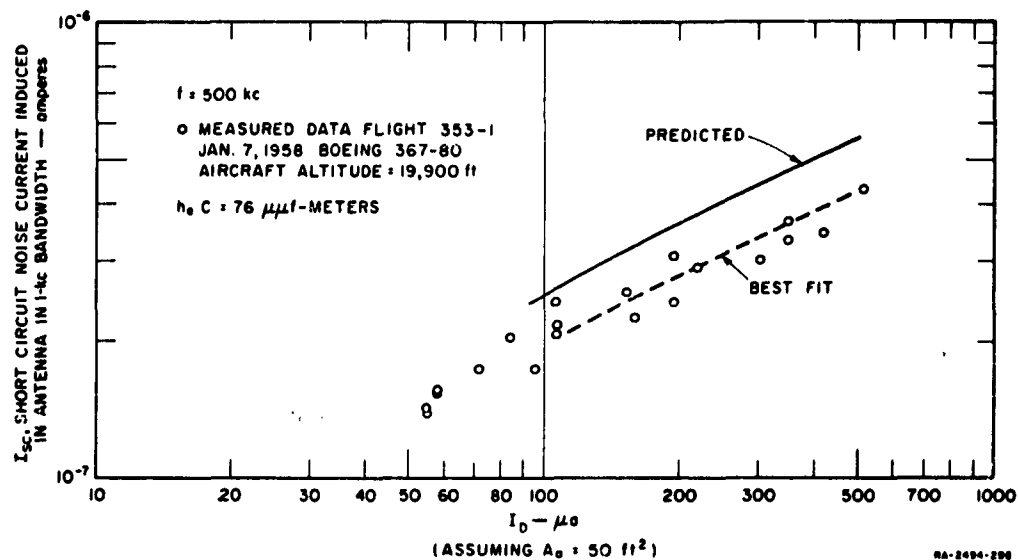
FIG. 44

VARIATION OF TAIL-CAP-ANTENNA NOISE CURRENT WITH DISCHARGE CURRENT

This calculation was repeated for several values of discharge current to yield the solid curve of Fig. 44. The upper curve of Fig. 45 was obtained by repeating the calculation for different values of frequency.

B. COMPARISON OF PREDICTED NOISE WITH FLIGHT-TEST MEASUREMENTS

Since flight-test measurements were made of the noise existing in the two antennas employed in obtaining the coupling data of Fig. 6, the validity of the precipitation-static noise theory may be tested by comparing the predicted noise with the results of these measurements.[10,11] The results of tail-cap antenna noise measurements made at a frequency of 500 kc on the unmodified aircraft were plotted, therefore, in Fig. 44. It is evident from the figure that the predicted noise current agrees remarkably well with the results of the flight-test measurements. It should be noted in connection with the flight-test data that I_d was not measured directly in flight. The charging rate, i_p, was measured, and it was assumed that the effective intercepting area, A_e, was 50 sq ft. (Measurements in clouds of this type indicated that A_e was generally within the range 30-70 sq ft.) If, for example, A_e were actually 30 sq ft

106
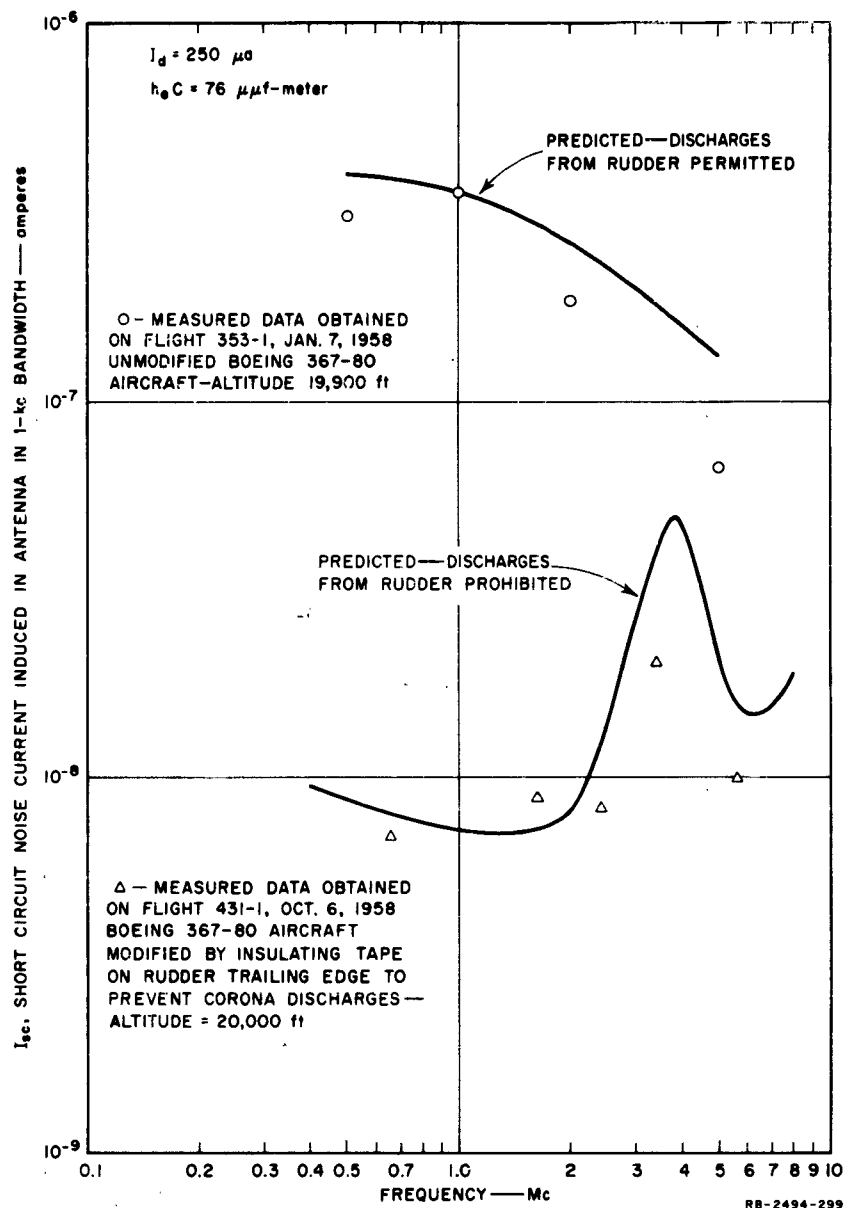
FIG. 45

TAIL-CAP-ANTENNA NOISE CURRENT AS A FUNCTION OF FREQUENCY

107
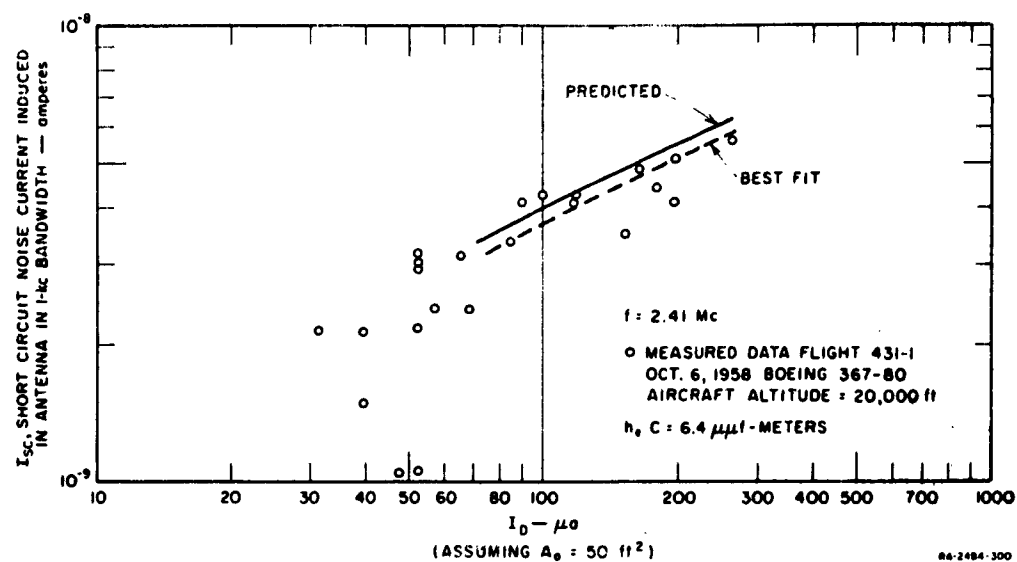
FIG. 46

VARIATION OF BELLY-ANTENNA NOISE CURRENT WITH DISCHARGE CURRENT
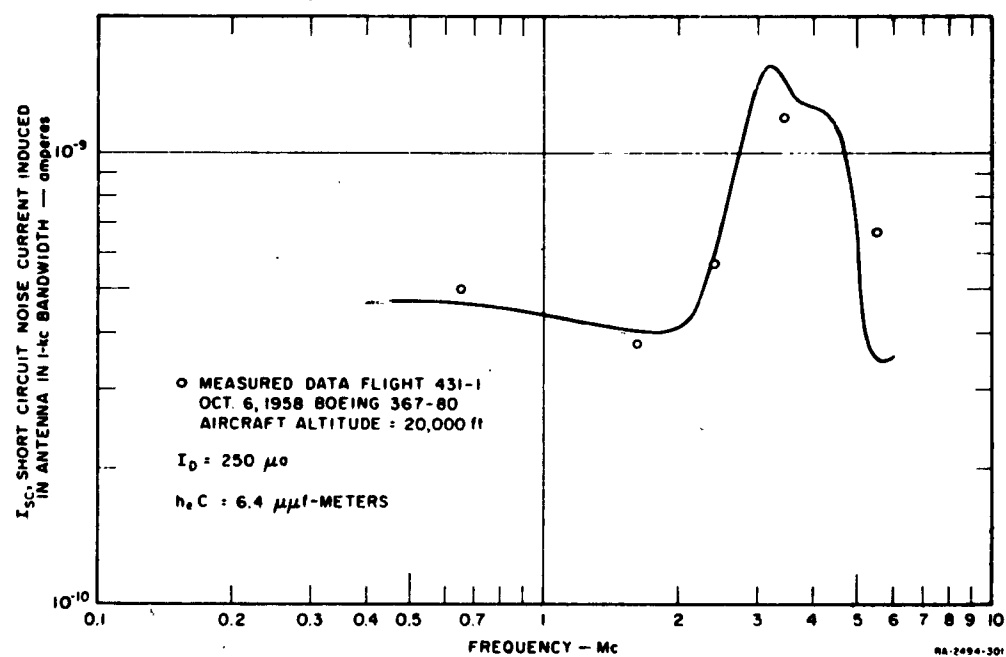
FIG. 47

BELLY-ANTENNA NOISE CURRENT AS A FUNCTION OF FREQUENCY

108

during the period in which the flight-test data were obtained, the agreement between measured and predicted results would be almost exact.

In the upper part of Fig. 45 also, there is good general agreement between predicted and measured noise data.

Upon observing from the flight-test data that the tail-cap antenna noise appeared indeed to be generated entirely by discharges from the rudder, an interesting experiment suggested itself. If a layer of insulating tape were applied to the trailing edge of the rudder, suppressing corona discharges from this region and forcing the current to leave from the other extremities where the coupling to the tail cap is much weaker, the tail-cap antenna noise spectrum should be modified drastically. Calculations, the results of which are shown in the lower curve of Fig. 45, were carried out, therefore, to predict the noise that should exist in the tail cap if all of the current were discharged from the wings and elevators. The results of the noise measurements on the modified aircraft, also shown in the figure, verified the predictions.

In predicting the noise from more than one source as in the lower curve of Fig. 45 one utilizes the fact that the noise currents from the various sources are incoherent. Thus, the noise current from each source is evaluated as was the rudder discharge noise in obtaining Fig. 44. The total noise current is obtained by adding the individual noise currents in root-mean square fashion.

As a further test of the theory, the values of the noise currents induced in the belly antenna on the flight-test aircraft were predicted and compared to the results of flight-test measurements as is indicated in Figs. 46 and 47. It is evident that almost perfect agreement was obtained. One may therefore conclude that the theories of noise generation and coupling are valid, and that inferences drawn from these theories will be accurate.

C.   EQUIVALENT NOISE FIELDS

Although the terminal noise current completely specifies the precipitation-static noise response of an antenna, the terminal current is not a familiar term. For example, upon inspecting Fig. 45, it is obvious that preventing discharges from the rudder reduced the low-frequency precipitation-static noise level in the tail-cap antenna by

roughly 35 db. Without further calculation, however, one is not certain whether the reduced noise is sufficiently low that it can be ignored or if, even with discharges from the rudder prohibited, precipitation-static interference is a serious problem. Terminal noise currents, furthermore, may be misleading when comparing the relative precipitation-static performance of antennas as, for example, in Fig. 47 and the lower curve of Fig. 45. Although the noise current is lower in the belly antenna, the sensitivity of this antenna is lower than that of the tail cap. Thus the signal-to-precipitation-static noise ratios in these two antennas will differ by far less than one might be led to believe from a comparison of the terminal currents.

It is apparent from the foregoing discussion that the precipitation-static noise data would be much more convenient if they were expressed in terms of the field intensity required to generate the calculated terminal current in the antenna. Whereas the antenna noise current is dependent upon the antenna size and sensitivity, the equivalent noise field applies to any antenna installed at a particular location. The equivalent-noise-field concept is also helpful in that one generally has an idea of the signal field strengths in which the receiving equipment is expected to operate. Thus, with the precipitation-static noise expressed as an equivalent field intensity, it is possible immediately to write the signal-to-precipitation-static noise ratio and to determine if communication is possible in the presence of precipitation-static interference.

Let us consider first the low-frequency case. If the dimensions of the aircraft are small compared to a wavelength at the frequency of interest, a dipole-type antenna mounted on the aircraft will have the radiation pattern of an elementary dipole.[12,13] The characteristics of the antenna in this case are determined by specifying the direction of the dipole axis and the value of a parameter called the induction area, a, of the antenna which is defined as

$$a = \frac{q}{\epsilon_0 E_i} \tag{34}$$

where E_i is the field intensity of the incident wave, q is the value of the induced charge on the antenna, and $\epsilon_0 = (1/36\,\pi) \times 10^{-9}$ farad/meter.

It should be noted that a is usually defined as the value obtained when the antenna is so oriented as to maximize q. In this analysis, however, it will be convenient to have a vary with the direction of arrival of the received signal E_i.

For the low-frequency case being considered, the current flowing at the short-circuited antenna terminals is $j\omega q$. Thus using Eq. (34) we may write

$$I_{sc} = j\omega\epsilon_0 aE_i \quad . \tag{35}$$

Considering the two forms of the equivalent circuit of the receiving antenna shown in Fig. 48, it is seen that the equivalent area serves in the equivalent current generator circuit, a function comparable to that served by the parameter h_e (effective height) in the voltage-generator circuit. In the equivalent circuits of the figure, if the antenna impedance is taken as a pure capacitive reactance, as is customary in dealing with the circuit aspects of small antennas, then h_e and a for a given antenna are related through the expression

$$\epsilon_0 a = h_e C \tag{36}$$

where C is the capacitance of the antenna. By rearranging Eq. (35) and making an analogy between noise and signal we can write

$$|E_n| = \frac{|I_n|}{\omega\epsilon_0 a} \tag{37}$$

FIG. 48

EQUIVALENT CIRCUITS
OF RECEIVING ANTENNA

where I_n is the terminal noise current, and E_n is defined as the equivalent noise field. It is worth noting that at low frequencies both the coupling, ψ, and source spectrum, $D(\omega)$, are constant so that I_n will be constant and E_n will vary inversely with frequency.

111
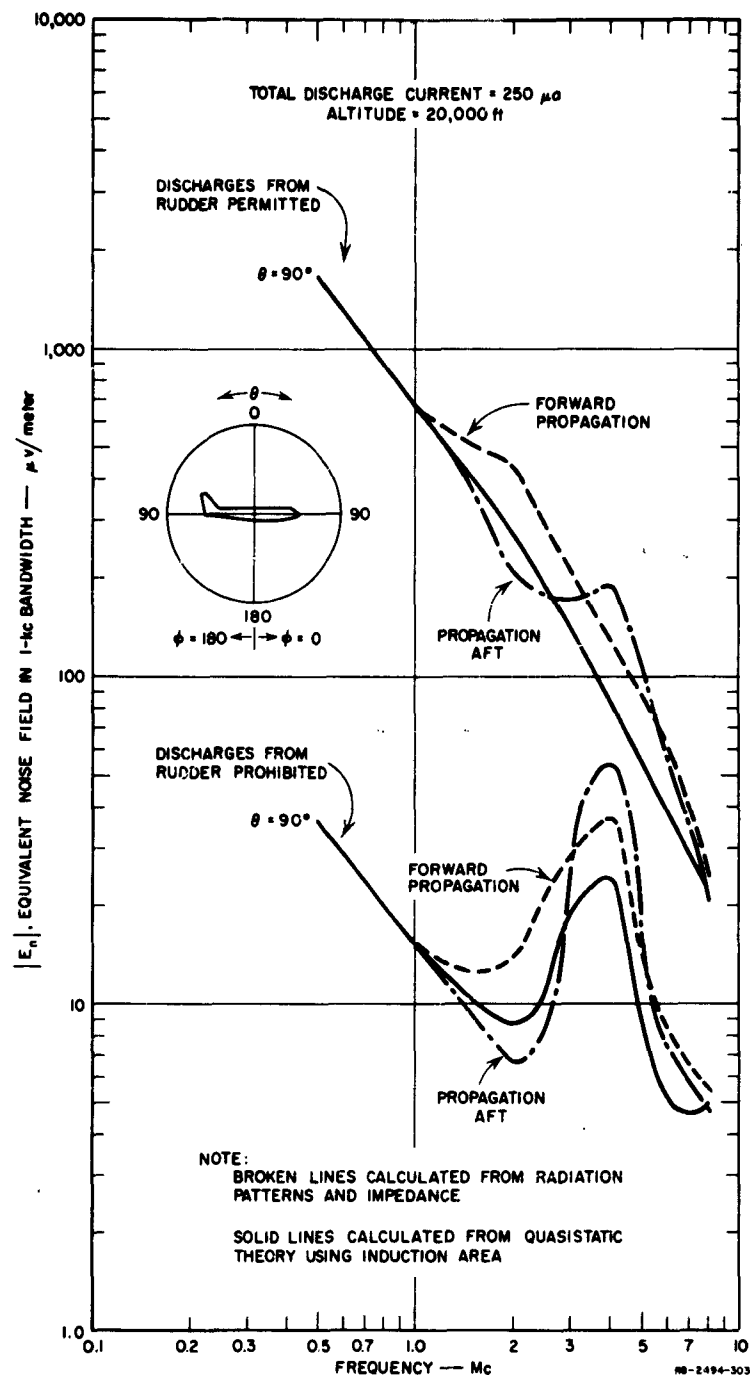
FIG. 49

COMPARISON OF METHODS USED TO CALCULATE EQUIVALENT
NOISE FIELDS AT TAIL-CAP ANTENNA

112

Referring to Fig. 45, we find that at a frequency of 500 kc, the short-circuit terminal current predicted in a 1-kc bandwidth in the tail-cap antenna on the unmodified aircraft is 4×10^{-7} amperes when the total discharge current is 250 microamperes. From laboratory measurements we know that the induction area, a, of this antenna, for a vertically-polarized, horizontally-propagating signal, is 8.6 square meters. Thus using Eq. (37) we can write

$$E_n = \frac{(4 \times 10^{-7})(36\pi \times 10^9)}{2\pi (5 \times 10^5)(8.6)}$$

$$= 1.675 \times 10^{-3} \text{ volts/meter} \quad .$$

Although Eq. (37) is valid only for low frequencies, it was used at frequencies as high as 8 Mc to compute the values of $|E_n|$ used in plotting the solid curves in Fig. 49. The high-frequency noise-field data computed in this manner will be compared to the data obtained using a method which is more valid at the frequencies above the quasi-static range, but which requires considerably more information about the characteristics of the antenna used in performing the noise-coupling measurements. Thus, since the induction area is easy to measure in the laboratory,[12,13] it was felt that an effort should be made to determine if the noise-field data computed using quasi static theory at the high frequencies might provide a sufficiently accurate estimate of $|E_n|$ for many purposes.

As the frequency is raised above the quasi-static range, the antenna can no longer be represented by a simple dipole. In calculating $|E_n|$, therefore, it is necessary to take into account changes in the radiation pattern and effects of aircraft resonances. The problem is most easily approached with the aid of the reciprocity relationship which applies to antennas in free space[20]

$$G = \frac{4\pi A}{\lambda^2} \tag{38}$$

where G = directive gain of antenna.

The receiving cross-section, A, is defined as the power extracted from the antenna by a conjugate matched load divided by the power density in the incident wave. It is a function of the polarization and angle of arrival of the incident wave.

In terms of the equivalent generator circuits of Fig. 48 the power delivered to a conjugate matched load is given by

$$ P = \frac{I_{sc}^2 |Z_a|^2}{4R_a} \tag{39} $$

where R_a = radiation resistance of antenna. Dividing this by E_i^2/η, the power density in the incident wave, leads to

$$ A = \frac{I_{sc}^2 |Z_a|^2 \eta}{4R_a E_i^2} \quad . \tag{40} $$

Substituting Eq. (40) into Eq. (38) yields the following expression for the incident field

$$ E_i = \frac{I_{sc} |Z_a|}{\lambda} \sqrt{\frac{\eta \pi}{R_a G}} \quad . \tag{41} $$

By making an analogy between noise and signal, this equation can be used to determine the equivalent noise field from the short-circuit noise current.

It is evident from Eq. (41) that in order to evaluate equivalent noise fields it is necessary to have radiation patterns and impedance data for the antenna in question. Unfortunately these data are not available for either of the antennas used in the flight tests conducted using the Boeing 367-80 aircraft. These data, however, are available for the fin-cap HF probe antenna used on the KC-135 and 707 aircraft.[21]

This antenna is located near the tail cap, and for frequencies such that the wavelength is large compared to the size of the antennas and the distance between them, the normalized coupling data of Fig. 6 will be valid for the probe antenna also. Since the induction area of the probe antenna

114

in response to a vertically-polarized, horizontally propagating signal
is 24.9 square meters, the short-circuit noise currents induced in it
will be 24.9/8.6 = 2.9 times as large as the values given for the tail-
cap antenna in Fig. 45. (The induction area, a, of the tail cap was
8.6 square meters.)

Equivalent noise fields existing at the fin cap for frequencies in
the range 2 Mc and higher were calculated from Eq. (41) using probe-
antenna noise currents together with the probe-antenna data of Ref. 21.
For frequencies below 2 Mc the fin-cap noise fields were calculated using
tail-cap antenna noise-current data in Eq. (37). Since antenna gain varies
with the direction of signal arrival, the equivalent noise field will not
have a unique value for a given frequency, but will be a function of di-
rection. A three-dimensional representation would be required to com-
pletely describe it. However, since much aircraft communication,
particularly in the case of commercial airlines, occurs in the fore
and aft direction, and since a complete set of radiation patterns was
not available, noise-field calculations were carried out only for the
longitudinal-vertical plane. The results of these calculations for vari-
ous vertical angles are presented for the forward direction in Fig. 50,
and for the aft direction in Fig. 51. In addition to the variations
caused by the effects of noise coupling changes, the curves are influenced
by the radiation patterns. In Fig. 50, for example, the peak in $|E_n|$ at
$\theta = 100°$ and $f = 2$ Mc is caused by a null in the radiation pattern which
exists at $\theta = 110°$ when $f = 2$ Mc. Similarly the peak in $|E_n|$ at $\theta = 70°$
and $f = 4$ Mc is caused by a null in the radiation pattern at $\theta = 60°$ when
$f = 4$ Mc.

The noise-field data computed for $\theta = 90°$ using the radiation-pattern
method were plotted as the broken lines in Fig. 49 for comparison with
the noise-field data obtained from quasi-static theory. Although the
noise fields obtained for a given direction of propagation using the quasi-
static method differ from the true values, a comparison of Figs. 49 and 50
indicates that this difference is not greater than that resulting from
small changes in the direction of propagation. Thus, the quasi-static
method provides a simple technique for estimating the order of magnitude
of noise field at an antenna location when pattern and impedance data for
an antenna at that location are not available. An estimate of this sort
is sufficient for many applications.

115
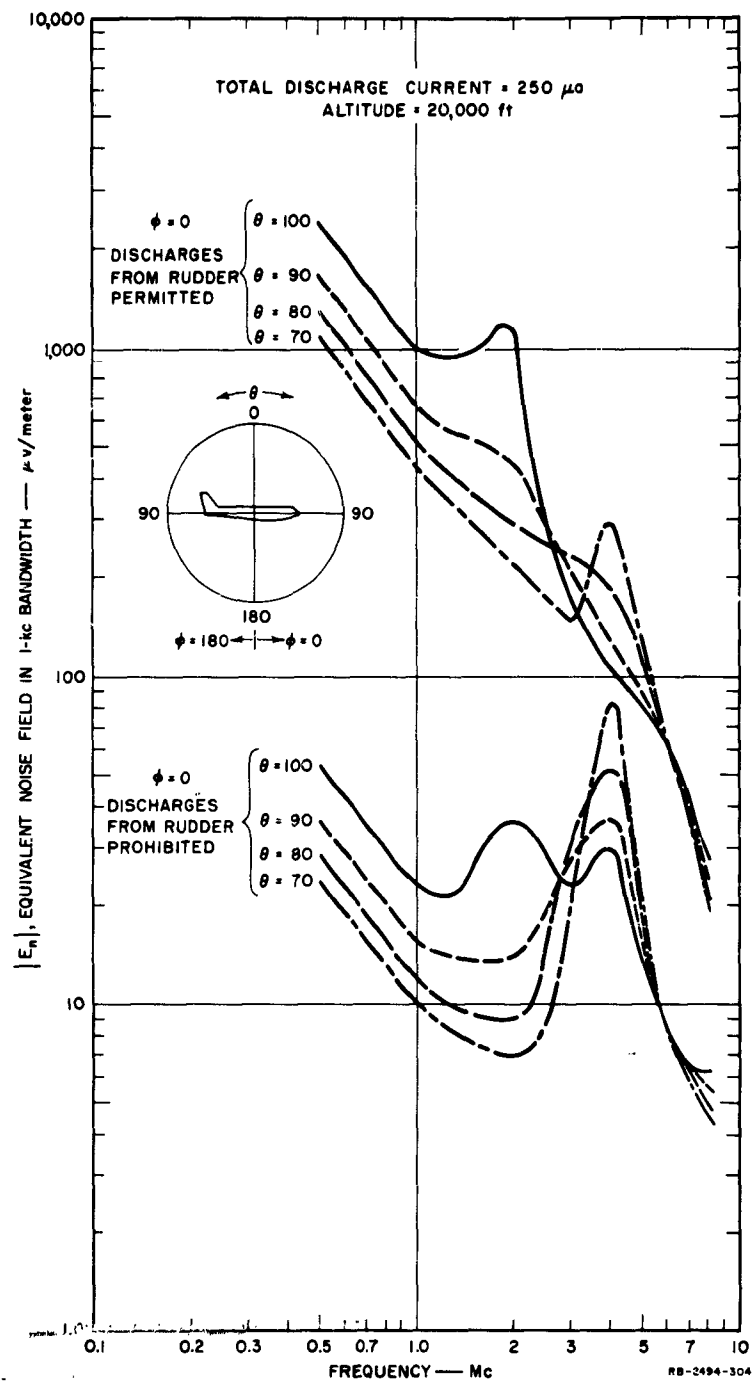
FIG. 50

EQUIVALENT NOISE FIELDS AT FIN CAP FOR FORWARD DIRECTIONS
OF PROPAGATION

116
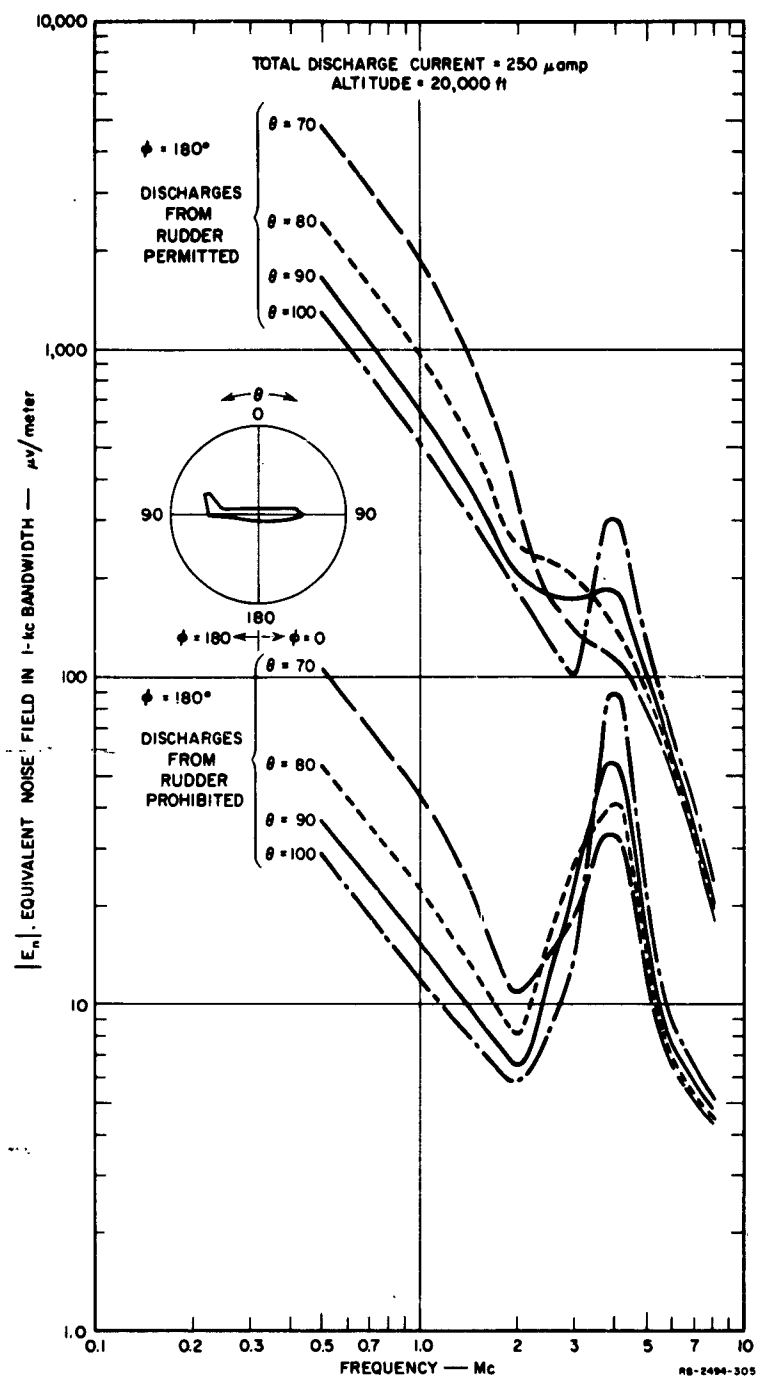
FIG. 51

EQUIVALENT NOISE FIELDS AT FIN CAP FOR AFT DIRECTIONS
OF PROPAGATION

Since pattern and impedance data were not available for the belly antenna used during the flight tests on the Boeing 367-80, the equivalent noise fields at the belly location shown in Fig. 52 were all computed using quasi-static theory and the induction area of the antenna. Comparison of Fig. 52 with the lower sets of curves in Figs. 50 and 51 indicates that, with discharges from the rudder prevented, the noise fields at the tail cap and belly are of the same order even though the noise current in the tail-cap antenna is much higher than in the belly (see Figs. 45 and 47).
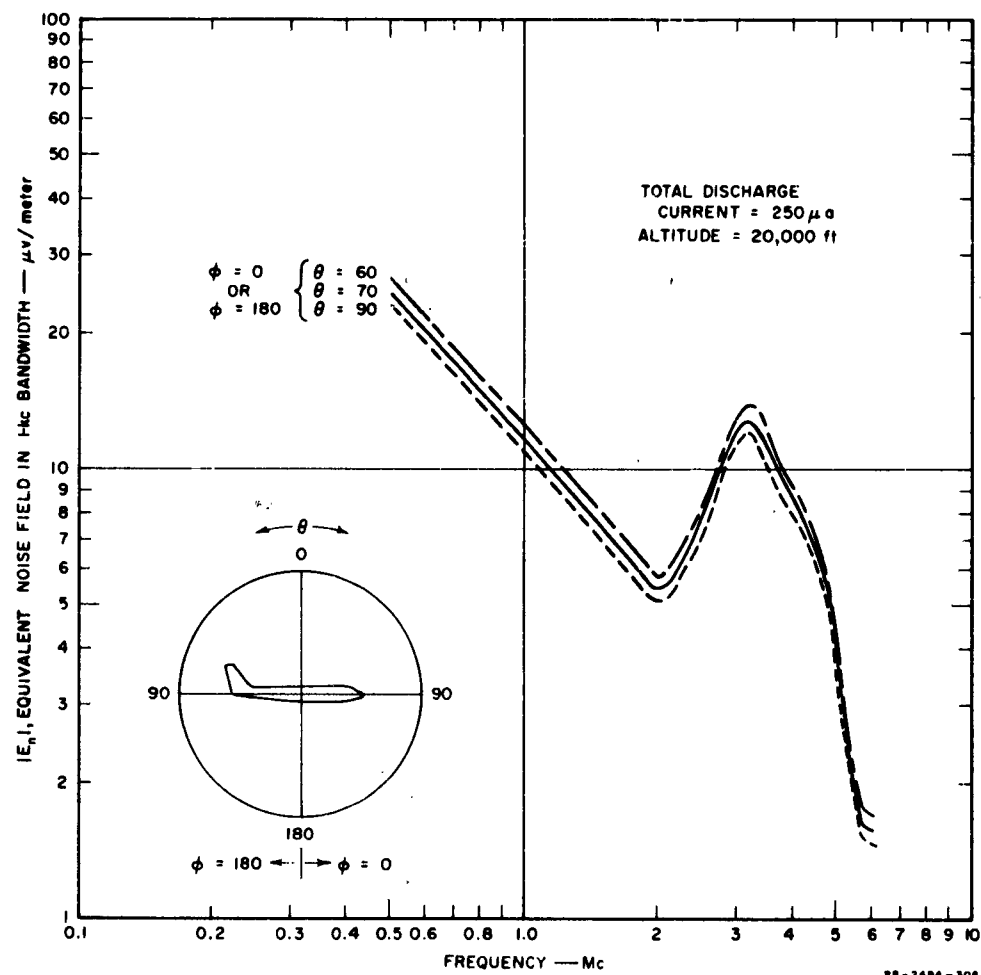
FIG. 52

EQUIVALENT NOISE FIELDS AT BELLY-ANTENNA LOCATION

118

It should be noted that the data presented in Figs. 49 through 52 assume that the discharge current is 250 microamperes and that the altitude is 20,000 feet. If the discharge current were increased to the not uncommon value of 1 ma, the equivalent noise fields would very nearly double. At a different altitude, both the magnitude and shape of the E_n-vs.-frequency curves would be changed in accordance with Fig. 12.

D. DEPENDENCE OF NOISE FIELD UPON AIRCRAFT SIZE

Since detailed calculations of noise fields generated by precipitation static have been carried out only for large aircraft of the size of the KC-135, it is of interest to investigate the manner in which the equivalent fields vary with aircraft size in order that the results may be applied to smaller aircraft. This problem may be studied by employing certain of the results obtained thus far.

Let us assume that we have two aircraft flying side by side in precipitation so that the intrinsic charging current per unit frontal area will be the same for both aircraft. Furthermore, let us assume that the two aircraft have similar shapes but that the dimensions of Aircraft No. 2, the smaller aircraft, are $1/n$ the dimensions of Aircraft No. 1 ($n > 1$). The projected frontal areas of the two aircraft, therefore, will be related by

$$A_{proj_2} = \frac{A_{proj_1}}{n^2} \quad .$$

From Fig. 19, however, we observe that as the dimensions of the aircraft are decreased, the percentage of the frontal area effective in intercepting particles increases. If the data of Fig. 19 are plotted on logarithmic paper the curves have average slopes approaching minus one. Thus, we must conclude that the effective intercepting area will vary only as the first power of the aircraft dimensions, or

$$A_{eff_2} = \frac{A_{eff_1}}{n} \quad . \tag{42}$$

119

Hence the total charging currents to the two aircraft will be related by

$$I_{ch_2} = \frac{I_{ch_1}}{n} \quad .$$

Since the noise spectrum amplitude $|D(\omega)|$ varies nearly as the square root of the discharge current, we obtain

$$|D(\omega)|_2 = \frac{|D(\omega)|_1}{\sqrt{n}} \quad . \tag{43}$$

Referring to Fig. 53 let us say that on Aircraft No. 1 we measured a coupling ψ_1 at the standard distance d_s from the edge of an extremity. Then on Aircraft No. 2, assuming that the dimensions of the antenna were scaled with the rest of the aircraft, the coupling to the scaled reference point at the distance d_s/n from the edge will in the quasi-static case be $\psi_2' = n\psi_1$. This result follows from the fact that the geometries of the reciprocal fields about the two aircraft are of similar form so that for a given voltage applied to the antenna the field intensities about the smaller aircraft must be n times those at corresponding points on the large
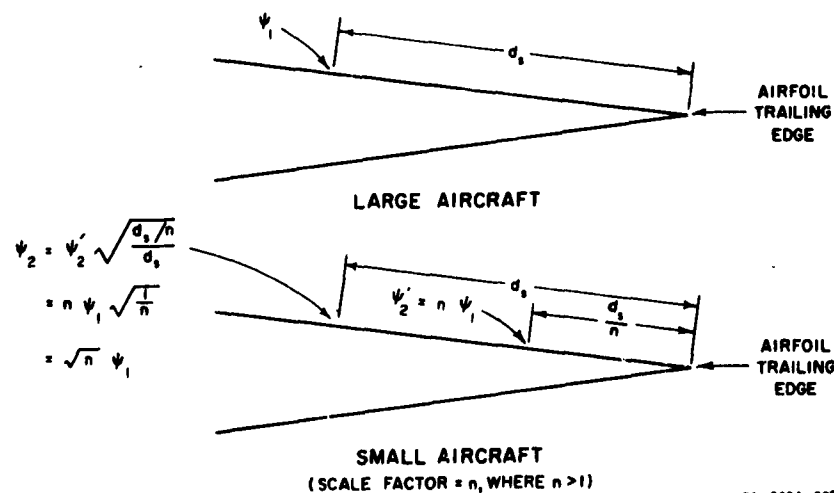
FIG. 53

ILLUSTRATION OF COUPLING RELATIONSHIPS

aircraft. To calculate noise, however, we must know the coupling at the standard distance d_s on Aircraft No. 2 also. It can be shown that the field intensity (and coupling) near the edge of a sheet varies inversely as the square root of distance to the edge. Thus as is indicated in Fig. 53 we find that, at the standard distance on Aircraft No. 2,

$$\psi_2 = \sqrt{n}\,\psi_1 \quad .$$

Substituting this result and Eq. (43) into Eq. (15) we obtain for the noise spectral density $\sqrt{G(\omega)}_2$ induced in the antenna on the second aircraft

$$\sqrt{G(\omega)}_2 = \sqrt{G(\omega)}_1 \quad .$$

Assuming the same receiving bandwidth on both aircraft this means that

$$I_{sc_2} = I_{sc_1} \quad . \tag{44}$$

Since the antennas were scaled with the rest of the aircraft, the following relationship will exist between the induction areas:

$$a_2 = \frac{a_1}{n^2} \quad .$$

Substituting this result and Eq. (44) into Eq. (37) we find that

$$E_2 = n^2 E_1 \quad . \tag{45}$$

In other words, for aircraft operating in the same precipitation at the same speed, the equivalent noise fields are inversely proportional to the square of the linear dimensions of the aircraft.

Perhaps the reader will object that we were not justified in applying the results of Fig. 19 to the entire aircraft, including the wings, in deriving Eq. (42). Let us, therefore, ignore Fig. 19 entirely and assume that

$$A_{eff_2} = \frac{A_{eff_1}}{n^2} \quad . \tag{46}$$

If we carry through the remaining arguments we will find that

$$E_2 = n^{3/2} E_1 \qquad\qquad (47)$$

which is only slightly different from Eq. (45).

To obtain an estimate of the magnitude of the noise fields which may be expected on smaller aircraft let us consider the belly (or canopy) antenna location on the F-86 aircraft. Since the dimensions of the Boeing 367-80 are roughly 3.3 times those of the F-86, the noise fields at the F-86 belly, using Eq. (45), will be roughly eleven times those at the 367-80 belly. For the charging conditions of Fig. 52 and a frequency of 500 kilocycles the noise field will be

$$E_{\text{F-86 Belly}} = 11 \ (25)$$

$$= 275 \ \mu\text{volt/meter}$$

in a bandwidth of 1 kc.

If we use Eq. (47) instead of Eq. (45) we obtain

$$E_{\text{F-86 Belly}} = 6 \ (25)$$

$$= 150 \ \mu\text{volt/meter}$$

in a bandwidth of 1 kc.

As was indicated earlier, the data of Fig. 52 were obtained in a region of light charging, and charging currents four times as high are quite common. Thus the noise fields will often be twice as high as those listed above. Since the receiver bandwidth is often as great as 5 kc, the equivalent noise fields listed above may have to be increased by an additional factor as great as $\sqrt{5} = 2.235$. It is apparent, therefore, that precipitation-static interference can be a particularly serious problem on small aircraft.

VII COMPARISON OF LOOP AND DIPOLE RECEIVING ANTENNAS

A. GENERAL

Although we have thus far confined our attention to the problem of
noise in dipole-type aircraft antennas, most of what has been said will
also apply to loop antennas. It is apparent, for example, that the rate
at which the aircraft charges, and the manner in which the discharges
distribute themselves among the extremities will not be affected by the
receiving antenna. Also, the spark-noise-source technique used to study
dipole-antenna noise coupling may be employed in the investigation of
loop antennas. One should not conclude, however, that loop and dipole
antennas are similar in all respects in regard to their susceptibility
to precipitation-static interference. Important differences exist between
these two antennas, as will be pointed out in the next section.

B. THEORETICAL CONSIDERATIONS

It will be of interest to compare the equivalent noise fields which
a discharge occurring at an extremity generates in loop and dipole antennas
in the quasi-static range. Let us assume that, as is indicated in Fig. 54,
a loop and a dipole are both installed at a distance z from some extremity
(say nose) of a major member of the aircraft (say fuselage). A noise source
at some other extremity excites a noise current I_n on the member under
consideration. This current will have a distribution on the member of
interest given by

$$I_n(z) = I_{n0} f(z) \quad . \tag{48}$$

If the cross-sectional area of the member is uniform throughout its length,
the current will have a triangular distribution, or

$$I_n(z) = I_{n0} z \quad . \tag{49}$$
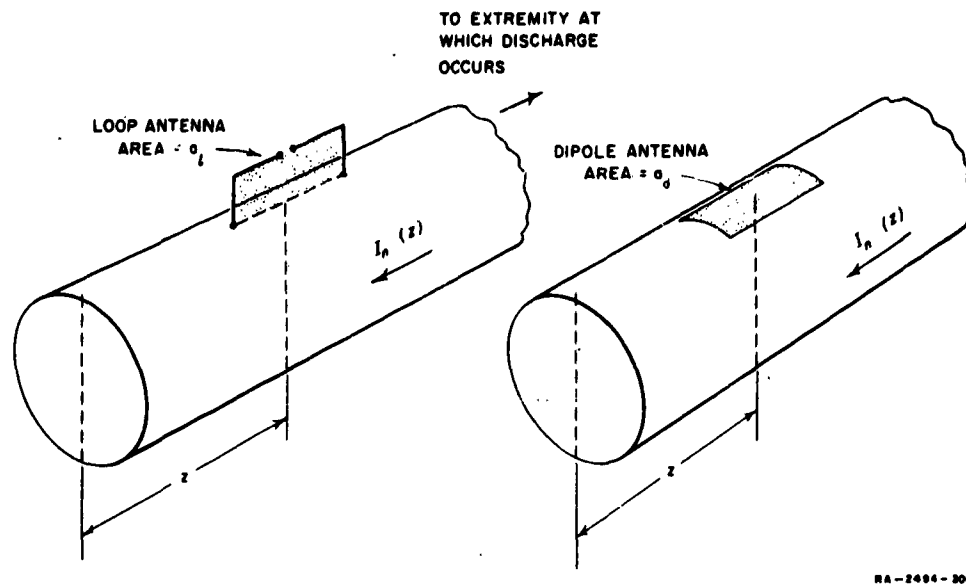
FIG. 54

LOOP AND DIPOLE INSTALLED ON AIRPLANE MEMBER

If s is the peripheral distance around the member, the surface current density at the position of the antennas is

$$J_n \;=\; \frac{I_n}{s}\,\rho \qquad\qquad (50)$$

where ρ is a factor indicating the relative current concentration at the point on the periphery where the antenna is situated.

Let us consider first the loop antenna. At the surface of the aircraft member

$$H_n \;=\; J_n$$

or upon substituting Eqs. (50) and (48)

$$H_n \;=\; \frac{\rho}{s} I_{n0} f(z) \qquad . \qquad\qquad (51)$$

124

The open-circuit noise voltage induced in the loop is given by

$$V_{n l} = a_l \dot{B}_n$$

$$= a_l \mu_0 \dot{H}_n$$

$$= a_l \mu_0 \omega H_n$$

which, upon substituting Eq. (51), becomes

$$V_{n l} = a_l \mu_0 \omega \frac{\rho}{s} I_{n0} f(z) \tag{52}$$

where a_l is the area of the loop.

For a signal field of strength E_s there will be a magnetic field at the position of the loop equal to

$$H_{s l} = \gamma \frac{E_s}{\eta_0} \tag{53}$$

where η_0 is the intrinsic impedance, and γ is the curvature factor giving the field concentration due to the presence of the conducting cylinder. From Eq. (53) we obtain

$$\dot{B}_{s l} = \frac{\gamma \mu_0}{\eta_0} \omega E_s$$

so that for the open-circuit signal voltage induced in the loop we obtain

$$V_{s l} = a_l \dot{B}_{s l}$$

$$= a_l \frac{\mu_0 \omega \gamma}{\eta_0} E_s \quad . \tag{54}$$

125

If we say that our noise voltage V_{nl} arises from an equivalent noise field E_{nl} in a manner analogous to the way V_{sl} comes from E_s in Eq. (54) we can write

$$V_{nl} = a_l \frac{\mu_0 \omega \gamma}{\eta_0} E_{nl} \quad .$$

Upon equating this expression to Eq. (52) we obtain

$$E_{nl} = \frac{\eta_0 \rho}{\gamma s} I_{n0} f(z) \tag{55}$$

For a triangular current distribution we can employ Eq. (49) in Eq. (55) and write for the noise field

$$E_{nl} = \frac{\eta_0 \rho}{\gamma s} I_{n0} z \quad . \tag{56}$$

Now let us consider the dipole antenna. From the equation of continuity we have

$$\frac{\partial I_n}{\partial Z} = - \frac{\partial Q_n}{\partial t} \tag{57}$$

where Q_n is the charge per unit length on the cylinder. If we now observe that

$$\dot{Q}_n = \omega Q_n$$

and

$$\frac{\partial I_n}{\partial Z} = I_{n0} f'(z)$$

and substitute these results into Eq. (57), we obtain

$$I_{n0} f'(z) = -\omega Q_n \quad .$$

126

If we consider magnitude only, this can be rewritten

$$Q_n = \frac{I_{n0}f'(z)}{\omega} \quad .$$ (58)

Defining σ as the surface density of charge on the airplane member, we have

$$\sigma_n = \frac{Q_n}{s}\rho$$

$$= \frac{\rho}{s}\frac{I_{n0}f'(z)}{\omega}$$

and the charge placed on the dipole antenna by the noise current is

$$q_n = a_d\sigma_n$$ (59)

$$= a_d\frac{\rho}{s}\frac{I_{n0}f'(z)}{\omega} \quad .$$

For a signal field E_s, the charge q_s induced on the dipole will be

$$q_s = a_d\epsilon_0\gamma E_s \quad .$$

Again by analogy we can define a noise field E_{nd} such that

$$q_n = a_d\epsilon_0\gamma E_{nd} \quad .$$

Upon equating this expression and Eq. (59) we obtain

$$E_{nd} = \frac{\rho}{s\epsilon_0\gamma\omega}I_{n0}f'(z) \quad .$$ (60)

For a triangular current distribution, $f'(z)$ equals unity, and Eq. (60) becomes

$$E_{nd} = \frac{\rho}{s\epsilon_0\gamma\omega}I_{n0} \quad .$$ (61)

127

It will be of interest at this time to compare the precipitation-static noise characteristics of these two antennas as given by Eqs. (56) and (61). It is evident, for example, from Eq. (61) that the dipole noise field is independent of position along the cylinder, whereas Eq. (56) indicates that the loop noise field increases with increasing distance from the end of the cylinder. Thus, the highest signal to precipitation-static noise ratio is achieved by mounting the loop antenna as close as possible to the nose of the aircraft.

It should also be noted that Eq. (56) is valid only if the loop is oriented as is indicated in Fig. 54 with its axis at right angles to the axis of the cylinder. If the loop is rotated 90 degrees, for example, until its axis is parallel to the axis of the cylinder there will be no coupling between the loop and the noise currents on the cylinder, and the equivalent noise field will be very low. Thus, if a null in the radiation pattern along the axis of the aircraft member can be tolerated, it is possible to achieve a further improvement in signal-to-precipitation-static-noise ratio by decoupling the loop from the noise currents flowing in the airframe by orienting the loop antenna so that its axis is parallel to the axis of the airframe member on which the loop is mounted.

Another interesting comparison between the characteristics of the loop and dipole may be made by noting from Eq. (61) that for a given noise current the equivalent noise field of a dipole varies inversely with frequency. [In connection with the discussion of Eq. (37) it was pointed out that in the quasi-static range, I_n is independent of frequency and that E_n does vary inversely with frequency. This result is verified by the data of Figs. 49 through 52.] Thus, although a given noise current may not produce serious interference at high frequencies, it may still disable communication and navigation equipment at the low frequencies. In the case of the loop antenna, however, Eq. (56) indicates that the noise field is independent of frequency. This is undoubtedly the reason for the frequently observed superiority of a shielded loop over a dipole for low-frequency reception under precipitation static conditions.

By combining Eqs. (55) and (60) we can write the ratio of the noise fields induced in the loop and the dipole, as follows:

128

$$\frac{E_{n l}}{E_{n d}} = \eta_0 \epsilon_0 \omega \frac{f(z)}{f'(z)}$$

$$= \omega \sqrt{\mu_0 \epsilon_0} \frac{f(z)}{f'(z)} \qquad (62)$$

$$= \frac{\omega}{c} \frac{f(z)}{f'(z)}$$

where $c = 3 \times 10^8$ meters/sec. For the case of the triangular current distribution, Eq. (62) becomes

$$\frac{E_{n l}}{E_{n d}} = \frac{\omega}{c} z \quad . \qquad (63)$$

This equation indicates that the superiority of the loop over the dipole increases as the frequency and distance from the end of the cylinder are decreased.

C. LABORATORY MEASUREMENTS

Although the coupling measurements discussed in Secs. II-D and II-E were performed using dipole type antennas, the same instrumentation and the same techniques may be used to study the noise coupling to loop antennas. From the results of the loop-coupling measurements it is possible to calculate the open-circuit voltage generated in the loop by a given discharge current. Then, using Eq. (54),

$$V_{n l} = a_l \frac{\mu_0 \omega \gamma}{\eta_0} E_{n l}$$

$$= \frac{a_l \omega \gamma}{c} E_{n l}$$

the signal induced in the loop may be expressed as an equivalent noise field, $E_{n l}$, generated at the loop location. In Sec. VI-C the results of dipole-coupling measurements were used together with Eq. (37) to determine

a value for the equivalent noise field, E_{nd}, generated at the dipole location. Thus, the laboratory measurements using loops and dipoles yield a value for E_{nl}/E_{nd} which can be compared to the results obtained from Eq. (62).

Loop and dipole noise-coupling measurements were made using antennas mounted at several positions within two meters of the nose of the model sketched in the upper part of Fig. 55. In order to obtain a predicted noise-field ratio from Eq. (62) for comparison with the results of the measurements, therefore, it was necessary to obtain expressions for the
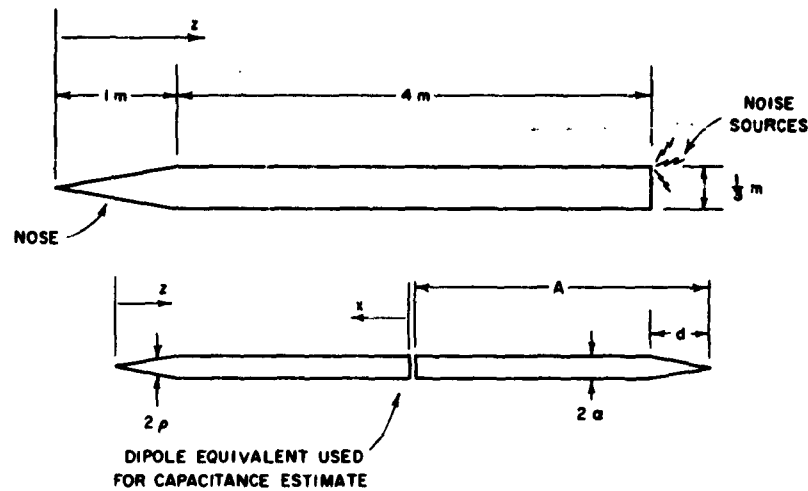
FIG. 55

MODEL USED FOR LOOP AND DIPOLE COMPARISON MEASUREMENTS

form of the noise current $f(z)$ and the charge $f'(z)$ as a function of position on the forward portion of the model. The charge per unit length $I_n'(z)$ at a particular position along the model will be proportional to the capacitance per unit of the model at that position. If we consider the model used in the measurements to be one-half of the short dipole illustrated in the lower part of Fig. 55 we may use the equation

$$C(x) = \frac{\pi\epsilon}{\log (2x/\rho)} \tag{64}$$

given by Schelkunoff[22] for the capacitance per unit length of a short dipole to determine the manner in which the capacitance per unit length varies near the nose of the model. From the lower part of Fig. 55 we note that

$$x = A - z$$

and

$$\rho = \frac{\alpha z}{d} \quad \text{for} \quad z < d$$

$$\rho = \alpha \quad \text{for} \quad z \geq d \quad .$$

Substituting these results into Eq. (64) we obtain

$$f'(z) = \frac{1}{\log \dfrac{2(A - z)d}{\alpha z}} \quad \text{for} \quad z \leq d$$

$$= \frac{1}{\log \dfrac{2(A - z)}{\alpha}} \quad \text{for} \quad z > d \quad .$$

(65)

Equation (65) was evaluated and plotted for $A = 5$, $d = 1$ and $\alpha = \frac{1}{6}$ in the range $0 < z < 2$. The form of the noise current, $f(z)$, was found by graphical integration of Eq. (65).

With the antennas located in the positions shown in the upper part of Fig. 56, the calculations indicate that $f(1.69m) = 0.39$ and $f'(1.69m) = 0.271$. Substituting these values into Eq. (62) we obtain for a frequency of 2 Mc,

$$\frac{E_{nl}}{E_{nd}}_{calc} = -24.3 \text{ db} \quad .$$

131
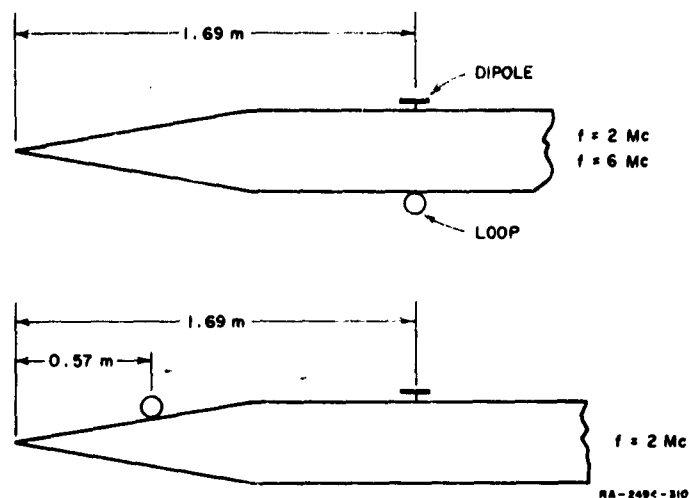
FIG. 56

ANTENNA LOCATIONS

The results of the coupling measurements conducted at this frequency with the antennas at these locations indicated that

$$\frac{E_{nl}}{E_{nd}}_{meas} = -28.7 \text{ db}$$

which is in reasonable agreement with the predicted value.

If the antennas are left in the positions shown in the upper part of Fig. 56 and the frequency raised to 6 Mc, one obtains from Eq. (62)

$$\frac{E_{nl}}{E_{nd}}_{calc} = -14.7 \text{ db}$$

which is in good agreement with the measured value

$$\frac{E_{nl}}{E_{nd}}_{meas} = -16.6 \text{ db} \quad .$$

132

Leaving the dipole at its original position, and moving the loop forward as is indicated in the lower part of Fig. 56 we obtain $f(0.57m) = 0.105$ and $f'(1.69m) = 0.271$, which, when substituted into Eq. (62), yield for a frequency of 2 Mc

$$\frac{E_{nl}}{E_{nd}}_{calc} = -35.6 \text{ db}$$

which is in very good agreement with the measured value

$$\frac{E_{nl}}{E_{nd}}_{meas} = -36.6 \text{ db}$$

An experimental investigation was made to determine the degree of decoupling which may be achieved in practice by orienting the loop for minimum coupling to the noise currents flowing in the airplane member on which the loop is mounted. With the loop in the position indicated in the upper part of Fig. 56, the spark-gap signal-source probe (see Figs. 4 and 5) used for the coupling measurements was held against the aft end of the model and the loop was rotated for minimum response. It was found that the spark-gap signal source did not have sufficient strength to produce a measurable signal in the receiver when the loop was positioned for minimum coupling. For this reason, the spark gap was replaced by a 2-Mc battery-operated oscillator which was mounted inside the model and excited a 1½-inch-long dipole protruding from the aft end of the model. Using this laboratory set-up, it was found that rotating the loop so that its axis was parallel to the axis of the model reduced the coupling to the noise currents by roughly 25 db. Thus a properly oriented loop antenna located near the end of an aircraft member can be almost immune to precipitation-static interference, provided corona discharges do not occur from the end in question

VIII   TECHNIQUES FOR REDUCING NOISE

A.   GENERAL

The success with which it was possible to predict the characteristics
of the precipitation-static interference generated in aircraft antennas in-
dicated that the mechanisms by which the noise is generated and coupled into
the receiving systems were well understood. It was felt, therefore, that
the same theories of noise generation and coupling should be applied to the
problem of eliminating precipitation-static interference.

In considering methods for precipitation-static elimination it is ap-
parent immediately that the problem would be solved if some means could be
developed to prevent the aircraft from charging. As was indicated in
Sec. I-A, however, early experiments demonstrated that this technique could
not be implemented in practice. For this reason, in devising techniques
for the elimination of precipitation static, it will be assumed that air-
plane charging is permitted to occur at its normal rate.

Several different approaches to the precipitation-static noise elimi-
nation problem are possible. We could decide, for example, that the noise-
reduction scheme should require no modification of the receivers. In this
case. it would be necessary to devise ways to reduce the noise current in-
duced in the antenna terminals. From Eq. (6) we find that one method for
reducing the noise current is to reduce the coupling ψ between the antenna
and the discharge-noise source. The coupling may be reduced either by
using specially designed receiving antennas or by causing the corona dis-
charges to occur from dischargers designed to minimize the noise coupling.
It is also evident from Eq. (6) that the noise current can be reduced by
reducing the source-spectrum amplitude $D(\omega)$ at the radio frequencies.
Since a corona discharge consists of a series of short current pulses, it
generates appreciable RF interference. If, for example, it were possible
to ionize the air in the vicinity of the aircraft, the same current could
be discharged without generating RF noise. Finally, we might decide to de-
vise schemes to operate on the noise signal after it reaches the receiving
systems. Various techniques which may be used to reduce precipitation
static will be discussed in considerable detail.

135

B. DECOUPLED ANTENNAS

A considerable decrease in precipitation-static equivalent noise field may be achieved through the use of antennas designed to be decoupled from the noise sources. In Secs. VII-B and -C it was demonstrated that the equivalent noise field of a loop antenna could be reduced by mounting it near the end of an airplane member since the loop tends to couple to the noise currents flowing in the member, and since these currents are small near the end of the member. For example, moving the loop from the position shown in the upper part of Fig. 56 to the position shown in the lower part of the figure, the measured noise field was reduced by 8 db. When the loop was moved out to the nose of the model the noise field was found to be 25 db lower than at the original position. Thus, a good position for a loop antenna is at the end of any member from which discharges do not occur (such as the nose of the fuselage).

In many instances, however, it is not possible to mount a loop at the very nose of the aircraft. One may in this case mount the antenna aft of the nose in a position such as that shown in the upper part of Fig. 56, but with the axis of the loop parallel to the axis of the member. As is indicated in Sec. VII-C, rotating the loop in this manner results in a decoupling of roughly 25 db. It should be noted that with this technique decoupling occurs only if the direction of current flow in the airplane member is parallel to the axis of the loop. Thus, the antenna should be mounted sufficiently near the end of the member that the direction of current flow does not vary with the position of the noise source. For example, if the loop were mounted on the fuselage near its junction with the wings, the direction of current flow generated by a discharge from the left wing would be different from the direction of the current generated by a discharge from the right wing. In this case it would be necessary to choose a compromise setting for the loop such that a certain amount of noise from one or both of the wings was picked up.

A problem associated with the use of a loop oriented with its axis parallel with the axis of the fuselage of the aircraft is that a null in the radiation pattern will exist in the fore and aft direction. This objection may be overcome by using two loops mounted on orthogonal members of the aircraft with the axis of each loop parallel with the axis of the member on which it is mounted (one loop on the fuselage and one loop on a wing, for example). With this mounting arrangement, each loop is

136

decoupled from the noise currents on its airplane member, but since the the two loops are mounted at right angles to one another, omniazimuthal pattern coverage is achieved.

Another decoupling scheme which requires two loops but which does not require that one be mounted on a wing may be used, provided a normal loop radiation pattern with a null athwartship of the aircraft is not objectionable. In this case, two loops should be mounted at the same fuselage station, one on the top centerline and one on the bottom centerline (for example, one at each of the two antenna locations shown in the upper part of Fig. 56). Each loop should be oriented with its axis athwartship. If the fuselage is symmetrical, the magnitudes of the desired signals induced in each of the two antennas will be equal, as will the magnitudes of the noise signals. The loops may be connected to the receiver in such a manner that the noise signals cancel and the desired received signals add. This decoupling technique was not investigated experimentally. However, experiments, which will be described later, using a pair of dipole antennas, indicates that decoupling of the order of 25 db may be expected if care is taken in balancing the two antennas.

By the use of a third loop it is possible to eliminate the null obtained in the radiation pattern when both antennas are mounted on the same member (such as the fuselage) in the scheme described above. If the third loop is mounted on the same member with its axis parallel to that of the member this loop will be decoupled from the noise currents by roughly 25 db so that its addition will not contribute appreciably more noise to the system. Its radiation pattern, however, will fill in the null in pattern of the original pair of loops.

Dipole antennas may also be decoupled from precipitation static interference. For example, let us assume that a dipole antenna is mounted at each of the antenna locations shown in the upper part of Fig. 56. If a noise current is induced in the fuselage by a discharge from an extremity we will find that the charge density resulting from this noise current will in general be the same at the lower and upper antenna location. Furthermore, the charge variation at the two locations will be in phase. Thus, equal, in-phase noise currents will be generated in the two antennas. A vertically-polarized signal, on the other hand, will induce equal signal currents 180 degrees out of phase in the two antennas. Thus, if the outputs from the two antennas are fed to a balanced input transformer the noise

137

currents will cancel and the signal currents will add. The radiation pattern of this antenna combination is omniazimuthal to vertically polarized signal with negligible response to horizontally polarized signals.

In the experimental investigation of this decoupling technique, balance of the two antennas was achieved by variable attenuators and a line stretcher in the lines to the antennas. It was found that it was possible to obtain at least 25 db of decoupling from noise generated at any of the aircraft extremities. For these tests the antennas were located on the fuselage two-thirds of the way from the nose to the leading edge of the wing.

It should be recognized that noise-canceling schemes using either loops or dipoles will work perfectly only if the aircraft is symmetrical about a horizontal plane, if the balanced antennas are symmetrically located with respect to this plane, and if all corona-noise sources lie in the plane, of symmetry. In this case an adjustment of balance which results in minimum noise from a source at one extremity will be optimum also for discharges from the other extremities. In actual aircraft these conditions are only approximated. Experiment indicates, however, that in the quasi-static frequency range a balance can be obtained that results in an over-all reduction of noise from sources at all extremities of greater than 25 db.

C. DECOUPLED DISCHARGERS

In the preceding section it was indicated that the severity of precipitation-static interference may be reduced considerably through the use of several receiving-antenna designs. It will be of interest next to consider the changes that can be made in the aircraft discharging processes in order to reduce the noise they generate in the antennas.

The coupling theorem of Eq. (1) indicates that the noise current induced in an antenna is maximized when the discharge characterized by the current density J_2 occurs in the direction of the reciprocal field E in the region of highest reciprocal field. Since the dc fields are maximum at the aircraft extremities the corona discharges occur there, but, from Fig. 7, it is apparent that the reciprocal coupling fields are also maximum at the extremities. If we consider the small region in the immediate vicinity of the trailing edge as is illustrated in Fig. 57, it is evident that the field configuration, either RF or static, is determined by the shape of the conductor forming the boundary. It follows from this observation that the discharge, which occurs in the direction of the maximum dc field, also lies

138
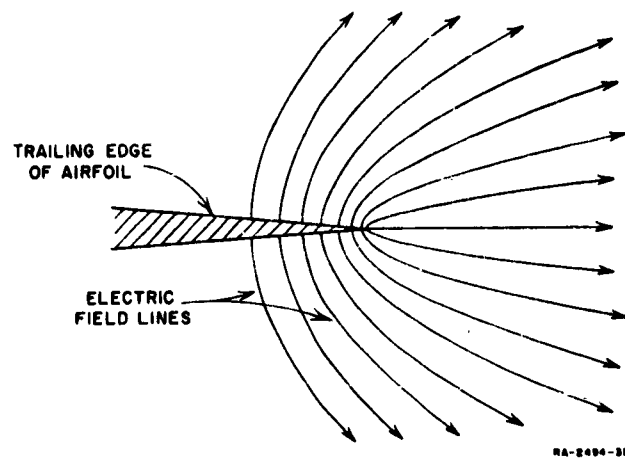
FIG. 57

ELECTRIC-FIELD CONFIGURATION
AT TRAILING EDGE OF AIRFOIL

in the direction of the maximum coupling field. Thus, perversely, corona
discharges from an aircraft occur in precisely the manner necessary to
couple the greatest noise into its receiving systems.

Referring again to Eq. (1) it is apparent that several approaches are
possible in an effort to modify the discharge region to produce minimum
noise in the receiving systems. One could, for example, endeavor to alter
the character of the discharge described by J_2 in an effort to reduce its
RF noise content. It was observed in Ref. 7 that the amplitude, A of
corona-noise pulses decreases with decreasing discharge point diameter.
If the amplitude of the pulses is decreased, but the pulse form is unaltered,
the number of pulses per second, ν, necessary to discharge a given current
must increase in such a manner that $A\nu$ remains constant. From Eq. (18) or
(19) we find that the noise-current spectral density $\sqrt{G}$ generated by a
series of corona pulses is proportional to the product $A\sqrt{\nu}$. Thus we can
write

$$\frac{\sqrt{G_1}}{\sqrt{G_2}} = \frac{A_1\sqrt{\nu_1}}{A_2\sqrt{\nu_2}}$$

which, upon substituting the condition $A_1\nu_1 = A_2\nu_2$, becomes

$$\frac{\sqrt{G_1}}{\sqrt{G_2}} = \sqrt{\frac{A_1}{A_2}} \tag{66}$$

139

which indicates that the noise current varies as the square root of the pulse amplitude. It should be possible, therefore, to achieve some noise reduction by reducing dimensions of the points from which the discharges occur.

An experiment was conducted to determine the amount of noise reduction that could be achieved in practice through the reduction of discharge-point size. Corona discharges were induced from a 0.020-inch-thick trailing-edge mock-up installed in the set-up of Figs. 8 and 9, and noise measurements were made. Next, etched tungsten points were attached 3/4-inch apart along the trailing edge of the mock-up in such a fashion that the pin points projected 1/4-inch aft of the trailing edge. The pins were conically tapered from the position of attachment to the point, which had a radius not exceeding 0.0005 inches. When high voltage was applied to the mock-up it was observed that all of the discharges occurred from the pins. For a given discharge current it was found that the noise was reduced by a factor not exceeding 6 db below the noise obtained with the unmodified 0.020-inch-thick trailing edge. Thus, only relatively insignificant noise reductions should be expected to result from the installation of small-diameter discharge points at the aircraft extremities.

Two other approaches to the problem of noise reduction are suggested by Eq. (1). These are reducing the magnitude of $\mathbf{E}$ in the discharge region, and forcing the discharge-current density $\mathbf{J}$ to lie in a direction orthogonal to the coupling field. Since the corona discharge characterized by $\mathbf{J}$ occurs in the direction of the maximum dc field, the foregoing requirement implies that we must devise a way of securing different structures for RF and dc fields in order that E_{RF} be orthogonal to E_{dc}, and that $E_{RF_{min}}$ occur at $E_{dc_{max}}$ in the region of the discharge. One way of accomplishing this objective is illustrated in Fig. 58. The upper part of the figure shows a cross section of the trailing edge of an airfoil surface in which the rearmost portion is electrically isolated from the remainder of the structure. It is evident that there are two lines along the isolated conductor on which the field is zero, and a considerable region over which the field is very small. If the isolated conductor is connected to the airframe by a sufficiently high resistance, the RF coupling field will still be that shown in the upper part of Fig. 58, and a corona discharge from a pin located on the line of zero coupling will produce no noise in the antenna. (The requirement on the resistance is that it be much greater than the capacitive reactance of the isolated conductor at the
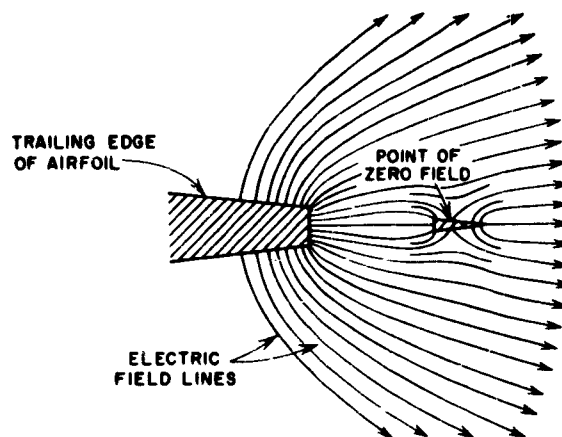
RF COUPLING FIELD CONFIGURATION
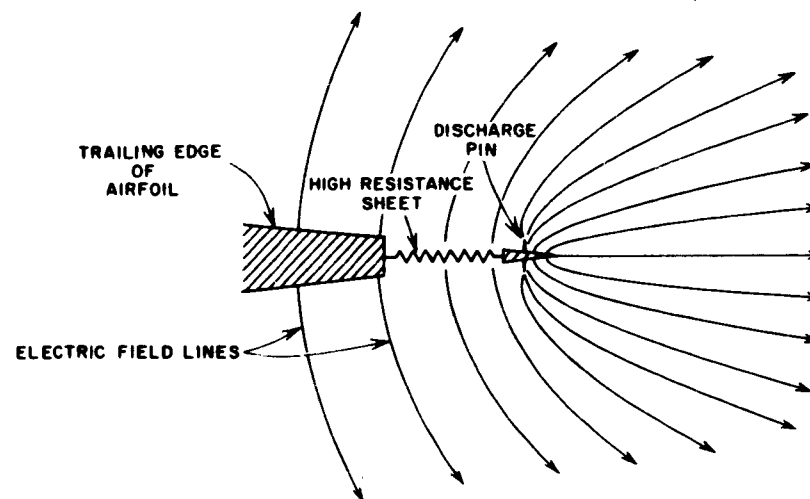
STATIC FIELD CONFIGURATION

RB-2494-312

FIG. 58

ILLUSTRATION OF FIELDS ABOUT FLUSH DECOUPLED DISCHARGER

141

frequency of interest--very high values of resistance will be required
at low frequencies.) To the dc field, however, the conductor will appear
to be connected to the airfoil, giving the field configuration shown in
the lower part of Fig. 58. The dc field is concentrated at the position
of zero coupling by the discharge pin located there, causing the discharge
to occur at that point. Comparing the two parts of the figure we observe
that with this structure $E_{dc_{max}}$ occurs at the position of $E_{RF_{min}}$ and, in
the vicinity of the discharge, the RF and static fields are very nearly
orthogonal. Thus, this discharger design fulfills the requirements for
minimum noise coupling. Laboratory tests indicated that noise reductions
exceeding 35 db were possible with this design. A practical flush dis-
charger designed in this manner and used in the flight tests conducted on
the Boeing KC-135 prototype in 1957-58 is shown in Fig. 59.[10,11,19]

Although tests of the flush dischargers were encouraging, they also
pointed out several drawbacks of this discharger type and prompted the
development and testing of other types. The major shortcoming of flush-
mounted dischargers is the high cost of retrofitting them to existing
aircraft. Of course, if the discharger design were considered early in
the development program of a new aircraft, its cost should not appreciably
exceed a normal section of trailing edge. Even where the cost of flush
dischargers is not an important consideration, however, their high corona-
threshold potential argues against their use, since a high aircraft potential
would be required to discharge a given current. (Aircraft potential should
be maintained at the lowest possible value to reduce the possibility of non-
decoupled discharges from the airframe itself.) For example, flight-test
measurements on the KC-135 prototype indicated that, at 30,000 feet altitude,
the trailing edges of the wings reached threshold at an aircraft potential
of 80 kilovolts. At the same altitude the threshold potential of the flush
dischargers was 75 kv while the threshold potential of a rod-shaped ortho-
decoupled discharger (discussed next) mounted near the tip of a wing was
only 8 kv.

In considering ways in which the decoupled discharger can be modified
to overcome the objections discussed in the preceding paragraph it is ap-
parent that the isolated conductor shown in the upper part of Fig. 58 need
not be continuous along the trailing edge. The arguments used in describing
the mechanisms by which decoupling is achieved in the flush discharger apply
equally well if we consider the discharge pins in the lower part of Fig. 58 to be
mounted in a cone-shaped conductor attached to a rod of high-resistance material.

METAL STRUCTURE OF WING OR TAIL

PLASTIC OUTBOARD TIP

FIBERGLASS PLASTIC

ROW OF DISCHARGE POINTS

ALUMINUM EXTRUSION

METAL STRUCTURE

FIBERGLASS WITH HIGH-RESISTANCE COATING

ALUMINUM EXTRUSION
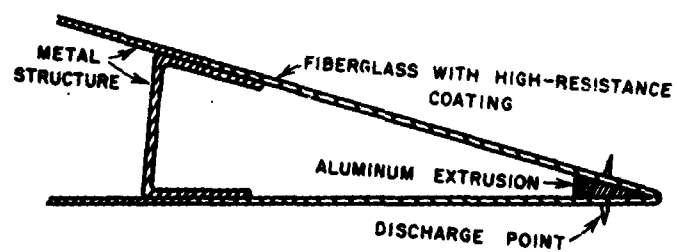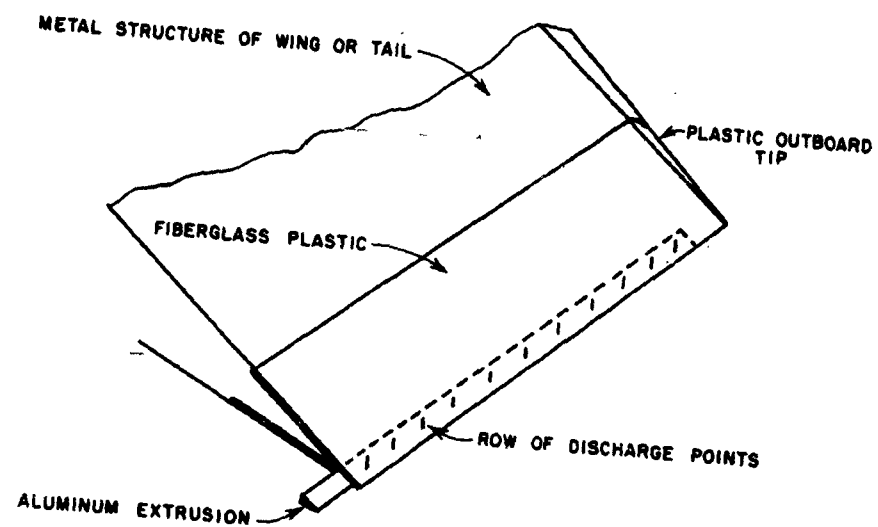
DISCHARGE POINT

(POSITION OF POINT FOR MINIMUM COUPLING DETERMINED BY ELECTROLYTIC TANK FIELD MAPPING TECHNIQUES)

RA-2095-F-21

FIG. 59
CONSTRUCTION OF FLUSH, ORTHO-DECOUPLED DISCHARGER

143

These rods may be attached at suitable intervals along the trailing edges
of the airfoils. It is evident that a rod protruding aft from the trailing
edge of the wing will tend to concentrate the static fields in this region,
so that the corona threshold of a discharger of this type should be much
lower than that of the trailing edge to which it is attached. Thus dis-
chargers of this type may be expected to discharge large currents before
the aircraft potential reaches the threshold value for discharges from
the airframe.

The initial cost of fabricating and installing a set of rod-shaped
decoupled dischargers on an aircraft should be much lower than the cost
of a flush discharger installation. Furthermore, depending upon the de-
sign of the flush discharger installation, the maintenance costs of the
rod-shaped dischargers may be lower.

The final design developed for the rod-shaped dischargers--hereafter
called Type A ortho-decoupled dischargers—is illustrated in Fig. 60.
Instead of mounting the discharging pin in a conductor at the end of the
high-resistance rod the pin was mounted directly in the rod itself at the
position of minimum coupling near the end of the rod. The magnitude of
the coupling as a function of position along the rod was calculated in
Appendix F by computing the radial field near the end of a high-resistance
rod attached to a conducting sheet immersed in an RF field. The results
of this calculation, shown in Fig. 61, indicate that the magnitude of the
coupling and the position of the minimum both are functions of frequency
and rod resistance. Thus, since a discharger is not a single-frequency
device, it was necessary to compromise somewhat to secure the best perfor-
mance over a wide frequency range. It is evident from the figure that if
the discharge pin is located at the position of the coupling minimum for
$\gamma^2 = 0.4$ (high frequencies) the performance of the discharger at low fre-
quencies will be far from optimum. If, however, the pin is moved in from
the end of the rod to the position of the minimum for $\gamma^2 = 40$, the high-
frequency performance of the discharger will be only slightly less than
optimum. Hence, insofar as discharger decoupling is concerned, it is
safest to err by positioning the discharge pin farther than necessary from
the outboard end of the rod. To minimize the discharger corona threshold
and to reduce the possibility of corona discharges from the end of the
high-resistance rod, however, the pin should be located as near as possible
to the end of the rod. On the dischargers used in the flight tests the
pins were located at $\xi = 0.166$ to $\xi = 0.125$ (one inch from the end of a

144

FIG. 60

TYPE A ORTHO-DECOUPLED DISCHARGER MOUNTS PARALLEL TO WINDSTREAM

145
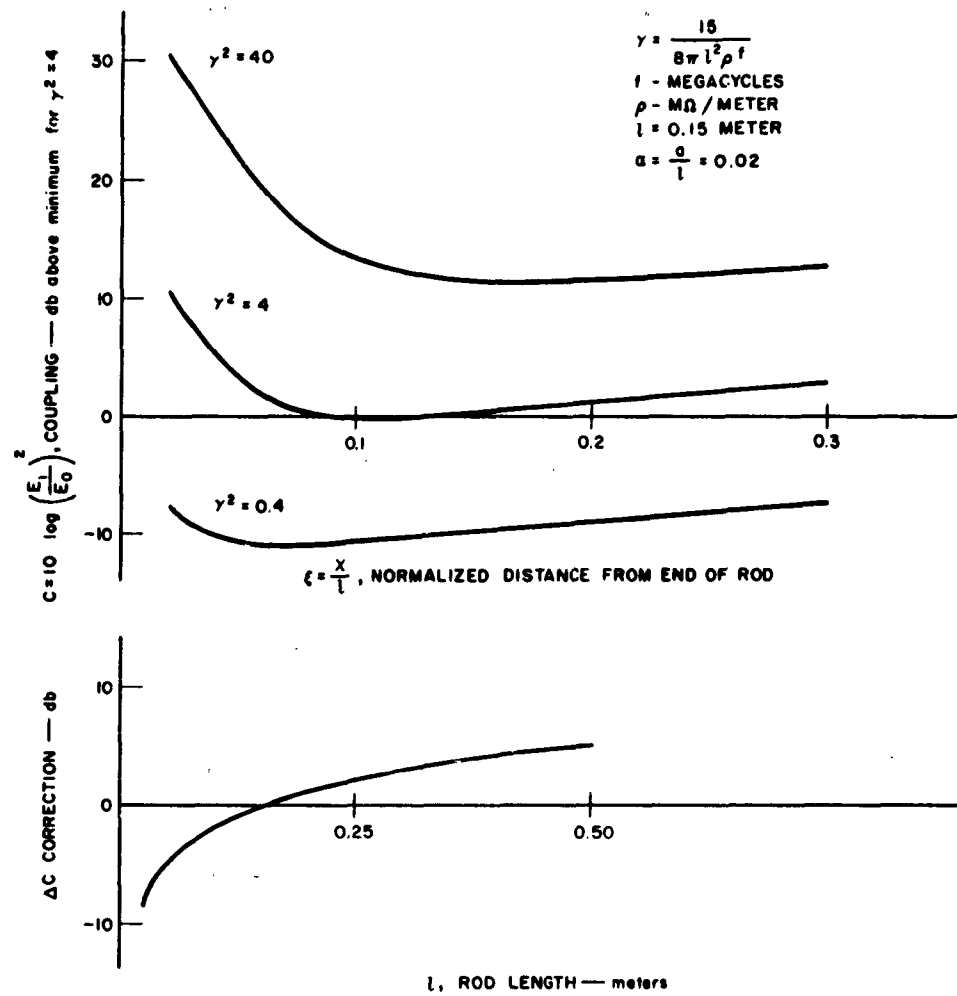
FIG. 61

DISCHARGER NOISE DECOUPLING

RA-2494-313

rod 6 to 8 inches in length). To prevent discharges from the end of the rod, the aft 1/2 inch of the rod was coated with a dielectric material applied over the conductive film on the rod as is shown in Fig. 60.

Before fabricating a large number of dischargers for flight-test evaluation, it was felt that it would be desirable to verify experimentally the position of coupling minimum along the discharger rod. This was done using the set-up shown in Fig. 62. The discharger rod was mounted on the trailing edge of the airfoil mock-up used to study corona-noise characteristics. One might now install a discharge pin at some point along the rod, and using the instrumentation shown in Fig. 8, induce a discharge from the pin and measure the noise generated in the set-up. The pin could then be moved to a different position and the measurement repeated.

A variation of this procedure was followed in the laboratory measurements. Instead of using the discharge from a pin, the spark probe shown in Fig. 5 moved from position to position along the rod served as the noise source. If the resistance per unit length of the high-resistance rod in the probe is high with respect to that of the discharger rod, the probe will not alter the coupling fields within the mock-up. Since the dimensions of the conductors forming the spark gap are comparable to the dimensions of the discharge pin they will produce roughly the same field distortion as would the discharge pin. Thus, the point at which the noise generated by the probe is minimum corresponds to the point of minimum coupling for a discharge from a pin. The spark probe offers the advantage that the spark produces much more noise than does a corona discharge, thereby reducing sensitivity requirements on the instrumentation. Furthermore, the spark is much easier to move from position to position than is a pin inserted into the discharger rod. The results of the laboratory measurements indicated that the optimum discharger-pin location is roughly one inch from the aft end of the rod used in the flight tests, in agreement with the results of the calculations shown in Fig. 61.

During the first set of flush discharger tests it was found that noise suddenly appeared in the receiving systems when the aircraft potential exceeded 1.3 times the discharger threshold potential.[10,11,19] This occurred when the current leaving via the wing dischargers exceeded 50 μa. It was hypothesized that the noise-producing discharges were occurring in the regions of vortex formation at the tips of the airfoil surfaces. The greatly reduced local pressures existing in the vortex

FIG. 62

EXPERIMENTAL DETERMINATION OF COUPLING MINIMUM POSITION

148

cores could lower the corona threshold of points having relatively large radii to values much below those predicted on the basis of still-air measurements. It was further theorized that if discharges occurring in the vortex regions were responsible for the noise observed, the noise could be eliminated by locating decoupled dischargers in this region to provide a source of ions to reduce the fields at the airfoil tips themselves.

The discharger developed for this purpose (called the Type B ortho-decoupled discharger) is illustrated in Fig. 63. Except for mechanical design it is identical to the Type A discharger in that it consists of a tungsten pin located at the point of minimum coupling along a band of resistive material. The position of the point of minimum coupling on the Type B discharger was found experimentally using the set-up of Fig. 62.

The effectiveness of the Type B dischargers was demonstrated on succeeding flight tests when, with flush dischargers and Type B dischargers installed, it was possible to discharge currents of 130 μa from the wings without generating discernible noise. Unfortunately, clear weather prevailed during this series of tests, and it was not possible to test this discharger combination at higher charging rates to determine its maximum discharging capability.

A typical installation of Type A and Type B dischargers on the wing of an aircraft is shown in Fig. 64. The measured corona thresholds of the various dischargers employed in the KC-135 prototype installation are given in Table V. Recalling that the threshold potential of the unmodified wing tip at 30,000 foot altitude is 80 kv, it is evident that the dischargers should discharge large currents before any other point on the aircraft reaches threshold.

The discharging capability of an installation of Type A and Type B dischargers was demonstrated during the KC-135 prototype flight tests when currents in excess of 3 ma (see the discharger currents listed in Table IV and Fig. 40) were discharged from the aircraft without generating measureable interference in any of the antennas. It is interesting to consider the implications of this result in terms of the effectiveness of the dischargers in eliminating noise. From the upper curve of Fig. 49 we observe that on the unmodified aircraft with a total discharge current of 250 μa the equivalent noise field at the tail-cap antenna at a frequency of 500 kc

149

RP-2848-8
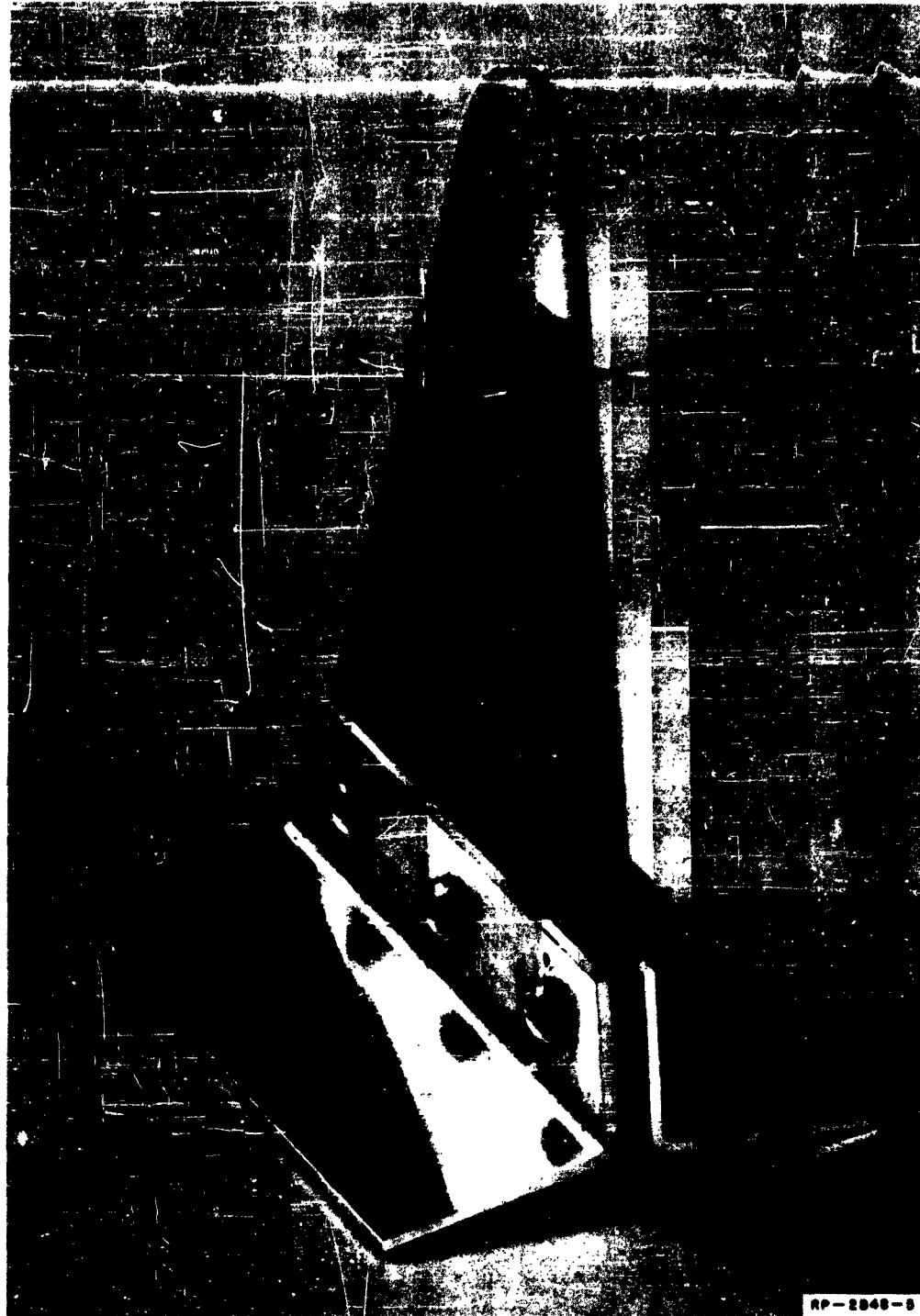
FIG. 63

TYPE B ORTHO-DECOUPLED DISCHARGER MOUNTS AT RIGHT ANGLES TO WINDSTREAM

150
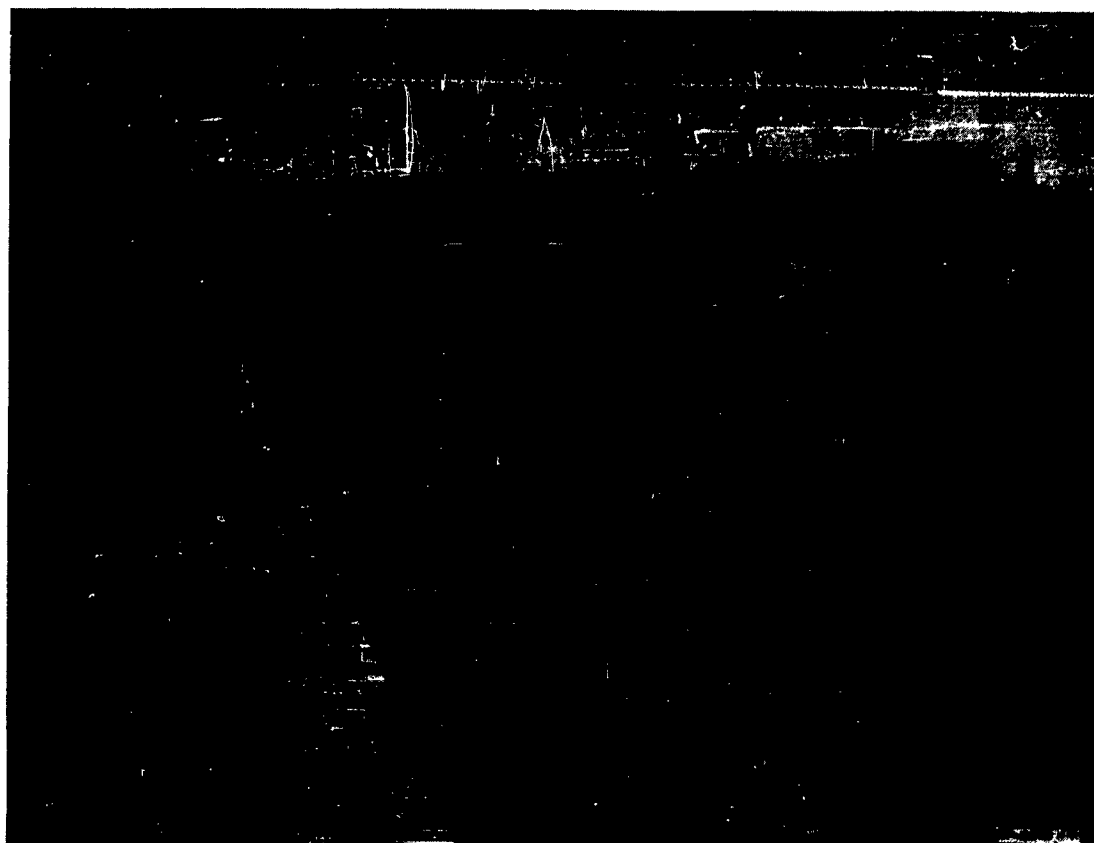
FIG. 64

LOCATIONS OF DISCHARGERS ON WING OF QANTAS 707 AIRCRAFT

TABLE V

THRESHOLD POTENTIALS OF TYPE-A AND TYPE-B DISCHARGERS
INSTALLED ON BOEING 367-80 AIRCRAFT

DISCHARGER AND LOCATION	AIRCRAFT POTENTIAL FOR CORONA THRESHOLD AT 30,000-FOOT ALTITUDE (kilovolts)
Type A, 0 inches from wingtip	7.8
Type A, 15 inches from wingtip	13
Type A, 45 inches from wingtip	15
Type A, 75 inches from wingtip	14
Type B, Aft	38
Type B, Forward	56

is 1650 μv per meter in a 1-kc bandwidth. If the current is increased to 3 ma the noise field will be roughly

$$E_n = \sqrt{\frac{3000}{250}} \, 1650$$

$$= 5720\mu \text{ volt/meter.}$$

With the dischargers installed, however, the precipitation static noise was so low that it was masked by the residual noise which had equivalent noise-field strengths of the order of 20 microvolts per meter per kilocycle bandwidth even in clear air. Thus, the noise reduction afforded by the dischargers as determined from the flight-test data was at least 50 db. The results of the discharger noise decoupling calculations of Appendix F indicate that the noise reduction at a frequency of 500 kc is 55.6 db. At higher frequencies the noise reduction is even higher.

From the foregoing discussion it is evident that decoupled dischargers provide an excellent means for discharging an aircraft without generating interference in the receiving systems. The dischargers do, however, have limitations which should be pointed out. As was indicated in Appendix E and in Sec. V-C-1, to increase the current leaving from a discharger it is necessary to increase the windspeed or the airplane potential. Thus, a discharger can handle only a limited current before the airplane potential exceeds the threshold of non-decoupled points on the airframe. An installation, therefore, should consist of sufficient dischargers to handle the maximum normal charging currents without exceeding this threshold.

On jet aircraft, which generally have no projections beyond the mold lines of the aircraft, the number of dischargers necessary to meet the above requirement may be less than the number necessary on a propeller-driven aircraft, even assuming that the total charging currents to the jet airplane are higher. On jet aircraft the regions with the lowest corona-threshold potentials are the airfoils, and, as is indicated in Fig. 43, the space charge generated by current leaving from the dischargers raises the threshold potentials of the airfoils. In the case of propeller-driven airplanes, however, there are regions of low threshold potential (such as propeller tips and fixed wire antennas) in which it is not possible to mount decoupled dischargers. Thus, in these regions the threshold potential is not increased by the space charge produced by current from

152

the dischargers. Hence, the maximum permissible aircraft potential may
be such that the current per discharger is considerably lower than it is
on a jet.

Unfortunately, it was not possible to investigate this problem
further. Corona thresholds of propellers cannot be estimated with any
accuracy from laboratory measurements since the amount of pressure reduc-
tion resulting from vortex formation at the tips is not known. All of the
flight tests, furthermore, were conducted on turbojet aircraft. From an
inspection of typical propeller tips, however, it appears that their
threshold potentials can be expected to be as low as the thresholds of
the wing tips, particularly in the case of aircraft on which the outboard
engines are mounted far out along the wing.

D. BIASED DECOUPLED DISCHARGERS

Although the decoupled dischargers discussed in the previous section
will discharge an aircraft without generating noise in its receiving systems,
the airplane potential must be several thousand volts before discharging
occurs. For certain special applications such as the study of atmospheric
electric fields it is necessary that the airplane potential be nearly zero.
Furthermore, the device used to maintain the aircraft at zero potential
should not generate interference in the receiving systems. The biased de-
coupled discharger used in the KC-135 prototype flight-test program met
these requirements. [11,19]

The discharger, shown in Fig. 65, consisted of a 36-inch long aluminum
rod of elliptical cross section mounted on glass fiber struts aft of the
tail cone, with the axis of the rod vertical, and with the major axis of
the ellipse parallel to the windstream. Thus, the rod is equivalent to the
isolated conductor in the upper part of Fig. 58 and there is a line of mini-
mum coupling along the minor axis of the ellipse. Pins protruding at right
angles to the airstream were inserted into the rod at three-inch intervals
along the line of minimum coupling, and the discharging element was connected
to a 0-to-60-kv high-voltage supply through a high resistance so that the
final configuration was similar to that of the decoupled discharger
illustrated in the lower part of Fig. 58.

When the aircraft becomes charged in precipitation a region of high
field will exist at the discharger, tending to induce negative-point corona
discharges from the pins. If the discharger is now biased negatively with

153
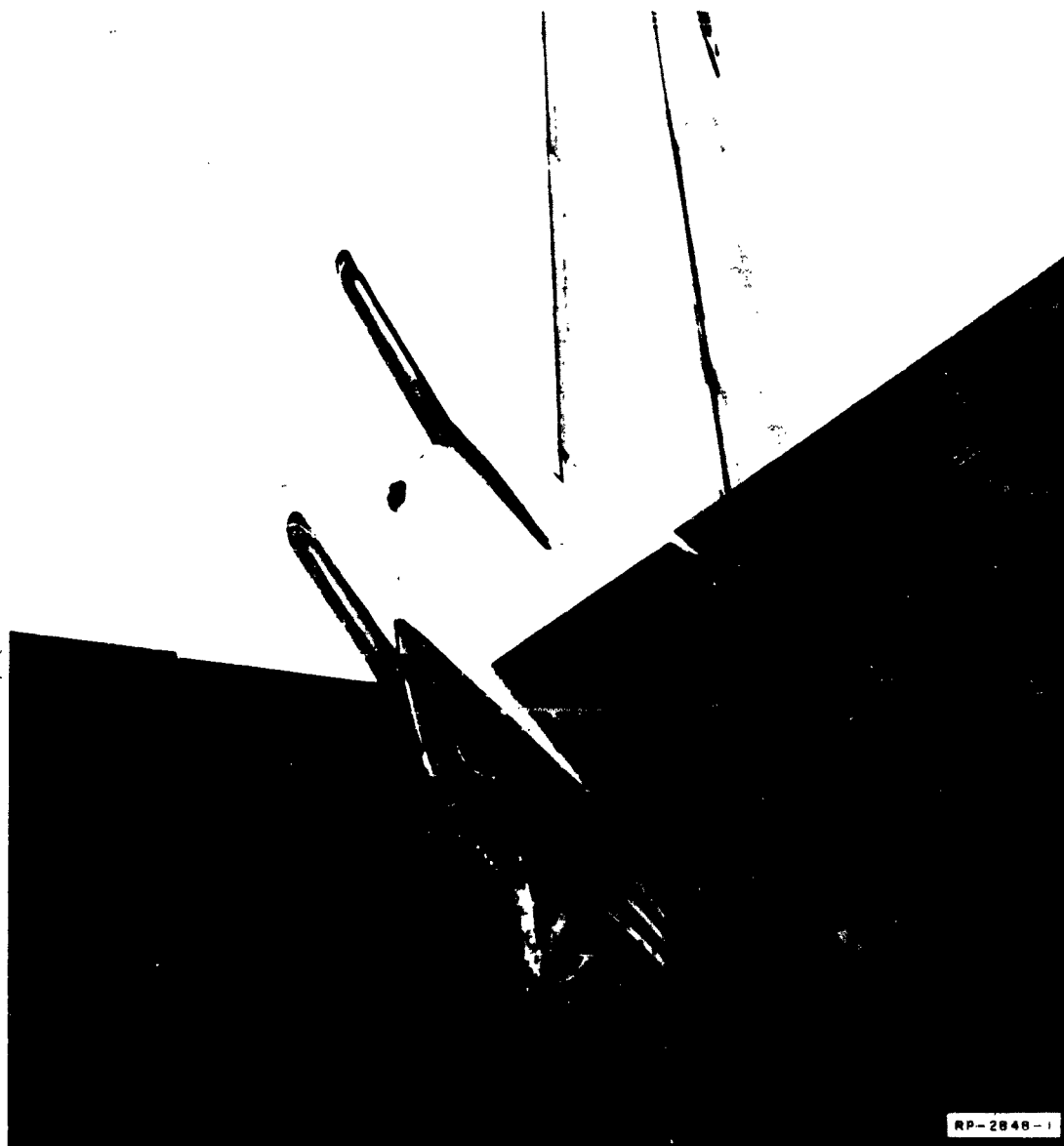
FIG. 65

TAIL-CONE CHARGER INSTALLED ON 367-80 AIRCRAFT

respect to the aircraft the fields generated by the applied bias will increase the field intensity at the pins, thereby increasing the current they discharge. If the bias is made sufficiently high it is evident that negative-point corona discharges can be produced at the discharge even when the airplane potential is zero. Thus it possible to maintain the aircraft at zero potential even in regions of charging. There is, however, an upper limit on the current that may be discharged from a given discharger, as will become evident from the following argument.

Let us assume that the potential of the aircraft is zero and that the discharger rod is maintained at a negative potential V_b with respect to the aircraft. In this case the field structure in the vicinity of the discharger is that illustrated in Fig. 66. It is evident from the figure that in the absence of wind there would be no net charge leaving the system. Negative ions produced by the corona discharges from the pins would be directed back to the aircraft by the field existing between the rod and the airframe. Under normal flight conditions, the wind stream overcomes the applied electric field and carries the ions away so that there is charge leaving the system. The wind may be considered to be equivalent to an electric field directed parallel to the wind-stream lines. The magnitude E_w of the wind field is given by

$$E_w = \frac{u}{k} \tag{67}$$

where u is the wind velocity and k is the ion mobility. Let us consider a surface through the points where the applied bias field E_b is parallel to u as is suggested by the dotted line in Fig. 66. If everywhere on this surface the magnitude of the wind field E_w exceeds the magnitude of the applied bias field E_b, then all of the current discharged from the points will be blown away. If the applied bias potential V_b is so high that the above condition does not apply over the entire surface, some of the discharge current will return to the aircraft. Thus, the limit of the discharging capability of a biased discharger is reached when the bias voltage is raised to the value required to cause current recirculation.

It will be interesting to determine if the design of the biased decoupled discharger used in the KC-135 flight tests was such that current recirculation could have occurred. From the structure sketched in Fig. 66 it is evident that the highest electric-field intensity exists along the
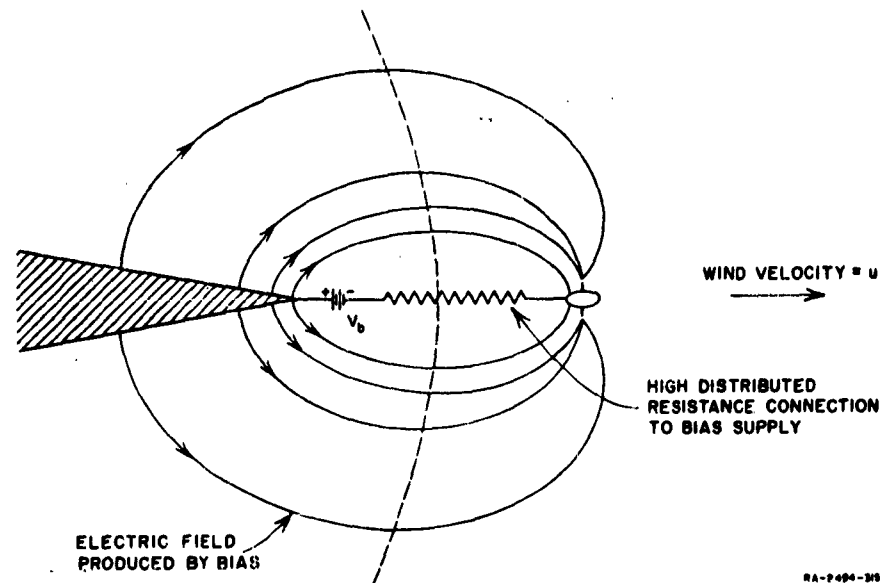
FIG. 66

STATIC FIELDS IN VICINITY OF BIASED DISCHARGER ON UNCHARGED AIRCRAFT

straight line joining the discharger and the airframe. Thus if E_w exceeds the minimum E_b along this line, then $E_w > E_b$ everywhere on the surface defined above and there will be no recirculation of current. Since the minimum E_b along the line joining the rod and the airframe is lower than the average value of field along this line we will be safe in using the average field. The minimum spacing between the rod and the airframe was 0.381 meters, and the maximum bias voltage employed was 60 kv. Thus the highest average field is

$$E_{b_{avg}} = \frac{60}{0.381} = 158 \text{ kv/meter} \quad . \tag{68}$$

Since the mobility increases with increasing altitude, the lowest wind field for a given airplane speed will exist at the maximum altitude (30,000 feet for the flights with the biased discharger). Taking the mobility at 30,000 feet altitude to be $k = 6.23 \times 10^{-4}$ meter/sec per volt/meter, and assuming the airspeed to be $u = 250$ meters/sec, we find from Eq. (67) that the wind field is

$$E_w = 400 \text{ kv/meter} \quad .$$

156

Thus if the wind speed at the location of the discharger is indeed 250 meters/sec, there will be no recirculation of current. The location of the biased discharger on the flight-test aircraft, however, was such that the effective wind speed in its vicinity was probably considerably lower than the airspeed of the aircraft. It is possible therefore that recirculation was on the verge of beginning at 30,000 feet altitude with 60 kv bias.

With this bias potential, currents as high as $250\ \mu a$ were discharged while maintaining zero aircraft potential. A system with greater discharging capacity may be achieved by installing additional biased rods of the same type at various points on the aircraft, such as the wing trailing edges, where the ions generated by discharges from the pins will be swept away by the airstream.

Another use to which the biased discharger may be put is charging the aircraft in the absence of precipitation to enable experiments requiring charge on the aircraft to be conducted in clear air. Let us assume that we wish to use the active discharger to artificially charge the aircraft to a negative potential V_0. The bias supply voltage in this case is determined by two requirements:

(1) The voltage must be sufficient to reduce the field at the pins to zero.

(2) After the pin field is zero, it must be possible to apply enough additional voltage to cause positive-point corona discharges to occur from the pins.

The voltage required to accomplish Item 1 may be determined by the following considerations.

If the discharger element is isolated from the airframe as is indicated in Fig. 67(a), the element will assume a potential V_1 with respect to the aircraft; and, as is indicated in the figure, the field at the discharger needles which are located along the line of symmetry of the ellipse will be zero. Thus with the aircraft at potential V_0 we may provide an electrical connection to the element and still maintain zero field at the pins, provided we apply a voltage V_1 between the element and the airframe as is shown in Fig. 67(b).

The additional voltage required by Item 2 may be found by the following reasoning. We know that if the discharging element is connected to

157
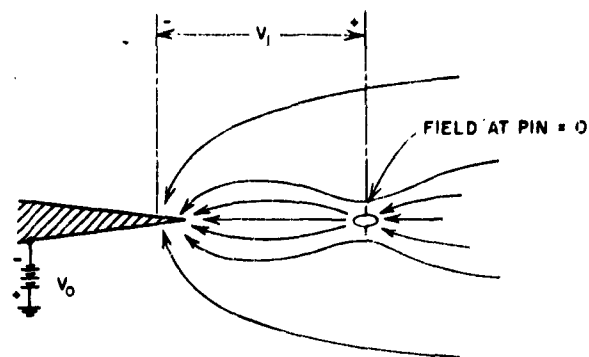
(a) ELEMENT ISOLATED
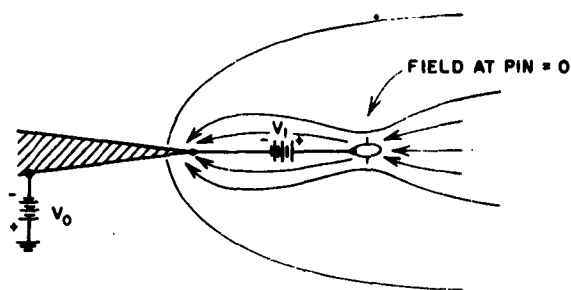
(b) BIAS VOLTAGE APPLIED

RA-2494-316

FIG. 67

ILLUSTRATION OF POTENTIAL REQUIRED TO PRODUCE
ZERO FIELD AT ACTIVE DISCHARGER PINS

the aircraft and placed aft of the trailing edge as is shown in Fig. 68(a),
positive-point corona discharges will certainly occur from the needles if
the aircraft potential is raised to V_T, the threshold potential of the
trailing edge alone. The field shown in Fig. 68(a) however, may be con-
sidered to be the sum of two fields:

(1) The field that would exist about the trailing edge if the
aircraft were at a positive potential V_T and the element
were isolated from the airframe as is shown in Fig. 68(b).
In this case the discharger element assumes a negative
potential V_2 with respect to the aircraft, and a region of
zero field exists at the pins.

(2) The field that would exist about the trailing edge if the
aircraft were uncharged and a potential V_2, positive with
respect to the aircraft, were applied to the discharger
element as is shown in Fig. 68(c).

158

(a)

(b)

(c)
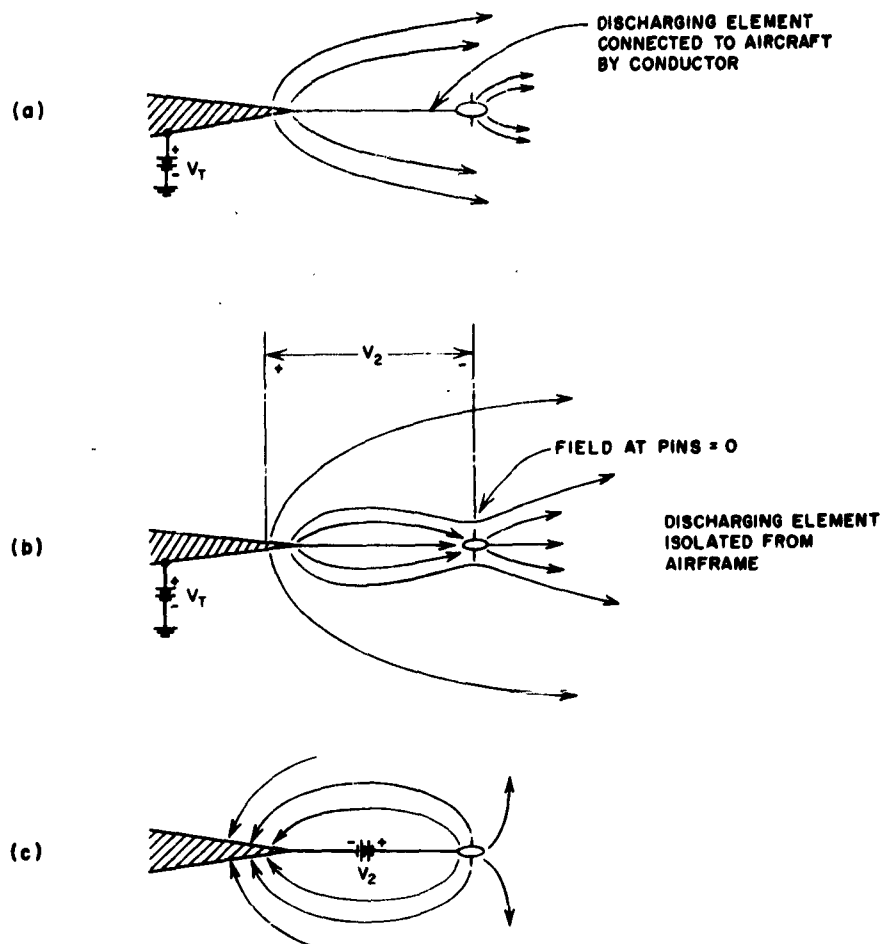
FIG. 68

THE USE OF SUPERPOSITION TO OBTAIN CORONA-INDUCING VOLTAGE

This result demonstrates that positive-point corona will occur from the pins if first the discharger element potential is adjusted to produce zero field at the pins, and then the potential is raised by V_2 volts. It is apparent, therefore, that to produce positive-point corona from the discharger when the aircraft is at a negative potential V_0 it is necessary only to apply a bias öf $V_1 + V_2$ volts to the discharge element, since voltage V_1 by itself reduces the field at the pins to zero. Furthermore, if the discharge current is blown away by the windstream and no charge is removed from the aircraft by other processes, the voltage $(V_1 + V_2)$ is sufficient to charge the aircraft to the potential V_0.

159

Voltages V_1 and V_2 were determined using modeling and charge-measuring techniques similar to those described in Appendix C. To determine V_1, a model of the aircraft is energized to some potential V_0'. The model of the discharger rod is placed in its normal position relative to the aircraft and momentarily connected to the aircraft. The charge that flows from the model to the rod is determined by the capacitance of the rod and by the equipotential surface in which the rod lies; hence a measure of the charge acquired by the rod is a measure of the potential of the equipotential surface.* If we call the potential, so determined, V_1', then

$$\frac{V_1'}{V_0'} = \frac{V_1}{V_0} \; . \tag{69}$$

The voltage V_2 is determined in a similar manner by charging the airplane model to some potential V_T' and momentarily connecting the discharger model [see Fig. 68(a)] to the trailing edge of some surface such as the wing for which the threshold potential V_T is known. If the potential determined from the laboratory measurement is called V_2', then

$$\frac{V_2'}{V_T'} = \frac{V_2}{V_T} \; . \tag{70}$$

Thus the bias potential required to charge the aircraft to a potential V_0 is

$$V_{bias} = V_1 + V_2 = V_0 \frac{V_1'}{V_0'} + V_T \frac{V_2'}{V_T'} \quad . \tag{71}$$

This method was used to calculate the positive bias potential required to raise the aircraft potential sufficiently to produce negative-point corona

---

* The rod may be calibrated in a known field so that the potential of the rod may be determined directly. If the rod is calibrated in a uniform field, a correction is necessary to take into account the capacitance change resulting from the change in field structure in transforming from the parallel plate geometry to the wing or tail cone. The magnitude of this correction in going from a plate to an edge was only 20%. In going from a plate to the tail cone the correction would be even less. Since we were seeking only approximate values of bias voltage, this correction was ignored.

RA-2494-318
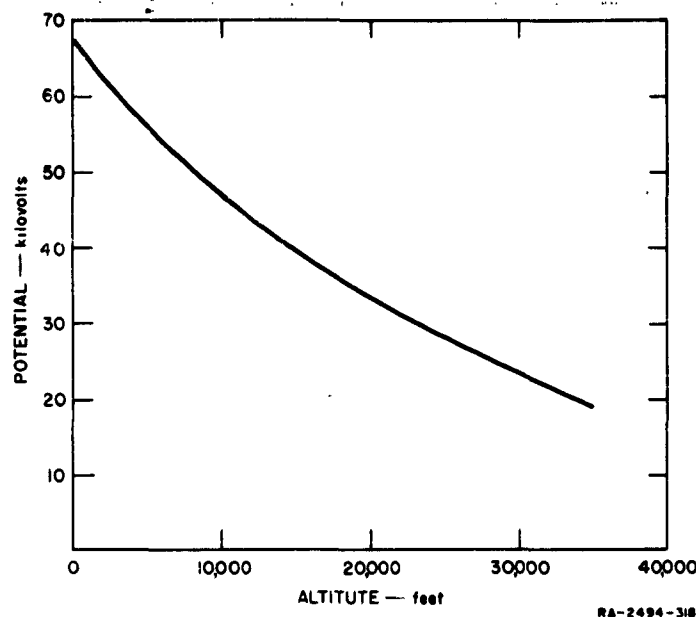
FIG. 69

POSITIVE BIAS POTENTIAL REQUIRED ON BIASED DISCHARGER
TO PRODUCE NEGATIVE-POINT CORONA AT WING TIP

from the wing tips. The results of the calculation, shown in Fig. 69, indicate that a 60-kv supply is sufficient to maintain aircraft corona threshold at all but the lowest altitudes, and that at the higher altitudes there should be sufficient excess bias potential to permit appreciable charging currents.

With the discharger shown in Fig. 65 it was possible to charge the aircraft at rates as high as 200 μa using a bias of 60 kv. To illustrate a typical value of V_0 which can be obtained with a reasonable bias voltage, at 14,000 feet altitude the airplane potential could be raised to a negative value of 135 kv with a positive bias-supply potential of 50 kv.

The reader should not be misled by Figs. 67 and 68 into thinking that the active discharger rod was connected to the bias supply by a piece of wire. To provide decoupling the connection was made as is indicated in Fig. 66 by a distributed resistance of 2 megohms extending across the 15-inch gap between the discharging element and the tail cone.

E. WICK DISCHARGERS

Currently the standard static discharger for use on military aircraft is the AN/ASA-3. It consists of a piece of graphite-impregnated

161

cotton wicking enclosed in a plastic tube which covers all but the aft inch of the wicking. The wicks are attached to the trailing edges of airfoils in much the same manner as are the Type-A decoupled dischargers in Fig. 64. Corona discharges occur from the conducting fibers at the aft end of the wick.

Since the resistance of the wick is extremely high, its presence does not alter the RF coupling fields about the airfoil on which it is mounted. The coupling fields, therefore, will have the configuration shown in Fig. 57. Since the discharge occurs in the region roughly 8 to 10 inches aft of the trailing edge, it is evident from Fig. 57 that as the result of field diminution the noise coupling at the position of the discharge is lower than it is at the trailing edge. Thus the wick achieves a certain degree of noise decoupling. It should be noted, however, that no effort is made to arrange for the discharge to occur at a position of minimum coupling field nor is the discharge current orthogonal to the coupling field.

An estimate of the maximum decoupling obtainable with a wick may be obtained by noting that the RF coupling field of Fig. 57 is given by

$$E(x) = \frac{A}{\sqrt{x}} \tag{72}$$

where x is distance aft of the trailing edge and A is a constant related to the amplitude of the applied voltage. The decoupling is given by

$$\frac{E_2}{E_1} = \sqrt{\frac{x_1}{x_2}} \tag{73}$$

where E_1 is the coupling field at the trailing edge and E_2 is the coupling field at the end of the discharger. Let us assume that the shape of the trailing edge is such that it can be represented by the shape of the equipotential surface passing through $x_1 = 0.1$ cm. Since the discharger is roughly 8 inches long, $x_2 = 20$ cm. Hence from Eq. (73) the maximum possible decoupling is

$$\frac{E_2}{E_1} = \sqrt{\frac{0.1}{20}}$$

$$= -30 \text{ db} .$$

As in the case of a discharge from a sharp pin, a given current discharged from a conductive cotton fiber will generate less noise than does the same current discharged from the trailing edge. If we assume that the discharge from the fiber is 6 to 10 db less noisy, the maximum noise reduction obtainable with a wick should be of the order of 36 to 40 db.

Thus it appears that the wick is capable of producing a considerable reduction in the precipitation-static noise level on an aircraft. Unfortunately the wick has several characteristics which render it less effective than the above figures might tend to indicate.

One important drawback is that wicks disintegrate very rapidly at the speeds of turbojet aircraft. For this reason they have not been installed on jets. Even on piston-engine aircraft the characteristics of the wicks were found to deteriorate relatively rapidly.

To study the problem of wick deterioration, arrangements were made with United Air Lines to remove sets of wicks from their DC-6 and DC-7 aircraft after they had been in service on these aircraft for periods ranging from 125 to 2000 flight hours. It should be noted in this regard that the aircraft from which the wicks were removed received no special treatment. The normal wick inspection, trimming, and replacement programs were followed on them. Hence, the sets of dischargers used in the laboratory tests were typical of the dischargers found on an aircraft a given number of hours after a new set has been installed. For example, a number of dischargers in the 2000-hour set were undoubtedly replacements that had not been on the aircraft for the full period of time.

The first characteristic studied was the corona threshold. Laboratory measurements conducted with the dischargers mounted on the wing mock-up in the set-up of Figs. 8 and 9 indicated that the threshold potential of a new wick is roughly the same as the threshold of a Type A decoupled discharger. The same laboratory set-up was used to measure the corona thresholds of the used dischargers. It is evident from the results of these measurements shown in Fig. 70 that the corona threshold increased very rapidly during the first few hundred hours of service, until after 400 hours the average threshold was four times that of a new wick. Furthermore, the thresholds of certain dischargers increased by a factor of seven.

In the same experiment measurements were made of the potential required to discharge a current of 100 μa from the wick. After 400 hours
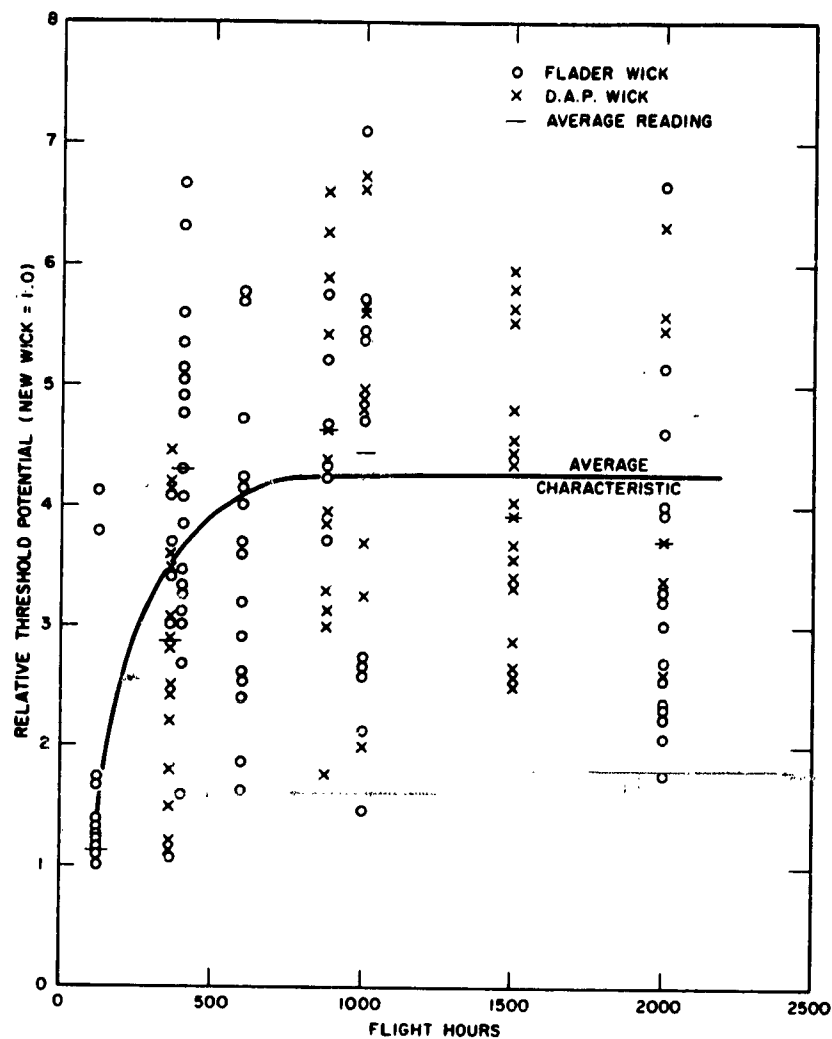
FIG. 70

ILLUSTRATION OF DETERIORATION OF WICK CORONA THRESHOLD
WITH SERVICE

of service the potential required for the average wick was increased by a factor of two, and for the worst wicks by a factor of three.

Again using the set-up of Figs. 8 and 9, measurements were made of the noise generated by currents ranging from 10 to 100 μa discharging from a wick. The results of these measurements are shown in Fig. 71 together with a curve indicating the noise generated by discharges from the trailing-edge mock-up. The noise generated by current discharged from the wicks with short service times was lower than the residual noise level of the
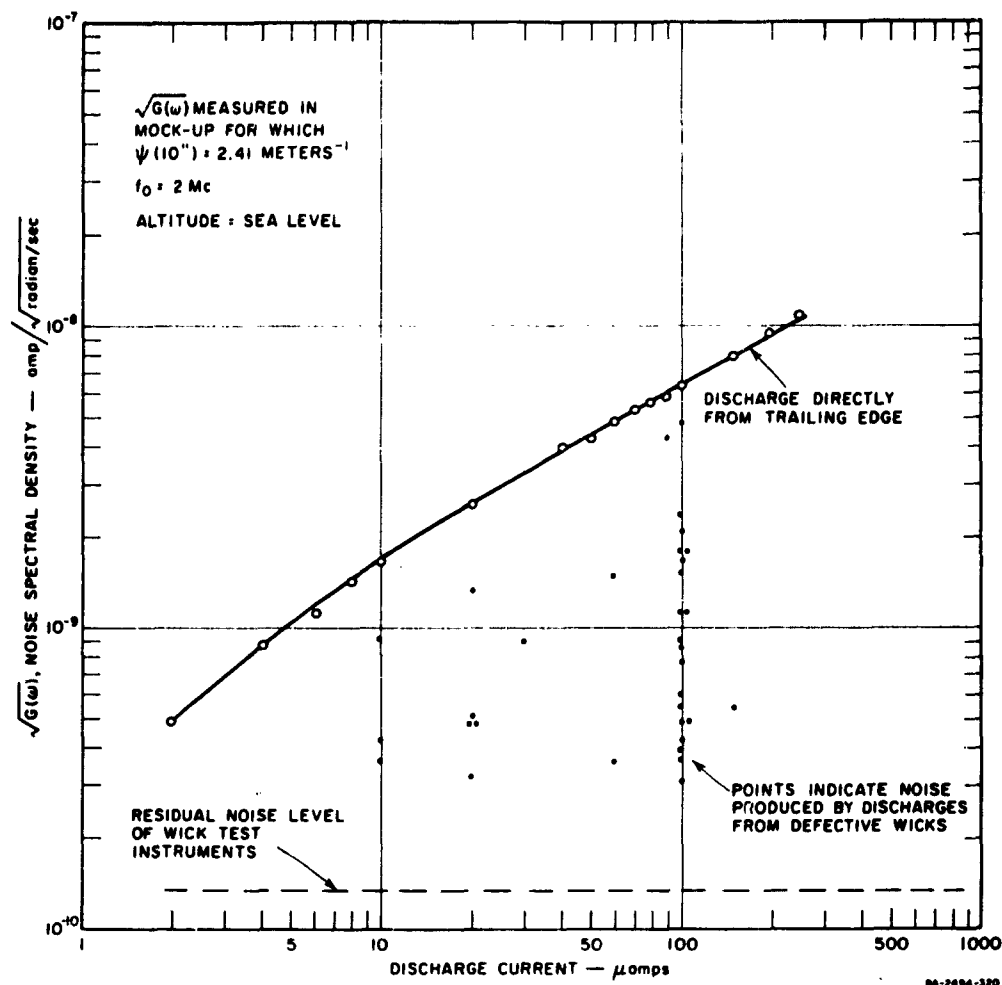
FIG. 71

SOME RESULTS OF WICK-DISCHARGER NOISE MEASUREMENTS

test instruments used, so that it was not possible to determine the noise reduction afforded by a good wick. It can be stated, however, that the noise was reduced by at least the ratio of the residual noise to the noise generated by 100 μa discharged from the trailing edge, or 33 db.

After a few hundred hours of service many of the wicks became noisy. In some cases, as is evident from the data points in Fig. 70, discharges from the wicks generated almost as much noise as would the same current discharging directly from the trailing edge. Furthermore, the noisy wicks included some which had only 375 hours of service.

165

Trimming the end of a wick to expose fresh fibers usually improved
its characteristics, but, even after trimming, used wicks were found to be
inferior to new ones. In the case of badly deteriorated wicks, trimming
resulted in almost no improvement in performance.

Perhaps the worst feature regarding the deterioration of wick perfor-
mance characteristics is that the deterioration is not apparent from a
visual inspection of the wick. Many wicks which appeared sound physically
were found to be badly deteriorated electrically. On the other hand, wicks
which appeared to be completely worn out with most of the conductive material
washed out of the exposed fibers often functioned better than the majority
of the others in their set.

F. BIASED ENGINE EXHAUSTS

The mechanism by which jet engines charge an aircraft is the result
of diffusion to the walls of the combustion chamber of free electrons
formed during combustion. Being highly mobile, electrons diffuse rapidly
out of the burning gas, while the less mobile positive ions diffuse much
more slowly. The gases ejected in the exhaust therefore carry a slight
positive space charge, leaving a negative charge on the aircraft. The
possibility presented itself, therefore, of utilizing the exhaust gas to
discharge the aircraft under conditions of precipitation charging if a
means could be devised to capture positive ions from the exhaust and re-
turn them to the aircraft. By reversing the polarity of the ion-capturing
device, furthermore, it could be made to capture electrons or negative ions,
thereby providing a method for artificially charging the aircraft during
precipitation-static experiments.

Ground tests designed to determine the magnitude of charging or dis-
charging current obtainable from a jet engine were conducted at Boeing
Airplane Company in Seattle. As is indicated in Sec. IV-D the results of
these tests indicated that only a very small current could be extracted
from the exhaust with any reasonable ion-capturing device using reasonable
biasing potentials. For this reason it was concluded that this discharging
scheme was not practical and no further effort was devoted to its investi-
gation. This result agrees with conclusions reached by workers at Denver
Research Institute.[6]

G. INTERFERENCE BLANKERS

In contrast to the aforementioned methods of precipitation-static reduction, the blanker approach attacks the problem at the receiver terminals. Thus, whereas other methods attempt to reduce the noise coupled into the antenna, the blanker is based on the idea that the signal-to-noise ratio can be appreciably improved by the electronic methods which will presently be described.

In principle, the blanker is an ideal switch which is placed ahead of the receiver so as to completely suppress both signal and noise whenever a noise pulse appears. Thus, when a noise pulse arrives, it triggers a gate which in turn shorts the receiver input for a brief period of time. This blanking period must of course be of sufficient duration that a significant portion of the high-energy pulse will be suppressed.

It is evident that as the length of the blanking period is increased the signal power at the output of the receiver will go down. Indeed, not only does the signal power decrease but the noise which is due to the blanker switching action increases. Thus it is of primary importance to make the blanking period as short as possible. It follows that the blanker must be located ahead of any filtering in the system, otherwise the noise pulses would be very much extended in time by the narrow-band filters.

The switching action of the blanker will introduce signal power at other frequencies. The power at these other frequencies provides no information, however, so that it is considered as noise. In a similar way, the requirement that no filtering be done ahead of the blanker opens the way for more noise in the output due to the switching modulation of outside carriers near the carrier of interest. It is important to note that some filtering could be accomplished before the blanker; however, the Q of the circuits must be so low that very little benefit is realized because it is the carriers near the signal carrier that contribute most heavily.

The simplest blanker that might be applied to noise suppression is one of fixed period. Thus, when a noise pulse arrives, if the receiver is not blanked, a blanking period of length t is initiated. If, on the other hand, the receiver is in the blanked position when a pulse arrives, it has no effect.

Some benefit will be experienced by using this blanker; however it should be noted that if the pulses are numerous, a large number of pulse

167

tails will still pass through so that there can still be appreciable noise power from the remains of the high-energy pulses in the output. In addition, there will also be the noise introduced due to the blanking function.

A more practical and efficient blanker is one which provides means of extending the blanking period whenever it is necessary. We assume that once a blanking period is initiated by a pulse it will last for a time t if no other pulses arrive. Otherwise, the period will be extended. Following this process further, it is apparent that the blanking period will continue until two pulses are separated by more than t in time. Thus, every pulse creates a gate of length t after it, and consequently all the tails of the noise pulses will be eliminated.

An analysis has been carried out[14] for the ideal blanker described above, followed by an ideal receiver. It is argued that the corona-noise pulses are governed by a Poisson distribution function, and using this, the statistics of the blanking-period length and occurrence are derived. Knowing this, the power spectrum at the output of the receiver is obtained easily.

Because the system is linear, it is instructive to consider a simple input to the system which consists of a single sine wave. It is apparent that the signal and noise power at the output of the blanker will be reduced to a fraction of the power contained in the signal. Note that we assume all power in the noise pulse is suppressed by the blanker. Thus, if the average blanking period is of length T and the average number occurring per second is ν then the total power out for a unit power input is obviously $(1 - \nu T)$.

Now, the output-power spectrum of the blanker, for a sine wave input consists of a discrete as well as a continuous spectrum. The discrete part, which represents signal power, is reduced to a power of $(1 - \nu T)^2$. The total power in the continuous spectrum is therefore $(1 - \nu T) - (1 - \nu T)^2 = \nu T(1 - \nu T)$, which is the difference between the total output power and the output signal power. Of course, it is not the total noise power that is of interest but only that part which will be passed by the filters of the receiver.

When a typical input to a blanker is considered, consisting of an amplitude-modulated carrier plus a number of outside carriers, it is obvious that each term will contribute discrete and continuous spectra

in the output of the blanker. The band-pass and low-pass filters of the receiver will eliminate all discrete signals with the exception of the modulation of interest. However, noise contribution from every term will pass through the filters and contribute to the output.

There is no question that a blanker can provide considerable improvement when there are only a few very-high-energy pulses to contend with. However, in the application to precipitation-static noise, the number of pulses, even in relatively light precipitation conditions, becomes very high while corona noise pulses are lengthened by the aircraft resonances.[14] Both of these facts contribute toward a decreasing effectiveness of the blanker.

A comparison has been made between the relative performance of a blanker and decoupled dischargers as means of reducing corona noise interference. The calculations were carried out for a Boeing 707 aircraft under a precipitation-static condition where the total discharge current was one milliampere. The decoupling provided by the dischargers was assumed to be 50 db while the blanker was assumed to be an ideal blanker of the type described above. Furthermore, it was assumed that there were no outside carriers present. In this favorable light the blanker was nevertheless found to be inferior in suppressing noise as compared to the decoupled dischargers. Another interesting point is the serious effect that outside carriers can have. For example, a single outside carrier in the frequency vicinity of the carrier of interest, which has an amplitude only 4.6 times that of the wanted carrier, will reduce the signal-to-noise ratio at the output by a factor of ten.

Another important effect of using a blanker is the serious loss of sensitivity which results due to the fact that no tuning can be accomplished at the antenna terminals. In this connection, a tuned blanker has been proposed which theoretically will have a high Q input until a noise pulse arrives; then the circuit Q is drastically reduced so as to prevent ringing. After the energy of the pulse has been dissipated, the circuit is again opened up. The difficulty with this process is not only that it takes time to dissipate the energy, but more important, the recovery time of the tuned circuit is very long so that effectively, under conditions of precipitation static, the blanker will virtually never be in an unblanked state. The only thing the tuned blanker might accomplish is to reduce the

outside carrier contribution of noise. At the same time, however, the signal-to-noise ratio, neglecting outside carriers, is worse than that for the untuned blanker.

Finally, the numerous practical limitations which must be met in a satisfactory blanker are very severe. For example, in presently available designs, a minimum blanking period of six microseconds is considered good. With blanking periods of this length it is easy to calculate that only a 10-db improvement in signal-to-noise ratio is afforded for the case of 1 ma discharge.

IX CONCLUSIONS

The principal objective in undertaking the research described in the foregoing chapters was to develop an understanding of the problem of precipitation-static noise generation and coupling which would eventually lead to the development of techniques for the elimination of this type of interference. It is possible to say in conclusion that this objective has been fulfilled.

A laboratory technique was developed to measure the coupling between an aircraft receiving antenna and regions on the aircraft, such as the airfoil extremities, in which noise-producing corona discharges normally occur. The measurements are made by using a special spark-noise source to explore the regions of interest on a model of the aircraft. Using this technique, coupling measurements were made for the two antennas employed in the precipitation-static flight-test program conducted on the Boeing KC-135 prototype aircraft under Contracts AF 33(616)-3914 and AF 33(616)-6561. From the results of these measurements it is evident that noise coupling is influenced by aircraft resonances. Another interesting result of the measurements was that, contrary to what one might conclude at first thought, increasing the separation between the antenna and the noise source may often increase the coupling between the two, thereby increasing the noise induced in the antenna.

Since negative-point corona discharges are the major source of precipitation-static interference, the characteristics of the discharges and the noise they generate were studied. Measurements were made of the noise spectra generated by discharges from airfoil trailing edges and extremities. It was found that the noise-current spectral density varies nearly as the square root of the discharge current. The character of the noise spectrum was found to vary with altitude. At sea level the spectrum is virtually flat up to a frequency of 3 megacycles. At higher altitudes the magnitude of the noise is greater, but the spectrum begins to fall off at successively lower frequencies.

171

In considering the factors which influence aircraft charging it appeared from the results of NACA studies that the frontal area on which particle impingement and charging occur should be much smaller than the projected frontal area of the aircraft. Furthermore, the results indicated that the effective area should vary with airspeed and precipitation characteristics. It is apparent that aerodynamic effects of this sort, if not understood, could cause considerable confusion in the interpretation of the results of precipitation-static flight tests. To investigate these aerodynamic effects, a technique was developed whereby flight-test measurements of intrinsic charging rate and aircraft potential could be used to determine the true total aircraft-charging current. When the method was applied to flight-test data obtained on the KC-135 prototype aircraft whose projected frontal area is roughly 400 square feet, it was found that the effective frontal area varied from 10 to 150 square feet, depending on flight conditions.

The manner in which corona discharges distribute themselves on an aircraft is important in the study of noise generation and in the design of dischargers. For this reason, the problem of space-charge-limited discharges from the edges of sheets and the ends of cylinders in the presence of wind streams was investigated theoretically. The theoretical results were employed to devise experimental techniques which permitted the distribution to be estimated from the results of measurements made on models in the laboratory. Very good agreement was obtained when the predicted results were compared with flight-test data

By combining the results of the studies of coupling, corona-noise characteristics, total charging rates, and discharge distribution, it was possible to predict the antenna noise currents that should exist during flight through precipitation. Excellent agreement was obtained between these predictions and noise measured in flight. The concept of equivalent noise field was employed to render the noise data applicable to any dipole antenna located at one of the positions studied. A theoretical study was made of the manner in which precipitation-static noise fields vary with aircraft size. It was concluded that susceptibility to precipitation-static interference increases rapidly as aircraft size diminishes.

A comparison was made of loop and dipole antennas in regard to their relative vulnerability to precipitation-static interference. It was demonstrated that, particularly at the low frequencies, a properly located

172

and properly oriented loop is far less susceptible to precipitation-static interference than is a dipole antenna. This result offers an explanation for the often observed superiority of loops over dipoles for low-frequency reception.

Finally, the results of the studies were applied to the problem of devising and analyzing techniques for the elimination of precipitation-static interference. It was shown that 25 db of noise reduction may be achieved through the use of decoupled loops or decoupled dipole antennas.

Theoretical analysis of a simple decoupled discharger designed to permit inexpensive installation on existing aircraft indicated that it should provide a noise reduction of the order of 56 db at a frequency of 500 kc. The analysis indicated that the noise reduction increases roughly 20 db per decade with increasing frequency. The results of flight tests in which currents in excess of 3 ma were discharged from the aircraft without generating detectable noise indicate that the noise reduction obtained with these dischargers was greater than 50 db.

A biased decoupled discharger was developed for special applications in which it is necessary to maintain the aircraft at zero potential. By changing the bias-supply polarity this device may be used to artificially charge the aircraft for precipitation-static experiments. When the decoupled discharger was flight tested, it was found that currents of roughly 250 microamperes could be discharged while maintaining zero aircraft potential. When the device was used as an artificial charger it charged the aircraft at rates of roughly 200 microamperes. No noise was detected in the receiving systems when the biased discharger was in operation.

Analysis of the AN/ASA-3 wick discharger indicated that it should reduce noise by 36 to 40 db. Laboratory tests of dischargers removed from operational aircraft, however, indicated that the characteristics of wick dischargers degenerate very rapidly during the first few hundred hours of flight. The average threshold potential increases by a factor of four, and many of the wicks become noisy. In fact, currents discharged from some of the wicks generated almost as much noise as they would if discharged directly from the airframe. It was found, furthermore, that it was not possible to detect the defective dischargers by a visual inspection.

A brief discussion is included on the use of interference "blankers"—
devices which disable the receiver for the duration of a noise pulse—to
eliminate precipitation-static interference at the receiver. Several
limitations of this technique are pointed out.

APPENDIX A

DERIVATION OF COUPLING THEOREM

DERIVATION OF COUPLING THEOREM

Let us consider a conducting body of arbitrary shape as shown in Fig. 1 (Sec. II). Two regions of particular interest are indicated. The first of these, T_1, represents a volume which has been removed from the original conducting body to form the antenna terminals. The second region, T_2, is external to the body and is defined by the volume in which charge moves.

We now postulate two independent situations characterized by independent solutions to the field equations. The field quantities which correspond to the two situations will be designated by subscripts 1 and 2. For each of the situations indicated it is possible to write Maxwell's curl equations relating the field quantities **E**, **H**, and **J**. These equations, in their Fourier transformed form, are shown below:

$$\nabla \times \mathbf{E} = -j\omega\mu\mathbf{H} \quad , \tag{A-1}$$

$$\nabla \times \mathbf{H} = j\omega\epsilon\mathbf{E} + \mathbf{J} \ . \tag{A-2}$$

We now form the vector quantity

$$\mathbf{E}_1 \times \mathbf{H}_2 - \mathbf{E}_2 \times \mathbf{H}_1$$

to which we apply Gauss's divergence theorem:

$$\oint (\mathbf{E}_1 \times \mathbf{H}_2 - \mathbf{E}_2 \times \mathbf{H}_1) \cdot dS = \int \nabla \cdot (\mathbf{E}_1 \times \mathbf{H}_2 - \mathbf{E}_2 \times \mathbf{H}_1) dv \quad . \tag{A-3}$$

By applying the vector identity

$$\nabla \cdot \mathbf{A} \times \mathbf{B} = \mathbf{B} \cdot \nabla \times \mathbf{A} - \mathbf{A} \cdot \nabla \times \mathbf{B}$$

177

to the right side of Eq. (A-3) and substituting from Eqs. (A-1) and (A-2),
several terms on the right are observed to cancel, and Eq. (A-3) becomes

$$\oint (\mathbf{E}_1 \times \mathbf{H}_2 - \mathbf{E}_2 \times \mathbf{H}_1) \cdot d\mathbf{S} = \int (\mathbf{E}_2 \cdot \mathbf{J}_1 - \mathbf{E}_1 \cdot \mathbf{J}_2) dv \quad . \qquad \text{(A-4)}$$

The volume included in the volume integral on the right is bounded
by the surface of the surface integral on the left. For the situation
under consideration the volume with which we are concerned is all space
external to the conductors of Fig. 1, including the regions T_1 and T_2.
The surface is therefore the surface of the conductors and the surface at
infinity.

The radiation condition of Sommerfeld insures that the contribution
to the surface integral over the surface at infinity vanishes.[24] The
boundary conditions at the surface of a perfect conductor guarantee that
any vector $\mathbf{E} \times \mathbf{H}$ lies in a plane tangent to the surface, whereas the ele-
ment vector $d\mathbf{S}$ is normal to the surface. The vectors $\mathbf{E} \times \mathbf{H}$ and $d\mathbf{S}$ are
therefore orthogonal and the surface integral is identically zero. Equa-
tion (A-4) can thus be written as

$$\int \mathbf{E}_2 \cdot \mathbf{J}_1 dv = \int \mathbf{E}_1 \cdot \mathbf{J}_2 dv \qquad \text{(A-5)}$$

where we are free to specify what conditions shall apply in Situations 1
and 2 (described below), provided only that the conditions that are speci-
fied are consistent with Maxwell's equations. The conditions obtaining
in Situations 1 and 2 are as follows:

> Situation 1: A voltage V_1 is applied to the antenna
> terminals, the current density J_1 has a finite value
> in region T_1 and is zero elsewhere. The integrand of
> the integral on the left side of Eq. (A-5) is there-
> fore non-zero only in region T_1.

> Situation 2: Motion of charge J_2 occurs in region T_2,
> and therefore the integrand of the right side of
> Eq. (A-5) is non-zero only in region T_2.

As a result of the specified conditions, Eq. (A-5) becomes

$$\int_{T_1} \mathbf{E}_2 \cdot \mathbf{J}_1 dv = \int_{T_2} \mathbf{E}_1 \cdot \mathbf{J}_2 dv \quad . \qquad \text{(A-6)}$$

We now define the integral on the left of Eq. (A-6) as the product $V_2 I_1$, and rearrange the equation into the form

$$V_2 = \frac{1}{I_1} \int_{T_2} \mathbf{E}_1 \cdot \mathbf{J}_2 \, dv \quad . \tag{A-7}$$

Equation (A-7) is one form of the basic coupling theorem in which we are interested. A more convenient form is obtained by dividing both sides of the equation by the antenna terminal impedance Z_{11}. The left side of Eq. (A-7) then becomes V_2/Z_{11}, which is the open-circuit voltage produced at the antenna terminals by the discharge divided by the impedance seen looking into these terminals. According to Thevenin's theorem the quantity thus obtained is the short-circuit current produced at the terminals by the discharge. We shall label this current I_2. It is quite evident that the product $I_1 Z_{11}$ which occurs in the denominator of the right side is the voltage V_1. Equation (A-7) can therefore be written

$$I_2 = \frac{1}{V_1} \int_{T_2} \mathbf{E}_1 \cdot \mathbf{J}_2 \, dv \quad . \tag{A-8}$$

APPENDIX B

POWER SPECTRUM FOR SIGNAL OF RANDOM PULSES

APPENDIX B

POWER SPECTRUM FOR SIGNAL OF RANDOM PULSES

Let us assume we have a signal which extends for the interval $-T < t < T$ and is zero outside this range. The signal is assumed to consist of $2N+1$ pulses occurring at random times at the average rate of ν pulses per second. Thus the signal may be written as

$$I(t) = \sum_{k=-N}^{N} f(t - t_k)$$

where

$$f(t - t_k) = 0 \qquad\qquad t < t_k$$

$$= A_k e^{-a_k(t - t_k)} \qquad t > t_k \qquad .$$

The Fourier transform of the signal is obtained

$$I(\omega) = \int_{-\infty}^{\infty} I(t)e^{-j\omega t}dt$$

$$= \sum_{k=-N}^{N} \frac{A_k}{a_k + j\omega} e^{-j\omega t_k} \qquad .$$

Then, the power spectrum which is defined as

$$G(\omega) = \lim_{T \to \infty} \frac{1}{2\pi T} |I(\omega)|^2$$

is found to be

$$G(\omega) = \lim_{T \to \infty} \frac{1}{2\pi T} \sum_{k=-N}^{N} \frac{A_k^2}{\omega^2 + a_k^2}$$

since the times t_k are assumed random. It follows, that if A_k and α_k are all identical we obtain

$$G(\omega) = \frac{\nu}{\pi} \frac{A^2}{\omega^2 + \alpha^2} \quad .$$

Next, let us assume that the amplitudes A_k and the decay constants α_k are independent random variables.

Let

$$\alpha_k = \alpha + \delta_k$$

where α is the average value and δ_k is a random variable such that at maximum it is small compared to α and $\overline{\delta}_k = 0$.

Then the power spectrum is

$$G(\omega) = \frac{1}{\omega^2 + \alpha^2} \lim_{T \to \infty} \frac{1}{2\pi T} \sum_{k=-N}^{N} \frac{A_k^2}{1 + \dfrac{2\alpha\delta_k + \delta_k^2}{\omega^2 + \alpha^2}} \quad ,$$

Since $\delta_k \ll \alpha$ and recalling that A_k and α_k are assumed to be independent, we find

$$G(\omega) = \frac{\overline{A^2}}{\omega^2 + \alpha^2} \lim_{T \to \infty} \frac{1}{2\pi T} \left\{ (2N + 1) - \frac{2\alpha}{\omega^2 + \alpha^2} \sum_{k=-N}^{N} \delta_k - \sum_{k=-N}^{N} \frac{1}{\omega^2 + \alpha^2} \left(1 - \frac{4\alpha^2}{\omega^2 + \alpha^2} \right) \delta_k^2 \right\}$$

and since $\overline{\delta}_k = 0$

$$G(\omega) = \frac{\nu}{\pi} \frac{A^2}{\omega^2 + \alpha^2} \left\{ 1 + \frac{3\alpha^2 - \omega^2}{(\omega^2 + \alpha^2)^2} \overline{\delta}_k^2 \right\}$$

Thus a good approximation is obtained by simply keeping the first term—that is,

$$G(\omega) = \frac{\nu}{\pi} \frac{\overline{A^2}}{\omega^2 + \alpha^2} \quad .$$

184

Consider for example that δ_k is equally probable in a 20% range of α, i.e., $-\alpha/10 < \delta_k < \alpha/10$. Then at high frequencies $\omega \gg \alpha$ there is negligible error using above expression. At mid frequencies, $\omega = \alpha$, the error is approximately $\frac{1}{2}$% while at low frequencies $\omega \ll \alpha$ the error is at worst approximately 3%.

APPENDIX C

**LABORATORY TECHNIQUES FOR THE STUDY
OF STATIC ELECTRIC FIELDS**

APPENDIX C

LABORATORY TECHNIQUES FOR THE STUDY
OF STATIC ELECTRIC FIELDS

In connection with precipitation-static investigations it has been necessary to study and duplicate in the laboratory the static electric fields surrounding various regions of interest on aircraft. Several interesting laboratory techniques to accomplish these objectives have been developed and are sufficiently useful to merit description.

Common to the various methods is the charge-separation technique for measuring static fields which was developed by Bolljahn in connection with low-frequency antenna studies.[12] Its operation is illustrated in Fig. C-1.

(a)   (b)   (c)
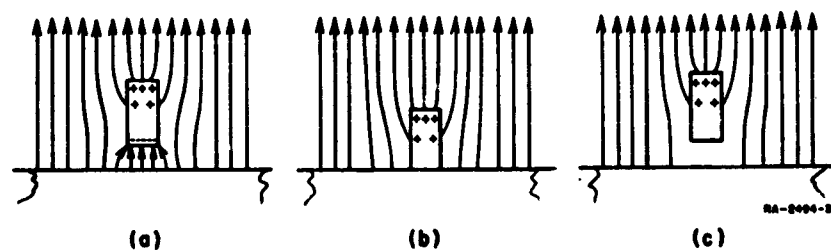
FIG. C-1

ILLUSTRATION OF CHARGE SEPARATION

If a small, uncharged probe is placed in the field near the surface of a conducting sheet the field will assume the form shown in Fig. C-1(a) where it is evident that a potential difference exists between the probe and the conductor. When the probe is placed in contact with the conductor as in Fig. C-1(b), therefore, charge will flow onto the probe. If the probe is now removed from the conductor as in Fig. C-1(c), the probe is left with an excess of charge, q_p. The amount of this charge is proportional to the field strength at the surface of the sheet, E, and to the induction area of the probe, a:

$$q_p = \epsilon_0 E a \quad . \qquad\qquad (C-1)$$

189

The charge acquired by the probe is measured using the electrometer shown in block form in Fig. C-2. To make a measurement the charged probe is touched to the inside of the charge receptacle causing the charge to flow from the probe to the outside of the receptacle. Part of this charge flows through the resistor R charging the motor-driven variable capacitor C_1. The periodic variations in capacitance of C_1 generate an alternating voltage, the amplitude of which is proportional to the charge on C_1, which in turn is proportional to the charge deposited in the charge receptacle. This alternating voltage is fed to an amplifier and thence to a detector which drives a meter calibrated in units of charge.
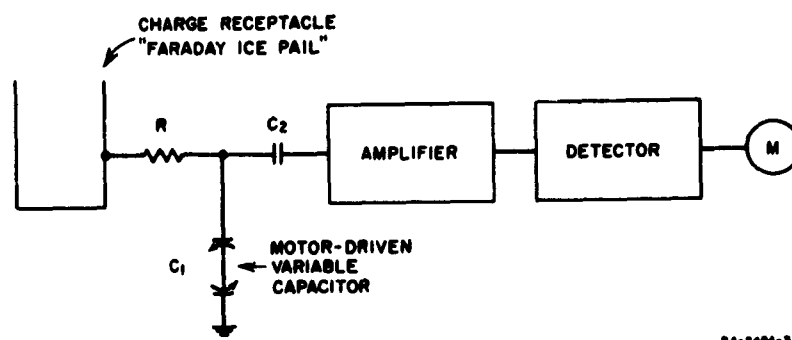
FIG. C-2

BLOCK DIAGRAM OF ELECTROMETER

With the particular electrometer used for the measurements it was possible to read charges as low as 1 $\mu\mu$coulomb with no difficulty. For the purposes of the measurements, the instrument could be considered to retain its charge indefinitely since the decay time is determined by the background radiation level. Readings can be taken many minutes after the charge is deposited.

Returning to Eq. (C-1), it is evident that the charge, q_p, acquired by the probe in a field of given intensity will depend upon the induction area of the probe. If, as in Fig. C-3(a), the probe is thin, the induction area will equal the cross-sectional area of the probe. However, if as in Fig. C-3(b) the probe has appreciable height, its induction area will be greater than its cross-sectional area. To measure absolute values of field, therefore, it is necessary that a method be available for

(a)   (b)
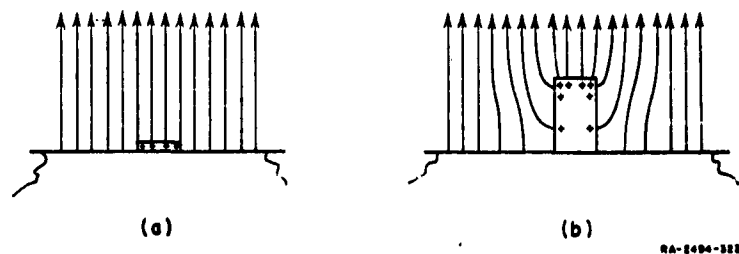
FIG. C-3

ILLUSTRATION OF EFFECT OF PROBE HEIGHT ON CHARGE TRANSFER
IN UNIFORM FIELD

calibrating the probe. This may be done by measuring the charge acquired by the probe in a field of known magnitude such as that between a pair of parallel conducting plates. It should be noted that it is not actually necessary to know the absolute value of the charge on the probe so long as the quantity measured is proportional to the charge. Thus, we require only that the deflection, d, of the measuring instrument be related to the probe charge by

$$d = \alpha q_p \qquad \text{(C-2)}$$

where α = constant. We may write

$$E = \frac{E_s}{q_s} q \qquad \text{(C-3)}$$

where

       E = unknown field
       q = charge acquired by probe in unknown field
       E_s = standard calibrating field
       q_s = charge acquired by probe in calibrating field.

Equation (C-3) may be rewritten

$$E = \frac{E_s}{\alpha q_s} \alpha q$$

which, upon substituting Eq. (C-2), becomes

$$E = \frac{E_s}{d_s} d . \qquad \text{(C-4)}$$

191

Thus, to calibrate the probe to perform surface-field measurements it is necessary only to know the relations E_s/d_s between the calibrating field and the deflection produced by the charge acquired by the probe in that calibrating field.

Strictly speaking, the concept of an induction area for the probe is meaningful only in a region where the field is uniform over the dimensions of the probe. Thus, unless special precautions are taken, field measurements should be made only on surfaces such that the radius of curvature is substantially larger than the greatest dimension of the probe. If, for example, as in Fig. C-4 the field at the surface of a cylinder were to be measured using two probes calibrated in a uniform field, the value obtained using the small probe would be very nearly correct, but the value obtained using the large probe would be low.

UNIFORM FIELD PROBE
CALIBRATION CAN BE USED
WITH LITTLE ERROR

USE OF UNIFORM FIELD PROBE
CALIBRATION WILL INTRODUCE
CONSIDERABLE ERROR

FIELD IS RELATIVELY
UNIFORM OVER
DISTANCE OCCUPIED
BY PROBE

FIELD VARIES OVER
DISTANCE OCCUPIED
BY PROBE

CHARGED CYLINDER

RA-2404-264
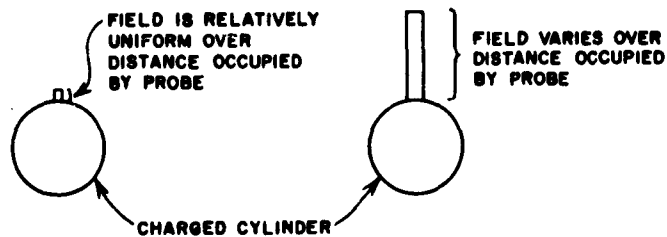
FIG. C-4

PROBE IN NON-UNIFORM FIELD

Occasionally it is necessary to make field measurements on an object such that the probe dimensions cannot be made smaller than the radius of curvature of the surface. (This was true of the laboratory measurements made to study discharge-current distribution as described in Sec. V-C, in which it was necessary to measure the field at the surface of small-diameter rods.) In this case it is possible to calibrate the probe in a standard geometry for which the fields can be calculated and in which the field structure duplicates that existing in the region where measurements are to be made. For example, the large probe of Fig. C-3 may be used to measure

the absolute magnitude of the field at the surface of the cylinder if it is calibrated on a cylinder of the same diameter. This may be done in a structure consisting of two concentric cylinders in which the magnitude of the surface field on the inner conductor is readily calculated.

The precipitation-static problem in connection with which these field-measuring techniques were first used is that of determining the relationship between the aircraft potential and the electric field at a field-meter location. This information was necessary to permit the calculation of the total aircraft charging current in Sec. IV-B. Stated more generally, the problem was that of determining the electric-field intensity at the surface of a charged body whose complicated geometry did not permit the field structure to be calculated.

The technique developed to make measurements of this type is illustrated in Fig. 23. Here a model of the aircraft in question is suspended in space and maintained at a known potential V_0. The field structure about the model is the same as that about the full-scale aircraft charged to the same potential, V_0. Field intensities on the model, however, are higher than they are on corresponding points on the aircraft by a factor equal to the model scale. Absolute magnitudes of the fields about the charged aircraft, therefore, may be determined by exploring the fields on the model in the laboratory and applying the proper correction factor.

A similar application is that of determining the relationship between the field intensity at a given point on an aircraft and the intensity of an externally-applied field. This may be done by suspending a model of the aircraft in the uniform field existing in an electrostatic cage and exploring the surface of the model with the field-measuring probe. The fields existing on the full-scale aircraft immersed in the same external field will, of course, be lower by a factor equal to the model scale.

Another application in which the field-exploring technique proved to be useful was in connection with the laboratory investigation of the corona thresholds of various points on an aircraft. Using a full-scale mock-up of an airfoil trailing edge, for example, in an electrode geometry such as that illustrated in Fig. 9, it was possible to induce corona from the mock-up. Measurements were made using the techniques developed for static-field studies, to determine the magnitude of the field at a given reference point on the full-scale mock-up (for example, a point 10 inches in from the

trailing edge) when corona threshold is reached. Subsequently, using a charged scale model of the aircraft as shown in Fig. 23, field measurements were made at the corresponding reference points on the wing and empennage surfaces thereby relating the reference-point fields to the aircraft potential. In this manner it is possible to determine in the laboratory the aircraft potential at which corona will occur from various interesting points on the aircraft.

It should be recalled that the thresholds determined in this manner apply to a stationary aircraft. In flight, localized pressure reductions may in certain locations reduce the threshold considerably below that indicated by the laboratory measurements.

APPENDIX D

TECHNIQUES FOR DETERMINING AIRCRAFT CHARGING PARAMETERS

APPENDIX D

TECHNIQUES FOR DETERMINING AIRCRAFT CHARGING PARAMETERS

By Kirchoff's law, the charge arriving on an aircraft must either be stored or discharged. Thus an aircraft in a charging situation may be represented by a capacitance in parallel with an unknown non-linear resistance, as is indicated in Fig. D-1. From the diagram we can write

$$I_{ch} = I_d(V) + C_a \frac{dV}{dt} \tag{D-1}$$

where

$\quad I_{ch}$ = total charging current

$\quad I_d$ = total discharge current

$\quad V$ = aircraft potential

$\quad C_a$ = capacitance of aircraft

$$I_c = C_a \frac{dV}{dt}$$
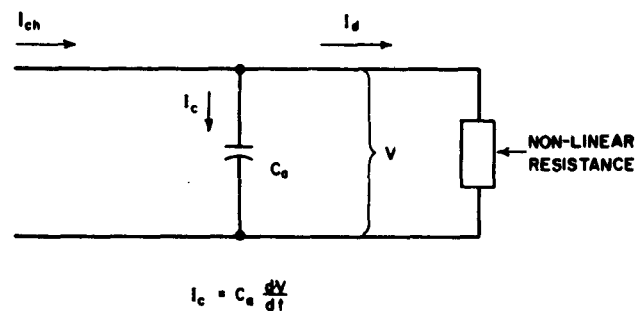
FIG. D-1

EQUIVALENT CIRCUIT OF AIRCRAFT

The aircraft potential, V, is easily measured in flight, and, C_a, may be determined by means of model measurements in the laboratory. In flight tests, however, it is difficult to measure quantities such as I_{ch}

197

and I_d. A quantity which can be measured easily in flight is the intrinsic charging rate per unit effective intercepting area, i_p. It is related to the total aircraft-charging current by the equation

$$I_{ch} = A_a i_p \qquad \text{(D-2)}$$

where

A_a = effective intercept area of aircraft.

Thus we are led to the useful normalized form of Eq. (D-1) given below

$$i_p = \frac{I_d}{A_a} + \frac{C_a}{A_a} \frac{dV}{dt} \qquad \text{(D-3)}$$

It is worth noting that if the discharge current, aircraft potential, and capacitance are known, then Eq. (D-1) may be used to compute the total charging current. Using Eq. (D-2), this could be compared to the measured charging rate, i_p, in order to obtain a value for A_a. Unfortunately this simple calculation generally cannot be carried out, since the discharge current usually is not known. For this reason, the following techniques must be employed in order to obtain estimates for the parameters of interest.

1. ASSUMED DISCHARGE CHARACTERISTICS

If, from a particular recording of flight-test data, a suitable section of record is selected such that the potential of the aircraft does not vary over a wide range, the discharge current, $I_d(V)$, may be expressed adequately by the first three terms of a Taylor expansion about the average potential for that section. Thus

$$I_d = I_0 + a_1(V - V_0) + a_2(V - V_0)^2$$

where V_0 is the average potential over the given period of time. When this is substituted into Eq. (D-3) we obtain

$$i_p = \frac{I_0}{A_a} + \frac{a_1}{A_a}(V - V_0) + \frac{a_2}{A_a}(V - V_0)^2 + \frac{C_a}{A_a}\frac{dV}{dt}$$

which may be written

$$i_p = \lambda_1 + \lambda_2(V - V_0) + \lambda_3(V - V_0)^2 + \lambda_4 C_a \frac{dV}{dt} \qquad \text{(D-4)}$$

where λ_i are unknown constants, and, in particular, $\lambda_4 = 1/A_a$.

From flight tests there are available continuous time records of charging rate and aircraft potential. Thus Eq. (D-4) provides a means of evaluating the unknown λ_i which are of interest. This is accomplished by approximating the measured charging rate, $(i_p)^*$, by the i_p calculated using Eq. (D-4) and the measured aircraft potential.

Specifically, let us suppose that the time record which has been selected is divided into a large number, N, of equal increments of time of length Δt (usually 0.1 sec). Then if the measured current at the jth interval is defined by $(i_p)^*_j$ while the voltage is V_j, the calculated charging current at the jth interval is given by

$$(i_p)_j = \lambda_1 + \lambda_2(V_j - V_0) + \lambda_3(V_j - V_0)^2 + \lambda_4 C_a \left(\frac{dV}{dt}\right)_j \qquad \text{(D-5)}$$

where

$$\left(\frac{dV}{dt}\right)_j = \frac{V_{j+1} - V_{j-1}}{2\Delta t} \ .$$

The approximation of the measured current by the calculated current is accomplished by the mean square error method. The sum of the errors over all the points must be minimized; thus the sum (sometimes called the residual)

$$R = \sum_{j=1}^{N} \{(i_p)^*_j - (i_p)_j\}^2 \qquad \text{(D-6)}$$

must be an extremum where

$(i_p)_j$ is given by Eq. (D-5).

The extremum conditions are given by the simultaneous equations:

$$\frac{\partial R}{\partial \lambda_k} = 0 \quad k = 1, 2, 3, 4.$$

199

When these partial derivatives of the residual R are taken, one obtains the following equations:

$$b_{11}\lambda_1 + b_{12}\lambda_2 + b_{13}\lambda_3 + b_{14}\lambda_4 = k_1$$

$$b_{21}\lambda_1 + b_{22}\lambda_2 + b_{23}\lambda_3 + b_{24}\lambda_4 = k_2$$

$$b_{31}\lambda_1 + b_{32}\lambda_2 + b_{33}\lambda_3 + b_{34}\lambda_4 = k_3 \qquad \text{(D-7)}$$

$$b_{41}\lambda_1 + b_{42}\lambda_2 + b_{43}\lambda_3 + b_{44}\lambda_4 = k_4$$

where:

$$b_{11} = N \qquad\qquad b_{33} = \sum_{j=1}^{N} (V_j - V_0)^4$$

$$b_{21} = b_{12} = \sum_{j=1}^{N} (V_j - V_0) = 0 \quad , \quad b_{34} = b_{43} = C_a \sum_{j=1}^{N} (V_j - V_0)^2 \left(\frac{dV}{dt}\right)_j$$

$$b_{31} = b_{22} = b_{13} = \sum_{j=1}^{N} (V_j - V_0)^2 \qquad b_{44} = C_a^2 \sum_{j=1}^{N} \left(\frac{dV}{dt}\right)_j^2$$

$$b_{14} = b_{41} = C_a \sum_{j=1}^{N} \left(\frac{dV}{dt}\right)_j \qquad\qquad k_1 = \sum_{j=1}^{N} (i_p)_j^*$$

$$b_{23} = b_{32} = \sum_{j=1}^{N} (V_j - V_0)^3 \qquad\qquad k_2 = \sum_{j=1}^{N} (i_p)_j^*(V_j - V_0)$$

$$b_{24} = b_{42} = C_a \sum_{j=1}^{N} (V_j - V_0)\left(\frac{dV}{dt}\right)_j \qquad k_3 = \sum_{j=1}^{N} (i_p)_j^*(V_j - V_0)^2$$

$$k_4 = \sum_{j=1}^{N} (i_p)_j^* \left(\frac{dV}{dt}\right)_j$$

Also recall

$$V_0 = \frac{1}{N} \sum_{j=1}^{N} V_j$$

$$\left(\frac{dV}{dt}\right)_j = \frac{V_{j+1} - V_{j-1}}{2\Delta t}$$

200

Thus all the coefficients b_{ij} and k_j in Eq. (D-7) may be calculated for the specific record which has been selected. These equations may then be solved simultaneously for the constants λ_k.

2. DISCHARGE CURRENT CALCULATED EMPIRICALLY

A second approach may be used if some method is available for estimating the discharge current I_d of Eq. (D-3). In the last series of flight tests conducted on the Boeing 367-80 aircraft, the current from a discharger at the wing tip was recorded. This current along with other flight information may be used to obtain an estimate of total discharge current. Thus we may assume that the total discharge current is a unique function of the wing-tip current:

$$I_d = f(i_w)$$

$$= B_1 i_w + B_2 i_w^2 \ . \tag{D-8}$$

The constants of this relation were calculated from flight-test data obtained on the Boeing 367-80 and 707 Aircraft and are given in Eq. (32).

The procedure in this case is similar to that used in Sec. 1 of this appendix.

Substituting Eq. (D-8) into Eq. (D-3), the calculated charging rate during the jth interval is given by

$$(i_p)_j = \beta[B_1(i_w)_j + B_2(i_w)_j^2] + \beta C_a \left(\frac{dV}{dt}\right)_j \tag{D-9}$$

where

$$\beta = \frac{1}{A} \ .$$

Again we require a mean-square error approximation to the measured charging current. Thus again for

$$R = \sum_{j=1}^{N} \left[(i_p)_j^* - (i_p)_j\right]^2$$

where $(i_p)_j$ is given by Eq. (D-9) to be an extremum, we must have $\partial R/\partial \beta = 0$.

201

We may write

$$\frac{\partial R}{\partial \beta} = \sum_{j=1}^{N} - 2\left[(i_p)_j^* - (i_\mu)_j\right] \frac{\partial (i_p)_j}{\partial \beta} \quad ,$$

and noting from Eq. (D-9) that

$$\frac{\partial (i_p)_j}{\partial \beta} = \frac{(i_p)_j}{\beta}$$

we obtain

$$\frac{\partial R}{\partial \beta} = -2 \sum_{j=1}^{N} \left[(i_p)_j^* - (i_p)_j\right] \frac{(i_p)_j}{\beta} \quad .$$

Noting that $(i_p)_j$ is not identically equal to zero, the requirement $\partial R / \partial \beta = 0$ implies that

$$\sum_{j=1}^{N} \left[(i_p)_j^* - (i_p)_j\right] = 0 \qquad \text{(D-10)}$$

or

$$\sum_{j=1}^{N} (i_p)_j^* = \beta \sum_{j=1}^{N} \left\{ [B_1 (i_w)_j + B_2 (i_w)_j^2] + C_a \left(\frac{dV}{dt}\right)_j \right\}. \qquad \text{(D-11)}$$

This equation may be solved for β and evaluated for the specific record which has been selected.

It is interesting to note that Eq. (D-10) can be written

$$\frac{1}{N} \sum_{j=1}^{N} (i_p)_j^* = \frac{1}{N} \sum_{j=1}^{N} (i_p)_j$$

which states simply that the best choice for β is that value which makes the average value of the computed charging rate equal the average value of the measured charging rate over the interval of interest.

SPACE-CHARGE-LIMITED CORONA DISCHARGE
IN THE PRESENCE OF WIND

APPENDIX E

SPACE-CHARGE-LIMITED CORONA DISCHARGE
IN THE PRESENCE OF WIND

One problem we are interested in solving is that of space-charge-limited corona current discharged from the edge of a semi-infinite conducting plate. Let us assume that a source of ions exists along the edge of the sheet, and let us consider first the case in which there is no wind. To obtain a solution to this problem, let us consider first the case of a line source of ions without the conducting plate. The relations to be satisfied are

$$\nabla \cdot \mathbf{E} = \rho/\epsilon_0 \quad \text{(Poisson's Eq. } \rho = \text{charge density)} \tag{E-1}$$

$$\nabla \cdot \mathbf{i} = 0 \quad \text{(Current continuity)} \tag{E-2}$$

$$\mathbf{i} = \rho\mathbf{u} = \rho k\mathbf{E} \quad \text{(Mobility Eq. } \mathbf{u} = \text{ion velocity, } k = \text{mobility)} \tag{E-3}$$

Cylindrical coordinates apply, and for conditions of cylindrical symmetry only r components of $\mathbf{u}$ and $\mathbf{E}$ exist, so that these equations become

$$\frac{1}{r} \frac{d}{dr} (rE) = \frac{\rho}{\epsilon_0} \tag{E-4}$$

$$\frac{1}{r} \frac{d}{dr} (r\rho u) = 0 \quad \text{(since} \quad \mathbf{i} = \rho\mathbf{u}) \tag{E-5}$$

$$u = kE \tag{E-6}$$

If the line source furnishes the current i per unit length, we have from Eq. (E-5)

$$r\rho u = \text{constant} = 1/2\pi$$

hence

$$\frac{\rho}{\epsilon_0} = \frac{i}{2\pi r u \epsilon_0}$$

and using Eq. (E-6)

$$\frac{\rho}{\epsilon_0} = \frac{i}{2\pi \epsilon_0 kEr} \quad .$$

Substituting this result into Eq. (E-4) gives

$$\frac{1}{r} \frac{d}{dr} (rE) = \frac{i}{2\pi \epsilon_0 kEr} \quad .$$

Multiplying through we obtain

$$rE \; d(rE) = \frac{1}{2\pi \epsilon_0 k} \; r dr$$

and integration gives

$$(rE)^2 = \frac{i}{2\pi \epsilon_0 k} \; r^2$$

or

$$E^2 = \frac{i}{2\pi \epsilon_0 k} \tag{E-7}$$

which indicates that the radial field about the ion source is uniform—*i.e.*, independent of r.

If a conducting plate is now introduced into the discharging region as is illustrated in Fig. E-1, in such a manner that the edge of the plate coincides with the ion source it is evident that the radial field about the line source emitting ion current provides a boundary for the uniform normal field existing above the conducting plate as is illustrated in the figure. In this case, the total current has half the value it did before the introduction of the conducting plate. Thus for the case of the ion source along the edge of a conducting plate in still air we obtain from Eq. (E-4)

$$E^2 = \frac{i}{\pi \epsilon_0 k} \quad . \tag{E-8}$$

207
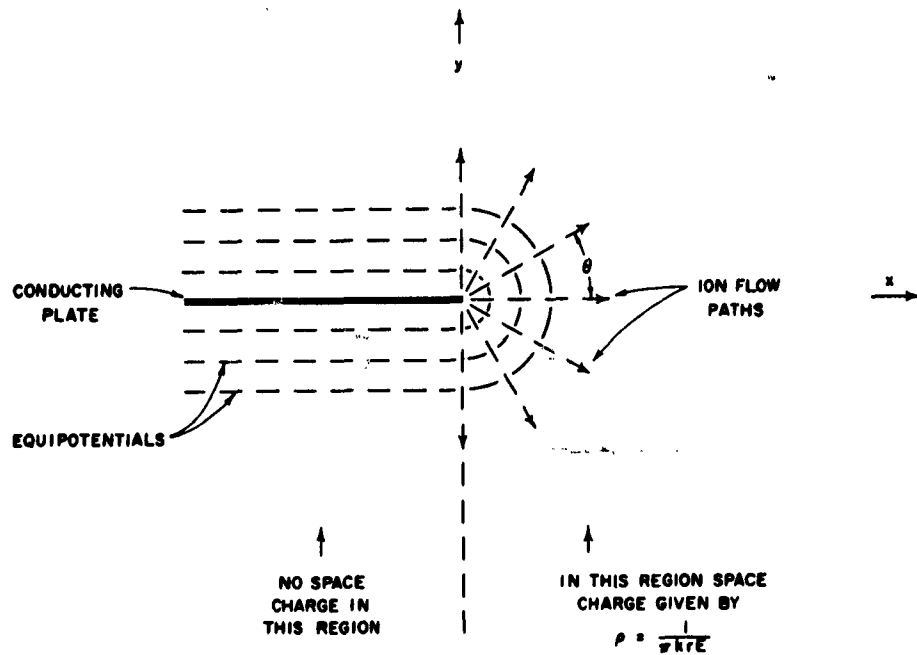
FIG. E-1

ILLUSTRATION OF DISCHARGE FROM EDGE OF PLATE IN ABSENCE OF WIND.

The field structure predicted by this analysis was verified in the laboratory using the set-up illustrated in Fig. E-2. Corona discharges were induced from the discharge points along the edge of the plane sheet by applying a high voltage to the V-shaped sheet. The field in the region between the two electrodes was explored by placing the radioactive probe at selected locations and, at each position, determining the backing voltage necessary to reduce the electrometer reading to zero.

The solution to the space-charge-limited corona problem obtained above can be extended to the case with wind by a change of variable as follows:

$$\nabla \cdot \mathbf{E} = \frac{\rho}{\epsilon_0} \tag{E-9}$$

$$\nabla \cdot \mathbf{i} = 0 \tag{E-10}$$

$$\mathbf{i} = \rho(k\mathbf{E} + \mathbf{W}) \tag{E-11}$$

$$\mathbf{W} = W\mathbf{x}_1$$

207
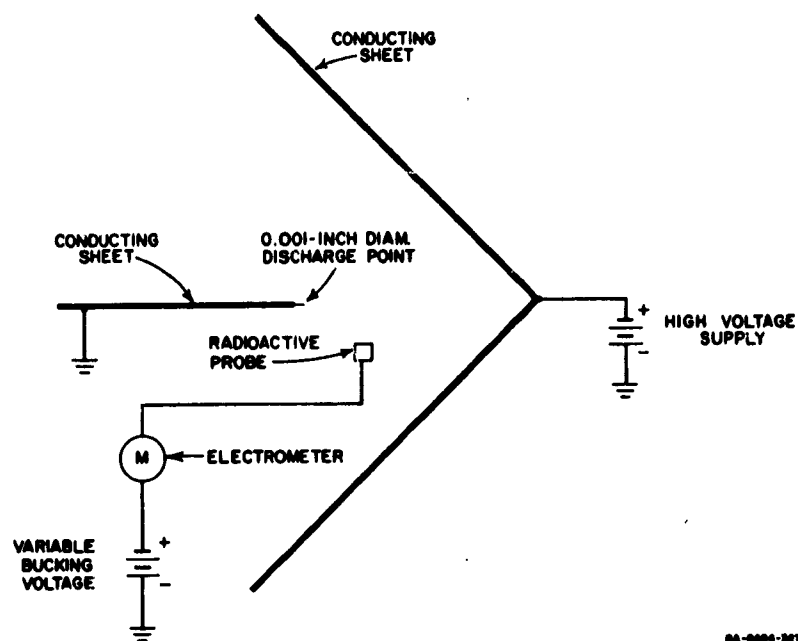
FIG. E-2

LABORATORY SET-UP USED TO VERIFY FIELD STRUCTURE
ABOUT DISCHARGING EDGE

where $\mathbf{W}$ is wind velocity, $\mathbf{x}_1$ is a unit vector in the x direction, like-
wise for $\mathbf{E}_1$ and θ_1. Let us now define

$$\mathbf{F} = \mathbf{E} + \frac{1}{k}\mathbf{W} \quad . \tag{E-12}$$

Then

$$\nabla \cdot \mathbf{F} = \frac{\rho}{\epsilon_0} \tag{E-13}$$

since

$$\nabla \cdot \mathbf{W} = 0$$

$$\nabla \cdot \mathbf{i} = 0 \tag{E-14}$$

$$\mathbf{i} = \rho k \mathbf{F} \quad . \tag{E-15}$$

208

Since Eqs. (E-13) through (E-15) correspond exactly to Eqs. (E-1) through (E-3) respectively, the solution obtained for $\mathbf{E}$ in Eq. (E-7) now holds for $\mathbf{F}$. Hence $\mathbf{F}$ about the ion source is radially directed and uniform, which may be stated mathematically as

$$\mathbf{F} = F\mathbf{r}_1 \tag{E-16}$$

where

$$F = \sqrt{\frac{i}{2\pi\epsilon_0 k}} \quad . \tag{E-17}$$

We also observe that

$$\rho = \frac{i}{2\pi k F r} \quad . \tag{E-18}$$

From Eq. (E-12) we obtain

$$\mathbf{E} = \mathbf{F} - \frac{1}{k}\mathbf{W}$$

$$= \left(F - \frac{W}{k}\cos\theta\right)\mathbf{r}_1 + \frac{W}{k}\sin\theta\,\boldsymbol{\theta}_1 \quad . \tag{E-19}$$

It should be noted that $\mathbf{E}$ has a constant value on each radial line $\theta = $ constant, as in the solution for $W = 0$. Hence, the solution of Eq. (E-19) can be discontinued and a constant field matched to it at that value of θ, say $\widehat{\theta}$, for which $\mathbf{E}$ is vertical, parallel to $\mathbf{y}_1$ in the manner illustrated in Fig. E-3. The relationship between $\mathbf{E}$ and $\mathbf{y}_1$ at $\theta = \widehat{\theta}$ may be expressed as

$$\mathbf{E} \times \mathbf{y}_1 = 0 \qquad \text{for} \quad \theta = \widehat{\theta} \quad . \tag{E-20}$$

The unit vector $\mathbf{y}_1$ may be written

$$\mathbf{y}_1 = \sin\theta\mathbf{r}_1 + \cos\theta\,\boldsymbol{\theta}_1 \quad . \tag{E-21}$$

209
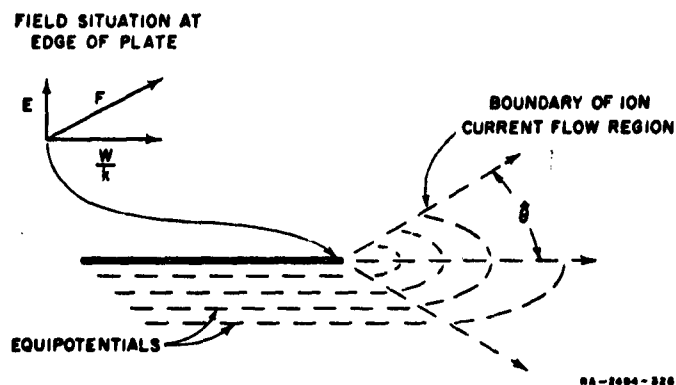
FIG. E-3

ILLUSTRATION OF DISCHARGE FROM EDGE OF PLATE
IN WIND STREAM

Substituting Eqs. (E-19) and (E-21) into Eq. (E-20) gives

$$\left[\left(F - \frac{W}{k} \cos \widehat{\theta}\right)\mathbf{r}_1 + \frac{W}{k} \sin \widehat{\theta} \, \boldsymbol{\theta}_1\right] \times [\sin \theta \mathbf{r}_1 + \cos \widehat{\theta} \, \boldsymbol{\theta}_1] \; = \; 0 \qquad (\text{E-22})$$

but, since

$$\mathbf{r}_1 \times \mathbf{r}_1 \; = \; \boldsymbol{\theta}_1 \times \boldsymbol{\theta}_1 \; = \; 0$$

and

$$\mathbf{r}_1 \times \boldsymbol{\theta}_1 \; = \; -\boldsymbol{\theta}_1 \times \mathbf{r}_1 \; = \; \mathbf{z}_1$$

Eq. (E-22) becomes

$$\left[\left(F - \frac{W}{k} \cos \widehat{\theta}\right) \cos \widehat{\theta} - \frac{W}{k} \sin^2 \widehat{\theta}\right]\mathbf{z}_1 \; = \; 0 \qquad (\text{E-23})$$

from which we find that

$$\cos \widehat{\theta} \; = \; \frac{W}{kF} \; . \qquad (\text{E-24})$$

We may now find the actual current discharged from the edge of the plate under the effects of the field $\mathbf{E}$ and the wind $\mathbf{W}$. In Eq. (E-17) we have an expression for the total current i flowing in the case where $\mathbf{F}$

210

has complete cylindrical symmetry. It will be recalled, however, that the solution to the problem with the conducting sheet illustrated in Fig. E-3 was obtained by retaining the wedge of ion current extending over the range $-\hat{\theta} < \theta < \hat{\theta}$ from the solution for the symmetrical problem. Thus we may write

$$\frac{\hat{i}}{i} = \frac{2\hat{\theta}}{2\pi} = \frac{\hat{\theta}}{\pi} \qquad (E\text{-}25)$$

where $\hat{i}$ is the current discharged in the wedge $-\hat{\theta} < \theta < \hat{\theta}$ illustrated in the figure. Also from the figure we can observe that

$$F^2 = E^2 + \left(\frac{W}{k}\right)^2 \qquad (E\text{-}26)$$

and

$$\hat{\theta} = \tan^{-1} \frac{Ek}{W} \qquad . \qquad (E\text{-}27)$$

From Eq. (E-17) we obtain

$$i = 2\pi\epsilon_0 k F^2$$

from which, by using Eqs. (E-25) to (E-27), we obtain

$$\hat{i} = \frac{\hat{\theta}}{\pi} i$$

$$= 2\hat{\theta}\epsilon_0 k \left(E^2 + \frac{W^2}{k^2}\right) \qquad (E\text{-}28)$$

$$= 2\left(E^2 + \frac{W^2}{k^2}\right)\epsilon_0 k \, \tan^{-1} \frac{Ek}{W} \qquad .$$

For high wind speeds such that $W/k \gg E$ we can observe that $\tan^{-1}(Ek/W) \cong Ek/W$ so that Eq. (E-28) reduces to

$$\hat{i} \cong 2\frac{W^2}{k^2} \epsilon_0 k \frac{Ek}{W} = 2W\epsilon_0 E \qquad . \qquad (E\text{-}29)$$

From Eq. (E-28) or Eq. (E-29) we can determine the current discharged per unit length along the edge of a plate, given the wind speed and the field existing near the edge of the plate when the discharge is in progress. It now remains to find a method by which E at the edge of the plate can be estimated in the laboratory.

Let us consider the airfoil from which the corona discharge occurs to be represented by a conducting strip of width $2h = 4a$ as is illustrated in Fig. E-4. It would appear intuitively that placing an ion source along the edge of the strip would result in a situation such as that pictured in Fig. E-4(a) where the field about the strip is approximately the same as the field about a strip twice as wide having twice as much charge as is illustrated in Fig. E-4(b). If the effect of the space charge can indeed be simulated by doubling the width of the strip, we have a simple technique for estimating the discharge current from a section of airfoil. Tabs which double the chord of the airfoil may be attached to the discharging region on a model of the aircraft charged to a potential V as is indicated in Fig. 30. The normal field measured at the junction of
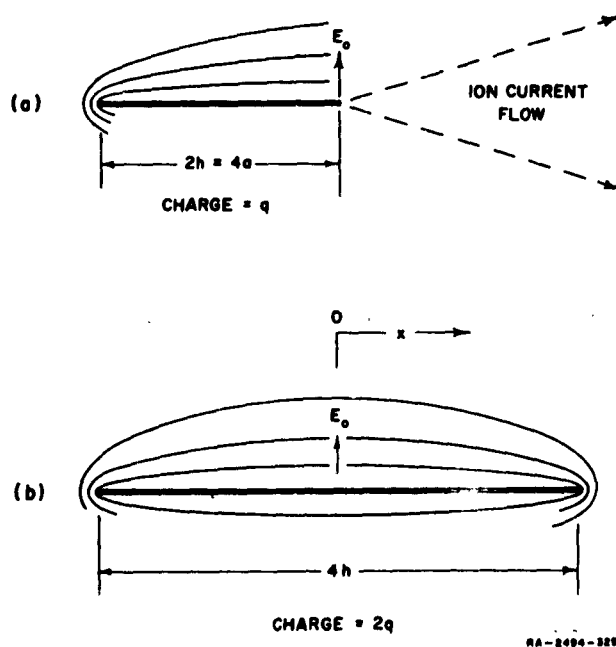
FIG. E-4

APPROXIMATE EFFECT OF SPACE CHARGE UPON FIELD
AT EDGE OF STRIP

213

the tab and the airfoil (reduced by the modeling factor) may be substituted into Eq. (E-28) or (E-29) to determine the discharge current at an aircraft potential V. We must now determine the conditions under which this procedure is valid.

As a preliminary let us note that the normal field E_0 in Fig. E-4(b) is given by

$$E_0 = \frac{q}{2\pi\epsilon_0 h} \quad .$$

(E-30)

This result may be obtained from the expression for the field about a charged cylinder by performing a conformal transformation which transforms the cylinder into a strip.

To solve the problem of a region of space charge near the edge of a conducting strip we will proceed as follows: First we will find the field produced by a line charge parallel to an uncharged conducting cylinder. Next we will map the cylinder into a strip. Then we will assume a space-charge distribution and integrate to find the field E_1 produced at the sheet by the space charge. To this we will add the field E_2 resulting from the charge q per unit length on the conducting strip, thereby obtaining the total field E_t about the strip. We will then determine the conditions under which E_t at the edge of the sheet equals E_0 at the center of a sheet of twice the width.

By the method of images the line charge $-\lambda$ parallel to the conducting cylinder may be replaced by three line charges as is indicated in Fig. E-5.[25] From the figure the complex potential may be written
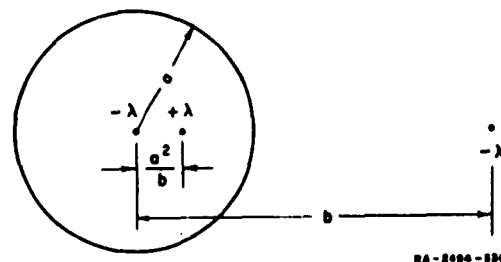
FIG. E-5

IMAGE IN CONDUCTING CYLINDER

$$V = -\frac{\lambda}{2\pi\epsilon_0}\left[\ln w - \ln\left(w - \frac{a^2}{b}\right)\right.$$

$$\left. + \ln(w - b) - \text{const.}\right] \quad .$$

(E-31)

213

If we stipulate that the potential of the cylinder is zero ($V = 0$ when $w = a$), we find that const. $= ln\ (-b)$ so that Eq. (E-31) becomes

$$V \;=\; -\frac{\lambda}{2\pi\epsilon_0}\cdot\left[ln\ w\ -\ ln\left(w\ -\ \frac{a^2}{b}\right)\ +\ ln\ (w\ -\ b)\ -\ ln\ (-b)\right] \qquad \text{(E-32)}$$

which, after algebraic manipulation becomes

$$V \;=\; -\frac{\lambda}{2\pi\epsilon_0}\ ln\ \frac{bw\ -\ w^2}{bw\ -\ a^2} \qquad . \qquad \text{(E-33)}$$

To map the cylinder into a strip let us use the transformation

$$z \;=\; w\ +\ \frac{a^2}{w} \qquad\qquad \text{(E-34)}$$

illustrated in Fig. E-6. Solving Eq. (E-34) for w we obtain

$$w \;=\; \frac{z}{2}\ +\ \sqrt{\left(\frac{z}{2}\right)^2\ -\ a^2} \qquad . \qquad \text{(E-35)}$$

$$z = w + \frac{a^2}{w}$$

RA-2494-351
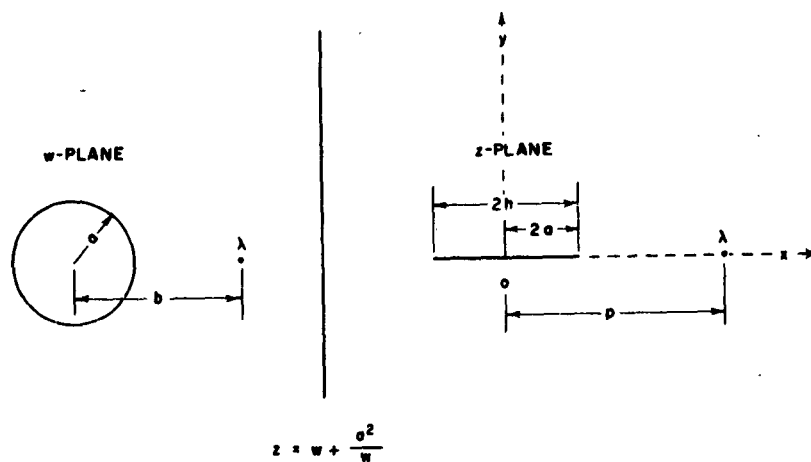
FIG. E-6

ILLUSTRATION OF CONFORMAL MAPPING

We will be interested in the fields in the z-plane, so let us evaluate

$$\frac{dV}{dz} = -E_\lambda(z) = \frac{dV}{dw}\frac{dw}{dz} \quad . \tag{E-36}$$

From Eq. (E-33) we obtain

$$E_\lambda(z) = \frac{\lambda}{2\pi\epsilon_0} \frac{(bw - a^2)}{(bw - w^2)} \cdot \frac{(bw - a^2)(b - 2w) - (bw - w^2)b}{(bw - a^2)^2} \tag{E-37}$$

which reduces to

$$E_\lambda(z) = \frac{\lambda}{2\pi\epsilon_0} \frac{bw^2 - 2a^2w + a^2b}{w[bw^2 - (a^2 + b^2)w + a^2b]} \quad . \tag{E-38}$$

Differentiating Eq. (E-35) we obtain

$$\frac{dw}{dz} = \frac{1}{2}\left(1 + \frac{\dfrac{z}{2}}{\sqrt{\left(\dfrac{z}{2}\right)^2 - a^2}}\right) \tag{E-39}$$

which, upon substituting Eq. (E-35), becomes

$$\frac{dw}{dz} = \frac{1}{2}\left(1 + \frac{w^2 + a^2}{w^2 - a^2}\right) \quad . \tag{E-40}$$

Substituting Eqs. (E-38) and (E-40) into Eq. (E-36) gives

$$E_\lambda(z) = \frac{\lambda}{4\pi\epsilon_0} \frac{bw^2 - 2a^2w + a^2b}{w[bw^2 - (a^2 + b^2)w + a^2b]}\left(1 + \frac{w^2 + a^2}{w^2 - a^2}\right) \tag{E-41}$$

which reduces to

$$E_\lambda(z) = \frac{\lambda}{2\pi\epsilon_0}\left[\frac{w^2 - 2\dfrac{a^2}{b}w + a^2}{w^2 - \dfrac{a^2 + b^2}{b}w + a^2}\right]\frac{w}{w^2 - a^2} \tag{E-42}$$

215

From Fig. E-6 and Eq. (E-34) we observe that

$$p = b + \frac{a^2}{b} = \frac{a^2 + b^2}{b} \qquad \text{(E-43)}$$

and

$$\frac{a^2}{b} = p - b \quad . \qquad \text{(E-44)}$$

Substituting Eqs. (E-43) and (E-44) into Eq. (E-42) we obtain

$$E_\lambda(z) = \frac{\lambda}{2\pi\epsilon_0} \frac{w^2 - 2(p - b)w + a^2}{w^2 - pw + a^2} \cdot \frac{w}{w^2 - a^2} \qquad \text{(E-45)}$$

which upon substituting Eq. (E-35) and reducing becomes

$$E_\lambda(z) = \frac{\lambda}{2\pi\epsilon_0} \frac{p - z - 2\sqrt{\left(\frac{p}{2}\right)^2 - a^2}}{p - z} \cdot \frac{\left(\frac{z}{2}\right) + \sqrt{\left(\frac{z}{2}\right)^2 - a^2}}{\left(\frac{z^2}{2}\right) - 2a^2 + z\sqrt{\left(\frac{z}{2}\right)^2 - a^2}} \qquad \text{(E-46)}$$

Substituting $h = 2a$, this becomes

$$E_\lambda(z) = \frac{\lambda}{2\pi\epsilon_0} \frac{p - z - \sqrt{p^2 - h^2}}{p - z} \cdot \frac{z + \sqrt{z^2 - h^2}}{z^2 - h^2 + z\sqrt{z^2 - h^2}} \qquad \text{(E-47)}$$

This can be further reduced to

$$E_\lambda(z) = \frac{\lambda}{2\pi\epsilon_0} \frac{(p - z) - \sqrt{p^2 - h^2}}{p - z} \cdot \frac{1}{\sqrt{z^2 - h^2}} \quad . \qquad \text{(E-48)}$$

By integrating Eq. (E-48) we can find $E_1(z)$, the field resulting from the space charge. Let us assume that the wind velocity is high, and that the negative space charge may be represented by a sheet of charge of uniform density lying between $z = h$ and $z = B$. In an actual charging

situation, the positive space charge is equal to the negative space charge but lies farther away. Let us approximate the situation by assuming a sheet of positive charge lying between B and $2B - h$.

For a sheet of charge of density σ coulombs per square meter, λ becomes σdp and Eq. (E-48) may be written

$$E_\sigma(z) \;=\; dE_1(z) \;=\; \frac{\sigma}{2\pi\epsilon_0} \; \frac{1}{\sqrt{z^2 - h^2}} \; \frac{(p - z) - \sqrt{p^2 - h^2}}{p - z} \; dp \quad . \quad \text{(E-49)}$$

If we now define

$$A \;=\; \frac{\sigma}{2\pi\epsilon_0} \; \frac{1}{\sqrt{z^2 - h^2}} \tag{E-50}$$

Eq. (E-49) reduces to

$$E_\sigma(z) \;=\; A \, \frac{(p - z) - \sqrt{p^2 - h^2}}{p - z} \; dp \quad . \tag{E-51}$$

The field due to space charge is given by

$$E_1(z) \;=\; A \int_h^B \frac{(p - z) - \sqrt{p^2 - h^2}}{p - z} \; dp \; - \; A \int_B^{2B-h} \frac{(p - z) - \sqrt{p^2 - h^2}}{p - z} \; dp \quad .$$

$$\text{(E-52)}$$

Defining

$$f(p) \;=\; \int \frac{(p - z) - \sqrt{p^2 - h^2}}{p - z} \; dp \tag{E-53}$$

the field may be written

$$E_1(z) \;=\; A\{[f(p)]_h^B - [f(p)]_B^{2B-h}\}$$

$$=\; A\{f(B) - f(h) - f(2B - h) + f(B)\} \tag{E-54}$$

$$=\; A\{2f(B) - f(h) - f(2B - h)\} \quad .$$

We will, therefore, integrate Eq. (E-53) to find $f(p)$, substitute the required limits, and substitute the resulting functions into Eq. (E-54). Let us now make the following change of variable

$$p - z = x \qquad (E-55)$$

hence

$$dp = dx$$

and

$$p^2 = (x + z)^2 = x^2 + 2xz + z^2 \qquad (E-56)$$

Let us now define

$$p^2 - h^2 = a + bx + cx^2 = X \qquad (E-57)$$

where

$$a = z^2 - h^2$$

$$b = 2z$$

$$c = 1 \quad .$$

Thus the integral of Eq. (E-53) becomes

$$f(p) = \int \frac{x - \sqrt{X}}{x} \, dx = \int 1 - \frac{\sqrt{X}}{x} \, dx \qquad (E-58)$$

$$= x - \int \frac{\sqrt{X}}{x} \, dx \quad .$$

Next, using integral 187 of Pierce,[26]

$$\int \frac{\sqrt{X}}{x} \, dx = \sqrt{X} + \frac{b}{2} \int \frac{dx}{\sqrt{X}} + a \int \frac{dx}{x\sqrt{X}} \qquad (E-59)$$

Using integral 160 of Pierce,

$$\frac{b}{2} \int \frac{dx}{\sqrt{X}} = \frac{b}{2} \ln \left(\sqrt{X} + x + \frac{b}{2} \right)$$

$$= \frac{b}{2} \sinh^{-1} \left(\frac{2x + b}{j2h} \right) \qquad \text{(E-60)}$$

$$= -j \frac{b}{2} \sin^{-1} \left(\frac{2x + b}{2h} \right)$$

where

$$j = \sqrt{-1} \quad .$$

Using integral 183 of Pierce

$$a \int \frac{dx}{x\sqrt{X}} = \frac{a}{\sqrt{a}} \sin^{-1} \left(\frac{bx + 2a}{2hx} \right) \quad . \qquad \text{(E-61)}$$

Upon assembling the various terms we obtain

$$f(p) = x - \sqrt{X} + j \frac{b}{2} \sin^{-1} \left(\frac{2x + b}{2h} \right) + j\sqrt{a} \sin^{-1} \left(\frac{bx + 2a}{2hx} \right) \quad \text{(E-62)}$$

but

$$\frac{2x + b}{2h} = \frac{2p - 2z + 2z}{2h} = \frac{p}{h}$$

and

$$\frac{bx + 2a}{2hx} = \frac{2zp - 2z^2 + 2z^2 - 2h^2}{2h(p - z)} = \frac{zp - h^2}{h(p - z)} \quad .$$

Thus

$$f(p) = p - z - \sqrt{p^2 - h^2} + j\left[z \sin^{-1} \frac{p}{h} + \sqrt{z^2 - a^2} \sin^{-1} \frac{zp - h^2}{h(p - z)} \right] \quad . \qquad \text{(E-63)}$$

But

$$\sin^{-1}\frac{p}{h} = \frac{\pi}{2} - j\ ln\left(\frac{p}{h} + \sqrt{\frac{p^2}{h^2} - 1}\right)$$

Hence,

$$f(p) = p - z - \sqrt{p^2 - h^2} + j\frac{\pi}{2}z + z\ ln\left(\frac{p}{h} + \sqrt{\frac{p^2}{h^2} - 1}\right) + j\sqrt{z^2 - h^2}\ \sin^{-1}\frac{zp - h^2}{h(p - z)} \quad .$$

$$(E\text{-}64)$$

Let us now substitute the required limits into the individual terms of Eq. (E-64) and combine the corresponding terms according to Eq. (E-54):

$$E_1(z) = A\ \left\{[2B - 2z - 2\sqrt{B^2 - h^2} - h + z - 2B + h + z + \sqrt{(2B - h)^2 - h^2}]\right.$$

$$+ \left[0\left(\text{from } j\frac{\pi}{2}z \text{ term}\right)\right]$$

$$+ z\left[2\ ln\left(\frac{B}{h}\ \sqrt{\frac{B^2}{h^2} - 1}\right) - ln\left(\frac{2B - h}{h} + \sqrt{\frac{(2B - h)^2}{h^2} - 1}\right)\right]$$

$$+ j\sqrt{z^2 - h^2}\ \left.\left[2\ \sin^{-1}\frac{zB - h^2}{h(B - z)} - \sin^{-1}\frac{zh - h^2}{h(h - z)} - \sin^{-1}\frac{z(2B - h) - h^2}{h(2B - h - z)}\right]\right\} \quad .$$

$$(E\text{-}65)$$

Let us now permit B to become large compared to h and $|z|$. Then we obtain for the various terms in Eq. (E-65)

$$[\text{First term in brackets}] = [\sqrt{(2B - h)^2 - h^2} - 2\sqrt{B^2 - h^2}]$$

$$= \sqrt{4B^2 - 4Bh} - 2B\sqrt{1 - h^2/B^2}$$

$$= 2B[\sqrt{1 - h/B} - \sqrt{1 - h^2/B^2}]$$

$$= 2B\left[\left(1 - \frac{1}{2}\frac{h}{B} + \dots\right) - \left(1 - \frac{1}{2}\frac{h^2}{B^2} + \dots\right)\right]$$

$$= -h$$

[Second term in brackets] $= z \left[\ln \dfrac{\left(\dfrac{B}{h} + \sqrt{\dfrac{B^2}{h^2} - 1} \right)^2}{\dfrac{2B - h}{h} + \sqrt{\dfrac{(2B - h)^2}{h^2} - 1}} \right]$

$$\cong z \left[\ln \frac{4B^2/h^2}{4B/h} \right]$$

$$= z \left[\ln B/h \right]$$

[Third term in brackets] $\cong j\sqrt{z^2 - h^2} \left[2 \sin^{-1} \dfrac{z}{h} \quad \sin^{-1} \dfrac{-h(h - z)}{h(h - z)} \quad \sin^{-1} \dfrac{z}{h} \right]$

$$= j\sqrt{z^2 - h^2} \left[\sin^{-1} \frac{z}{h} - \sin^{-1} (-1) \right]$$

$$= j\sqrt{z^2 - h^2} \left[\frac{\pi}{2} + \sin^{-1} \frac{z}{h} \right] .$$

Upon assembling these terms we obtain

$$E_1(z) = A \left\{ -h + z \ln \frac{B}{h} + j\sqrt{z^2 - h^2} \left(\frac{\pi}{2} + \sin^{-1} \frac{z}{h} \right) \right\} \tag{E-66}$$

which upon substituting Eq. (E-50) becomes

$$E_1(z) = \frac{\sigma}{2\pi\epsilon_0} \frac{1}{\sqrt{z^2 - h^2}} \left\{ -h + z \ln \frac{B}{h} + j\sqrt{z^2 - h^2} \left(\frac{\pi}{2} + \sin^{-1} \frac{z}{h} \right) \right\} . \tag{E-67}$$

This is an approximate expression for the field about the strip due to space charge.

The field due to a charge q on the strip is given by

$$E_2 = \frac{-q}{2\pi\epsilon_0\sqrt{z^2 - h^2}} . \tag{E-68}$$

This result may be obtained from the field about a charged cylinder by means of the transformation of Eq. (E-34).

The total field E_t is given by $E_t = E_1 + E_2$

$$E_t = \frac{1}{2\pi\epsilon_0\sqrt{z^2 - h^2}} \left\{ -q + \sigma\left[-h + z\, \ln\frac{B}{h} + j\sqrt{z^2 - h^2}\left(\frac{\pi}{2} + \sin^{-1}\frac{z}{h}\right)\right]\right\}$$

$$= j\sigma\frac{\dfrac{\pi}{2} + \sin^{-1}\dfrac{z}{h}}{2\pi\epsilon_0} + \frac{1}{2\pi\epsilon_0\sqrt{z^2 - h^2}}\left[-q + \sigma\left(-h + z\, \ln\frac{B}{h}\right)\right]$$

which for $z = x$ and $x < h$ becomes

$$E_t = j\sigma\frac{\dfrac{\pi}{2} + \sin^{-1}\dfrac{x}{h}}{2\pi\epsilon_0} - j\,\frac{1}{2\pi\epsilon_0\sqrt{h^2 - x^2}}\left[-q + \sigma\left(-h + x\, \ln\frac{B}{h}\right)\right] \quad . \tag{E-69}$$

In order that Eq. (E-69) remain finite as $x \to h$ we must have

$$q = \sigma\left(-h + h\, \ln\frac{B}{h}\right) \tag{E-70}$$

or

$$\sigma = \frac{q}{h\left(-1 + \ln\dfrac{B}{h}\right)} \tag{E-71}$$

which means that Eq. (E-69) becomes for $x \to h$

$$E_t\bigg|_{x=h} = j\sigma\frac{\dfrac{\pi}{2} + \sin^{-1}\dfrac{h}{h}}{2\pi\epsilon_0} = j\sigma\frac{1}{2\epsilon_0} \tag{E-72}$$

where σ is related to the charge on the strip by Eq. (E-71).

222

Let us now substitute for q the expression

$$q = 2\pi\epsilon_0 hE_0 \qquad \text{(E-73)}$$

obtained from Eq. (E-30) to relate the field existing with the discharge to the field E_0 measured when the strip width is doubled. Equation (E-71) becomes

$$\sigma = \frac{2\pi\epsilon_0 hE_0}{h\left(-1 + ln\dfrac{B}{h}\right)} = \frac{2\pi\epsilon_0 E_0}{\left(-1 + ln\dfrac{B}{h}\right)} \qquad . \qquad \text{(E-74)}$$

When this is substituted into Eq. (E-72) we obtain

$$E_t\bigg|_{x=h} = jE_0 \frac{\pi}{\left(-1 + ln\dfrac{B}{h}\right)} \qquad . \qquad \text{(E-75)}$$

Thus the field at the edge of the discharging strip equals E_0 if

$$ln\frac{B}{h} = \pi + 1 \qquad . \qquad \text{(E-76)}$$

It is worth noting that because of the logarithmic dependence, the value of the field (and hence the discharge current) is not critically dependent upon B. If $ln (B/h) = \pi + 1$ the discharge current has the value obtained by substituting E_0 into Eq. (E-28) or (E-29). This corresponds to $B/h = 64$. In other words if recombination begins at a distance 32 times the width of the strip, the current approximates that obtained using E_0. If recombination begins at a distance twice this great, the current is lower by approximately 20%, and if the distance is half as great, the current is higher by approximately 25%.

The problem of corona discharge from the end of a cylinder will be treated with much less rigor. Let us assume that the discharger consists of a conducting rod of radius, a, so oriented that a wind of velocity W is directed along its axis, as is indicated in Fig. E-7. Let us assume, furthermore, that an ion source is placed at the end of the rod. If a

223
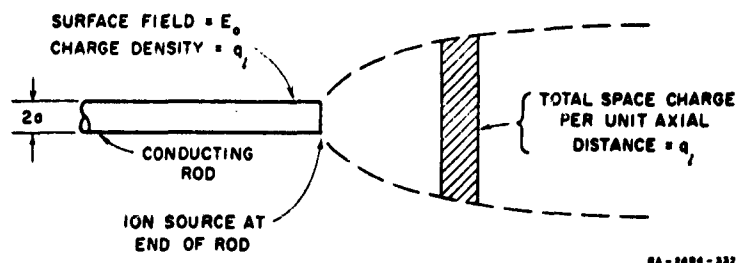
FIG. E-7

ILLUSTRATION OF DISCHARGE FROM END OF ROD

voltage is now applied to the rod, it will acquire a charge per unit length q_l given by

$$q_l = 2\pi\epsilon_0 a E_0 \qquad \text{(E-77)}$$

where ϵ_0 is the permittivity of free space and E_0 is the field strength at the surface of the rod. As a result of the applied voltage, current will be discharged from the end of the rod and carried away by the wind, forming a space-charge cloud. The magnitude of the axial charge density within this cloud may be inferred from a consideration of the fields near the end of the rod. If we assume, for example, that the charge per unit length on the rod is greater than in the space charge, there will exist an axial component of field tending to force additional charge into the space charge region. If, on the other hand, the charge per unit length in the space charge is greater than on the rod, an axial component of field will be generated, tending to reduce the current into the space-charge region. Equilibrium is established when the charge per unit length in the space charge equals the charge density on the rod, since, in this case, a purely radial field exists near the end of the rod and there is no tendency to either increase or decrease the current entering the space-charge cloud. Thus we may write for the current carried away by the wind

$$i = q_l W \qquad \text{(E-78)}$$

or, substituting Eq. (E-77)

$$i = 2\pi\epsilon_0 a E_0 W \qquad \text{(E-79)}$$

224

which states that the discharge current is directly proportional to the wind velocity and to the surface field near the end of the rod. In the case of a practical discharger, Eq. (E-79) is not valid for small field strengths since the threshold field of the rod is not zero. For values of E_0 well above the threshold field, however, the current given in Eq. (E-79) should be a very good approximation to the blow-away current.

These results suggest a useful laboratory technique for studying discharge-current capacities of discharger installations. One of the problems in a study of this sort is that of adequately reproducing the effect of the space charge generated by the discharger. Since it was shown that the fields about a discharger and its space charge are the same as those around an infinite conducting cylinder, the effects of the space charge may be simulated by attaching at the end of the discharger a conducting rod whose diameter equals that of the discharger. If a voltage is now applied to the aircraft model, the surface field measured near the junction of the discharger and "space charge cylinder" may be used together with Eq. (E-79) to determine the discharge current.

This simple technique is useful only in the study of high discharge currents when the finite corona threshold of the discharger is unimportant. Since in a practical discharger a non-zero axial field is required at the end of the discharger rod to maintain the discharge, the charge per unit length in the space charge is lower than on the discharger rod. To simulate this effect in the laboratory, it would be necessary to use a smaller-diameter space-charge cylinder or to simulate the space charge in some other fashion.

APPENDIX F

ANALYSIS OF THE DECOUPLING OF A DISCHARGER

APPENDIX F

ANALYSIS OF THE DECOUPLING OF A DISCHARGER

Let us assume that we have a resistive rod of radius a, resistance per unit length ρ, and total length l, mounted on the edge of a semi-infinite conductive sheet which is immersed in an RF field as is illustrated in Fig. F-1. In the region to the left of the sheet and in the plane of the sheet the applied field, unperturbed by charge on the rod, is given by

$$E_a(x,0) = \frac{A}{\sqrt{l-x}} \tag{F-1}$$

where A is a constant related to the amplitude of the applied RF voltage.
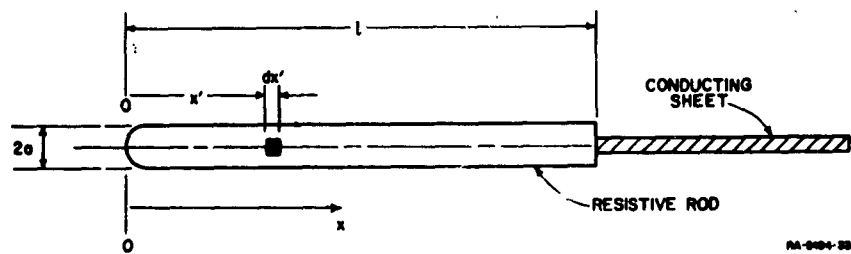
FIG. F-1

MODEL USED FOR CALCULATION OF DECOUPLING

The tangential field at the surface of the rod due to charge flow consists of two components: that due to IR drop and that due to the Coulomb field from charge accumulated on the rod. The tangential field due to the current $I(x)$ flowing in the rod is

$$E_i(x,a) = I(x)\rho \quad . \tag{F-2}$$

Assuming the Coulomb field to be the same as if the charge were concentrated on the axis of the rod, the x-component of this field due to a charge per unit length $q(x)$ on the rod is

229

$$E_q(x,a) \;=\; -\frac{\partial}{\partial x}\,V(x,a) \;=\; -\frac{\partial}{\partial x}\left[\frac{1}{4\pi\epsilon_0}\int_0^l \frac{q(x')dx'}{\sqrt{(x-x')^2+a^2}}\right] \quad . \qquad \text{(F-3)}$$

Making use of the continuity equation for steady-state sinusoidal signals, the charge per unit length can be related to the current in the rod by

$$\frac{\partial I(x')}{\partial x'} \;=\; -j\omega q(x') \qquad\qquad \text{(F-4)}$$

where $j = \sqrt{-1}$. Solving Eq. (F-4) for $q(x')$ and substituting into Eq. (F-3) we obtain

$$E_q(x,a) \;=\; \frac{j}{4\pi\epsilon_0\omega}\int_0^l \frac{(x-x')\dfrac{\partial I(x')}{\partial x'}}{[(x-x')^2+a^2]^{3/2}}\,\partial x'\,dx' \quad . \qquad \text{(F-5)}$$

If we now observe that the applied field at the surface of the rod is essentially equal to field along the axis of the rod we can equate the applied field given by Eq. (F-1) to the field due to charge flow given by the sum of Eq. (F-2) and Eq. (F-5).

$$I(x)\rho + \frac{j}{4\pi\omega\epsilon_0}\int_0^l \frac{(x-x')\dfrac{\partial I(x')}{\partial x'}}{\left[(x-x')^2+a^2\right]^{3/2}}\,dx' \;=\; \frac{A}{\sqrt{l-x}} \quad . \qquad \text{(F-6)}$$

Differentiating with respect to x and dividing by ρ we obtain

$$\frac{\partial I(x)}{\partial x} + \frac{j}{4\pi\omega\epsilon_0\rho}\int_0^l \frac{a^2-2(x-x')^2}{\left[(x-x')^2+a^2\right]^{3/2}}\,\frac{\partial I(x')}{\partial x'}\,dx' \;=\; \frac{A}{2\rho(l-x)^{3/2}} \qquad \text{(F-7)}$$

which is a standard form of Fredholm's integral equation of the second kind in the unknown $\partial I(x)/\partial x$. To simplify the notation, let

$$\frac{\partial I(x)}{\partial x} \;=\; \phi(x) \quad \text{and} \quad \frac{j}{4\pi\omega\epsilon_0\rho} \;=\; \lambda \quad . \qquad \text{(F-8)}$$

Then Eq. (F-7) becomes

$$\phi(x) + \lambda \int_0^l \frac{a^2 - 2(x - x')^2}{\left[(x - x')^2 + a^2\right]^{5/2}} \phi(x')dx' = \frac{A}{2\rho(l - x)^{3/2}} \quad . \quad \text{(F-9)}$$

The form of the kernel and the fact that the driving function has a singularity at $x = l$ make it extremely difficult to obtain an exact solution to Eq. (F-9). However, by expanding the driving function as a binomial series and using the method of iterated kernels, an approximate solution can be obtained for $x < l$. Since it is known from experiment that the point of minimum coupling lies near the end of the rod (i.e., near $x = 0$), and approximate solution of this form will be satisfactory. The solution is[27]

$$\phi(x) = \sum_{n=0}^{\infty} (-\lambda)^n \phi_n(x) \quad \text{(F-10)}$$

where

$$\phi_0(x) = \frac{A}{2\rho(l - x)^{3/2}} \simeq \frac{A}{2\rho l^{3/2}} \left[1 + \frac{3}{2}\frac{x}{l} + \frac{15}{8}\left(\frac{x}{l}\right)^2 + \ldots\right]$$

$$\phi_1(x) = \int_0^l \frac{a^2 - 2(x - x'')^2}{\left[(x - x')^2 + a^2\right]^{5/2}} \phi_0(x')dx'$$

$$\phi_2(x) = \int_0^l \frac{a^2 - 2(x - x')^2}{\left[(x - x')^2 + a^2\right]^{5/2}} \phi_1(x')dx'$$

etc.

An approximate solution is obtained by taking the first two terms of Eq. (F-10), giving

$$\phi(x) \simeq \frac{A}{2\rho(l - x)^{3/2}} - \frac{\lambda A}{2\rho l^{3/2}} \int_0^l \frac{a^2 - 2(x - x')^2}{\left[(x - x')^2 + a^2\right]^{5/2}} \left[1 + \frac{3}{2}\frac{x'}{l} + \frac{15}{8}\left(\frac{x'}{l}\right)^2\right]dx'$$

$$\text{(F-11)}$$

231

where $\phi_0(x)$ has been approximated by the first three terms of the binomial expansion under the integral. Although somewhat lengthy, the integral in Eq. (F-11) is simple and straightforward. Upon integration, Eq. (F-11) becomes

$$\phi(\xi) \cong \frac{A}{2\rho l^{3/2}} \left\{ \frac{1}{(1-\xi)^{3/2}} - \lambda/24 l^2 \left[\frac{126\xi^2 - 357\xi + 231 + 126\alpha^2}{\left[(\xi-1)^2 + \alpha^2\right]^{3/2}} \right. \right.$$
$$\left. \left. - \frac{36\xi^2 - 24\xi + 36\alpha^2}{(\xi^2 + \alpha^2)^{3/2}} + 90 \ln \frac{\sqrt{(\xi-1)^2 + \alpha^2} + \xi - 1}{\sqrt{\xi^2 + \alpha^2} + \xi} \right] \right\} \quad (F-12)$$

where $\xi = x/l$ and $\alpha = a/l$.

From the coupling theorem it is noted that for minimum coupling between the discharge and the receiving antennas, the reciprocal field in the direction of the discharge current flow should be minimum. For the rod discharger under consideration, the reciprocal field is the radial field about the rod. This field, however, is proportional to the distributed charge on the rod, which in turn is related to $\phi(\xi)$ by Eqs. (F-4) and (F-8). The reciprocal field in the vicinity of the discharge is thus

$$E_1 = \frac{q}{2\pi\epsilon_0 a} = j \frac{\phi(\xi)}{2\pi\epsilon_0 \omega a} \quad (F-13)$$

where the nomenclature of Eq. (1), Sec. II of this report has been used for the reciprocal field. If the relative magnitude of the reciprocal field is plotted as a function of discharge location as illustrated in Fig. 61, the point of minimum coupling for a given frequency and rod resistance is readily apparent. The coupling data have been normalized to the value of the minimum coupling for $\gamma^2 = 4$. The condition $\gamma^2 = 4$ describes, at a frequency of 0.1 Mc, the dischargers used in the flight tests for which

$$l = 6 \text{ inch} \cong 0.15 \text{ meter}$$

$$a = 1/8\text{-inch} \cong 0.03 \text{ meter}$$

$$\rho = 133 \text{ megohm per meter.}$$

In calculating the data of Fig. 61 the normalized rod radius was fixed at the value $\alpha = 0.02$, but as can be seen from Eq. (F-12) when ξ is much

larger than α the influence of α becomes negligible. Hence for normal discharger designs, the value of α has little influence upon the location of the minimum point or upon the magnitude of the coupling at the minimum point. A discharger rod length $l = 0.15$ meters was assumed in computing the coupling data. The data, however, may be applied to dischargers of other lengths by determining the required correction for the curve in the lower part of Fig. 61.

To determine the advantage of the decoupled discharger over a discharge from the airfoil trailing edge it is first necessary to calculate the relative coupling of the two. This can be done with the aid of Eq. (1) of Sec. II:

$$I_2(\omega) \quad = \quad \frac{1}{V_1(\omega)} \int_{T_2} E_1 \cdot J_2 dv \tag{1}$$

where it will be recalled that V_1 is the voltage which, when applied to the antenna terminals, produces the reciprocal field E_1 in the region of the discharge T_2, and I_2 is the noise current flowing in the short-circuited antenna terminals when the discharge characterized by the current density J_2 flows in the region T_2. Let us assume that the discharge in both cases occurs from a needle 0.25 inch long. This assumption simplifies the problem considerably. Since the form of the current density J_2 is determined by the details of the discharge point, specifying that the discharge occurs from the same type of point on the trailing edge and on the discharger is equivalent to specifying that J_2 is identical in the two discharges. Furthermore, the form of E_1 in the region of the discharge is determined by the boundary conditions imposed by the point. Thus the form of E_1 in the two cases will be the same although the magnitudes will be different. Thus it is apparent that the integral of Eq. (1) need not be evaluated since, except for absolute magnitudes, the integrals for the two cases are identical. Hence, the ratio of the two short-circuit currents is equal to the ratio of the magnitudes of the fields existing at the tips of the two pins. The magnitude of the coupling field at the end of a discharge pin is proportional to the potential shorted out by the pin.

After calculating the noise reduction obtained assuming both discharges occur from sharp pins, we can relate this result to the actual

233

situation by employing the experimental result discussed earlier in this section that a discharge from a pin is 6 db less noisy than a discharge from a trailing edge.

In the case of the decoupled discharger, the reciprocal field in the direction of the discharge pin is

$$E_{1_r} = j \frac{\phi(\xi d)}{2\pi\omega\epsilon_0 r}$$

when ξ_d is the location of the discharge point and r is the radial distance from the center of the rod. The potential shorted by the pin is, therefore,

$$V_{pin\ disch} = \frac{j\phi(\xi_d)}{2\pi\omega\epsilon_0} \int_a^{3a} \frac{dr}{r} \tag{F-14}$$

where the limits of integration are chosen from the dimensions of the dischargers used during the flight tests.

When the discharge occurs from the trailing edge, the reciprocal field in the direction of the discharge pin is given by Eq. (F-1) so the potential shorted by the pin is

$$V_{pin\ trail\ edge} = A \int_l^{l-2a} \frac{dx}{\sqrt{l - x}} \tag{F-15}$$

Upon substituting the values $\xi = 0.1$, $l = 0.15$ meters, $\rho = 133$ megohm per meter, $\alpha = 0.02$, and $f = 100$ kilocycles, we find from Eqs. (F-14) and (F-15) that the decoupling is

$$\frac{V_{pin\ disch}}{V_{pin\ trail\ edge}} = -35.6\ db \tag{F-16}$$

Taking into account the fact that a discharge from the trailing structure is 6 db noisier than a discharge from a pin in the same location, the noise reduction obtained at 100 kc by the installation of decoupled dischargers is

234

$$\frac{I_{n_{disch}}}{I_{n_{trail \cdot edge}}} = -(35.6 + 6)$$

$$= -41.6 \text{ db} \quad .$$

It should be recalled that this is the noise reduction at frequencies lower than those normally used for aircraft communication and navigation systems. From Fig. 61 it is evident that at higher frequencies the noise reduction will be much greater. For example, at a frequency of one mega-cycle, the noise reduction is 61.6 db.

235

ACKNOWLEDGMENTS

KC-135 and 707) to test many of the theories proposed. The authors are
particularly grateful to the ground and flight crews for their interest
in this program and for their cooperation in making the flight tests
successful. Most especially they would like to acknowledge the help of
Mr. J. O. Stenoien, who initiated the cooperative effort, and who fol-
lowed and supported the work during the entire program, and, in partic-
ular, during the disheartening early phases.

REFERENCES

1. H. G. Hucke, "Precipitation Static Interference," *Proc. IRE* **27**, 5 (May 1939).

2. R. C. Ayers and J. O. Jarrard, "Aircraft Precipitation Static Investigation," Contract W 33-106 SC-70, Trans-World Airlines Inc. (August 1944).

3. Ross Gunn *et al.*, "Army-Navy Precipitation Static Project," *Proc. IRE* **34**, 4 and 5 (1946).

4. H. J. Dana, "Block and Squirter for Reduction of Precipitation Static," Second Air Force Operations Analysis Report 15 (February 1945).

5. Philco Corp., Research Division, "Final Engineering Report on Precipitation Static Reduction," USAF Contract W 33-038 ac 20763 (9 February 1950).

6. Denver Research Institute, "Development of Aircraft Discharge Methods," Final Report, Contract AF 33(616)-157, University of Denver, Denver, Colorado (15 April 1956).

7. R. L. Tanner, "Radio Interference from Corona Discharges," Tech. Report 37, SRI Project 591, Contract AF 19(604)-266, Stanford Research Institute, Menlo Park, California (April 1953).

8. R. L. Tanner and J. E. Nanevicz, "Radio Noise Generated on Aircraft Surfaces," Final Report, SRI Project 1267, Contract AF 33(616)-2761, Stanford Research Institute, Menlo Park, California (September 1956).

9. J. E. Nanevicz, "A Study of Precipitation-Static Noise Generation in Aircraft Canopy Antennas," Tech. Report 62, SRI Project 1197, Contract AF 19(604)-1296, Stanford Research Institute, Menlo Park, California (December 1957).

10. J. E. Nanevicz and R. L. Tanner, "Investigation of Precipitation Static Noise in High-Speed Aircraft," WADC Tech. Report 59-521, Wright Air Development Division, ARDC, Wright-Patterson Air Force Base, Ohio (September 1959).

11. J. E. Nanevicz, R. L. Tanner, E. F. Vance, "Evaluation of Natural Interference Reduction Techniques on High-Speed Aircraft," WADC Tech. Note 60-153, Wright Air Development Division, ARDC, Wright-Patterson Air Force Base, Ohio.

12. J. T. Bolljahn, "The Measurement of Low Frequency Antenna Properties Using Electrostatic Techniques," Tech. Report 19, SRI Project 188, Stanford Research Institute, Menlo Park, California (September 1951).

13. J. T. Bolljahn and R. F. Reese, "Electrically Small Antennas and the Low-Frequency Aircraft Antenna Problem," *IRE Trans.*, PGAP-1, 2 (October 1953).

14. A. Vassiliadis, "A Study of Corona Discharge Noise in Aircraft Antennas," Tech. Report 70, SRI Project 2494, Contract AF 19(604)-3458, Stanford Research Institute, Menlo Park, California (July 1960).

15. R. J. Brun and R. G. Dorsch, "Impingement of Water Droplets on an Ellipsoid with Fineness Ratio 10 in Axisymmetric Flow," NACA Tech. Note 3147, NACA, Washington, D.C. (May 1954).

16. R. G. Dorsch, R. J. Brun, and J. L. Gregg, "Impingement of Water Droplets on an Ellipsoid with Fineness Ratio 5 in Axisymmetric Flow," NACA Tech. Note 3099, NACA, Washington, D.C. (March 1954).

17. R. J. Brun, H. M. Gallegher, and D. C. Vogt, "Impingement of Water Droplets on NACA 65-208 and 65-212 Airfoils at 4° Angle of Attack," NACA Tech. Note 2952, Washington, D.C. (May 1953).

18. R. L. Tanner, J. E. Nanevicz, E. F. Vance, "Development and Evaluation of Natural Interference Reduction Techniques on High-Speed Aircraft," SRI Project 2848, Contract AF 33(616)-6561, Stanford Research Institute. Menlo Park, California. (In preparation—will be available as a WADD Technical Report after July 1961).

239

REFERENCES

19. R. L. Tanner and J. E. Nanevicz, "Tests of Ortho-Decoupled Aircraft Static Dischargers," AEEC Letter No. 60-2-6, Aeronautical Radio, Inc., 1700 K Street N.W., Washington 6, D.C. (26 April 1960).

20. S. Silver, *Microwave Antenna Theory and Design*, Radiation Laboratory Series, No. 12 (McGraw-Hill Book Company, Inc., New York City, 1949).

21. C. O. Lennstrom, "Development of an HF Antenna for Use with the AN/ARC-21 Equipment on KC-135 Airplane," Document No. D6-1315, Contract AF 33(600)-28410, Boeing Airplane Company, Seattle, Washington (September 1957).

22. S. A. Schelkunoff and H. T. Friis, *Antennas Theory and Practice* (John Wiley and Sons, Inc., New York City, 1952).

23. D. P. Coffin, Jr., "Integration of Interference Blanker Techniques into LF Receivers," WADC Tech. Report 59-529, WADC, Wright-Patterson Air Force Base, Ohio.

24. J. A. Stratton, *Electromagnetic Theory*, pp. 485-6 (McGraw-Hill Book Company, Inc., New York City, 1941).

25. W. R. Smythe, *Static and Dynamic Electricity*, 1st ed., p. 69 (McGraw-Hill Book Company, Inc., New York City, 1939).

26. B. O. Peirce, *A Short Table of Integrals*, 3rd rev. ed., (Ginn and Company, New York City, 1929).

27. H. Margenau and G. M. Murphy, *The Mathematics of Physics and Chemistry*, 2nd ed. (D. Van Nostrand Company, Inc., 1956).

TECHNICAL REPORTS IN THIS SERIES

Reports Issued on Contract AF 19(122)-78

1. "Electric Dipoles in the Presence of Elliptic and Circular Cylinders," by W. S. Lucke, September 1949.

2. "Asymmetrically Fed Antennas," by C. T. Tai, November 1949.

3. "Double Fed and Coupled Antennas," by C. T. Tai, February 1949.

4. "Equivalent Radii of Thin Cylindrical Antennas with Arbitrary Cross Sections," by Carson Flammer, March 1950.

5. "Use of Complementary Slots in Aircraft Antenna Impedance Measurements," by J. T. Bolljahn, February 1950.

6. "Wing-Cap and Tail-Cap Aircraft Antennas," by J. V. N. Granger, March 1950.

7. "Investigation of Current Distribution on Asymmetrically-Fed Antennas by Means of Complementary Slots," by R. M. Hatch, Jr., February 1950.

8. "Electromagnetic Resonance Phenomena in Aircraft Structures," by A. S. Dunbar, May 1950.

9. "The Effect of a Grounded Slab on the Radiation from a Line Source," by C. T. Tai, June 1950.

10. "A Method for the Calculation of Progressive-Phase Antennas for Shaped Beams," by A. S. Dunbar, June 1950.

11. "Admittance of an Open-Ended Coaxial Line in an Infinite Grounded Plane," by W. S. Lucke, June 1950.

12. "A Variational Solution to the Problem of Cylindrical Antennas," by C. T. Tai, August 1950.

13. "Uniform Progressive-Phase Antennas Having Asymmetrical Amplitude Distributions," by A. S. Dunbar, September 1950.

14. "Small Dipole-Type Antennas," by J. T. Bolljahn, September 1950.

15. "Tables of Modified Cosine Integrals," January 1951.

16. "Prolate Spheroidal Wave Functions," by Carson Flammer, February 1951.

17. "An Antenna Evaluation Method," by W. S. Lucke, April 1951.

18. "Radar Response from Thin Wires," by C. T. Tai, March 1951.

19. "The Measurement of Low-Frequency Aircraft Antenna Properties Using Electrostatic Methods," by J. T. Bolljahn, September 1951.

20. (Dropped).

21. "A Method for the Calculation of Progressive-Phase Antennas for Shaped Beams,"
    Part II, by A. S. Dunbar, May 1951.

22. "The Prolate Spheroidal Monopole Antenna," by Carson Flammer, August 1957, issued
    on Contract AF 19(604)-1296.

23. "Variational Solution for the Problem of the Asymmetric Dipole," by I. Reese,
    August 1951.

24. "Quasi-Static Solution for Diffraction of a Plane Electromagnetic Wave by a Small
    Oblate Spheroid," by C. T. Tai, September 1952 [Issued on Contract AF 19(604)-266].

25. "Transmission Through a Rectangular Aperture in an Infinite Screen," by W. S. Lucke,
    September 1951.

Reports Issued on Contract AF 19(604)-266

26. "Improvements in Instrumentation for the Investigation of Aircraft Antenna Radi-
    ation Patterns by Means of Scale Models," by R. M. Hatch, Jr., August 1952.

27. "The Vector Wave Solution of the Diffraction of Electromagnetic Waves by Circular
    Disks and Apertures," by Carson Flammer, September 1952.

28. "An Investigation of the Distribution of Current on Collinear Parasitic Antenna
    Elements," by R. M. Hatch, Jr., August 1952.

29. "On the Theory of Diffraction of Electromagnetic Waves by a Sphere, by C. T. Tai,
    October 1952.

30. "High-Frequency Airborne Direction Finding," by P. S. Carter, Jr., December 1952.

31. "An Electrolytic Tank Method for Low-Frequency Loop Antennas Studies," by R. F. Reese,
    July 1953.

32. "Radiation from a Uniform Circular Loop Antenna in the Presence of a Sphere," by
    C. T. Tai, December 1952.

33. "A Computer for Use with Antenna Model Ranges," by C. E. Fisher, February 1953.

34. "Tail-Cap Antenna Radiation Pattern Studies," by J. H. Bryan, January 1953.

35. "U-H-F Tail-Cap Antenna Pattern Characteristics and Their Control," by A. R. Ellis,
    March 1955 [issued on Contract AF 19(604)-1296].

36. "Mutual Admittance of Slots in Cylinders," by W. S. Lucke, February 1953.

37. "Radio Interference from Corona Discharges," by R. L. Tanner, April 1953.

38. "Effects of Airframe Configuration on Low-Frequency Antenna Characteristics,"
    by C. M. Hoblitzell, April 1953.

39. "The Effects of Thin Resistive Coatings on Low-Frequency Aircraft Antenna Performance,"
    by C. W. Steele [issued on Contract AF 19(604)-1296] January 1956.

40. "Analysis of the Overstation Behavior of Airborne ADF Systems," by H. H. Ward, June 1954.

41. "Some Electromagnetic Problems Involving a Sphere," by C. T. Tai, April 1953.

42. "Radiation Pattern Measurements of Stub and Slot Antennas on Spheres and Cylinders," by J. Bain, April 1953.

43. "Current Distribution on Wing-Cap and Tail-Cap Antennas," by Irene C. Carswell, May 1954.

44. "A Study of Radiating Structures for Perpendicularly-Polarized Flush Radar Antennas," by Edward M. T. Jones and Seymour B. Cohn, July 1953.

45. "Radiation from Current Elements and Apertures in the Presence of a Perfectly Conducting Half-Plane Sheet," by C. T. Tai, July 1954.

46. "A Glossary of Dyadic Green's Functions," by C. T. Tai, July 1954.

47. "Horizontally Polarized Long-Slot Array," by R. C. Honey, August 1954.

Reports Issued on Contract AF 19(604)-1296

48. "Microwave Radiation from Large Finite Bodies," by Seymour B. Cohn and Tetsu Morita, January 1955.

49. "Radiation from Electric and Magnetic Dipoles in the Presence of a Conducting Circular Disk," by Carson Flammer, February 1955.

50. "A Study of Some Inherent Errors in the Three-Dimensional Raydist System," by Irene Carswell, March 1955.

51. "Operating Characteristics of Flush-Mounted Bombing Antennas," by E. M. T. Jones, November 1955.

52. "Properties of the Asymmetric Dipole," by Irene Carswell, December 1955.

53. "Notch Coupling to the Electromagnetic Resonance of a Delta-Wing Aircraft," by William L. Jones, December 1955.

54. "A Flush-Mounted Horizontally Polarized Directional Antenna," by R. C. Honey, January 1956.

55. "Radiation from a Flush-Mounted Scanning Antenna on the Nose Section of a Supersonic Aircraft," by J. K. Shimizu and T. Morita, December 1955.

56. "An Economical Logarithmic Recording System," by Lloyd A. Robinson, June 1956.

57. "Variational Formulae for Domain Functionals in Electromagnetic Theory," by Carson Flammer, March 1957.

58. "Systems Considerations for High Speed Missile Seeker Antennas," by Donald L. Margerum and E. Thomas Brandon, May 1957. Confidential.

59. "High-Strength Dielectric Materials for Very Fast Aircraft," by Henry J. Sang, March 1957.

60. "Impedance Matching Limitations with Application to the Broadband Antenna Problem," by Arthur Vassiliadis, January 1957.

61. "Shunt-Fed and Notch-Fed Aircraft Antennas," by Robert L. Tanner, July 1957.

62. "A Study of Precipitation-Static Noise Generation in Aircraft Canopy Antennas," by Joseph E. Nanevicz, September 1957.

63. "Electromagnetic Wave Propagation in a Medium with Variable Dielectric Constant $1 + kr^{-1}$," by Carson Flammer, January 1958.

Reports Issued on Contract AF 19(604)-3458

64. "The Back-Scattering Cross Sections of Missile Trails," by Carson Flammer, June 1958.

65. "Ray-Tracing and Diffraction in a Medium with Variable Permittivity and Attenuation," by James A. Cochran, October 1958.

66. "Feasibility Study of Aircraft Antennas for Forward-Scatter and Meteor-Burst Communication," by J. F. Cline, July 1959.

67. "A Study of Possibilities for Improving Space Utilization and Performance of Rhombic Antennas," by Angel Martin-Caloto, July 1959.

68. "Aerodynamic Characteristics of Trailing-Wire Antennas at Supersonic Speeds," by F. B. Harris, Jr., March 1960.

69. "Voltage Breakdown of Antennas at High Altitudes," by W. E. Scharfman and T. Morita, April 1960.

70. "A Study of Corona Discharge Noise in Aircraft Antennas," by A. Vassiliadis, August 1960.

71. "Theoretical Limitations on the Broadbanding Potential of Antennas, with Application to Cavity Backed Slots and Other Antennas," by A. Vassiliadis and R. L. Tanner, August 1960.

72. "A New Approach to the Evaluation of HF Aircraft Antennas," by J. F. Cline, March 1961

73. "Precipitation Charging and Corona-Generated Interference in Aircraft," by R. L. Tanner and J. E. Nanevicz, May 1961.

73. "Transmission Through an Ionized Medium in the Presence of a Strong Magnetic Field," by H. S. Rothman and T. Morita.

DISTRIBUTION LIST

CODE	ORGANIZATION	NO. OF COPIES	CODE	ORGANIZATION	NO. OF COPIES
AF 29	ARXC (PGTRI, Tech Library) Eglin AFB, Fla.	1	AF 308	WADD (WWDXTR, Mr. A. D. Clark) Directorate of System Engineering Dyna Soar Engineering Office Wright-Patterson AFB, Ohio	1
AF 124	RADC (RCOIL-2) Griffiss AFB, N.Y.	1	Ar 42	Director U.S. Army Ordnance Ballistic Research Laboratories Aberdeen Proving Ground, Maryland Attn: Ballistic Measurements Laboratory	1
AF 143	RADC (RCE) Attn: Dr. John S. Burgess Griffiss AFB, N.Y.	1			
AF 139	AF Missile Dev. Cen. (MDGRT) Atten: Technical Library Holloman AFB, New Mexico	1	Ar 47	Ballistic Research Laboratories Aberdeen Proving Ground, Maryland Attn: Technical Information Branch	1
AF 69	Director of Resident Training 3380th Technical Training Group Keesler AFB, Mississippi Atten: OA-3011 Course	1	Ar 3	Director Evans Signal Laboratory Belmar, New Jersey Attn: Mr. O. C. Woodyard	1
AF 18	AUL Maxwell AFB, Ala.	1			
AF 86	SAC (Operations Analysis Office) Offutt AFB, Nebraska	1	Ar 5	U.S. Army Signal Engineering Laboratories Evans Signal Laboratory Belmar, New Jersey Attn: Technical Document Center	1
AF 5	AF Missile Test Center Patrick AFB, Fla Attn: AFMTC, Tech Library, MU-135	1			
AF 227	USAF Security Service (CLR) San Antonio, Texas	1	AF 330	Hq. ARDC (RDR-62) Reference 4600-CA Andrews AFB, Washington 25, D.C.	3
AF 28	Hq. USAF (Major R. L. Stell) Tactical Air Group Wash 25, D.C.	1	AF 253	EOARDC Shell Building 47 Rue Cantersteen Brussels, Belgium	1
AF 91	AFOSR (SRY, Technical Director) 14th Street and Constitution Avenue Wash, D.C.	1	Ar 10	Massachusetts Institute of Technology Signal Corps Liaison Officer Cambridge 39, Mass. Attn: A. D. Bedrosian, Room 26-131	1
AF 166	Hq. USAF (AFOAC-S/E) Communication-Electronics Directorate Wash 25, D.C.	1	Ar 49	Commanding General U.S. Army Signal Engineering Laboratories Fort Monmouth, New Jersey Attn: SIGFM/EL-AT	1
AF 314	Director of Air Force Research Division AFTD Wash, D.C.	1			
AF 63	WADD (WCLRSA, Mr. Portune) Wright-Patterson AFB, Ohio	1	Ar 39	Commander USASRDL Fort Monmouth, New Jersey Attn: Mr. F. J. Triola	1
AF 43	WADD (WCLJA-2) Attn: Aeronautical Systems Center (AMC) Wright-Patterson AFB, Ohio	1	Ar 67	Commander Army Rocket & Guided Missile Agency Redstone Arsenal, Alabama Attn: Technical Library, ORDXR-OTL	4
AF 68	WADD (WWRNRE 3) Attn: Mr. Paul Springer Wright-Patterson AFB, Ohio	1	Ar 9	Chief of Research & Development Department of the Army Wash 25, D.C. Attn: Scientific Information Branch	1
AF 231	Director, Electronics Division Air Technical Intelligence Center Attn: AFCIN-4E1, Colonel H. K. Gilbert Wright-Patterson AFB, Ohio	1	Ar 41	Office of Chief Signal Officer Engineering & Technical Division Wash 25, D.C. Attn: SIGNET-5	1

CODE	ORGANIZATION	NO. OF COPIES	CODE	ORGANIZATION	NO. OF COPIES
Ar 18	Guided Missile Fuze Library Diamond Ordnance Fuze Laboratories Wash 25, D.C. Attn: R. D. Hatcher, Chief Microwave Development Section	1	N 9	Chief, Bureau of Ordnance Department of the Navy Wash 25, D.C. Attn: Code Ad3	1
G 59	Advisory Group on Electronic Parts Room 103, Moore School Building 200 South 33rd Street Philadelphia 4, Pennsylvania	1	N 16	Commander U.S. Naval Air Missile Test Center Point Mugu, California Attn: Code 366	1
G 2	ASTIA Arlington Hall Station Arlington 12, Virginia	10	N 23	U.S. Naval Ordnance Laboratory White Oak, Silver Spring 19, Maryland Attn: The Library	1
G 103	National Aeronautical Space Agency Langley Aeronautical Research Laboratory Langley, Virginia Attn: Mr. Cliff Nelson	1	N 26	Commander U.S. Naval Ordnance Test Station China Lake, California Attn: Code 753	1
G 8	Library National Bureau of Standards Boulder Laboratories Boulder, Colorado	2	N 27	Librarian U.S. Naval Postgraduate School Monterey, California	1
G 13	National Bureau of Standards U.S. Department of Commerce Wash 25, D.C. Attn: Mr. A. G. McNish	1	N 29	Director U.S. Naval Research Laboratory Washington 25, D.C. Attn: Code 2027	2
G 27	National Bureau of Standards U.S. Department of Commerce Wash 25, D.C. Attn: Gustave Shapiro, Chief Engineering Electronics Section Electricity and Electronics Division	1	N 30	Dr. J. I. Bohnert, Code 5210 U.S. Naval Research Laboratory Wash 25, D.C.	1
G 6	Office of Technical Services Department of Commerce Washington 25, D.C. Attn: Technical Reports Section	2	N 35	Commanding Officer and Director U.S. Navy Underwater Sound Laboratory Fort Trumbull, New London, Connecticut	1
			N 37	Chief of Naval Research Department of the Navy Wash 25, D.C. Attn: Code 427	1
M 6	AFCRL Office of Aerospace Research (USAF) (CRRELT) L. G. Hanscom Field, Bedford, Mass.	10	N 48	Commanding Officer U.S. Naval Air Development Center Johnsville, Penn. Attn: NADC Library	1
M 17	AFCRL Office of Aerospace Research (USAF)(CRRD) Attn: Carlyle J. Sletten L. G. Hanscom Field, Bedford, Mass.	3	N 85	Commanding Officer and Director U.S. Navy Electronics Laboratory (Library) San Diego 52, Cal.	1
	AFCRL Office of Aerospace Research (USAF)(CRRD) Attn: Contract Files L. G. Hanscom Field, Bedford, Mass.	2	N 86	Chief, Bureau of Ordnance Department of the Navy Surface Guided Missile Branch Wash 25, D.C. Attn: Code ReS1-e	1
M 54	Hq. AFCCDD (CCRRC, Capt. John J. Hobson) L. G. Hanscom Field, Bedford, Mass.	1	N 87	Chief, Bureau of Ordnance Department of the Navy Wash 25, D.C. Attn: Fire Control Branch (ReS4)	1
M 59	AFCCDD L. G. Hanscom Field, Bedford Mass.	1	N 88	Department of the Navy Bureau of Aeronautics Technical Data Division, Code 4106 Wash 25, D.C.	1
N 1	Director, Avionics Division (AV) Bureau of Aeronautics Department of the Navy Wash 25, D.C.	1			
N 3	Chief, Bureau of Ships Department of the Navy Washington 25, D.C. Attn: Code 690	1	N 91	Commander U.S. Naval Air Test Center Patuxent River, Maryland Attn: ET-315, Antenna Branch	1

CODE	ORGANIZATION	NO. OF COPIES	CODE	ORGANIZATION	NO. OF COPIES
N 92	New York Naval Shipyard Material Laboratory, Code 932 Brooklyn 1, New York Attn: Mr. Douglas First	1	I 247	Bendix Radio Division Bendix Aviation Corporation E. Joppa Road Towson 4, Maryland Attn: Dr. D. M. Allison, Jr Director Engineering & Research	1
N 93	Commanding Officer U.S. Naval Ordnance Laboratory Corona, Cal. Attn: Documents Librarian	1	I 248	Bjorksten Research Laboratories, Inc. P.O. Box 265 Madison, Wisconsin Attn: Librarian	1
N 141	ANUC Regional Office c/o Departemnt of the Navy Room 4549, Munitions Building Wash 25, D.C.	1	I 249	Boeing Airplane Company Pilotless Aircraft Division P.O. Box 3707 Seattle 24, Washington Attn: R. R. Barber, Library Supervisor	2
N 73	Office of Naval Research Branch Office, London Navy 100, Box 39 F.P.O. New York, N.Y.	10	I 250	Boeing Airplane Company Wichita Division Engineering Library Wichita 1, Kansas Attn: Kenneth C. Knight, Library Supervisor	1
I 601	Aero Geo Astro Corp. 1200 Duke Street Alexandria, Virginia Attn: Library	1	I 892	Boeing Airplane Company 7755 East Marginal Way Seattle 24, Washington Attn: Mr. D. L. Scidmore	1
I 1	Airborne Instruments Laboratory, Inc. Division of Cutler Hammer Walt Whitman Road Melville, L.I. New York Attn: Library	1	I 253	Chance Vought Aircraft, Inc. 9314 West Jefferson Street Dallas, Texas Attn: A. D. Pattullo, Librarian	1
I 3	Andrew Alford, Consulting Engineers 299 Atlantic Avenue Boston 10, Mass.	1	I 470	Chu Associates P.O. Box 387 Whitcomb Avenue Littleton, Mass.	1
I 374	ACF Industries, Inc. Southeast Corner, 52nd Avenue and Jackson Street Bladensburg, Prince George's County, Maryland Attn: Librarian	1	I 918	Collins Radio Co. 855 35th Street, N.E. Cedar Rapids, Iowa Attn: Dr. R. L. McCreary	1
I 205	Battelle Memorial Institute 505 King Avenue Columbus 1, Ohio Attn: Wayne E. Rife, Project Leader Electrical Engineering Division	1	I 919	Collins Radio Co. 1200 North Alma Road Richardson, Texas Attn: C. D. Tipton	1
I 8	Bell Aircraft Corporation Post Office Box One Buffalo 5, New York Attn: Eunice P. Hazelton, Librarian	1	I 126	Convair, A Division of General Dynamics Corp. Fort Worth, Texas Atten: K. G. Brown Division Research Librarian	1
I 469	Bell Telephone Laboratories Murray Hill New Jersey	1	I 254	Convair, A Division of General Dynamics Corp. 3165 Pacific Highway San Diego 12, Cal. Attn: Mrs. Dora B. Burke, Engineering Librarian	1
I 13	Bell Telephone Laboratories, Inc. Whippany Laboratory Whippany, New York Attn: Technical Information Library	1	I 25	Cornell Aeronautical Laboratory, Inc 4455 Genesee Street Buffalo 21, New York Attn: Librarian	1
I 246	Bendix Corporation Pacific Division 11600 Sherman Way North Hollywood, Cal. Attn: Engineering Library	1			
I 940	Aerospace Corp. Box 95085 Los Angeles 45, Calif. Attn: Library	1	I 255	Dalmo Victor Company A Division of Textron, Inc. 1515 Industrial Way Belmont, Cal. Attn: Mary Ellen Addems, Technical Librarian	1

CODE	ORGANIZATION	NO. OF COPIES		CODE	ORGANIZATION	NO. OF COPIES
I 28	Dorne and Margolin, Inc. 29 New York Avenue Westbury, Long Island, N.Y.	1		I 893	General Electric Company 3750 D Street Philadelphia 24, Pa. Attn: Mr. H. G. Lew Missile and Space Vehicle Department	1
I 257	Douglas Aircraft Co., Inc. 827 Lapham Street El Segundo, Cal. Attn: Engineering Library	1		I 270	General Precision Laboratory, Inc. 63 Bedford Road Pleasantville, New York Attn: Librarian	1
I 258	Douglas Aircraft Company, Inc. 3000 Ocean Park Boulevard Santa Monica, Cal. Attn: Peter Duyan, Jr. Chief, Electrical/Electronics Section	1		I 48	Goodyear Aircraft Corp. 1210 Massillon Road Akron 15, Ohio Attn: Library, Plant G	1
I 259	Douglas Aircraft Company, Inc. 2000 North Memorial Drive Tulsa, Oklahoma Attn: Engineering Librarian, D-250	1		I 448	Granger Associates Electronics Systems, 974 Commercial St Palo Alto, California Attn: John V. N. Granger, President	1
I 187	Electromagnetic Research Corporation 5001 College Avenue College Park, Maryland Attn: Mr. Martin Katzin	1		I 272	Grumman Aircraft Engineering Corporation Bethpage, Long Island, New York Attn: Engineering Librarian, Plant No. 5	1
I 415	Electronics Communication 1830 York Road Timonium, Maryland	1		I 273	Hallicrafters Company 4401 West 5th Avenue Chicago 24, Illinois Attn: LaVerne LaGioia, Librarian	1
I 299	Electronic Specialty Comapany 5121 San Fernando Road Los Angeles 39, Cal. Attn: Donald L. Margerum Chief Engineer, Radiation Systems Division	1		I 737	The Hallicrafters Co. 5th and Kostner Avenues Chicago 24, Illinois Attn: Henri Hodara, Head of Space Communication	1
I 204	Emerson and Cuming, Inc. 869 Washington Street Canton, Mass. Attn: Mr. W. Cuming	1		I 311	Hermes Electronics Company 75 Cambridge Parkway Cambridge, Mass Attn: Mrs. Lois Seulowitz Technical Librarian	1
I 262	Emerson Electric Mfg. Co. 8100 West Florissant Avenue St. Louis 21, Missouri Attn: Mr. E. R. Breslin, Librarian	1		I 274	Hoffman Electronics Corp. 3761 South Hill Street Los Angeles 7, California Attn: Engineering Library	1
I 147	Emerson Radio-Phonograph Corp. Emerson Research Laboratories 701 Lamont Street, N W. Washington 10, D.C. Attn: Mrs. R. Corbin, Librarian	1		I 270	Hughes Aircraft Company Antenna Department Building 12, Mail Station 2714 Culver City, California Attn: Dr. W. H. Kummer	1
I 264	Fairchild Aircraft, Missiles Division Fairchild Eng. and Airplane Corp. Hagerstown, Maryland Attn: Library	1		I 56	Hughes Aircraft Company Florence and Teale Streets Culver City, California Attn: Mr. Louis L. Bailin Manager, Antenna Department	1
I 266	Federal Telecommunication Laboratories 500 Washington Avenue Nutley 10, New Jersey Attn: Technical Library	1		I 302	International Business Machines Corp. Space Guidance Center-Federal Systems Division Oswego, Tioga County New York Attn: Technical Reports Center	1
I 269	General Electric Company Electronics Park Syracuse, New York Attn: Documents Library B. Fletcher, Building 3-143A	1		I 265	I T T Laboratories 3700 East Pontiac Street Fort Wayne 1, Indiana Attn: Technical Library	1
I 793	General Electric Company Missile and Space Vehicle Department 3198 Chestnut Street, Philadelphia, Penn. Attn: Documents Library	1				

CODE	ORGANIZATION	NO. OF COPIES	CODE	ORGANIZATION	NO. OF COPIES
I 241	Dr. Henry Jasik, Consulting Engineer 298 Shames Drive Brush Hollow Industrial Park Westbury, New York	1	I 145	Microwave Radiation Company, Inc. 11121 Hindry Avenue Los Angeles 45, California Attn: Mr. Morris J. Ehrlich, President	1
I 279	Lockheed Aircraft Corporation 2555 N. Hollywood Way California Division Engineering Library Department 72-25, Plant A-1, Building 63-1 Burbank, California Attn: N. C. Harnois	1	I 648	The Mitre Corporation 244 Wood Street Lexington 73, Mass. Attn: Mrs. Jean E. Claflin, Librarian	1
I 468	Lockheed Aircraft Corporation Missile Systems Division Research Library Box 504, Sunnyvale, California Attn: Miss Eva Lou Robertson, Chief Librarian	1	I 934	Motorola, Inc. Phoenix Research Laboratory 3102 N. 56th Street Phoenix, Arizona Attn: Dr. A. L. Aden	1
I 136	The Martin Company P.O. Box 179 Denver 1, Colorado Attn: Mr. Jack McCormick	1	I 641	National Research Council Radio & Electrical Engineering Division Ottawa, Ontario, Canada Attn: Dr. G. A. Miller, Head Microwave Section	1
I 280	The Martin Company Baltimore 3, Maryland Attn: Engineering Library Antenna Design Group	1	I 284	North American Aviation, Inc. 12214 Lakewood Boulevard Downey, California Attn: Technical Information Center (495-12) Space & Information Systems Division	1
I 63	Mathematical Reviews 190 Hope Street Providence 6, Rhode Island	1	I 285	North American Aviation, Inc. Los Angeles International Airport Los Angeles 45, California Attn: Engineering Technical File	1
I 66	The W. L. Maxson Corporation 475 10th Avenue New York, New York Attn: Miss Dorothy Clark	1	I 286	Page Communications Engineers, Inc. 2001 Wisconsin Avenue, N.W. Washington 7, D.C. Attn: (Mrs.) Ruth Temple, Librarian	1
I 282	McDonnell Aircraft Corporation, Dept. 644 Box 516, St. Louis 66, Missouri Attn: C. E. Zoller, Engineering Library	1	I 287	Philco Corporation C and Tioga Streets Philadelphia 34, Pa. Attn: Mrs. Dorothy B. Collins Research Librarian	1
I 283	McMillan Laboratory, Inc. Brownville Avenue Ipswich, Mass. Attn: Security Officer, Document Room	1	I 225	Pickard and Burns, Inc. 240 Highland Avenue Needham 94, Mass. Attn: Dr. Richard H. Woodward	1
I 116	Melpar, Inc. 3000 Arlington Boulevard Falls Church, Virginia Attn: Engineering Technical Library	1	I 288	Polytechnic Research & Development Co. Inc. 202 Tillary Street Brooklyn 1, New York Attn: Technical Library	1
I 471	Microwave Associates, Inc. South Avenue Burlington, Mass.	1	I 232	Radiation Engineering Laboratory Main Street Maynard, Mass. Attn: Dr. John Ruze	1
I 390	Microwave Development Laboratory 90 Broad Street Wellesley 57, Mass. Attn: N. Tucker, General Manager	1	I 289	Radiation, Inc. P.O. Drawer 37 Melbourne, Florida Attn: Technical Library, Mr. M. L. Cox	1
I 379	Microwave Engineering Laboratories, Inc. 943 Industrial Avenue Palo Alto, California Attn: J. L. Melchor, President	.1			

CODE	ORGANIZATION	NO. OF COPIES	CODE	ORGANIZATION	NO. OF COPIES
I 914	Radiation Systems, Inc. 440 Swann Avenue Alexandria, Virginia Attn: Library	1	I 294	Raytheon Company Wayland Laboratory Wayland, Mass. Attn: Miss Alice G. Anderson, Librarian	1
I 233	Radio Corporation of America RCA Laboratories Rocky Point, New York Attn: P. S. Carter, Lab. Library	1	I 472	Raytheon Company Missile Systems Division Hartwell Road, Bedford, Mass. Attn: Donald H. Archer	1
I 290	RCA Laboratories David Sarnoff Research Center Princeton, New Jersey Attn: Miss Fern Cloak, Librarian	1	I 295	Republic Aviation Corporation Farmingdale, Long Island, New York Attn: Engineering Library	1
I 291	Radio Corporation of America Defense Electronic Products Building 10, Floor 7 Camden 2, New Jersey Attn: Mr. Harold J. Schrader, Staff Engineer Organization of Chief Technical Administrator	1	I 184	Ryan Aeronautical Company 2701 Harbor Drive Lindbergh Field San Diego 12, California Attn: Library	1
I 473	Radio Corporation of America Missile Control & Electronics Division Bedford Street, Burlington, Mass. Attn: Librarian	1	I 391	Sage Laboratories, Inc. 3 Huron Drive Natick, Mass.	1
I 757	Radio Corporation of America Surface Communications Systems Laboratory 75 Varick Street New York 13, N.Y. Attn: Mr. S. Krevsky	1	I 142	Sanders Associates, Inc. 95 Canal Street Nashua, New Hampshire Attn: Mr. Norman R. Wild	1
I 789	Radio Corporation of America West Coast Missile and Surface Radar Division Engineering Library, Building 306/2 Attn: L. R. Hund, Librarian 8500 Balboa Boulevard, Van Nuys, California	1	I 96	Sandia Corporation, Sandia Base P.O. Box 5800, Albuquerque, New Mexico Attn: Classified Document Division	1
I 930	Radio Corp. of America Defense Electronic Products Advanced Military Systems Princeton, New Jersey Attn: Mr. David Shore	1	I 546	Sandia Corporation Attn: Organization 1423 Sandia Base, Albuquerque, New Mexico	1
			I 682	Scanwell Laboratories, Inc. 6601 Scanwell Lane Springfield, Va.	1
I 292	Director, USAF Project RAND Via: AF Liaison Office The Rand Corporation 1700 Main Street Santa Monica, California	1	I 312	Space Technology Laboratories, Inc. P.O. Box 95001 Los Angeles 45, California Attn: Mrs. Margaret C. Whitnah Chief, Information Services	1
I 547	The Rand Corporation 1700 Main Street Santa Monica, California Attn: Technical Library	1	I 297	Sperry Gyroscope Company Great Neck, Long Island, New York Attn: Florence W. Turnbull Engineering Librarian	1
I 373	Rantec Corporation 23999 Ventura Boulevard Calabasas, California Attn: Grace Keener, Office Manager	1	I 367	Stanford Research Institute Documents Center Menlo Park, California Attn: Acquisitions	1
			I 104	Sylvania Electric Products, Inc. 100 First Avenue. Waltham 54, Mass. Attn: Charles A. Thornhill, Report Librarian Waltham Laboratories Library	1
I 293	Raytheon Company State Road, Wayland Laboratory Wayland, Mass. Attn: Mr. Robert Borts	1	I 260	Sylvania Elec. Prod Inc. Electronic Defense Laboratory P.O. Box 205 Mountain View, California Attn: Library	1

DISTRIBUTION LIST *Continued*

CODE	ORGANIZATION	NO. OF COPIES	CODE	ORGANIZATION	NO. OF COPIES
U 22	The Johns Hopkins University Homewood Campus Baltimore 18, Maryland Attn: Dr. Donald E. Kerr, Dept. of Physics	1	U 96	Northwestern University Microwave Laboratories Evanston, Illinois Attn: R. E. Beam	1
U 105	The Johns Hopkins University Applied Physics Laboratory 8621 Georgia Avenue Silver Spring, Maryland Attn: Mr. George L. Seielstad	1	U 78	Ohio State University Research Foundation 1314 Kinnear Road Columbus 8, Ohio Attn: Dr. T. E. Tice Department of Electrical Engineering	1
U 228	University of Kansas Electrical Engineering Department Lawrence, Kansas Attn: Dr. H. Unz	1	U 109	The University of Oklahoma Research Institute Norman, Oklahoma Attn: Prof. C. L. Farrar, Chairman Electrical Engineering	1
U 68	Lowell Technological Institute Research Foundation P.O. Box 709, Lowell, Mass. Attn: Dr. Charles R. Mingins	1	U 45	The Pennsylvania State University Department of Electrical Engineering University Park, Pennsylvania	1
U 32	Massachusetts Institute of Technology Research Laboratory of Electronics Building 26, Room 327 Cambridge 39, Mass. Attn: John H. Hewitt	1	U 185	University of Pennsylvania Institute of Cooperative Research 3400 Walnut Street, Philadelphia, Pa. Attn: Department of Electrical Engineering	1
U 26	Massachusetts Institute of Technology Lincoln Laboratory P.O. Box 73 Lexington 73, Mass. Attn: Mary A. Granese, Librarian	1	U 48	Polytechnic Institute of Brooklyn Microwave Research Institute 55 Johnson Street, Brooklyn, New York Attn: Dr. Arthur A. Oliner	1
U 34	McGill University Montreal, Canada Attn: Prof. G. A. Woonton Director, The Eaton Electronics Research Laboratory	1	U 97	Polytechnic Institute of Brooklyn Microwave Research Institute 55 Johnson Street Brooklyn, New York Attn: Mr. A. E. Laemmel	1
U 79	University of Michigan Engineering Research Institute Radiation Laboratory 912 N. Main Street, Ann Arbor, Michigan Attn: Prof. K. M. Siegel	1	U 184	Purdue University Department of Electrical Engineering Lafayette, Indiana Attn: Dr. Schultz	1
U 37	University of Michigan Engineering Research Institute Willow Run Laboratories, Willow Run Airport Ypsilanti, Michigan Attn: Librarian	1	U 176	Stanford University W. W. Hansen Laboratory of Physics Stanford, California Attn: Microwave Library	1
U 108	University of Minnesota Minneapolis 14, Minnesota Attn: Mr. Robert H. Stumm, Library	1	U 110	Syracuse University Research Institute Collendale Campus Syracuse 10, N.Y. Attn: Dr. C. S. Grove, Jr., Director of Engineering Research	1
U 194	Physical Science Laboratory New Mexico College of Agriculture and Mechanic Arts State College, New Mexico Attn: Mr. H. W. Haas	1	U 309	Technical University Oestervoldgade 10 G Copenhagen, Denmark Attn: Prof. Hans Lottrup Knudsen	1
U 39	New York University Institute of Mathematical Sciences Room 802, 25 Waverly Place New York 3, New York Attn: Professor Morris Kline	1	U 186	University of Tennessee Ferris Hall W. Cumberland Avenue Knoxville 16, Tennessee	1
			U 111	The University of Texas Electrical Engineering Research Lab. P.O. Box 8026, University Station Austin 12, Texas Attn: Mr. John R. Gerhardt Assistant Director	1

CODE	ORGANIZATION	NO. OF COPIES	CODE	ORGANIZATION	NO. OF COPIES
I 818	Sylvania Reconnaissance Systems Lab. Box 188, Mountain View, California Attn: Marvin D. Waldman	1	U 289	University of Southern California University Park Los Angeles, California Attn: Dr. Raymond L. Chaun Director, Engineering Center	1
I 240	TRG, Inc. 2 Aerial Way Syosset, New York Attn: M. L. Henderson, Librarian	1	U 239	Case Institute of Technology Electrical Engineering Department 10900 Euclid Avenue Cleveland, Ohio Attn: Professor Robert Plonsey	1
I 338	A. S. Thomas, Inc. 355 Providence Highway Westwood, Mass. Attn: A. S. Thomas, President	1	U 183	Columbia University Department of Electrical Engineering Morningside Heights, New York, N.Y. Attn: Dr. Schlesinger	1
I 708	Texas Instruments, Inc. 6000 Lemmon Avenue Dallas 9, Texas Attn: John B. Travis Systems Planning Branch	1	U 238	University of Southern California University Park Los Angeles 7, California Attn: Z. A. Kaprielian Associate Professor of Electrical Engineering	1
I 464	Trans-Tech, Inc. P.O. Box 346 Rockville, Maryland Attn: Mr. A. C. Blankenship Chief Electronics Engineer	1	U 10	Cornell University School of Electrical Engineering Ithaca, New York Attn: Prof. G. C. Dalman	1
I 139	Westinghouse Electric Corp. Electronics Division Friendship Int'l Airport Box 1897 Baltimore 3, Maryland Attn: Engineering Library	1	U 86	University of Florida Department of Electrical Engineering Gainesville, Florida Attn: Prof. M. H. Latour, Library	1
I 300	Zenith Plastics Company 1600 W. 135th Street Gardena, California Attn: Mr. S. S. Oleesky	1	U 59	Library Georgia Technology Research Institute Engineering Experiment Station 722 Cherry Street, N.W. Atlanta, Georgia Attn: Mrs. J. H. Crosland, Librarian	1
U 1	Library Geophysical Institute of the University of Alaska College, Alaska	1			
U 61	Brown University Department of Electrical Engineering Providence, Rhode Island Attn: Dr. C. M. Angulo	1	U 102	Harvard University Technical Reports Collection Gordon McKay Library 303 Pierce Hall Oxford Street, Cambridge 38, Mass. Attn: Librarian	1
U 157	California Institute of Technology Jet Propulsion Laboratory 4800 Oak Grove Drive Pasadena, California Attn: Mr. I. E. Newlan	1	U 103	University of Illinois Documents Division Library Urbana, Illinois	1
U 99	California Institute of Technology 1201 E. California Street Pasadena, California Attn: Dr. C. Papas	1	U 104	University of Illinois College of Engineering Urbana, Illinois Attn: Dr. P. E. Mayes, Department of Electrical Engineering	1
U 3	Space Sciences Laboratory Leuschner Observatory University of California Berkeley 4, California Attn: Dr. Samuel Silver, Professor of Engineering Science and Director, Space Sciences Laboratory	1	U 169	Illinois Institute of Technology 3301 S. Dearborn Street Chicago 16, Illinois Attn: Dr. George I. Cohn	1
U 100	University of California Electronics Research Lab. 332 Cory Hall, Berkeley 4, California Attn: J. R. Whinnery	1	U 240	Illinois Institute of Technology Technology Center Department of Electrical Engineering Chicago 16, Illinois Attn: Paul C. Yuen Electronics Research Laboratory	1

CODE	ORGANIZATION	NO. CF COPIES	CODE	ORGANIZATION	NO. OF COPIES
U 51	The University of Texas Defense Research Laboratory Austin, Texas Attn: Claude W. Horton, Physics Library	1	U 133	University of Washington Department of Electrical Engineering Seattle 5, Washington Attn: G. Held, Associate Professor	1
U 133	University of Toronto Department of Electrical Engr. Toronto, Canada Attn: Prof. G. Sinclair	1	U 187	University of Wisconsin Department of Electrical Engineering Madison, Wisconsin Attn: Dr. Scheibe	1

STANFORD
RESEARCH
INSTITUTE

Menlo Park, California

REGIONAL OFFICES AND LABORATORIES

SOUTHERN CALIFORNIA LABORATORIES
820 Mission Street
South Pasadena, California

NEW YORK OFFICE
270 Park Avenue
New York 17, N. Y.

WASHINGTON OFFICE
711 14th Street, N. W.
Washington 5, D. C.

EUROPEAN OFFICE
Pelikanstrasse 37
Zurich 1, Switzerland

RESEARCH REPRESENTATIVES

HONOLULU, HAWAII
Finance Factors Building
195 South King Street
Honolulu, Hawaii

PORTLAND, OREGON
Suite 914, Equitable Buildin
421 Southwest 6th Avenue
Portland, Oregon

PHOENIX, ARIZONA
Suite 216, Central Plaza
342₄ North Central Avenue
Phoenix, Arizona